Nanostructured Polysulfone-Based Block Copolymer Membranes

Dissertation by

Yihui Xie

In Partial Fulfillment of the Requirements

For the Degree of

Doctor of Philosophy of Science

King Abdullah University of Science and Technology

Thuwal, Kingdom of Saudi Arabia

EXAMINATION COMMITTEE APPROVALS FORM

The dissertation of Yihui Xie is approved by the examination committee.

Committee Chairperson: Professor Suzana Nunes
Committee Members: Assistant Professor Peiying Hong, Professor Nikolaos Hadjichristidis, Professor David Haddleton

ABSTRACT

Nanostructured Polysulfone-Based Block Copolymer Membranes

Yihui Xie

The aim of this work is to fabricate nanostructured membranes from polysulfone-based block copolymers through self-assembly and non-solvent induced phase separation. Block copolymers containing polysulfone are novel materials for this purpose providing better mechanical and thermal stability to membranes than polystyrene-based copolymers, which have been exclusively used now.

Firstly, we synthesized a triblock copolymer, poly(*tert*-butyl acrylate)-*b*-polsulfone-*b*-poly(*tert*-butyl acrylate) through polycondensation and reversible addition-fragmentation chain-transfer polymerization. The obtained membrane has a highly porous interconnected skin layer composed of elongated micelles with a flower-like arrangement, on top of the graded finger-like macrovoids. Membrane surface hydrolysis was carried out in a combination with metal complexation to obtain metal-chelated membranes. The copper-containing membrane showed improved antibacterial capability.

Secondly, a poly(acrylic acid)-*b*-polysulfone-*b*-poly(acrylic acid) triblock copolymer obtained by hydrolyzing poly(*tert*-butyl acrylate)-*b*-polsulfone-*b*-poly(*tert*-butyl acrylate) formed a thin film with cylindrical poly(acrylic acid) microdomains in polysulfone matrix through thermal annealing. A phase inversion membrane was prepared from the same polymer *via* self-assembly and chelation-assisted non-solvent induced phase separation. The spherical micelles pre-formed in a selective solvent mixture packed into an ordered lattice in aid of metal-poly(acrylic acid) complexation. The space between

micelles was filled with poly(acrylic acid)-metal complexes acting as potential water channels. The silver^{0} nanoparticle-decorated membrane was obtained by surface reduction, having three distinct layers with different particle sizes. Other amphiphilic copolymers containing polysulfone and water-soluble segments such as poly(ethylene glycol) and poly(*N*-isopropylacrylamide) were also synthesized through coupling reaction and copper^{0}-mediated reversible-deactivation radical polymerization.

Finally, phase inversion membranes were prepared from polytriazole-polysulfone random copolymers, which were obtained by "clicking" 1,2,3-triazole ring substituents bearing OH groups onto the polysulfone backbone *via* copper^{I}-catalyzed azide-alkyne cycloaddition. The increased hydrophilicity of membranes imparted the higher water permeability and fouling resistance to the ultrafiltration membranes. Polytriazole-*b*-polysulfone-*b*-polytriazole triblock copolymer was synthesized by RAFT and post-polymerization click modification. Hydrogen bond-mediated self-assembly induced the formation of a nanostructured polytriazole-*b*-polysulfone-*b*-polytriazole / poly(acrylic acid)-*b*-polysulfone-*b*-poly(acrylic acid) blend membrane with a 1: 1 stoichiometric ratio of triazole and acid. String-like fused micelles with polytriazole/poly(acrylic acid) corona were present on the membrane surface, after immersion in a coagulation bath of copper^{2+} aqueous solution.

ACKNOWLEDGEMENTS

First I would like to thank my supervisor, Professor Suzana Nunes for giving me the opportunity to material and polymer chemistry that has fascinated me, for all the guidance and inspiration throughout the course of study. My appreciation also goes to another important person, Dr. Russell Tayouo, who helped initiate the project and taught me so many valuable hands-on skills in the lab. I want to extend my gratitude to the postdocs in our group for sharing their knowledge generously. Special thanks to the experienced chemists, Dr. Stefan Chisca and Dr. Christopher Waldron for providing suggestions on polymer synthesis and characterization. I would like to thank my fellow students for useful discussions and assistance. Among them, Mr. Burhannudin Sutisna and Mr. Nicolas Moreno Chaparro contributed a lot to the self-assembly studies in this thesis. Many thanks to Dr. Ali Reza Behzad and Dr. Rachid Sougrat from the core lab for helping with advanced electron microscopies. Finally, my genuine gratitude is extended to my family and friends. I cannot finish this thesis without their encouragement and support. Thank all of you (including numerous people unmentioned) for making my six-year Ph.D. study at KAUST such an amazing and rewarding experience!

TABLE OF CONTENTS

LIST OF ABBREVIATIONS

AAO	anodic aluminum oxide
AFM	atomic force microscopy
AIBN	2,2'-azobis(2-methylpropionitrile)
AQPs	aquaporins
ATRP	atom transfer radical polymerization
BiBB	α-bromoisobutyryl bromide
BPA	bisphenol-A
BSA	bovine serum albumin
CIPS	complexation-induced phase separation
CNTs	carbon nanotubes
CRP	controlled/living radical polymerization
CTA	chain transfer agent
CuAAC	copper^{I}-catalyzed azide-alkyne cycloaddition
CuAAC	copper(I)-catalyzed azide-alkyne cycloaddition
cyro-FESEM	cryo-field emission scanning electron microscopy
cyro-TEM	cryo-transmission electron microscopy
DCC	N,N'-dicyclohexylcarbodiimide
DCDPS	bis(4-chlorophenyl) sulfone
DCM	dichloromethane
DCTB	*trans*-2-[3-(4-*tert*-Butylphenyl)-2-methyl-2-propenylidene]malononitrile
DF	degree of functionalization
DLS	dynamic light scattering
DMA	dynamic mechanical analysis
DMAc	N,N-dimethylacetamide
DMAP	4-(dimethylamino)pyridine
DMF	dimethylformamide
DMSO	dimethyl sulfoxide
DMSO	dimethyl sulfoxide
DOX	dioxane
DP	degree of polymerization
DPD	dissipative particle dynamics
DSC	differential scanning calorimetry
EDS	energy-dispersive X-ray spectroscopy
EELS	electron energy loss spectroscopy
FESEM	field emission scanning electron microscopy

FRP	free radical polymerization
FTIR-ATR	fourier transform infrared - attenuated total reflectance spectroscopy
GISAXS	grazing incidence small-angle X-ray scattering
GPC	gel permeation chromatography
HMTETA	hexa-methyltriethylenetetramine
LALS	low-angle light scattering
LAMMPS	large-scale atomic/molecular massively parallel simulator
LCST	lower critical solution temperature
MAIpG	3-O-methacryloyl-1,2:5,6-di-O-isopropylidene-$_D$-glucofuranose
MALDI-TOF MS	matrix assisted laser desorption ionization - time of flight mass spectroscopy
MD	molecular dynamics
Me_6TREN	tris[2-(dimethylamino)ethyl]amine
MF	microfiltration
MFP	mean flow pore size
M_n	number-average molecular weight
M_w	weight-average molecular weight
MWCO	molecular weight cut-off
NF	nanofiltration
NIPAM	*N*-isopropylacrylamide
NIPS	non-solvent induced phase separation
NMP	nitroxide-mediated polymerization or N-methyl-2-pyrrolidone
NMR	nuclear magnetic resonance spectroscopy
ODT	order-to-disorder transition
OSET	outer-sphere single electron transfer
PAA	poly(acrylic acid)
PAA-PSU-PAA	poly(acrylic acid)-*b*-polysulfone-*b*-poly(acrylic acid)
PAN	polyacrylonitrile
PDI	polydispersity index
PEG	poly(ethylene glycol)
PEGMA	poly(ethylene glycol) methyl ether methacrylate
PEG-PNIPAM	poly(ethylene glycol)-*b*-Poly(N-isopropylacrylamide)
PEG-PNIPAM-PSU-PNIPAM-PEG	poly(ethylene glycol)-*b*-poly(N-isopropylacrylamide)-*b*-polysulfone-*b*-poly(N-isopropylacrylamide)-*b*-poly(ethylene glycol)
PEG-PSU-PEG	poly(ethylene glycol)-*b*-polysulfone-*b*-poly(ethylene glycol)
PEO	poly(ethylene oxide)
PES	polyethersulfone

PES	polyethersulfone
PI	polyisoprene
PMDETA	N,N,N′,N″,N″-pentamethyldiethylenetriamine
PN_3-PSU-PN_3	poly(vinylbenzyl azide)-*b*-polysulfone-*b*-poly(vinylbenzyl azide)
PNIPAM	poly(*N*-isopropylacrylamide)
PPS-PI-PPS	poly (4-vinylphenyl-dimethyl-2-propoxysilane)-*b*-polyisoprene-*b*-poly (4-vinylphenyl-dimethyl-2-propoxysilane)
PS-*b*-P2VP	polystyrene-*b*-poly(2-vinylpyridine)
PS-*b*-P4VP	polystyrene-*b*-poly(4-vinyl pyridine)
PS-*b*-PAA	polystyrene-*b*-poly(acrylic acid)
PS-*b*-PI-*b*-PLA	polystyrene-*b*-polyisoprene-*b*-polylactide
PS-*b*-PLA	polystyrene-*b*-polylactide
PS-*b*-PMMA	poly(styrene-*b*-methyl methacrylate)
PSU	polysulfone
P*t*BA-PSU-P*t*BA	poly(*tert*-butyl acrylate)-*b*-polsulfone-*b*-poly(*tert*-butyl acrylate)
P*t*BS	poly(*tert*-butyl styrene)
PTMSS	poly(4-trimethylsilyl styrene)
PTrN	polytriazole
PTrN-PSU-PTrN	polytriazole-*b*-polysulfone-*b*-polytriazole
PTrN-PSU-PTrN	polytriazole-*b*-polysulfone-*b*-polytriazole
PVBC-PSU-PVBC	poly(4-vinylbenzyl chloride)-*b*-polysulfone-*b*-poly(4-vinylbenyl chloride)
PVDF	polyvinylidene fluoride
PWP	pure water permeance
RAFT	reversible addition-fragmentation chain-transfer
RAFT	reversible addition fragmentation chain transfer
RALS	right-angle light scattering
RDRP	reversible-deactivation radical polymerization
R_g	radius of gyration
RI	refractive index
RIE	reactive ion etch
RO	reverse-osmosis
SCNIPS	self-assembly and chelation-assisted non-solvent induced phase separation
SET-LRP	single electron transfer living radical polymerization
SNIPS	self-assembly and non-solvent induced phase separation
SNPs	single nucleotide polymorphisms
*t*BA	*tert*-butyl acrylate

TEA	triethylamine
TEM	transmission electron microscopy
TFA	trifluoroacetic acid
TFC	thin film composite
T_g	glass transition temperature
TGA	thermogravimetric analysis
THF	tetrahydrofuran
TREN	tris(2-aminoethyl)amine
TsCl	*p*-Toluenesulfonyl chloride
UF	ultrafultration
$VBBI^{+}Tf_2N^{-}$	1-(4-vinylbenzyl)-3-butylimidazolium bis(trifluoromethylsulfonyl) imide
VBC	4-Vinylbenzyl chloride

LIST OF ILLUSTRATIONS

LIST OF TABLES

CHAPTER 1

Introduction and Background

1.1 A Brief History of Synthetic Membranes

A membrane is a selective barrier between two phases[1] that allows the passage of specific particles or molecules and retains other substances when exposed to a driving force. The main advantages of membrane technology include no additives or regeneration of spent media, lower energy consumption, easy scale-up and integration into other separation or reaction processes.[2] Currently four types of pressure-driven membranes are employed in

Table 1.1. Membrane classification by pore size and target species

Membrane type	Pore size (nm)	Target species
microfiltration (MF)	> 50	particles, sediments, algae, protozoa, bacteria
ultrafiltration (UF)	2 ~ 50	small colloids, viruses, proteins
nanofiltration (NF)	< 2	dissolved organic matter, divalent ions (Ca^{2+}, Mg^{2+})
reverse-osmosis (RO)	nonporous	monovalent Species (Na^{+}, Cl^{-})

water reuse and desalination: microfiltration (MF), ultrafiltration (UF), nanofiltration (NF), and reverse-osmosis (RO) membranes.[3] Their characteristic pore size and targeted solutes is shown on Table 1.1.

The history of systematic studies of membrane phenomena can be traced to the eighteenth century. The French scientist Abbe Nollet discovered the semipermeability of diaphragm by chance in 1748, and coined the word “osmosis” to describe permeation of water through the animal membrane.[4] Within nearly 200 years, the theories of modern membrane science have been established by numerous scientific contributions after Nollet. Meanwhile synthetic membranes had been developed to replace animal diaphragm, e.g., the parent of artificial membranes -- collodion (nitrocellulose) membranes, and cellulose acetate microfiltration membranes.[5] However, by 1960 no significant membrane industry existed at all. Their widespread industrial use as a separation process was prohibited by four problems: They were too unreliable, too slow, too unselective, and too expensive.[6]

A critical breakthrough that transformed membrane separation from a laboratory study to a widely practiced technology in industry was then achieved by the development of asymmetric membranes, discovered by Loeb and Sourirajan.[7] These membranes have a porosity gradient with a thin denser toplayer or skin (thickness < 1 μm) and a highly permeable sublayer (50-200 μm) of increasing pore size, which provides mechanical stability. The ultrathin skin represents the actual selective barrier and determines the permeation rate, which is inversely proportional to the thickness. Thus asymmetric membranes show an unprecedentedly high flux.

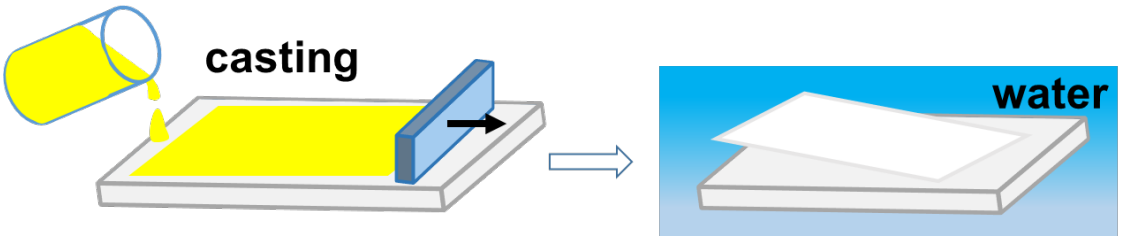

Figure 1.1. Preparation method of a typical asymmetric membrane by non-solvent induced phase separation (NIPS).

The technique Loeb and Sourirajan introduced for making asymmetric membranes now is also known as non-solvent induced phase separation (NIPS) or phase inversion.[8, 9] In this process, a concentrated polymer solution (~ 20 wt%) or dope is cast onto a supporting layer, for example a non-woven polyesters or a glass plate, by a casting knife with a gap of 50 to 500 μm. The cast film is then immersed in a coagulation bath containing a non-solvent (water). The solvent - non-solvent exchange leads to polymer solution separation into two phases: a solid, continuous polymer-rich phase that forms the matrix of the membrane and a liquid, polymer-poor phase that forms the membrane pores. Figure 1.1 describes this process. The surface of the cast film touches water first and precipitates rapidly, forming the dense, selective skin. This skin slows the entry of water into the underlying polymer solution, which precipitates then slowly. Thus the pore forming liquid droplets are able to agglomerate while the casting solution is still fluid. As a result, an asymmetric structure with a more porous sublayer is formed.[10-12] Although originally this procedure was proposed to prepare cellulose acetate reverse osmosis membranes, it has been successfully adapted to make almost all ultrafiltration and many gas separation membranes.[13] Furthermore, this process can be easily scaled up to continuously produce commercial membranes of large area.

1.2 Nanoporous Block Copolymer Membranes *via* Bulk Self-assembly

The unique benefits of the asymmetric membranes prepared by phase inversion are so great that they have dominated the membrane market over the past half-century.[13, 14] However the conventional phase inversion membranes prepared from homopolymers still suffer from one fundamental problem: pores formed during phase separation have a broad size distribution with a disordered structure. Nanoporous block copolymer membranes are radically different, providing extremely sharp pore size distribution and ultrahigh porosity.[15-18] They have tremendous potential to be the next generation of separation materials and open the door for membranes to many other applications such as drug delivery.

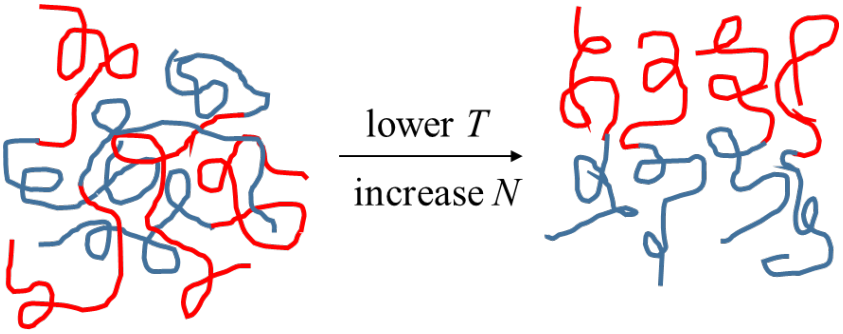

Figure 1.3. Microphase separation in a block copolymer melt.

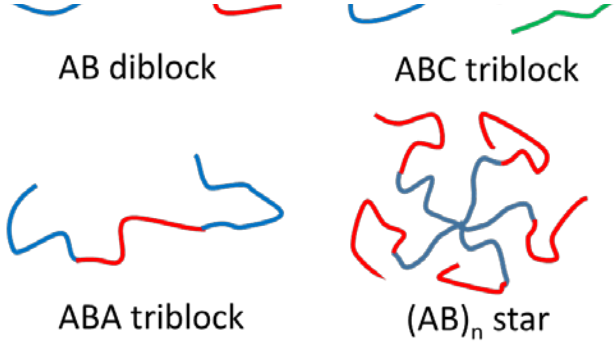

Figure 1.2. Various block copolymer architectures.

A block copolymer consists of two or more chemically distinct polymer chains (i.e., blocks) covalently bonded together to form a single macromolecule. Anionic polymerization[19] and further developments in various types of controlled/living polymerization techniques enable polymer chemists to synthesize well-defined linear homopolymers, block copolymers and more complex architectures with low molecular weight and compositional polydispersity.[20] A stunning array of block copolymer configurations is illustrated by Figure 1.2, which depicts merely a small part of the enormous range of molecular architectures.[21]

Block copolymers are known to undergo microphase separation of the components into nanoscale domains in melt state or bulk, driven by chemical incompatibilities between the different blocks.[22-27] But in order to keep the immiscible A and B portions of each

molecule apart, copolymer chains must adopt extended configurations, as illustrated in Figure 1.3.[24] Since there are fewer configurations available to extended polymer chains than to those in their native randomly coiled state, an entropic restoring force from the covalent linkages is generated that serves to counterbalance the tendency for the blocks to segregate and limit the phase separation between two blocks to nanoscale. In a word, the competition between favored enthalpic demixing and the entropic penalty (reduction) for stretching of polymer chains to fill space uniformly governs the thermodynamics of block copolymer melts and their phase behavior.

In the simplest case of a diblock copolymer, the microphase separation depends on three parameters:[25] (1) the total degree of polymerization, N, (2) the volume fractions of one block, $f_A = N_A/N$, where N_A is the number of A monomers per molecule, and (3) the Flory–Huggins interaction parameter, χ_{AB}, which describes the free energy cost per monomer of contacts between the A and B monomeric units and is given by:[26]

$$\chi_{AB} = \left(\frac{z}{k_B T}\right)\left[\varepsilon_{AB} - \frac{1}{2}(\varepsilon_{AA} + \varepsilon_{BB})\right]$$

Equation 1.1

where z is the number of nearest neighbors per monomeric unit in the polymer, k_B is the Boltzman constant, $k_B T$ is the thermal energy, and ε_{AB}, ε_{AA}, and ε_{BB} are the interaction energies per monomeric unit of A–B, A–A, and B–B, respectively. Positive χ_{AB} indicates net repulsion between species A and B, whereas a negative value indicates a free-energy drive towards mixing of unlike monomeric units. For typical block copolymers, in which there are no strong specific interactions like hydrogen bonding or ionic charges, χ_{AB} is

positive that shows repulsion. Moreover, χ_{AB} is inversely proportional to temperature, so that demixing is promoted as the temperature decreases. The translational and configurational entropy contribution to the free energy is proportional to the total degree of polymerization, N, which is another parameter that strongly influences phase behavior of block copolymers. For large N the loss of entropy leads to a reduction of the A-B monomer contacts and thus to local ordering. Since the entropic and enthalpic contributions to the free energy scale as N^{-1} and χ, respectively, it is the product χN that determines the degree of segregation of block copolymers. When χN exceeds a critical value, the transition from a homogeneous melt of chains to periodically ordered domain occurs, called order-to-disorder transition (ODT).

The equilibrium morphology of the ordered phase depends on the composition (volume fraction) of the block copolymer, f. For nearly symmetric diblocks ($f \sim 1/2$), a lamellar (L) phase occurs, with alternating layers of the constituent blocks. For moderate asymmetries, a complex bicontinuous state, known as the gyroid (G) phase, has been observed in which the minority blocks form domains consisting of two interweaving three fold-coordinated lattices. At yet higher asymmetries, the minority component forms hexagonally packed cylinders (C). When the compositional asymmetry is further increased, it gives way to a body-centered cubic spherical (S) phase. As the molecules become asymmetric, structures with more curvature are preferred.[23]

The phenomena of morphological transitions can be explained by a cone-column mechanism[28] as illustrated in Figure 1.4. In microphase separation, the formation of the various morphologies is attributed to two competing factors: interfacial energy between the two domains (an enthalpic contribution), and chain stretching (an entropic contribution). Phase transitions in block copolymers are driven by the tendency to curve the interface as the copolymer becomes asymmetric in composition. The curvature allows the molecules to balance the degree of stretching between the A and B blocks, and at the same time minimize interfacial area in order to lower the total interfacial energy. When the diblocks are highly asymmetric, i.e. the volume fraction of block A is small, the A blocks prefer to aggregate into spherical microdomains, leaving the B blocks to surround them as ‘‘coronas’’ (Figure 1.4a). This energetically preferable arrangement allows the longer B blocks to reside on the convex side of the A-B interface, which affords them more configurational entropy. For more asymmetric copolymers it becomes energetically

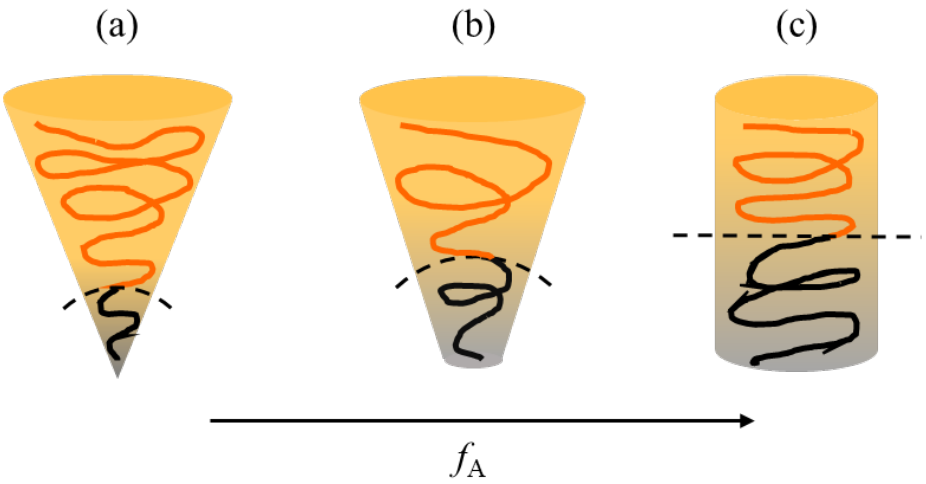

Figure 1.4. Schematic illustration of polymer chain arrangements in different morphologies of AB diblocks changing from sphere (a) to cylinder (b) and to lamella (c), as the volume fraction of the A block (black), f_A, increases to 0.5.

more favorable for phases with curved interfaces to form. As f_A increases, the corona volume fraction decreases and less curved interfaces are formed (Figure 1.4b and c), the polymer chains have to adopt new arrangements to reduce their stretching, leading to a morphological transition from spheres to cylinders and to lamellae.

The extensive studies of block copolymer self-assembly in bulk since the 1960s have been driven not only by the scientific curiosity, but by the tremendous potential utility of the periodically regular structures with compositional heterogeneities in nanotechnological applications. The sizes of characteristic microdomains rich in one block normally are of the order of a few times the radius of gyration (R_g) of the constituent blocks and thus range from a few to 100 nm on the mesoscale.[29] By removing the minority component in the microdomain, nanoporous materials with pore dimensions less than 100 nm can be generated from the ordered block copolymer precursors, which act as templates.[15, 29-32] These nanoporous materials have attracted considerable scientific interest in a variety of advanced applications because of their preciously controlled pore size and tailored chemical properties of nanochannels. One of the successful and well-known examples is block copolymer nanolithography employing nanoporous templates.[33] Nanoporous membranes are another important group of ordered block copolymer materials, being pursued for water filtration and other controlled separation process.[15] The most common fabrication methodology involves selective removal of the sacrificial blocks (minority component) or dissolution of corresponding homopolymers in a dense thin film (initially cast onto a substrate) of block copolymer having hexagonally packed cylinders oriented perpendicular to the surface after thermal or solvent annealing. A typical scheme of fabrication is shown in Figure 1.5.

The first work was performed by Lee et al. in 1998,[34] in which a triblock copolymer of poly (4-vinylphenyl-dimethyl-2-propoxysilane)-*b*-polyisoprene-*b*-poly (4-vinylphenyl-dimethyl-2-propoxysilane) (PPS-PI-PPS) that formed a lamellar morphology was cast into a thin film, crosslinked by acid hydrolysis of the alkylsiloxane moiety, treated with O_3 and washed with methanol to remove the PI component, and the membrane pores (20 nm) were formed. Inspired by this pioneering work, the past several years have witnessed burgeoning endeavors in this rewarding research area. Recent reviews are available with a comprehensive summary on various block copolymers with sacrificial components and degradation techniques that have been developed to generate nanoporous membranes.[32, 35] Some classic examples in the literature are described below.

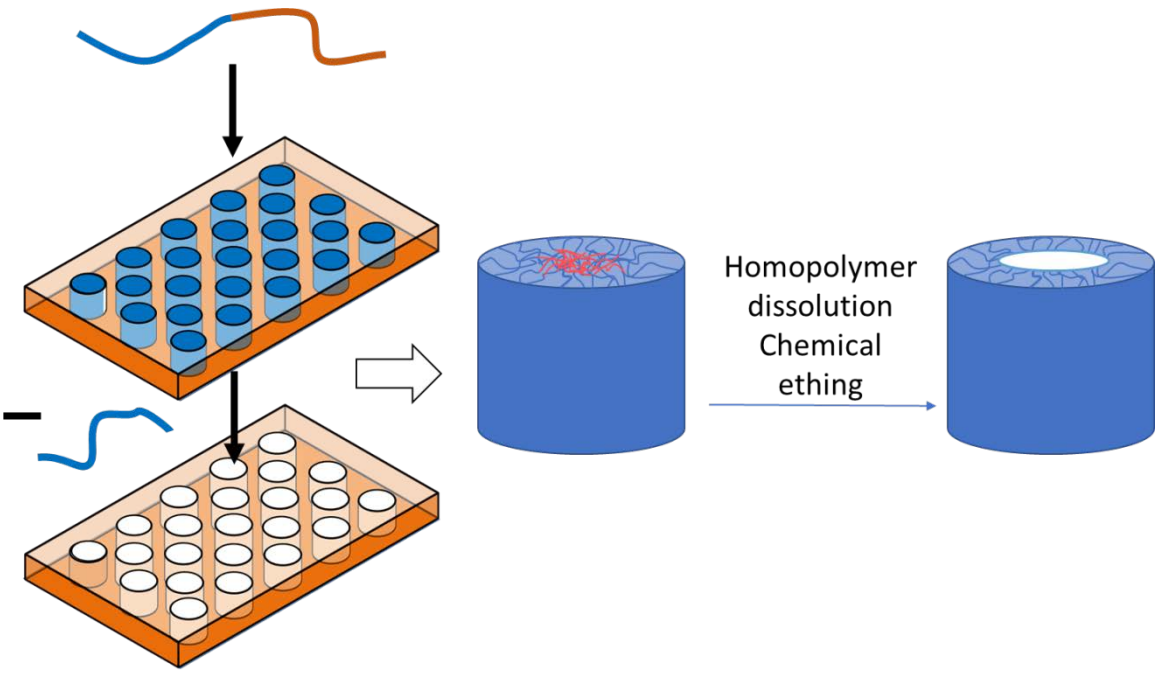

Figure 1.5. Schematic representation of the procedure for preparing nanoporous membrane, starting from cylinder-forming diblock copolymer thin film, to nanoporous membrane obtained by selective etching/dissolution.

Yang et al.[36, 37] prepared thin films of poly(styrene-*b*-methyl methacrylate) (PS-*b*-PMMA) on PS-*r*-PMMA-coated silicon wafers. After thermal annealing, the film with perpendicular cylindrical PMMA domains was floated from the substrate by treating with HF and transferred to a porous membrane support. The well-ordered array of cylindrical pores of diameter 15 nm with a narrow distribution was obtained after removal of sacrificial PMMA component, which could be blended homopolymer[37] or UV-etched block,[36] by rinsing with acetic acid. The composite membrane with such a mesoporous PS selective layer exhibits ultrahigh selectivity and flux for the virus filtration. Further applications include controlled delivery of protein drugs, and single nucleotide polymorphisms (SNPs) detection by functionalizing nanopores with single-stranded DNA.[38, 39]

Hillmyer and Cussler developed a strategy for preparing nanoporous membranes templated by polystyrene-*b*-polylactide (PS-*b*-PLA) self-assembly.[40] By directly casting the block copolymer with the appropriate solvents on the water-filled polyethersulfone (PES) support and controlling the solvent evaporation rate,[41] a thin film with PLA cylinders perpendicular to the surface was produced without thermal annealing. Once dried, UV treatment improved adhesion and promoted cross-linking. Subsequent immersing the composite membrane in a dilute NaOH solution selectively etched the PLA block, leading to the monodisperse nanopores of 24 nm diameter. Later, they proposed a nanoporous ultrafiltration membrane with a thin selective layer (80 nm) derived from a triblock copolymer polystyrene-*b*-polyisoprene-*b*-polylactide (PS-*b*-PI-*b*-PLA).[42] A spontaneous perpendicular alignment of the core (PLA)-shell (PI) cylindrical domains was achieved without any additional annealing or careful control after spin-

coating of copolymer solution on top of the support membrane. Base degradation of PLA and a short O_2 reactive ion etch (RIE) left 20 nm cylindrical PI-lined channels, which reinforced the mechanical robustness of the PS matrix. This membrane showed a higher hydraulic permeability due to the ultrathin block copolymer toplayer, and a sharp solutes rejection, which agrees with theoretical predictions.

Recently a nondestructive pore-making method, "selective swelling" or "solvent-induced reconsctruction",[43-46] has been employed to fabricate nanoporous membranes derived from ordered block copolymer thin film.[47, 48] Wang et al. reported a fast alignment of perpendicular cylinders in polystyrene-*b*-poly(2-vinylpyridine) (PS-*b*-P2VP) films by annealing with a neutral solvent chloroform. When the thin film is immersed in hot ethanol, the osmotic pressure generated by the swelling of the P2VP chains in the cylindrical domains drives the overflow of the P2VP chains and the deformation of the non-swollen PS matrix as the volume of P2VP expands. Upon the evaporation of ethanol in air, the compressed structure of PS matrix is fixed and cannot recover to its initial state, while the P2VP chains shrink with the loss of ethanol and collapse on the matrix walls. Consequently, the space initially occupied by the swollen P2VP transformed into straight nanopores lined with P2VP.[43, 47, 48]

1.3 Self-assembly and Non-solvent induced Phase Separation

Although nanoporous membranes have been successfully fabricated *via* bulk self-assembly of block copolymer melts followed by etching or selective dissolution of the minority component, this approach increases the number and complexity of fabrication

steps, e.g., modification of substrates, annealing, etching and transferring, making it only available on laboratory scale so far. Furthermore, complete etching is difficult to achieve for open cylindrical nanopores that span the entire film, making their permeability too low to compete with phase inversion membranes.[42] On the other hand, solution-based block copolymer self-assembly[24, 25, 49-52] offers another important and useful route to devise facile processing methodologies towards large scale manufacturing. In the following, the principles of self-assembly in solution will be described.

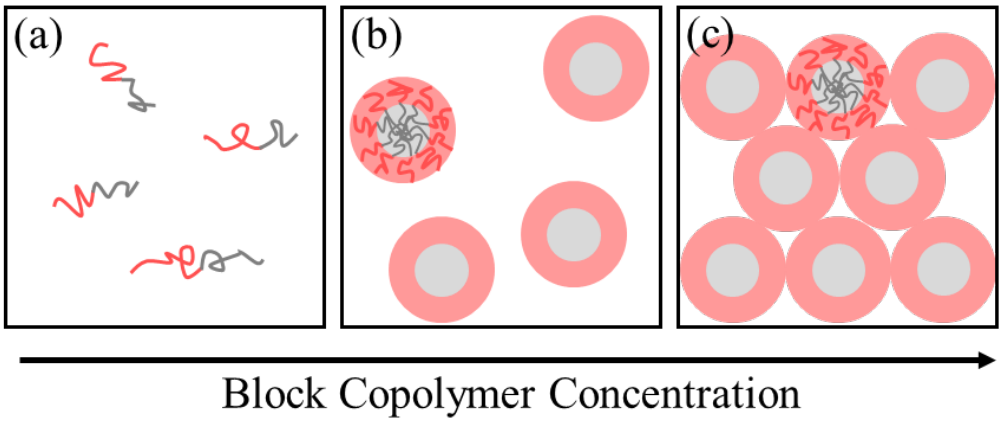

Figure 1.6. Schematic representation of (a) unimers under the critical micelle concentration (cmc), (b) micelles formed when concentration above cmc, and (c) supramolecular assembly of micelles occurred in concentrated solution.

When amphiphilic block copolymer are dissolved in a selective solvent, the two blocks are not only incompatible, but might interact very differently with their environment due to their chemical nature and behave distinctively.[24, 50] These differences can induce microphase separation of block copolymers in bulk and with the introduction of solvent increases the level of complexity of self-assembly.[25] The self-assembly of diblock copolymers in solvent–nonsolvent mixtures involves six χ-parameters, namely χ_{AB}, χ_{AS}, χ_{AS}, χ_{BS}, χ_{BN}, χ_{SN}, where A and B represent the two blocks, S expresses the good solvent for both blocks, and N denotes the nonsolvent (selective solvent) for one of the blocks. The more components are present in the solution, the more complex is the self-assembly process. The phase behavior of block copolymers in solution include two basic processes: micellization and supramolecular assembly of micelles,[24] illustrated in Figure 1.6.

Micellization occurs when block copolymer chains associate into micelles in dilute solution with a selective solvent.[51] The core of the micelle is formed by the insoluble or

poorly solvated block, shielded from the solvent, whereas the corona contains the selectively solvated block being oriented towards the continuous solvent medium. The concentration at which the first micelle forms is called the critical micelle concentration (cmc) (Figure 1.6b).[52] Below cmc only molecularly dissolved and nonassociated copolymer is present in solution, usually as unimers (Figure 1.6a). Supramolecular assembly of micelles occurs from the semi-dilute and concentrated block copolymer solutions over a certain concentration when the intermicellar entanglement results in an arrangement of ordered micelles by (Figure 1.6c). In dilute solution, the micelles appear as isolated aggregates with no or low spatial correlation. At higher concentration, chains begin to overlap, and this can lead to the formation of a lyotropic liquid crystalline phase (lattice) such as a closed packed cubic phase of spherical micelles, a hexagonal phase of rod-like micelles or a lamellar phase.

In an early contribution, de Gennes considered three terms for the free energy of a micelle: (1) the deformation free energy of core-forming blocks, associated with the constraints among the core-forming blocks from stretching, (2) the deformation free energy of corona-forming blocks from the repulsion among chains forming the corona, and (3) the interfacial energy between the core and the solvent outside.[52] Thus the total Gibbs free energy $G(micelle)$ of the micelle can be estimated as the sum of these contributions:

$$G(micelle) = G(core) + G(shell) + G(interface)$$

Equation. 1.2

Like all the other physicochemical processes, the self-assembly of block copolymer is

driven by the negative total standard Gibbs free energy of micelles.

$$\Delta G^0 = \Delta H^0 - T\Delta S^0$$

Equation. 1.3

In organic solution the micellization of block copolymers is an enthalpic driven process, resulting from the dominant ΔH^0 values with respect to ΔS^0 which is also negative. The negative values of ΔH^0 arise from the exothermic energy interchange due to the replacement of polymer/solvent interactions by polymer/polymer and solvent/solvent interactions. These negative values of ΔS^0, unfavorable to micellization, arise from the loss in the combinatorial entropy because the copolymer chains are less swollen in the micelles than in the unassociated state. The number of possible conformations is also decreased due to the placement of block junctions at the core/shell interface of the micelles. In conclusion, the self-assembly process sacrifices the entropy of the single chains, but prevents a larger enthalpy penalty resulting from energetically unfavorable polymer/solvent interactions, and therefore lowers the total free energy of the system ($\Delta G^0 < 0$).[25] However, in aqueous medium the driving force behind the self-assembly is normally of entropic origin.[52]

The higher level of complexity of block copolymer self-assembly in solution stimulates richer and more varied morphologies than bulk. Although the spherical micelles are most common aggregates to form in the majority of systems, more than 20 accessible self-assembled structures have been identified.[25] For diblock copolymers, the micellar structures can be divided into two groups, depending on the composition of starting

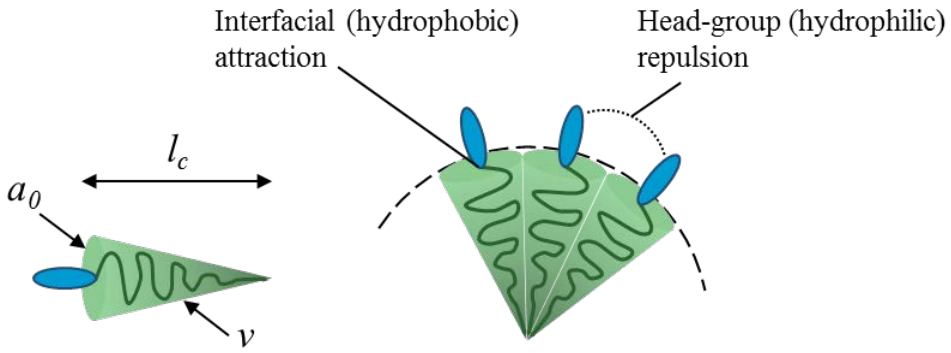

Figure 1.7. Schematic illustration of the two contributing forces: interfacial attraction and head-group repulsion, and three geometric parameters, a_0, v and l_c that defines the packing of block copolymers into micelles which in turn determines the final micelle structures.

polymers: (1) crew-cut micelles with a large core and a short, highly stretched coronal chains (2) star-like micelles with a small core compared to the much larger corona. An astonishing spectrum of micelle morphologies formed from polystyrene-*b*-poly(acrylic acid) (PS-*b*-PAA) under different conditions has been depicted in the literature.[53]

With the thermodynamics of micellization in mind, one can infer that these multiple morphologies are the results of the balance between the three contributions to the G of the micelle. The shape and size of the stable aggregates correspond to the minimum free energy. A variety of parameters that affect the free energy of the micelle core, corona or interface can influence the morphology of the micelles. Eisenberg investigated a series of major factors in a system of PS-*b*-PAA in solvent-water mixture, e.g., copolymer composition and concentration, water content in the solution, nature of the common solvent, and presence of additives such as ions or homopolymers.[54-57]

Many theories, such as scaling theory[58] and self-consistent mean field theory[59], have been

developed in an attempt to describe the phase behavior of block copolymers in solution and understand the effect of decisive parameters. Israelachvili proposed a simple but widely used model based on geometrical considerations, initially developed for low molecular weight surfactants, to explain the micellization phenomenon and predict the resultant morphologies.[60] For amphiphilic block copolymers, it assumes geometric properties of a micelle depend on three parameters as shown in Figure 1.7: the optimal surface area of corona at the interface a_0 determined by the competition between repulsive head-group (hydrophilic block) forces and attractive interfacial forces from insoluble hydrophobic block, the volume v occupied by the core block chains, and it maximum length l_c. They are interrelated by a packing parameter, p:

$$p = \frac{v}{a_0 l_c}$$

Equation. 1.4

p represents the geometric constraints that determine which structures the molecules can pack into. Spherical micelles are formed when $p \leq 1/3$ and grow to nonspherical (ellipsoidal) micelles with the increase of p $(1/3 \sim 1/2)$. When p reaches about 0.5, rods or cylinders are preferred. At higher p (0.5~1), they evolve to interconnected networks (e.g., hexagonal or cubic). Vesicles and extended bilayers appear when $p \approx 1$. The micelle morphologies turn to a mirrored family of inverted structures when p is greater than unity.

The myriad of micelle morphologies adopted by block copolymers through self-directed assembly in solution have been employed to design numerous “smart” nanodevices as

chemical or biological sensors, encapsulators, or carriers, etc., highly interested by the cosmetics and pharmaceutical industries.[49, 61, 62] In membrane area, the solution-based block copolymer self-assembly also sparked the development of the most successful methodology to date for nanoporous membranes.[63] Peinemann et al. first reported a highly ordered, asymmetric porous membrane derived from polystyrene-*b*-poly(4-vinyl pyridine) (PS-*b*-P4VP) with a conventional phase inversion process, using a mixture of tetrahydrofuran (THF) and dimethylformamide (DMF) as casting solvent.[64] This one-step fast procedure provides the key to solve the long-standing issue of large scale manufacturing of nanoporous membranes because it is compatible with current commercial machines and no additional time-consuming step is required. Moreover, a macroporous sponge-like substructure can be formed simultaneously under the ultrathin selective layer containing hexagonally packed nanopores. This desirable integral asymmetric structure contributes to the exceptionally high water flux, which is at least one order of magnitude higher than commercial membranes with comparable pore size,[65] and enhances the mechanical strength.

Later Nunes et al. investigated the mechanism of membrane formation by utilizing various advanced microscopies and modeling tools, and first recognized the role of supramolecular micelle assemblies. This approach, now, has been referred as “self-assembly and non-solvent induced phased separation” (SNIPS). When a PS-*b*-P4PV block copolymer is dissolved in a P4VP selective THF/DMF mixture, the styrene blocks assemble into the micelle core surrounded by a P4VP shell, tending to avoid unfavorable contacts with the DMF-rich medium. The formation of “pearl necklace-like” crew-cut micelle strings in solution prior to immersing in water has been confirmed by cryo-

transmission electron microscopy (cyro-TEM) and cryo-field emission scanning electron microscopy (cyro-FESEM).[65, 66] An ordered 2D hexagonal structure of micelle assemblies can be probed from the quantitative analysis of the polymer casting solutions through small-angle X-ray scattering (SAXS), and this micelle order is directly correlated to the final pore geometry.[67] A triblock copolymer, polyisoprene-*b*-polystyrene-*b*-poly(4-vinyl pyridine) (PI-*b*-PS-*b*-P4VP), with body-centered cubic (BCC) ordering in solution leads to the formation of the membrane with cubic pore order.[68]

Once the solution is cast on the substrate by a doctor blade with about 200 μm gap, a partial evaporation step is crucial to the formation of ordered surface morphology. SAXS characterization and Dissipative particle dynamics (DPD) modeling have demonstrated that highest hexagonal order appears at a certain higher concentration. Above this concentration the transition to lamellar morphology occurs.[69] The resultant membrane structures also follow this disordered-ordered hexagonal-horizontal lamellar trend with the increase of onset concentration or evaporation time. Because the high viscosity of the solution with the maximum regularity (> 20 wt%) makes it difficult to process, membranes are cast from lower concentration solutions containing volatile solvent like THF and allowed to evaporate shortly (20 s) to reach the desired concentration on the top surface. Real time *in situ* studies on the morphology evolution by using time-resolved grazing incidence small-angle X-ray scattering (GISAXS) suggest that curvatures or cavities might be created during solvent evaporation, which are recorded as strong scattering sites in GISAXS. Cyro-FESEM of the doctor-bladed solution film after 4 s evaporation visually confirms the presence of these voids between aligned micelle strings orthogonal to the film surface being the precursors of the membrane pores.[70]

At the last step, the wet thin film is plunged into water. A fast solvent-water exchange leads to an abrupt decrease of chain mobility fixing the polymer-polymer entanglement. The non-solvent kenitically freezes the pre-determined morphology on the top of the solution layer and enters the cylindrical intermicellar channels with smallest resistance, giving rise to a highly homogeneous porous surface. But during this process, if the micellar structure is not strong enough, the system can be considerably disturbed and lose the order by rapid water extrusion. In order to stabilize the micelle assemblies, dioxane (DOX), a poorer solvent for P4VP has been introduced to the solvent system.[66] Due to the decreased solvent quality for P4VP, the polar P4VP blocks become more contract and less deformable. Furthermore, the interaction between P4VP segments is preferential so they tend to form stronger entanglement, leading to a higher friction between different micelle shells and a reduction of the micelles' mobility. A strong intersegmental interaction also can be promoted by the addition of Cu^{2+} to the solution to stabilize the order.[65, 71] Copper ions are known to form Cu^{2+}-pyridine complex with the lone pair on nitrogen as the coordination site. So, Cu^{2+} can act as a physical cross-linker between micelle coronas and keep the micelle intact and assembled. Beside metal salts, other complexing agents contribute to the stability of the self-assembled structure as well, such as -OH and -COOH bearing organic molecules.[72] The hydrogen bonding between organic molecules and pyridine facilitates the formation of compact spherical micelles and the intermicellar linking, which favor the hexagonal pore order in the final membrane. When added to the solution, pyridinium and imidazolium-based ionic liquids behave as both polar solvents that selectively solvate P4VP corona, and salts inducing strong interaction (hydrogen bonding or coulombic) with pyridine. It have been demonstrated that aprotic

ionic liquid can stabilize the micelles in a hexagonal arrangement.[73] The effect of various additives on the pore structure of nanoporous membranes also have been reported by other groups, including carbohydrates[74], magnesium acetate[75] and glycerol[76].

1.4 Synthesis of polysulfone-based block copolymers

The unparalleled potential of nanoporous membranes prepared *via* SNIPS has been highlighted by several studies based on PS-*b*-P4VP with practical applications varying from catalysis,[77] antibacterial filtration,[78] to selective separation[79] and controlled release[80] of proteins. Recently, the SNIPS strategy has been expanded to other diblock or triblock copolymers beyond PS-*b*-P4VP.[68, 81-84] However all copolymers used in SNIPS so far have polystyrene as the main component. Polystyrene is easy to copolymerize by different methods and in combination with hydrophilic blocks (e.g., P4VP, PAA and poly(ethylene oxide) (PEO)) is known to self-assemble in different solvents and in the bulk.[25] A common disadvantage of polystyrene-based membranes is their lower mechanical stability, when compared to homopolymers like polysulfone (PSU) and polyvinylidene fluoride (PVDF), traditionally used in membrane manufacture. Moreover, the low glass transition temperature (T_g) of polystyrene (100 °C) limits the thermal stability of such membranes. To overcome these drawbacks, a few tailor-made block copolymers have been proposed in an attempt to improve stability. One approach is the substitution of polystyrene with poly(*tert*-butyl styrene) (P*t*BS) and poly(4-trimethylsilyl styrene) (PTMSS) that have higher T_g to improve the thermal and chemical stability.[82]

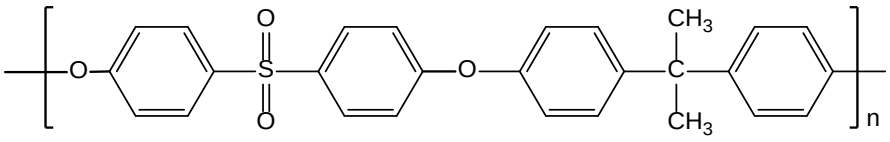

Figure 1.8. The chemical structure of polysulfone.

Another example is the incorporation of rubbery polyisoprene (PI) block into hydrophobic domain to toughen the PI-*b*-PS-*b*-P4VP triblock terpolymer membrane.[68] However polystyrene or derivatives in both cases remains the major monomer and improvements are only incremental.

This drawback motivates us to search for alternative block copolymers for more robust and reliable membranes. It will be a large step forward leading to commercialization of nanoporous membranes. In this dissertation, polysulfone-based block copolymers are synthesized and used to fabricate novel nanostructured membranes *via* SNIPS. PSU is one of the most widely used polymer families for membrane fabrication, featuring good pore forming property, high resistance in extreme pH conditions and chlorinated disinfectants, and excellent mechanical strength and thermal stability with a T_g of 190 °C.[85] The incorporation of PSU within the block copolymer membranes will unlock the door to more demanding applications due to their increased robustness.

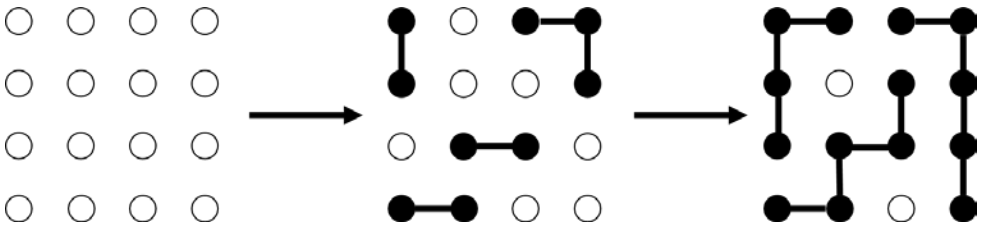

Figure 1.10. Diagrammatic representation of the step-growth condensation polymerization. Individual white spots denote monomers and connected black spots denote reacted monomers incorporated into the polymer chains.

Polysulfone as an amorphous thermoplastic, contains para-linked diphenylenesulfone group and aromatic ether in their repeating units.[86] Its chemical structure is shown in Figure 1.8. The most common synthetic method for commercial polysulfones is polyetherification based on an aromatic nucleophilic substitution, as shown in Figure 1.9.[87] The first step is the formation of bisphenolate anion from the deprotonation of aromatic bisphenol with a weak base (K_2CO_3) or a strong base (NaOH). Then the produced bisphenolate anion reacts with an activated aromatic dihalide bearing sulfone groups to yield the basic repeat unit of polysulfone with a diaryl ether linkage and eliminate KCl or NaCl salts.

The propagation proceeds following a typical step-growth mechanism with A-A

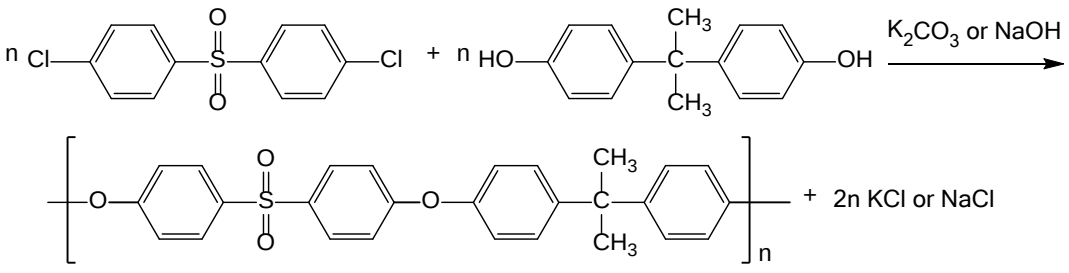

Figure 1.9. Synthesis of polysulfone *via* aromatic nucleophilic substitution with aromatic dihalide and bisphenol monomers in the presence of base.

and B-B type monomers to obtain the high molecular weight polymers.[88] According to the basic assumption in step-growth systems proposed by Flory that all functional groups are equally reactive, a monomer reacts with another monomer or growing polymer species with same ease. The progress of the polymerization is illustrated in Figure 1.10. Dimers, trimers, tetramers and a mixture of longer polymer chains will form step-wise with essentially identical reaction mechanism and rate.

The molecular weight of the step-growth polymers is controlled by the extend of the reaction and stoichiometry of the two functionalities. If N_0 and N is the total number of molecules before the polymerization and at time t, respectively, the extend of reaction, $p = (N_0 - N)/N_0$, defined as the proportion of the reacted functional groups of either A or B. The stoichiometric imbalance of the reactants can be expressed by r (> 1), which is the ratio of the number of the reactants. A parameter of describing the average number of repeat units in the polymer, the number-average chain length x_n is defined by:

$$x_n = \frac{\sum N_i x_i}{\sum N_i}$$

Equation 1.5

where N_i is the number of molecules of species i which has the number of repeat units x_i. W.H. Carothers, the great pioneer of step-growth polymers, proposed the following equation relating x_n to p and r.

$$x_n = \frac{1 + r}{1 + r - 2rp}$$

Equation 1.6

One can conclude from this simple equation that stoichiometric balance is crucial to obtain high molecular weight as x_n increases when r is closer to 1. It also can be understood in this way: an excess of monomer A-A over monomer B-B will eventually produce a polymer capped by two A groups incapable of further growth when B functionalities are completely consumed. For the polysulfone synthesis, the strong base such as NaOH may undesirably hydrolyze the dihalide, which changes the stoichiometry. This disadvantage can be eliminated by employing a weak base potassium carbonate in an aprotic polar solvent to avoid the hydrolysis, despite the fact that the industrial production takes the strong base approach for its faster reaction rate. Even the water produced by the deprotonation of bisphenol can hydrolyze the dihalide. Therefore, water is usually thoroughly removed by azeotropic distillation prior to adding dihalide monomer.

As a characteristic of step-growth reaction, the increase of chain length by the covalent linking of small molecules is a random process, giving rise to polymers of widely differing chain lengths, associated with molecular weight averages, rather than a single value. By analogy with the number-average chain length x_n, the number-average molecular weight M_n is defined by:

$$M_n = \frac{\sum N_i M_i}{\sum N_i}$$

Equation 1.7

where M_i is the number of molecules of species i of molecular weight M_i. By using another averaging method, weight-average molecular weight M_w is obtained based on the weight of species w_i as:

$$M_w = \frac{\sum w_i M_i}{\sum w_i} = \frac{\sum N_i M_i^2}{\sum N_i M_i}$$

Equation 1.8

The ration of M_w to M_n is often used to describe the breadth of molecular weight distribution, called polydispersity index or PDI:

$$PDI = \frac{M_w}{M_n}$$

Equation 1.9

Because of the nature of random events, the distribution of molecular weight in a linear step-growth polymerization system can be estimated by simple statistical arguments, leading to the following relationship:

$$PDI = 1 + p$$

Equation 1.10

Hence, for high molecular weight polymers, which usually require $p > 0.99$, the most probable PDI is about 2.

However, most of the self-organized structures either in bulk or solution are derived from nearly monodispersed block copolymers ($PDI < 1.2$). Thus, the difficulty of using polysulfone-based material to prepare nanoporous membranes lies in the broad molecular weight distribution of polysulfone. In order to obtain block copolymers with reasonable polydispersity required for self-assembly, our strategy is to minimize the total PDI by employing reversible-deactivation radical polymerization (RDRP) previously called controlled/living radical polymerization (CRP) to prepare the second blocks.[89, 90] Excess bisphenol in the reaction system affords hydroxyl-terminated telechelic polysulfone. The reactive chain ends allow the incorporation of different segments into polysulfone through (1) growing from PSU macroinitiator with RDRP, (2) coupling the pre-made homogeneous polymer chains with PSU backbone. RDRP techniques that are used in this dissertation will be briefly introduced in the following.

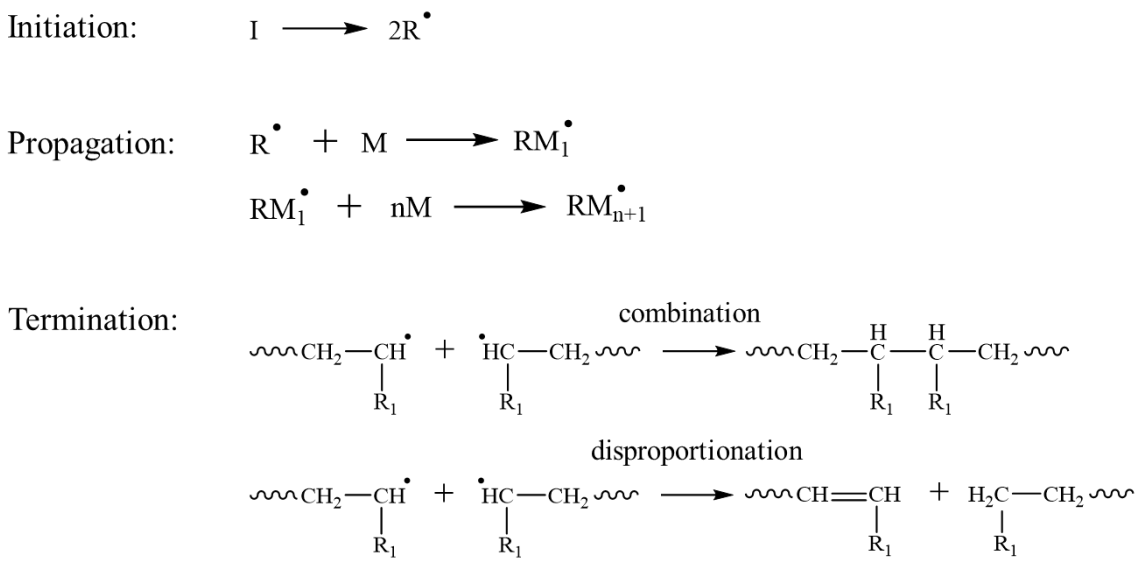

Figure 1.11. Mechanism of conventional free radical polymerization.

Free radical polymerization (FRP) represents chain-growth reactions, another important subdivision of polymerization mechanism, parallel to step-growth.[91, 92] In FRP, monomers are usually olefinic compounds with the general structure $CH_2=CR_1R_2$. The free radical can readily react with the π-orbital in the double bond and the spontaneous rearrangement will generate a radical chain carrier at the end that can retain the activity from the unpaired electron to grow long chains. Three distinct stages are involved in FRP: (1) initiation, where stable radicals are typically created by thermal decomposition or photolysis of an initiator such as organic peroxides and azo compounds; (2) propagation, when the repeated addition of monomers to the growing chains through the active center acting as a chain carrier takes place in a sequential manner; and (3) termination, leading to a halt of the chain propagation by the irreversible neutralization of active centers, which can occur *via* two most important bimolecular routes: combination and

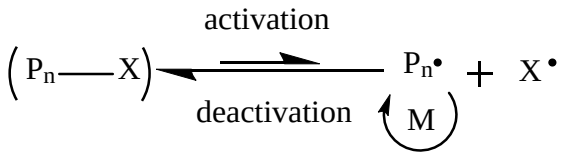

Figure 1.12. General process of reversible-deactivation radical polymerization.

disproportionation. Figure 1.11 illustrates the three steps in the procedure of radical polymerization.

Due to its simplicity, insensitivity to impurities, and compatibility with a wide range of monomers, free radical polymerization are used on an industrial scale to produce important commodity (co)polymers from vinyl monomers like polystyrene and poly(vinyl chloride). But it has no control over the molecular weight and end group functionalities because of the fast, irreversible termination and various side reactions. The interest in nanostructured polymer materials for modern applications (e.g., nanoporous block copolymer membranes and vesicles as drug carriers) spurs the development of a group of RDRP techniques, where polymerizations take place in a “living/controlled” manner analogous to living anionic system, resulting in polymers with low polydispersities and well-defined structure. The most important feature of RDRP that differs from conventional FRP is the establishment of a rapid dynamic equilibrium between a very small amount of free radicals as the growing chains and a large excess of the dormant species. The extremely low concentration of propagating radicals minimize the chance to collide with each other leading to dead chains.

In an activation/growth/deactivation cycle as shown in Figure 1.12, a mediating radical $X^{\bullet}$ is incapable of initiating chain growth but only the propagating chain

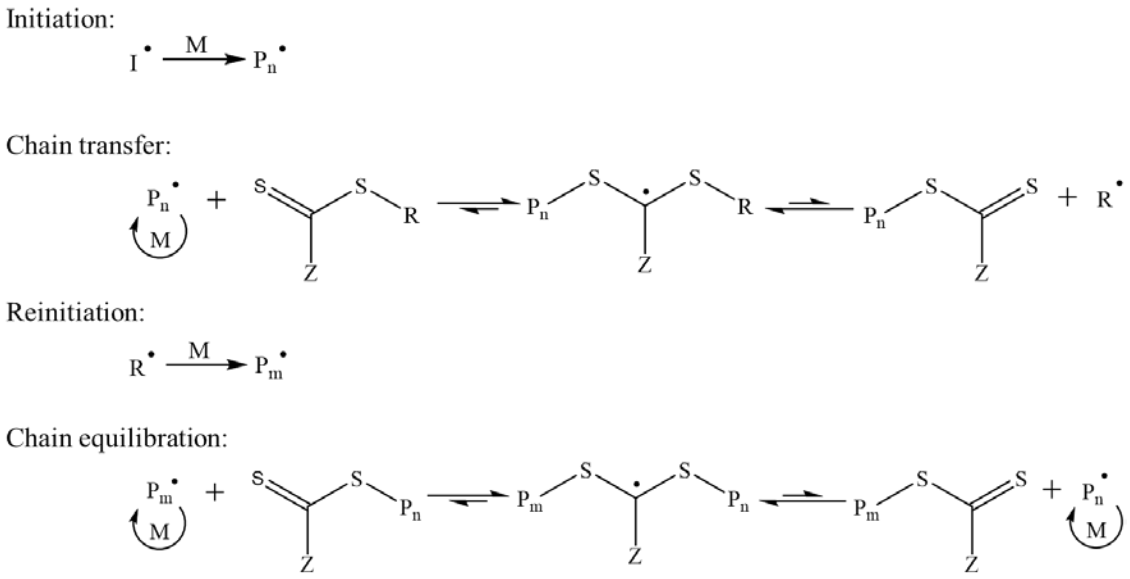

Figure 1.13. Mechanism of RAFT polymerization. In a typical CTA, R = CH_2Ph, $C(CH_3)_2CN$, etc., and Z = aryl, alkyl, S-, O-, N-, etc.

$P_n^{\bullet}$, which undergoes a frequent reversible termination to form dormant species end capped with X that dominates the equilibrium. This reversible trapping process also ensures the polymer chains to have an equal chance to grow and the length will increase steadily with time. The successful RDRP techniques developed so far include nitroxide-mediated polymerization (NMP)[93-95], atom transfer radical polymerization (ATRP)[96-100], reversible addition fragmentation chain transfer (RAFT)[101-105], and single electron transfer living radical polymerization (SET-LRP)[106-109] based on the same principle but different deactivation mechanisms. Since the synthesis of polysulfone-based block copolymer in this thesis involves with RAFT and SET-LRP. These two techniques will be discussed below.

The popularity of the RAFT process has dramatically increased since the first report by Rizzardo and co-workers at the Commonwealth Scientific and Industrial

Research Organization (CSIRO) in 1998.[101] RAFT uses chain transfer agent (CTA) in the form of thiocarbonylthio compounds, such as di- or trithiocarbonates, thiocarbamates, and xanthates, to mediate the polymerization *via* a reversible chain-transfer process.[102, 105] It begins with the formation of short polymeric radicals ($P_n^{\bullet}$) through traditional free radical initiators (I). Next, these propagation radicals add to the CTA to generate a radical intermediate, followed by its fragmentation, leading to a macro-CTA and a new radical ($R^{\bullet}$). This expelled CTA-derived initiator will react with monomers to give a new propagating chain ($P_m^{\bullet}$). The dynamic exchange of propagating chains on CTA with a rapid equilibrium between the active and dormant state provides equal opportunity for them to grow and imparts a good control over the polymerization. The mechanism is outlined in Figure 1.13.

RAFT polymerization is recognized as the most versatile RDRP process since almost all the monomers that can undergo radical polymerization are able to be well controlled including poly(vinyl acetate) and poly(*N*-vinyl pyrrolidone) which are big challenges to competing techniques. From the viewpoint of process development, the introduction of CTA is the only deviation required by RAFT from a conventional FRP protocol, making it easily adopted by industry.[104] Despite the distinct advantages of RAFT, its drawback is that suitable CTA has to be carefully selected or sometimes synthesized for the desired monomer by altering the Z or R group.[103] Additionally, the sulfur-containing CTA group on the polymer chain ends often imparts undesirable color and smell to the final products.

The concept of SET-LRP was reported by Percec and co-workers in 2006.[108] They proposed an outer-sphere single electron transfer (OSET) mechanism similar to ATRP that relies on the equilibrium between active propagating chains and dormant species capped with halide with the help of a copper/ligand complex, as illustrated in Figure 1.14. However, by contrast with ATRP, the activator is zero-valent copper (Cu^0) rather than Cu^I. In SET-LRP, Cu^0 species as electron donors abstract the halogen from an alkyl halide initiator (R-X) *via* an OSET process, producing a radical anion intermediate which rapidly decompose to give propagating chain $P_n^\bullet$ and Cu^IX/L with a one electron reduction. The Cu^IX/L undergoes a "spontaneous" disproportionation to produce Cu^0 and $Cu^{II}X_2/L$ for activation and deactivation, respectively. The latter can transfer the halogen back to $P_n^\bullet$, forming the dormant chain P_n-X and regenerating Cu^IX/L, which self-

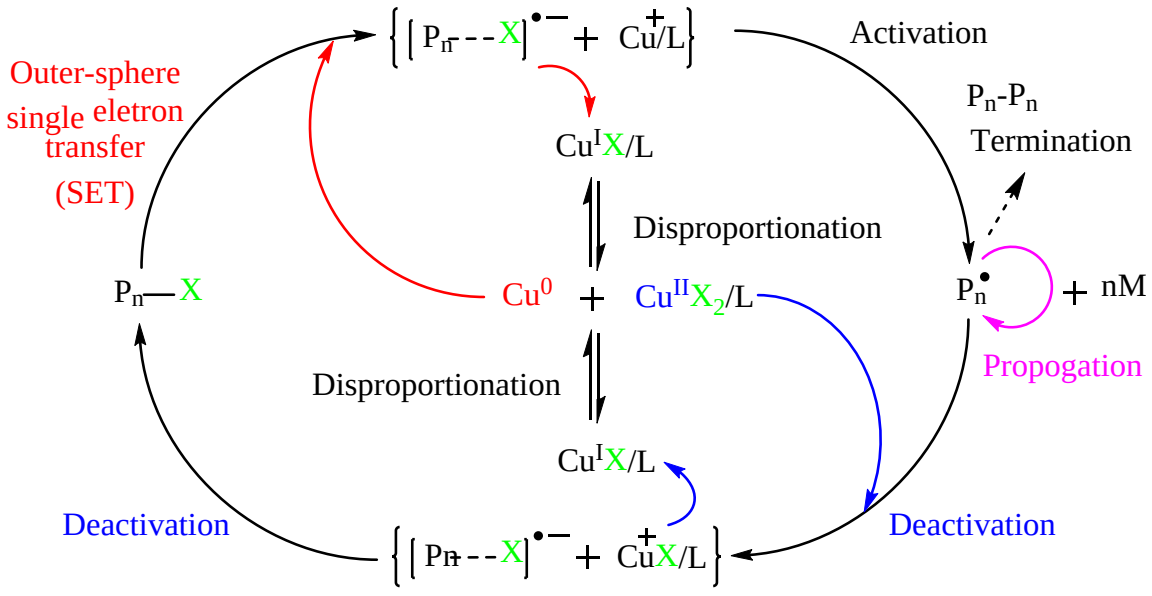

Figure 1.14. Mechanism of SET-LRP.

disproportionates again to drive the reversible activation-termination process.[108, 109]

A critical requirement for a successful SET-LRP that occurs in a controlled manner is to maintain the levels of Cu^0 and Cu^{II} by an efficient disproportionation. To establish the equilibrium, the initial Cu^0 can be brought to the system in the form of copper wire or powder, or the "nascent" Cu^0 in situ generated from Cu^I precursors (e.g., CuBr). Some nitrogen-containing ligands such as tris[2-(dimethylamino)ethyl]amine (Me_6TREN), tris(2-aminoethyl)amine (TREN), N,N,N′,N″,N″-pentamethyldiethylenetriamine (PMDETA) and 1,1,4,7,10,10-Hexa-methyltriethylenetetramine (HMTETA) in polar solvents (e.g., H_2O, dimethyl sulfoxide (DMSO), alcohols and ionic liquids, etc.) have been reported to encourage the disproportionation of Cu^I into Cu^0 and Cu^{II} species.[106] The extremely reactive Cu^0-mediated system offers a lot of attractive advantages, for example, ultrafast polymerization (< 30 min for N-isopropylacrylamide to reach full conversion[107]) often with narrow molecular weight distribution ($PDI \sim 1.1$), only catalytic amount of copper, no need for strict oxygen removal (bubbling with nitrogen is sufficient) and ambient reaction temperature or below, thus suppressing side reactions.[106]

1.5 References

1. J. Mulder, *Basic principles of membrane technology*, Springer Science & Business Media, 2012.

2. M. M. Pendergast and E. M. V. Hoek, *Energy Environ. Sci.*, 2011, 4, 1946-1971.

3. J. C. Crittenden, R. R. Trussell, D. W. Hand, K. J. Howe and G. Tchobanoglous, *MWH's Water Treatment: Principles and Design*, John Wiley & Sons, 2012.

4. J. A. Nollet, *J. Membr. Sci.*, 1995, 100, 1-3.

5. K. W. Böddeker, *Liquid separations with membranes*, Springer, 2008.

6. R. W. Baker, *Membrane Technology and Applications*, John Wiley & Sons, 2004.

7. L. Sidney and S. Srinivasa, in *Saline Water Conversion-II*, AMERICAN CHEMICAL SOCIETY, 1963, vol. 38, ch. 9, pp. 117-132.

8. G. R. Guillen, Y. Pan, M. Li and E. M. V. Hoek, *Ind. Eng. Chem. Res.*, 2011, 50, 3798-3817.

9. B. S. Lalia, V. Kochkodan, R. Hashaikeh and N. Hilal, *Desalination*, 2013, 326, 77-95.

10. S. P. Nunes and T. Inoue, *J. Membr. Sci.*, 1996, 111, 93-103.

11. I. Pinnau and W. J. Koros, *J. Polym. Sci. Part B Polym. Phys.*, 1993, 31, 419-427.

12. P. van de Witte, P. J. Dijkstra, J. W. A. van den Berg and J. Feijen, *J. Membr. Sci.*, 1996, 117, 1-31.

13. E. Drioli and L. Giorno, *Comprehensive membrane science and engineering*, Newnes, 2010.

14. S. P. Nunes and K.-V. Peinemann, *Membrane technology: in the chemical industry*, John Wiley & Sons, 2006.

15. E. A. Jackson and M. A. Hillmyer, *ACS Nano*, 2010, 4, 3548-3553.

16. S. P. Nunes and A. Car, *Ind. Eng. Chem. Res.*, 2013, 52, 993-1003.

17. M. A. Shannon, P. W. Bohn, M. Elimelech, J. G. Georgiadis, B. J. Marinas and A. M. Mayes, *Nature*, 2008, 452, 301-310.

18. L. Upadhyaya, M. Semsarilar, S. Nehache, A. Deratani and D. Quemener, *Eur. Phys. J. Spec. Top.*, 2015, 224, 1883-1897.

19. N. Hadjichristidis, M. Pitsikalis, S. Pispas and H. Iatrou, *Chem. Rev.*, 2001, 101, 3747-3792.

20. N. Hadjichristidis, S. Pispas and G. Floudas, *Block copolymers: synthetic strategies, physical properties, and applications*, John Wiley & Sons, 2003.

21. I. W. Hamley, *Developments in block copolymer science and technology*, Wiley Online Library, 2004.

22. V. Abetz and P. F. W. Simon, in *Block Copolymers I*, ed. V. Abetz, Springer Berlin Heidelberg, Berlin, Heidelberg, 2005, DOI: 10.1007/12_004, pp. 125-212.

23. F. S. Bates and G. H. Fredrickson, *Phys. Today*, 1999, 52, 32-38.

24. I. W. Hamley, *The Physics of Block Copolymers*, Oxford University Press, 1998.

25. Y. Mai and A. Eisenberg, *Chem. Soc. Rev.*, 2012, 41, 5969-5985.

26. M. W. Matsen and F. S. Bates, *Macromolecules*, 1996, 29, 7641-7644.

27. L. Leibler, *Macromolecules*, 1980, 13, 1602-1617.

28. D. E. Discher and F. Ahmed, *Annu. Rev. Biomed. Eng.*, 2006, 8, 323-341.

29. J. K. Kim, S. Y. Yang, Y. Lee and Y. Kim, *Prog. Polym. Sci.*, 2010, 35, 1325-1349.

30. M. A. Hillmyer, in *Block Copolymers II*, ed. V. Abetz, Springer Berlin Heidelberg, Berlin, Heidelberg, 2005, DOI: 10.1007/12_002, pp. 137-181.

31. D. A. Olson, L. Chen and M. A. Hillmyer, *Chem. Mater.*, 2008, 20, 869-890.

32. J. Zhao, X. Zhao, Z. Jiang, Z. Li, X. Fan, J. Zhu, H. Wu, Y. Su, D. Yang, F. Pan and J. Shi, *Prog. Polym. Sci.*, 2014, 39, 1668-1720.

33. M. Park, C. Harrison, P. M. Chaikin, R. A. Register and D. H. Adamson, *Science*, 1997, 276, 1401-1404.

34. J. S. Lee, A. Hirao and S. Nakahama, *Macromolecules*, 1988, 21, 274-276.

35. D. Wu, F. Xu, B. Sun, R. Fu, H. He and K. Matyjaszewski, *Chem. Rev.*, 2012, 112, 3959-4015.

36. S. Y. Yang, J. Park, J. Yoon, M. Ree, S. K. Jang and J. K. Kim, *Adv. Funct. Mater.*, 2008, 18, 1371-1377.

37. S. Y. Yang, I. Ryu, H. Y. Kim, J. K. Kim, S. K. Jang and T. P. Russell, *Adv. Mater.*, 2006, 18, 709-712.

38. S. Y. Yang, S. Son, S. Jang, H. Kim, G. Jeon, W. J. Kim and J. K. Kim, *Nano Lett.*, 2011, 11, 1032-1035.

39. S. Y. Yang, J.-A. Yang, E.-S. Kim, G. Jeon, E. J. Oh, K. Y. Choi, S. K. Hahn and J. K. Kim, *ACS Nano*, 2010, 4, 3817-3822.

40. W. A. Phillip, B. O'Neill, M. Rodwogin, M. A. Hillmyer and E. L. Cussler, *ACS Appl. Mater. Interfaces*, 2010, 2, 847-853.

41. W. A. Phillip, M. A. Hillmyer and E. L. Cussler, *Macromolecules*, 2010, 43, 7763-7770.

42. S. E. Querelle, E. A. Jackson, E. L. Cussler and M. A. Hillmyer, *ACS Appl. Mater. Interfaces*, 2013, 5, 5044-5050.

43. J. Yin, X. Yao, J.-Y. Liou, W. Sun, Y.-S. Sun and Y. Wang, *ACS Nano*, 2013, 7, 9961-9974.

44. Y. Wang and F. Li, *Adv. Mater.*, 2011, 23, 2134-2148.

45. S. Park, J.-Y. Wang, B. Kim, J. Xu and T. P. Russell, *ACS Nano*, 2008, 2, 766-772.

46. T. Xu, J. Stevens, J. A. Villa, J. T. Goldbach, K. W. Guarini, C. T. Black, C. J. Hawker and T. P. Russell, *Adv. Funct. Mater.*, 2003, 13, 698-702.

47. Z. Wang, L. Guo and Y. Wang, *J. Membr. Sci.*, 2015, 476, 449-456.

48. W. Sun, Z. Wang, X. Yao, L. Guo, X. Chen and Y. Wang, *J. Membr. Sci.*, 2014, 466, 229-237.

49. J. Rodríguez-Hernández, F. Chécot, Y. Gnanou and S. Lecommandoux, *Prog. Polym. Sci.*, 2005, 30, 691-724.

50. J.-F. Gohy, in *Block Copolymers II*, ed. V. Abetz, Springer Berlin Heidelberg, Berlin, Heidelberg, 2005, DOI: 10.1007/12_048, pp. 65-136.

51. G. Riess, *Prog. Polym. Sci.*, 2003, 28, 1107-1170.

52. P. Alexandridis and B. Lindman, *Amphiphilic block copolymers: self-assembly and applications*, Elsevier, 2000.

53. N. S. Cameron, M. K. Corbierre and A. Eisenberg, *Can. J. Chem.*, 1999, 77, 1311-1326.

54. L. Zhang and A. Eisenberg, *Macromolecules*, 1999, 32, 2239-2249.

55. L. Zhang and A. Eisenberg, *Polymer. Adv. Tech.*, 1998, 9, 677-699.

56. Y. Yu, L. Zhang and A. Eisenberg, *Macromolecules*, 1998, 31, 1144-1154.

57. L. Zhang and A. Eisenberg, *J. Am. Chem. Soc.*, 1996, 118, 3168-3181.

58. A. Halperin, *Macromolecules*, 1987, 20, 2943-2946.

59. J. Noolandi and K. M. Hong, *Macromolecules*, 1983, 16, 1443-1448.

60. J. N. Israelachvili, *Intermolecular and surface forces: revised third edition*, Academic press, 2011.

61. J. Nicolas, S. Mura, D. Brambilla, N. Mackiewicz and P. Couvreur, *Chem. Soc. Rev.*, 2013, 42, 1147-1235.

62. J. S. Lee and J. Feijen, *J. Control. Release*, 2012, 161, 473-483.

63. Y. Zhang, J. L. Sargent, B. W. Boudouris and W. A. Phillip, *J. Appl. Polym. Sci.*, 2015, 132, n/a-n/a.

64. K.-V. Peinemann, V. Abetz and P. F. W. Simon, *Nat. Mater.*, 2007, 6, 992-996.

65. S. P. Nunes, R. Sougrat, B. Hooghan, D. H. Anjum, A. R. Behzad, L. Zhao, N. Pradeep, I. Pinnau, U. Vainio and K. V. Peinemann, *Macromolecules*, 2010, 43, 8079-8085.

66. S. P. Nunes, M. Karunakaran, N. Pradeep, A. R. Behzad, B. Hooghan, R. Sougrat, H. He and K. V. Peinemann, *Langmuir*, 2011, 27, 10184-10190.

67. R. M. Dorin, D. S. Marques, H. Sai, U. Vainio, W. A. Phillip, K. V. Peinemann, S. P. Nunes and U. Wiesner, *ACS Macro Lett.*, 2012, 1, 614-617.

68. W. A. Phillip, R. Mika Dorin, J. Werner, E. M. V. Hoek, U. Wiesner and M. Elimelech, *Nano Lett.*, 2011, 11, 2892-2900.

69. D. S. Marques, U. Vainio, N. M. Chaparro, V. M. Calo, A. R. Bezahd, J. W. Pitera, K. V. Peinemann and S. P. Nunes, *Soft Matter*, 2013, 9, 5557-5564.

70. D. S. Marques, R. M. Dorin, U. Wiesner, D. M. Smilgies, A. R. Behzad, U. Vainio, K. V. Peinemann and S. P. Nunes, *Polymer*, 2014, 55, 1327-1332.

71. S. P. Nunes, A. R. Behzad, B. Hooghan, R. Sougrat, M. Karunakaran, N. Pradeep, U. Vainio and K. V. Peinemann, *ACS Nano*, 2011, 5, 3516-3522.

72. P. Madhavan, K. V. Peinemann and S. P. Nunes, *ACS Appl. Mater. Interfaces*, 2013, 5, 7152-7159.

73. P. Madhavan, R. Sougrat, A. R. Behzad, K.-V. Peinemann and S. P. Nunes, *J. Membr. Sci.*, 2015, 492, 568-577.

74. J. I. Clodt, S. Rangou, A. Schröder, K. Buhr, J. Hahn, A. Jung, V. Filiz and V. Abetz, *Macromol. Rapid Commun.*, 2013, 34, 190-194.

75. M. Gallei, S. Rangou, V. Filiz, K. Buhr, S. Bolmer, C. Abetz and V. Abetz, *Macromol. Chem. Phys.*, 2013, 214, 1037-1046.

76. Y. Gu and U. Wiesner, *Macromolecules*, 2015, 48, 6153-6159.

77. R. Hilke, N. Pradeep, P. Madhavan, U. Vainio, A. R. Behzad, R. Sougrat, S. P. Nunes and K.-V. Peinemann, *ACS Appl. Mater. Interfaces*, 2013, 5, 7001-7006.

78. P. Madhavan, P.-Y. Hong, R. Sougrat and S. P. Nunes, *ACS Appl. Mater. Interfaces*, 2014, 6, 18497-18501.

79. X. Qiu, H. Yu, M. Karunakaran, N. Pradeep, S. P. Nunes and K.-V. Peinemann, *ACS Nano*, 2013, 7, 768-776.

80. H. Yu, X. Qiu, S. P. Nunes and K.-V. Peinemann, *Angew. Chem. Int. Ed.*, 2014, 53, 10072-10076.

81. A. Jung, S. Rangou, C. Abetz, V. Filiz and V. Abetz, *Macromol. Mater. Eng.*, 2012, 297, 790-798.

82. J. Hahn, V. Filiz, S. Rangou, B. Lademann, K. Buhr, J. I. Clodt, A. Jung, C. Abetz and V. Abetz, *Macromol. Mater. Eng.*, 2013, 298, 1315-1321.

83. M. Karunakaran, S. P. Nunes, X. Qiu, H. Yu and K. V. Peinemann, *J. Membr. Sci.*, 2014, 453, 471-477.

84. R. A. Mulvenna, J. L. Weidman, B. Jing, J. A. Pople, Y. Zhu, B. W. Boudouris and W. A. Phillip, *J. Membr. Sci.*, 2014, 470, 246-256.

85. Y. Xie, R. Tayouo and S. P. Nunes, *J. Appl. Polym. Sci.*, 2015, 132, n/a-n/a.

86. O. Olabisi and K. Adewale, *Handbook of Thermoplastics, Second Edition*, Taylor & Francis, 2015.

87. C. Dizman, M. A. Tasdelen and Y. Yagci, *Polym. Int.*, 2013, 62, 991-1007.

88. J. M. G. Cowie and V. Arrighi, *Polymers: Chemistry and Physics of Modern Materials, Third Edition*, CRC Press, 2007.

89. W. A. Braunecker and K. Matyjaszewski, *Prog. Polym. Sci.*, 2007, 32, 93-146.

90. A. D. Jenkins, R. G. Jones and G. Moad, *Pure Appl. Chem*, 2009, 82, 483-491.

91. K. Matyjaszewski and T. P. Davis, *Handbook of Radical Polymerization*, Wiley, 2003.

92. G. Moad and D. H. Solomon, *The Chemistry of Radical Polymerization*, Elsevier, 2006.

93. R. B. Grubbs, *Polym. Rev.*, 2011, 51, 104-137.

94. C. J. Hawker, A. W. Bosman and E. Harth, *Chem. Rev.*, 2001, 101, 3661-3688.

95. J. Nicolas, Y. Guillaneuf, C. Lefay, D. Bertin, D. Gigmes and B. Charleux, *Prog. Polym. Sci.*, 2013, 38, 63-235.

96. V. Coessens, T. Pintauer and K. Matyjaszewski, *Prog. Polym. Sci.*, 2001, 26, 337-377.

97. M. Kato, M. Kamigaito, M. Sawamoto and T. Higashimura, *Macromolecules*, 1995, 28, 1721-1723.

98. K. Matyjaszewski and J. Xia, *Chem. Rev.*, 2001, 101, 2921-2990.

99. J.-S. Wang and K. Matyjaszewski, *J. Am. Chem. Soc.*, 1995, 117, 5614-5615.

100. J.-S. Wang and K. Matyjaszewski, *Macromolecules*, 1995, 28, 7901-7910.

101. J. Chiefari, Y. K. Chong, F. Ercole, J. Krstina, J. Jeffery, T. P. T. Le, R. T. A. Mayadunne, G. F. Meijs, C. L. Moad, G. Moad, E. Rizzardo and S. H. Thang, *Macromolecules*, 1998, 31, 5559-5562.

102. M. Destarac, C. Brochon, J.-M. Catala, A. Wilczewska and S. Z. Zard, *Macromol. Chem. Phys.*, 2002, 203, 2281-2289.

103. A. Favier and M.-T. Charreyre, *Macromol. Rapid Commun.*, 2006, 27, 653-692.

104. D. J. Keddie, *Chem. Soc. Rev.*, 2014, 43, 496-505.

105. G. Moad, E. Rizzardo and S. H. Thang, *Polymer*, 2008, 49, 1079-1131.

106. A. Anastasaki, V. Nikolaou and D. M. Haddleton, *Polym. Chem.*, 2016, 7, 1002-1026.

107. Q. Zhang, P. Wilson, Z. Li, R. McHale, J. Godfrey, A. Anastasaki, C. Waldron and D. M. Haddleton, *J. Am. Chem. Soc.*, 2013, 135, 7355-7363.

108. V. Percec, T. Guliashvili, J. S. Ladislaw, A. Wistrand, A. Stjerndahl, M. J. Sienkowska, M. J. Monteiro and S. Sahoo, *J. Am. Chem. Soc.*, 2006, 128, 14156-14165.

109. V. Percec, A. V. Popov, E. Ramirez-Castillo, M. Monteiro, B. Barboiu, O. Weichold, A. D. Asandei and C. M. Mitchell, *J. Am. Chem. Soc.*, 2002, 124, 4940-4941.

CHAPTER 2

Highly Porous Poly(*tert*-butyl acrylate)-*b*-Polysulfone-*b*-Poly(*tert*-butyl acrylate) Asymmetric Membranes

2.1 Introduction

The fabrication of highly ordered, asymmetric isoporous membranes based on block copolymers using self-assembly combined with conventional non-solvent induced phase separation was first reported by Peinemann et al.[1] Although there are a lot of published works on block copolymer films and membranes,[2-5] given that no additional annealing or etching step is needed with the new proposed method, this was a great step towards large-scale manufacture. The mechanism could only be understood later, after recognizing the role of supramolecular micelle assemblies in the formation of the nanoporous membranes.[6-11] The potential of these flexible membranes has been demonstrated by several studies mainly based on poly(styrene)-*b*-poly(4-vinyl pyridine) copolymers (PS-*b*-P4VP) with practical applications varying from catalysis,[12] antibacterial filtration,[13] to selective separation[14] and controlled release[15] of proteins.

This method, now referred as "self-assembly and non-solvent induced phase separation" (SNIPS),[16] is simple, reproducible and compatible with existing technical machines. Recently, the SNIPS strategy has been expanded to other diblock or triblock copolymers beyond PS-*b*-P4VP.[17-21] However all copolymers used in SNIPS so far have polystyrene as the main component. Polystyrene is easy to copolymerize by different

methods and in combination with hydrophilic blocks is known to self-assemble in different solvents and in the bulk.[22] A common disadvantage of polystyrene-based membranes is their lower mechanical stability, when compared to homopolymers like polysulfone and polyvinylidene fluoride, traditionally used in membrane manufacture. Moreover, the low glass transition temperature (T_g) of polystyrene (100 °C) limits the thermal stability of such membranes. To overcome these drawbacks, a few tailor-made block copolymers have been proposed in an attempt to improve stability. One approach is the substitution of polystyrene with poly(*tert*-butyl styrene) (P*t*BS) and poly(4-trimethylsilyl styrene) (PTMSS) that have higher T_g to improve the thermal and chemical stability.[18] Another example is the incorporation of rubbery polyisoprene (PI) block into hydrophobic domain to toughen the PI-*b*-PS-*b*-P4VP triblock terpolymer membrane.[19] However polystyrene or derivatives in both cases remains the major monomer and improvements are only incremental.

In this chapter, we report novel nanostructured membranes *via* SNIPS, made from polysulfone-based triblock copolymer, poly(*tert*-butyl acrylate)-*b*-polysulfone-*b*-poly(*tert*-butyl acrylate) (P*t*BA-*b*-PSU-*b*-P*t*BA) for the first time.[23] Polysulfone (PSU) is one of the most widely used polymer families for membrane fabrication, featuring good pore forming property, high resistance in extreme pH conditions and chlorinated disinfectants, and excellent mechanical strength and thermal stability with a T_g of 190 °C.[24] The incorporation of PSU within the block copolymer membranes will open the door to more demanding applications due to their increased robustness. Nevertheless, the difficulty lies in the fact that polysulfone can be synthesized only by step-growth polycondensation, rendering broad molecular weight distribution.[25] Even worse is that

block copolymers are normally unachievable using this technique. In order to obtain polysulfone-based triblock copolymer with reasonable polydispersity required for ordered micro-phase separation, we combined the condensation and reversible addition fragmentation chain transfer[26] (RAFT) polymerization. To the best of our knowledge, this is the first SNIPS contribution using copolymers containing blocks of high-performance engineering resin such as polysulfone for membranes. Therefore, we believe this synthetic methodology will expand the material arsenal for SNIPS membranes with improved performance and enriched functions.

2.2 Experimental Section

2.2.1 Materials

Polysulfone (average M_n ~22,000 g/mol, Aldrich) and potassium carbonate (K_2CO_3, Aldrich) was dried overnight in vacuum oven prior to use. Bis(4-chlorophenyl) sulfone (DCDPS, 98%, Aldrich) was recrystallized twice from hot toluene (DCDPS: Toluene = 1:1.1) prior to use. Bisphenol-A (BPA, 99%, Aldrich) was recrystallized twice from hot toluene (BPA: Toluene = 1:5.3). The crystals were dried at 75 °C for 12h, cooled, well powdered and dried again for 12h at 90°C[27]. *Tert*-butyl acrylate (*t*BA, > 99%, Alfa Aeser) was extracted three times with 5% NaOH and six times with water. The organic layer was dried over $NaSO_4$, filtrated and then distilled under reduced pressure (60 °C/60 mmHg). 2,2'-Azobis(2-methylpropionitrile) (AIBN, 98%, Aldrich) was recrystallized twice from hot methanol. 4-Cyano-4-[(dodecylsulfanylthiocarbonyl)sulfanyl]pentanoic acid (97%, Aldrich), 4-(dimethylamino)pyridine (DMAP, ≥ 99%, Fluka), N,N'-

dicyclohexylcarbodiimide (DCC, ≥ 99%, Fluka), ethanol absolute (p.a, Aldrich), dichloromethane (DCM, ≥ 99.9%, Aldrich), methanol (≥ 99%, Fisher), N-methyl-2-pyrrolidone (NMP, ≥ 99.5%, Aldrich), toluene (≥ 99.5%, Aldrich), N,N-dimethylacetamide (DMAc, ≥ 99.8%, Aldrich), hydrochloric acid (36.5-38.0%, Alfa Aeser), copper(II) sulfate pentahydrate (98-102%, Fisher) and iron(III) chloride hexahydrate (≥ 98%, Sigma-Aldrich) were used as received. Poly(ethylene glycol) 3000, 6000, 10000, 35000 and 100000 were purchased from Sigma-Aldrich.

2.2.2 Synthesis of Poly(*tert*-butyl acrylate)-*b*-polysulfone-*b*-poly(*tert*-butyl acrylate) Triblock Copolymer (P*t*BA-PSU-P*t*BA)

2.2.2a α,ω-dihydroxy-Terminated Polysulfone (HO-PSU-OH)

Dihydroxy-terminated PSU polymers were synthesized by condensation of bis(4-chlorophenyl) sulfone (DCDPS) with an excess of bisphenol A calculated with the Carothers equation according to the literature procedure[27-30]. BPA (20 g, 87.6 mmol), DCDPS (24.4 g, 85 mmol), K_2CO_3 (36.32 g, 26.3 mmol), NMP (75 mL) and toluene (25 mL) were placed in a 250 ml three-neck round bottom flask equipped with a mechanical stirrer, a condenser, a thermometer, a Dean-Stark trap and a nitrogen inlet/outlet. K_2CO_3 was employed as a base, to generate the phenoxide ion of BPA in situ, which subsequently reacted with DCDPS at higher temperature. The reaction mixture was stirred at room temperature under nitrogen protection for 2 h to dissolve the reactants and gradually heated to reflux at 152 °C for 8 h to dehydrate completely via azeotropic

distillation with toluene. Then, the toluene was distilled thoroughly at 160 °C. The reaction mixture was heated to 175°C for 8 h to start polymerization until the solution became too viscous. After cooling, the viscous mixture was precipitated into aqueous HCl/methanol (v/v = 2:1) with vigorous stirring in order to remove salts (KCl). The obtained polymer was dissolved in THF and reprecipitated into aqueous HCl/methanol trice, followed by filtration, then washing in water at 80 °C for 4 h to remove the remaining salts and solvents. After final filtration, the polymer was dried under vacuum at 90 °C for 24 h.

2.2.2b RAFT CTA-Terminated Polysulfone (CTA-PSU-CTA)

RAFT chain transfer agent-capped polysulfone was synthesized through the Steglich esterification.[31] HO-PSU_{14k}-OH (20 g, 1.4 mmol, $M_{n,GPC}$ = 14 kg/mol, PDI = 2.1) was dissolved with 150 mL dry dichloromethane in 250 mL three-neck round bottom flask equipped with a magnetic stirrer, a condenser and a gas inlet/outlet. 4-Cyano-4-[(dodecylsulfanylthiocarbonyl)sulfanyl]pentanoic acid (1.7 g, 4.3 mmol) and 4-(dimethylamino)pyridine (52 mg, 0.4 mmol) were added to the flask. The solution was stirred at 0 °C under nitrogen flow for 3 h. Then a solution of N,N'-dicyclohexylcarbodiimide (0.9 g, 4.3 mmol) dispersed in small amount of dichloromethane was added dropwise to the mixture. Subsequently the temperature was allowed to rise to room temperature and the reaction was continued under stirring for 3 days. The solution was filtered to remove catalyst and concentrated by rotavapor, followed by precipitation into methanol. The crude product was dissolved in dichloromethane again and reprecipitated into methanol (3 times), finally filtrated and

dried in vacuum at 60 °C to obtain CTA-terminated polysulfone.

2.2.2c Poly(*tert*-butyl acrylate)-*b*-Polysulfone-*b*-Poly(*tert*-butyl acrylate) Triblock Copolymer (P*t*BA-PSU-P*t*BA)

The RAFT polymerization of P*t*BA-PSU-P*t*BA was carried out using CTA-PSU_{14k}-CTA as macro chain transfer agent and *tert*-butyl acrylate as monomer in DMAc at 80 °C, as follows: CTA-PSU-CTA (5 g, 0.3 mmol) was first dissolved with anhydrous DMAc (20 ml) in 100 ml of dry schlenk flask equipped with a magnetic stirrer. Next, AIBN (20 mg, 0.1 mmol) and *t*BA (30 mL, 0.2 mol) were added quickly, before the flask was sealed with a rubber septum, and then the reaction mixture was degassed by three freeze-pump-thaw cycles to switch the atmosphere to nitrogen. Finally, the schlenk flask with the reaction mixture was placed in a thermostatic bath at 80 °C for 24 h. After the reaction mixture was stopped by exposure of the solution to air and cooled down to room temperature, it was precipitated into water. The precipitate was recovered by filtration, washed with methanol and dried in vacuum. The polymer was solubilized with DMAc and reprecipitated into water. The purification step was repeated three times. After drying under reduced pressure, the triblock copolymer PtBA_{30k}-PSU_{14k}-PtBA_{30k} was obtained as yellowish solids.

2.2.3 Polymer Characterization

^{1}H and ^{13}C NMR spectra of polymers were recorded with a Bruker AVANCE-III spectrometer at a frequency of 400 MHz at room temperature and deuterated solvents

containing tetramethylsilane $Si(CH_3)_4$ as an internal standard. Polymer molecular weight and distribution were determined by triple detection gel permeation chromatography (GPC) from Viscotek using a GPCmax module (model VE-2001) and a GPC-TDA 305 system equipped with two columns (LT4000L, Mixed, Low Org. 300 mm X 8.0 mm, exclusion limit 400 kDa for polystyrene) eluted at 1.0 mL min^{-1} in stabilized THF at 35 °C. Three detectors are light scattering (RALS and LALS), refractive index, and viscometer. Absolute molecular weights were determined using polystyrene standards for calibration. Thermogravimetric analysis (TGA) was conducted using a TGA Q50 (TA instruments) with a heating rate of 10 °C min^{-1} under nitrogen flow from 25 to 800 °C. Differential scanning calorimetry (DSC) was carried out on a Perkin-Elmer DSC 204 F1 NETZSCH under nitrogen flow. The heating rate was 10 °C min^{-1} and the cooling rate was 5 °C min^{-1} in the range of temperature from -50 to 180 °C. The glass transition temperature (T_g) was taken from the second heating scan.

2.2.4 Membrane Fabrication

The casting solution from 20 wt % P*t*BA_{30k}-PSU_{14k}-P*t*BA_{30k} in DMAc was stirred for 12 h to obtain a homogeneous solution and kept still for another 12 h to release bubbles. This viscous solution was cast onto a clean glass plate by a doctor blade with 200 μm gate height. The plate was then immersed quickly and smoothly into the coagulation bath of deionized water at room temperature. An opaque film formed and left the plate in a few minutes spontaneously. Then the membrane was transferred to a fresh water bath for exhaustive extraction of solvent overnight. The resulting membrane was stored in water

at 4 °C before ultrafiltration experiment and surface modification. Some part of the membrane was freeze-dried for various characterization.

2.2.5 Computational Modeling of BAB Copolymer Self-assembly

We model self-assembly of BAB block copolymer using a meso-scale method Dissipative Particle Dynamics (DPD).[32, 33] The simulations use an open-source software Large-scale Atomic/Molecular Massively Parallel Simulator (LAMMPS).[34] These simulations use the standard DPD units[35] of length ($r_c = 1$), mass ($m = 1$), energy ($\epsilon = k_B T = 1$), and time ($\tau = 1$). We discretize each triblock copolymer chain with 148 particles, connected with spring potentials with an equilibrium bond length $r_o = 0.8 r_c$ and spring constant $K_s = 50 k_B T$. We impose periodic boundary conditions in cubic simulation boxes of size $L = 111.34 r_c$. The box size is defined to be approximately 12-fold the unperturbed radius of gyration ($L \sim 12 R_g^o$).[36] The particle-number density in all the simulations is $\rho_n = 3$ particles/r_c^3. The simulations evolve for 1 million of time steps, using a time step 0.04τ to ensure a proper control of the temperature of the system. The visualization of the computational results uses the software OVITO.[37] Detailed parameters definition and descriptions of the simulation method are provided in the Appendices.

2.2.6 Membrane Modification

The as-formed P*t*BA-PSU-P*t*BA membrane was immersed into 37% hydrochloric acid (HCl) solution for 30 minutes with gentle swirling to partially cleave the *tert*-butyl

groups to yield carboxylic acid functions. After hydrolysis in the HCl bath, the membrane was immediately moved to a beaker with 0.1 M $CuSO_4$ or $FeCl_3$ solution. The metal salt solution was refreshed at least three times in order to wash away remaining acid. The membrane was allowed to sit in the solution for 24 h to achieve complete metal complexation with carboxylic acid. Finally excess uncomplexed metal ions were washed out by DI water.

2.2.7 Membrane Characterization

The surface and cross-section morphologies of the membranes were observed by field emission scanning electron microscopy (FESEM) in a FEI Nova Nano SEM. For surface imaging, a small piece of membrane sample was mounted on a flat aluminum stub, fixed by aluminum conductive tapes. For cross-section, the membrane sample was freeze-fractured in liquid nitrogen, and mounted on a 90° aluminum stub vertically with tapes. The samples were sputter-coated with 2 nm Iridium nanoparticles to prevent electron charging using Quorum Q150T before imaging.

Cyro SEM experiments were carried out to examine the bulk structure of membrane casting solution. A PP2000T cryo transfer system (Quorum Technologies, UK) attached to a FEI Nova Nano FEG SEM was used for this purpose. Small amount of sample was transferred onto the opening of a rivet (2 mm in diameter) that was mounted onto an aluminum stub. The sample was frozen in liquid nitrogen and transferred under vacuum into a PP2000T cryo preparation chamber precooled at -180 °C. Frozen sample was sputter coated with 5 nm-thick platinum in an argon atmosphere at -150 °C. The top part

of the frozen sample was hit with a knife precooled at -150 °C to produce the fractured planes. In order reveal the detailed structure of fractured planes, the samples were sublimed at -90°C and sputter coated with 2.5 nm-thick platinum in an argon atmosphere at -150 °C. The sample was then transferred to SEM cryo stage, held at -130 °C, and high quality SEM images were captured. The secondary electrons were captured by the through the lens detector for imaging using accelerating voltages of 3-5 kV and working distance of 5 mm.

For transmission electron microscopy (TEM), the membranes were embedded in epoxy and polymerized for 16 h at 60 °C. The P*t*BA-PSU-P*t*BA membrane was stained with RuO_4 vapor for 4 hours before embedding. Ultra-thin sectioning was performed using a Leica EM UC6. 100 nm thin sections were examined using a Titan G2 TEM operating at 300 kV (FEI company) equipped with a 4 k × 4 k CCD camera and an energy filter model GIF Tridiem (Gatan, Inc.). Electron energy loss spectroscopy (EELS) signal from the Cu L edge (Cu-L edge of 931 eV) and Iron (Fe-L edge of 721 eV) were acquired in energy-filtered TEM (EFTEM) mode for the distribution of Cu and Fe phases in the samples. Each elemental map was created by using a 3-window method.

The pore size distribution was evaluated by capillary flow porometry was measured in a POROLUX^{TM} 1000 porometer. Porefill (16 mN m^{-1}) was used as the wetting liquid, which was displaced by nitrogen gas flow with the pressure up to 34.5 bar.

Dynamic mechanical analysis (DMA) experiments of the membrane films were performed using a TA Instruments DMA Q800. A piece of rectangular membrane was fixed by tension (film) clamps and tested under stress/strain controlled force mode with a

force ramp rate of 0.1 N min^{-1}.

Contact angle measurement was performed on a Kruss Easydrop equipment in static mode at ambient temperature with 1 μL water drop size. Each reported contact angle is the average of three measurements.

2.2.8 Ultrafiltration Experiments

Ultrafiltration experiments were conducted using a dead-end magnetically stirred homemade stainless steel cell with an effective membrane area of 1.04 cm^2 to evaluate the membrane performance. The membrane was precompacted by deionized water for 30 min at operation pressure of 1 bar. The stable pure water permeance J_w was calculated by using the following equation,

$$J_w = V/tS\Delta P$$

Equation 2.1

where V and t are the volume of the permeate and the time to collect it, respectively; S is the effective membrane area; ΔP is the transmembrane pressure. Afterwards the feed solution was replaced by a total of 0.5 wt% poly(ethylene glycol) mixture solution (0.1 wt % each of 3000, 6000, 10000, 35000, and 100000 g/mol). Samples of the feed solution and permeate were collected after the filtration test in the same manner. The rejection ratio of PEGs with different molar mass R, was calculated according to the equation,

$$R = (1 - C_p/C_f) \times 100\ \%$$

Equation 2.2

where C_p and C_f are the PEG concentrations of each specific molecular weight in the permeate and feed solution, respectively. The concentration was measured by Agilent 1200 GPC using water as eluting solvent, two columns Agilent PL aquagel OH 60 μm and Agilent PL aquagel OH 40 μm. Molecular weight cut-off (MWCO) of the membranes was determined as the smallest molecular weight of PEG for which the membrane has more than 90 % rejection.

2.2.9 Antibacterial Efficacy of the Copper-containing Cross-linked Membrane

Pseudomonas aeruginosa PAO1 was used to evaluate the antibacterial efficacy. The methods and conditions were as described previously but with minor modifications.[38] Briefly, *Pseudomonas aeruginosa* PAO1 was inoculated into 30 mL LB Broth (Lennox) (Sigma-Aldrich Co. LLC, St. Louis, MO, USA). After incubating for 24h at 37 ^{o}C, the bacterial culture was diluted with 0.85% w/v NaCl to an OD_{600} of 0.07. This OD measurement at 600 nm wavelength corresponds to an approximate cell density of 10^8 cells/mL. Prior to experiment, membranes were aseptically cut into 2 cm × 1.5 cm, and were respectively immersed into 10 mL diluted *Pseudomonas aeruginosa* PAO1 cell suspension. The cell suspensions were incubated in a 200 rpm shaker incubator at 37 ^{o}C for 24 h. After that, the membranes were removed from the cell suspensions with sterilized forceps and placed into individual tubes with 2 mL of 0.85% w/v NaCl. The tubes then were unltrasonicated for 3 min by a Q500 sonicator (Qsonica) at 25% amplitude to dislodge the attached bacteria into the suspension. This cell suspensions

were diluted by 2000-fold with 0.85% w/v NaCl. LIVE/DEAD ® BacLight TM Bacterial Viability and Counting Kit (L13152) (Thermo Fisher Scientific Inc., America) was used to stain the bacteria based on manufacturer's protocol prior to live count cells by flow cytometry on Accuri C6 (BD Bioscience, NJ, USA). The attached bacterial cells on the membrane surfaces were also observed by FESEM after fixing the cells with a 4% w/v paraformaldehyde solution.

2.3 Results and Discussion

2.3.1 Synthesis of P*t*BA-PSU-P*t*BA Triblock Copolymer

Scheme 2.1 depicts the reaction procedure aiming at poly(*tert*-butyl acrylate)-*b*-polysulfone-*b*-poly(*tert*-butyl acrylate) (P*t*BA-PSU-P*t*BA) triblock copolymer. The difficulty in synthesizing well-defined block copolymers comprising of step-growth condensation and vinyl polyaddition segments arises from the distinct nature of the respective polymerization mechanisms. This difference can be bridged by mechanistic transformation techniques,[39, 40] in which a polymer chain synthesized by a certain mechanism is functionalized for the initiation of consecutive polymerization through another mechanism. In the present work, a hydroxyl-terminated telechelic polysulfone was prepared by polycondensation of bis(4-chlorophenyl) sulfone with an excess of diol monomer, bisphenol-A, according to the literature.[25] The hydroxyl chain-end functionality may be facilely transformed to the initiating site for chain-growth polymer on the polysulfone backbone, which serves as the central block of the triblock copolymers. For the subsequent chain extension step, reversible-deactivation radical

polymerization (RDRP) is commonly used to afford complex macromolecular

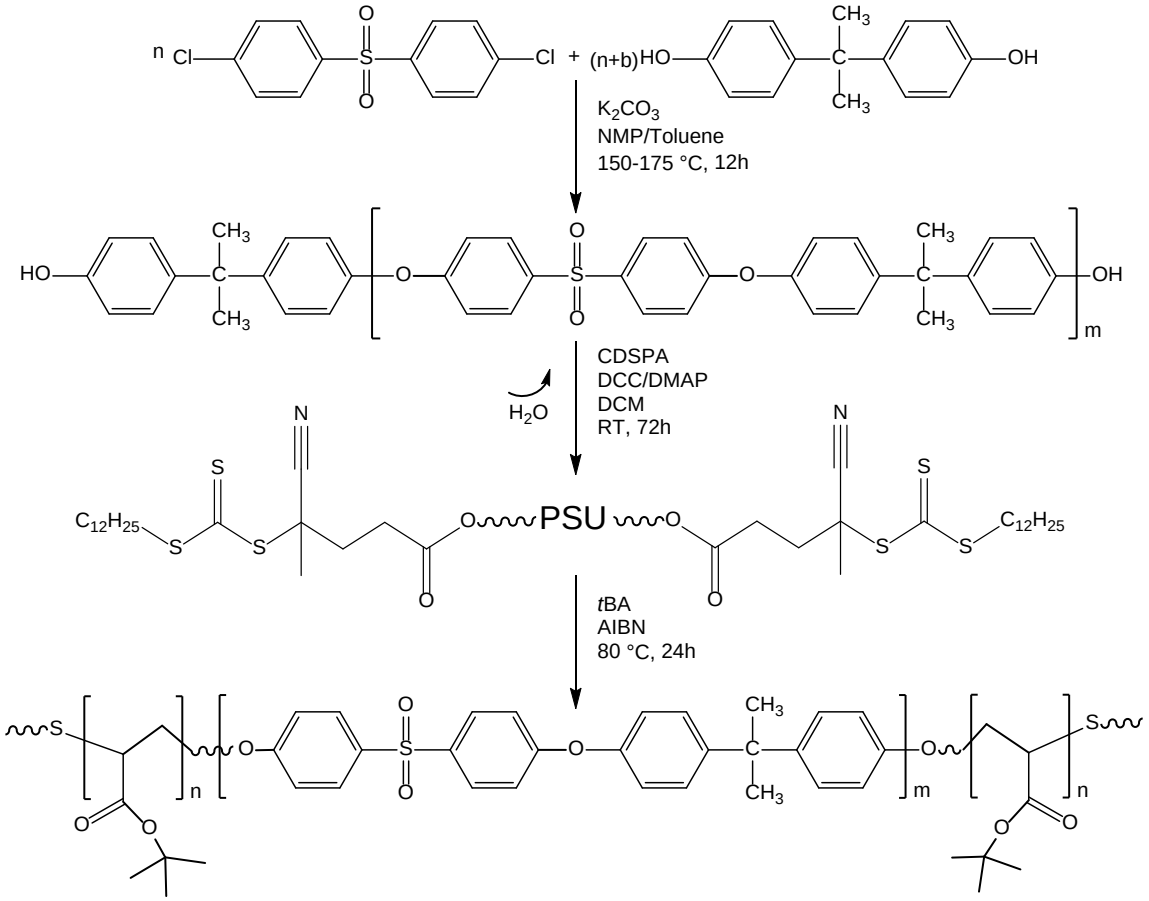

Scheme 2.1. Synthesis route of Poly(*tert*-butyl acrylate)-*b*-polysulfone-*b*-poly(*tert*-butyl acrylate) (P*t*BA-PSU-P*t*BA).

architectures with a well-controlled manner. For example, after the hydroxyl group was

converted to an atom transfer radical polymerization (ATRP) alkyl halide initiator, *n*-butyl acrylate,[30, 41] styrene,[41] poly(ethylene glycol) methyl ether methacrylate (PEGMA),[42] 3-O-methacryloyl-1,2:5,6-di-O-isopropylidene-$_D$-glucofuranose (MAIpG),[42] 2,3,4,5,6-pentafluorostyrene,[43, 44] methyl methacrylate,[44] and the ionic liquid monomer, 1-(4-vinylbenzyl)-3-butylimidazolium bis(trifluoromethylsulfonyl) imide ($VBBI^+Tf_2N^-$)[44]

were successfully polymerized from the polysulfone macroinitiators to generate the outer blocks. Yet another important RDRP technique, RAFT polymerization has not been fully exploited to prepare polysulfone-based triblock copolymers. Only Yi et al.[29] reported the synthesis of PPEGMA-*b*-polyethersulfone (PES)-*b*-PPEGMA with the PES macro-CTA formed by an esterification of the hydroxyl end group with a carboxyl-functional

trithiocarbonate RAFT agent. In this study, we applied this RAFT methodology to obtain P*t*BA-PSU-P*t*BA triblock copolymer, which has not been reported in the literature so far.

As shown in Scheme 2.1, the α, ω-dihydroxyl-terminated polysulfone from condensation, was reacted with a carboxylic acid-terminated RAFT agent, 4-cyano-4-[(dodecylsulfanylthiocarbonyl)sulfanyl]pentanoic acid using N,N'-

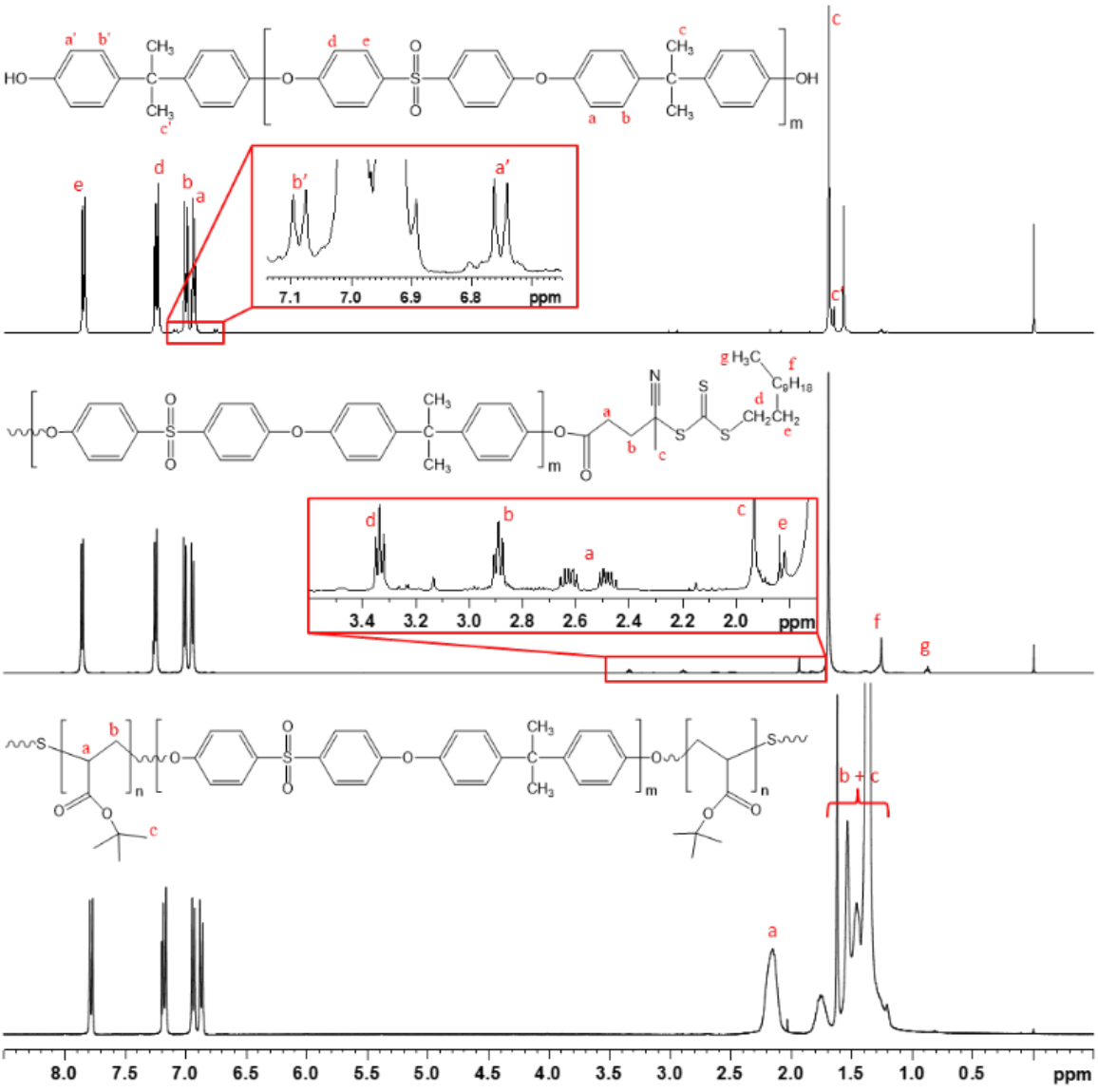

Figure 2.1. ^{1}H NMR spectra for HO-PSU-OH, CTA-PSU-CTA, P*t*BA-PSU-P*t*BA recorded in $CDCl_3$.

dicyclohexylcarbodiimide (DCC) as a coupling reagent and 4-(dimethylamino)pyridine (DMAP) as a catalyst to obtain the trithiocarbonate RAFT chain transfer agent-capped polymer, CTA-PSU-CTA as an esterification product.[31] ^{1}H NMR spectra are given in Figure 2.1 for HO-PSU-OH, CTA-PSU-CTA and P*t*BA-PSU-P*t*BA. The chemical shifts at δ = 6.74-7.85 ppm are assigned to the aromatic protons of the PSU backbone, among which two small doublets centered at 6.75 and 7.09 ppm belong to the protons located at ortho and meta position to –OH in the terminal phenyl rings, respectively. The peak at 1.74 ppm is attributed to aliphatic protons of the isopropylidene. After esterification with RAFT agent, the complete end group functionalization can be confirmed by the emergence of new protons corresponding to the CTA groups,[45] as indicated by the CTA-

PSU-CTA NMR spectrum. The subsequent RAFT polymerization towards triblock copolymer P*t*BA-PSU-P*t*BA was carried out with [AIBN]: [CTA-PSU-CTA]: [*t*BA] = 1: 3: 1800 in DMAc at 80 °C for 24 hrs. The spectrum for P*t*BA-PSU-P*t*BA confirms the successful polymerization by a peak corresponding to methylidyne protons (-CH_2-C***H***(CO_2)-) on the P*t*BA main polymer chain at δ = 2.15 ppm, and broad peaks from 0.9 to 1.67 ppm corresponding to the methylene (-C***H***$_2$-CH(CO_2)-) and *tert*-butyl protons (-CO_2C(C***H***$_3$)$_3$). ^{13}C NMR spectra and assignment can be found in Figure A2.1 (Appendices). Furthermore, the presence of P*t*BA block is confirmed by the strong peak for ester C=O stretch at 1723 cm^{-1} in the FTIR spectrum (Figure 2.2), increased peak intensity for alkyl C-H stretch on the P*t*BA main chain in the region 2800-3150 cm^{-}

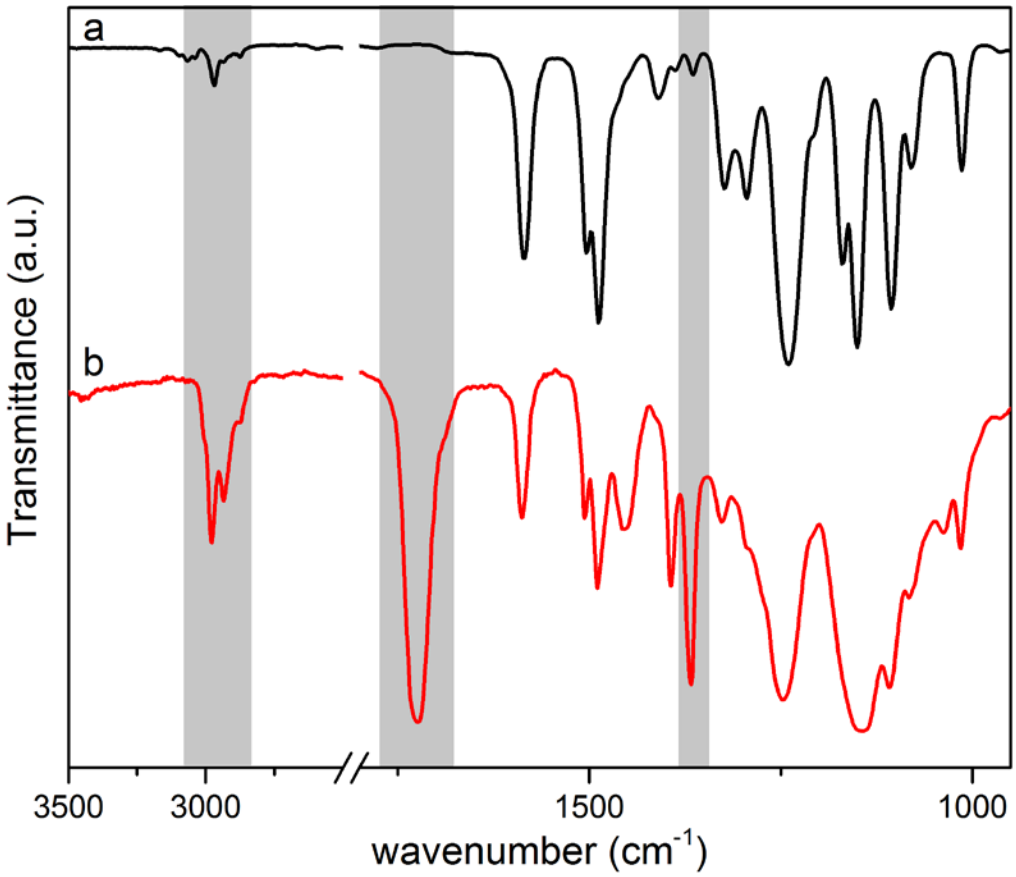

Figure 2.2. FTIR spectra for (a) HO-PSU-OH and (b) P*t*BA-PSU-P*t*BA.

[1] and C-H bending of $C(CH_3)_3$ at 1367 cm^{-1}.[46, 47] Absorption bands related to the PSU macro-CTA are also visible in the spectrum of triblock copolymer, e.g. 1294, 1150 and 1080 cm^{-1} for -$S(O_2)$-, and 1584 and 1488 cm^{-1} for aromatic C-C stretch.[48, 49]

The GPC curves for polysulfone homopolymer and P*t*BA-PSU-P*t*BA triblock copolymers are shown in Figure 2.3. The peak after RAFT copolymerization has a clean shift to shorter retention time than the homopolymer, indicating higher molecular weight. The GPC curve for P*t*BA-PSU-P*t*BA is monomodal without any apparent shoulder, which suggests that the CTA moiety was coupled onto the polysulfone chain ends with high yield and was later the functionality used for RAFT polymerization. Notably, the

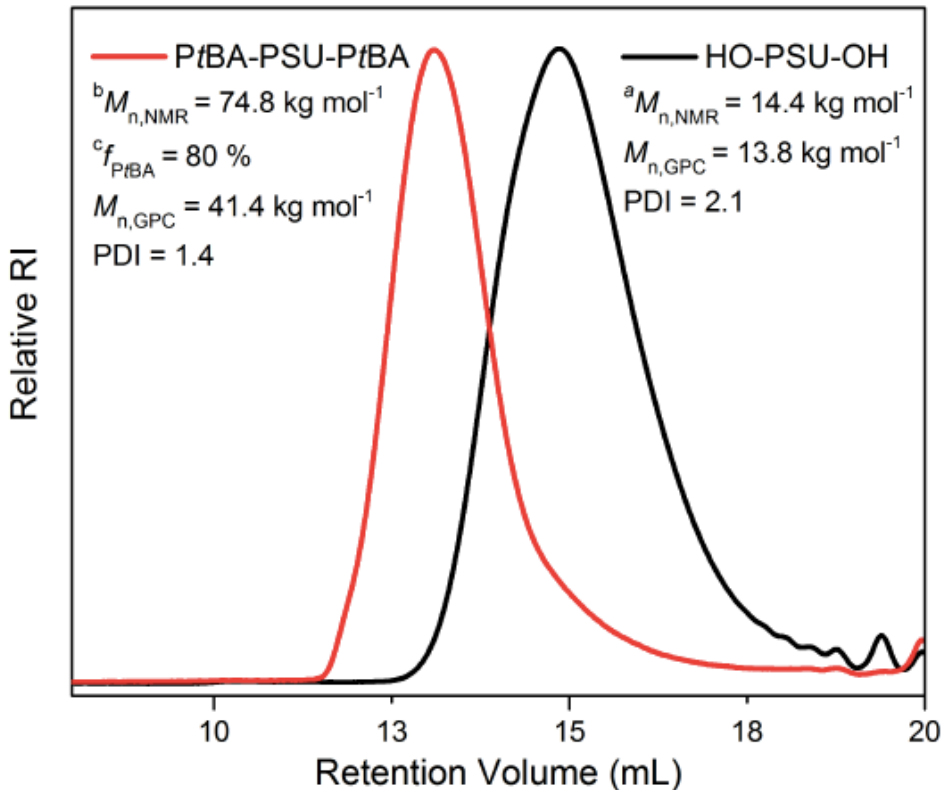

Figure 2.3. GPC curves with refractive index detector (RI) and the corresponding parameters for HO-PSU-OH and P*t*BA-PSU-P*t*BA. $^{a}M_{n,NMR}$ for HO-PSU-OH was calculated from the integral of ^{1}H NMR peak for ortho hydrogen on terminal phenol (δ=6.75 ppm); $^{b}M_{n,NMR}$ for P*t*BA-PSU-P*t*BA was determined by taking into consideration the $M_{n,NMR}$ for HO-PSU-OH and $^{c}f_{PtBA}$, calculated from the integral of ^{1}H NMR peak for –C***H***CH_2– on P*t*BA backbone (δ =2.15 ppm).

molecular weight distribution of triblock copolymer is narrower than the PSU obtained from polycondensation, as the polydispersity decreases from 2.1 to 1.4, due to the incorporation of well-defined P*t*BA side blocks. This phenomenon has been observed for ATRP as well.[41] The number-average molecular weight of polysulfone determined by NMR is 14.4 kg mol^{-1}, lower than the commercial Udel polysulfone (~30 kg mol^{-1}) that is commonly used for membrane fabrication, because the degree of polymerization is limited by the difference in stoichiometry between monomers according to the Carothers

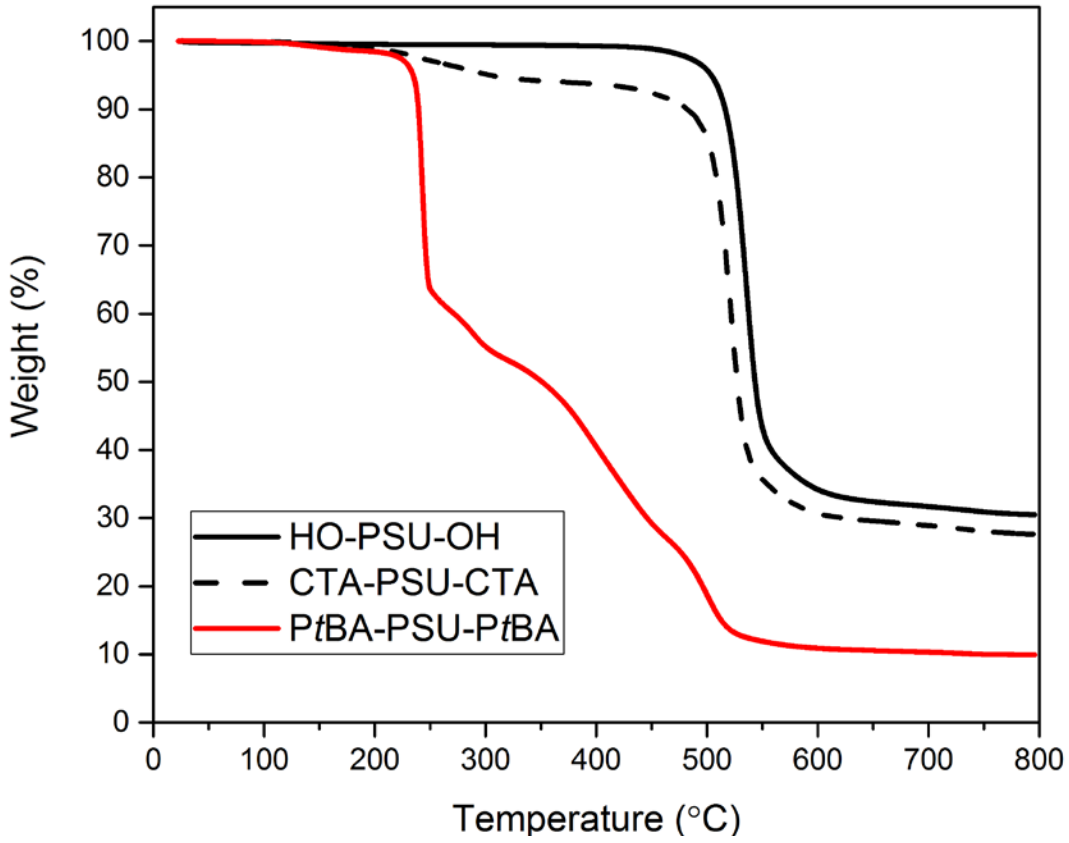

Figure 2.4. TGA curves for HO-PSU-OH, CTA-PSU-CTA and P*t*BA-PSU-P*t*BA under N_2.

equation.[27] This value agrees with the M_n measured by GPC using 99 kg mol^{-1} polystyrene standard. A comparison between the integral of protons on P*t*BA backbone in NMR and that of PSU protons gives the weight fraction of P*t*BA segment (f_{PtBA}), which is 80 %. Based on that, the molar mass of P*t*BA was calculated as 58 kg mol^{-1}, and the total molar mass of P*t*BA-PSU-P*t*BA as 74.8 kg mol^{-1}, higher than M_n determined by GPC (Figure 2.3) which implies hydrodynamic size cannot reflect the true molar mass of copolymer.

The thermal properties of the polymers were evaluated by measuring their thermal decomposition and glass transition temperature. Figure 2.4 shows the TGA curves of the

polysulfone precursor, end-group functionalized macro-CTA and P*t*BA-PSU-P*t*BA triblock copolymer. PSU homopolymer exhibits a sharp weight loss starting from 450 °C which demonstrates its high thermal stability. After end-group functionalization, the CTA-PSU-CTA has a small weight loss from 200 to 330 °C corresponding to the thermal homolysis of C-S bonds in the anchored RAFT agent.[50] A multi-stage weight loss profile can be observed from P*t*BA-PSU-P*t*BA thermogram, consistent with the experimental data reported by literature.[51, 52] It begins with the initial elimination of *tert*-butyl group at 220 °C, which releases isobutylene. The produced carboxylic acid groups on the backbone dehydrate to give six-member cyclic anhydride structure and water. When heated up to 250 °C, the degradation of the side group or P*t*BA backbone leads to a gradual weight loss, followed by the decomposition of PSU mid-block. Estimated from the TGA curve of HO-PSU-OH and P*t*BA-PSU-P*t*BA, the weight loss caused by P*t*BA block is around 80 wt%, correlated well with the weight fraction obtained from ^{1}H NMR. The glass transition temperature of HO-PSU-OH is determined by differential scanning calorimetry (DSC) to be approximately 167 °C. P*t*BA-PSU-P*t*BA displays only one transition at about 46 °C which belongs to P*t*BA. There is no detectable T_g originating from PSU block probably due to its low fraction in the triblock copolymer. The DSC curves are shown in Figure A2.2, Appendices.

2.3.2 Formation of Nanostructured Membranes *via* SNIPS

We used the synthesized P*t*BA-PSU-P*t*BA triblock polymer to fabricate asymmetric membranes *via* the SNIPS technique.[16] Our previous studies have demonstrated that in

Table 2.1. Values of Hansen solubility parameter for polymer segments and solvents

	δ^a [MPa]$^{1/2}$				$\chi_{polymer\text{-}solvent}$
	δ_D	δ_P	δ_H	δ_T	
P*t*BA	16.0	2.3	3.1	16.4	1.35
PSU	16.6	6.0	6.6	18.8	0.49
DMAc	16.8	11.5	9.4	22.4	--
H_2O	15.5	16.0	42.3	47.8	--

[a] δ of P*t*BA is calculated by HSPiP software 4th Edition, others are cited from reference 53, $\delta_T = (\delta_D^2 + \delta_H^2 + \delta_P^2)^{1/2}$

this process the block copolymer micellization and the micelle supramolecular assembly in solution play a decisive role for the pore formation in the upper layer of the membrane. The morphology starts to be induced even before immersion in water. Different than in other explored cases, instead of AB diblock copolymers,[1, 7, 9-11] the present work uses an amphiphilic BAB triblock copolymer in a selective organic solvent, whose middle block (A) is solvophilic, while the two outer blocks (B) are relatively solvophobic.

2.3.2a BAB Copolymer Micellization with Flower-like Organization

20 wt% of the synthesized P*t*BA_{30k}-PSU_{14k}-P*t*BA_{30k} was dissolved in N,N-dimethylacetamide (DMAc). The Flory-Huggins interaction parameters (χ) can be estimated, by using Hansen solubility parameters (δ).[53] Table 2.1 shows the different contributions to δ (i.e., dispersion force (δ_D), polarity (δ_P), and hydrogen bonding (δ_H)), and the computed interaction parameter $\chi_{polymer\text{-}solvent}$ between each polymer segment and

solvent pairs in the casting solution. From Table 2.1, it is evident that DMAc is a

selective solvent for the polysulfone block, whereas the interaction with the poly(*tert*-

butyl acrylate) is poorer. To avoid the less favorable P*t*BA contact with DMAc, the block

copolymers are expected to assemble into a “flower-like” morphology, as depicted in

Figure 2.5a. The middle PSU blocks form loops, which constitute the corona and the

P*t*BA blocks segregate into the micelle core. The self-assembly of other BAB copolymers

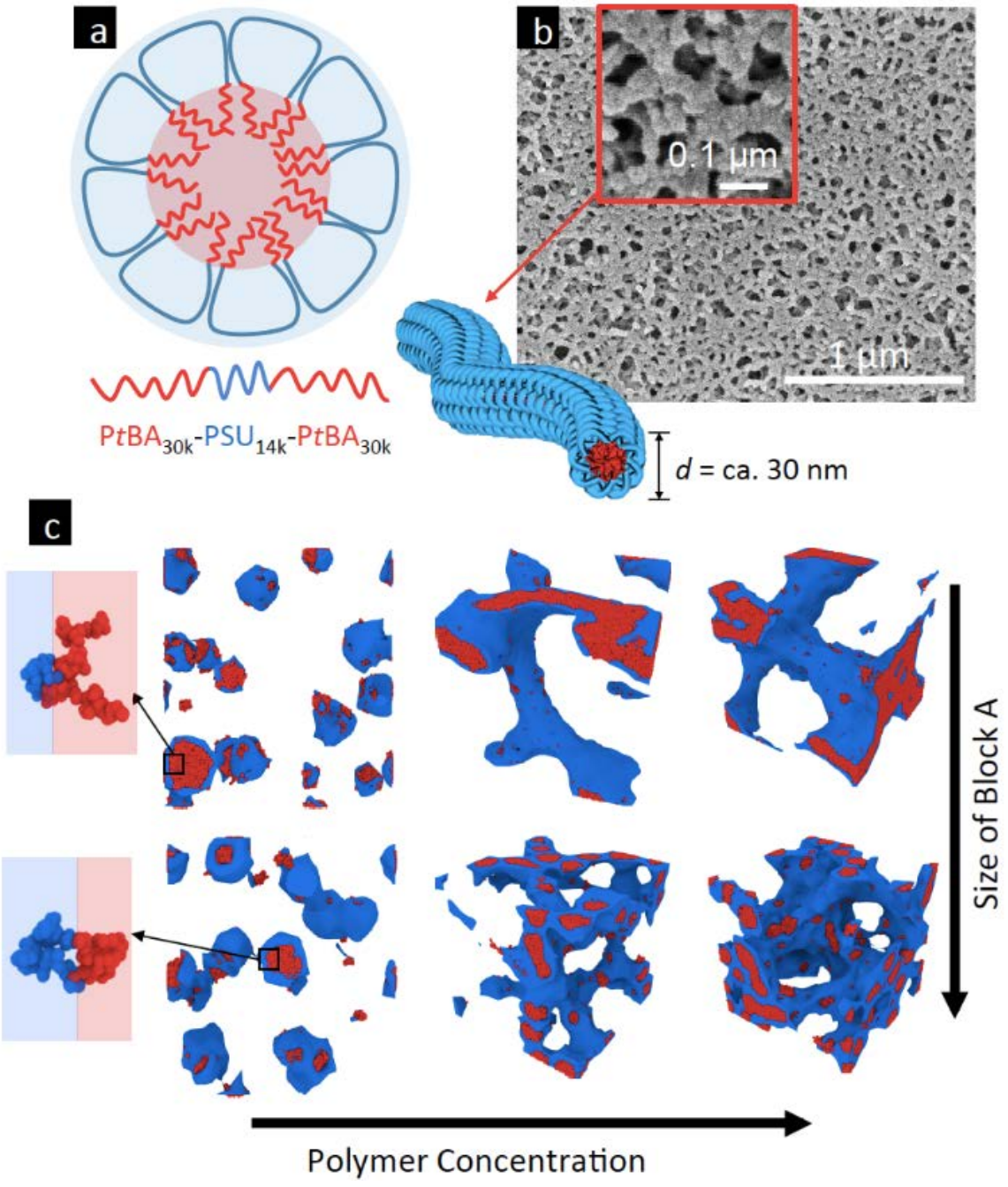

Figure 2.5. (a) Schematic illustration of flower-like micelles formed by BAB triblock copolymer: red represents the two end P*t*BA blocks, while blue denotes the middle PSU block; (b) Cryo field emission scanning electron microscopy (cyro-FESEM) image for worm-like cylindrical micelles in solution (20 wt% P*t*BA-PSU-P*t*BA in DMAc) with a diameter of about 30 nm; (c) DPD simulation of the effect of the BAB copolymer concentration and size of block A over the morphology of the assembled micelles. The blue contours correspond to block A, whereas the red particles represent block B. The solvent representation as particles was removed to facilitate the visualization.

has been investigated before[54-56] and the existence of flower-like micelles have been demonstrated.[57, 58] The free energy G of this type of corona-core structures can be expressed Equation 3,

$$G = G_{corona} + G_{core} + G_{interface}$$

Equation 2.3

where the G_{corona} and G_{core} account mainly for the stretching of block segments from their unperturbed condition to the conformation they assume in the corona and core; $G_{interface}$ is related to the formation of the P*t*BA-PSU and PSU-solvent interfaces. The interfacial free energy typically depends on the total interfacial areas ($A_{interface}$) and the interfacial tensions (γ) as Equation 2.4.

$$G_{interface} = \gamma A_{interface}$$

Equation 2.4

During the formation of flower-like micelles the reduction of the total interfacial free

energy competes with the entropic penalty caused by looping middle block. To alleviate the entropy loss, some of the B blocks might dangle in solution, or associate into neighboring micelles to form a branched structure bridged by polymer chains of well-solvated block.[54, 59, 60]

2.3.2b Worm-like Cylindrical Micelle Formation

Cryo-electron microscopy (cryo-EM) is a powerful tool to directly reveal the morphology of block copolymer micelles in solution.[6] Figure 2.5b shows the cryo field emission scanning electron microscopy (Cryo-FESEM) image of a fractured droplet of a 20 wt% P*t*BA-PSU-P*t*BA casting solution in DMAc. This image shows that triblock copolymers assemble into worm-like cylindrical micelles with a diameter of around 30 nm, distributed in a random network. Some interconnected or fused strings suggest the coexistence of branched structures besides the isolated micelles.

Spherical geometry has been reported for flower-like micelles of BAB triblock copolymers.[57, 58] We believe the formation of cylindrical morphologies in this work is a consequence of the increase of the micelle size, reflected in the aggregation number (N_{agg}) and micelle core size (R_{core}). The growth of micelles is energetically favorable because it decreases the total interfacial area ($A_{interface}$), minimizing the free energy contribution $G_{interface}$. However, as the size of the micelles increases the stretching of the core-forming blocks imposes an entropic penalty over the free energy G_{core}. As N_{agg} grows, the assembly of the copolymer chains into spherical micelles requires a high degree of stretching of the P*t*BA core-forming blocks. Thus, non-spherical micelles are preferred in order to reduce the deformation energy needed (G_{core}) to confine them into

the core.

Competing entropic (affected by the composition of the triblock copolymer and polymer concentration) and enthalpic (affected by the polymer-solvent interactions) contributions determines the total free energy G.[22] In particular, for the casting solutions used to prepare the membranes, we found that the balance of these effects on G stabilizes the assemblies shapes illustrated in Figure 2.5. The shape of amphiphiles assemblies in solution is usually correlated to the packing parameter, p,

$$p = v/(a_0\, l_c)$$

Equation 2.5

where v and l_c is the chain volume and length of core block, respectively, and a_0 is the optimum surface area of corona block at the interface. Spherical micelles are formed when $p \leq 1/3$. When p increases to about 0.5, rods or cylinders are preferred. At higher p (0.5~1), they evolve to interconnected networks.[61] In order to better rationalize the formation of cylindrical assemblies we model the self-assembly of a triblock copolymer BAB in a selective solvent favorable for A, as illustrated in Figure 2.5c. To construct the computational model we use the dissipative particle dynamics (DPD) method. We refer the reader to the Appendices for a detailed description of the DPD computational model.

The polymer concentration in the casting solution strongly influences the morphology. In general, an increase of copolymer concentration leads to micelle growth with a corresponding increase in N_{agg} and R_{corona}.[62] A further increase of concentration might induce a morphological transition to non-spherical micelles. Our computational model

captures this concentration effect in the simulations. Figure 2.5c shows the morphological transition of assemblies from spherical to an interconnected network as the polymer concentration increases, simulated by DPD. In addition to the overall polymer concentration, the block lengths of P*t*BA-PSU-P*t*BA affect the assembly morphology.[22] In our systems we have micelles with a relatively small corona, due to the low fraction of PSU in the block copolymer. This facilitates the fusion of spherical micelles into a network with elongated cores at large copolymer concentrations. In contrast, when the length of the middle block is larger, thicker coronas are formed and the fusion of micelle cores becomes entropically less favorable. We demonstrate this effect by modeling the morphological transitions of a copolymer $B_{20k}A_{34k}B_{20k}$, which has the same total molecular weight as the copolymer experimentally used in this study (B_{30k}-A_{14k}-B_{30k}), but has a larger fraction of A. Figure 2.5c shows the formation of assemblies with larger N_{agg} in the form of a network. As the polymer concentration increases, larger A blocks favor the formation of a network constituted by a fused corona and an array of segregated cores.

Similarly to the copolymer block length, the polymer–solvent interactions can change the dimension of both core and corona domains, modifying the final morphogenesis of the assemblies.[63] Herein, DMAc prefers PSU blocks, however, because of partial solubility of P*t*BA homopolymer in DMAc, some degree of core swelling is expected. The core swelling facilitates the formation of elongated assemblies, which interconnect in a network. The similar phenomenon related to the solvent has been described by Quémener et al.[64] In their work, by increasing the content of toluene in the mixed solvent with DMF, the shape of poly(styrene-co-acrylonitrile)-*b*-poly(ethylene oxide)-*b*-poly(styrene-co-

acrylonitrile) flower-like micelles changed from spherical nanoparticles to a worm-like network, similar to those structures we obtained for P*t*BA-PSU-P*t*BA copolymer.

2.3.2c Membrane Formation by Immersion in Water

Water is a nonsolvent for P*t*BA-PSU-P*t*BA. All solubility parameter contributions for water are far from those of rather hydrophobic P*t*BA and PSU blocks (Table 2.1). When the solution is cast as a thin film and immersed into water, a fast solvent-water exchange leads to an abrupt decrease of chain mobility fixing the polymer-polymer entanglement and kinetically trapping the morphology formed in solution. Therefore, the worm-like cylindrical morphology on the top of the solution layer is completely immobilized, giving rise to the nanostructured membrane with a highly porous surface. Field-emission scanning electron microscopy (FESEM) was employed to investigate the membrane surface and the image shown in Figure 2.6a confirms the correlation between the

interconnected 3D porous structure of the triblock copolymer membrane and the worm-like network formed by cylindrical micelles in the bulk of the solution before immersion. DMAc is rapidly replaced by water. A network of assembled copolymer will form the membrane matrix and the pore walls. The space in between, which is depleted in copolymer, with be filled by water. Solvent-water exchange proceeds in layers far from the water-copolymer solution interface, but at a lower rate, because the water and solvent will have to be transported through the already solidified top layer. As the water content increases a macroscopic phase separation is induced. Macrophase separation follows the mechanism of spinodal decomposition and/or nucleation and growth, similar to what

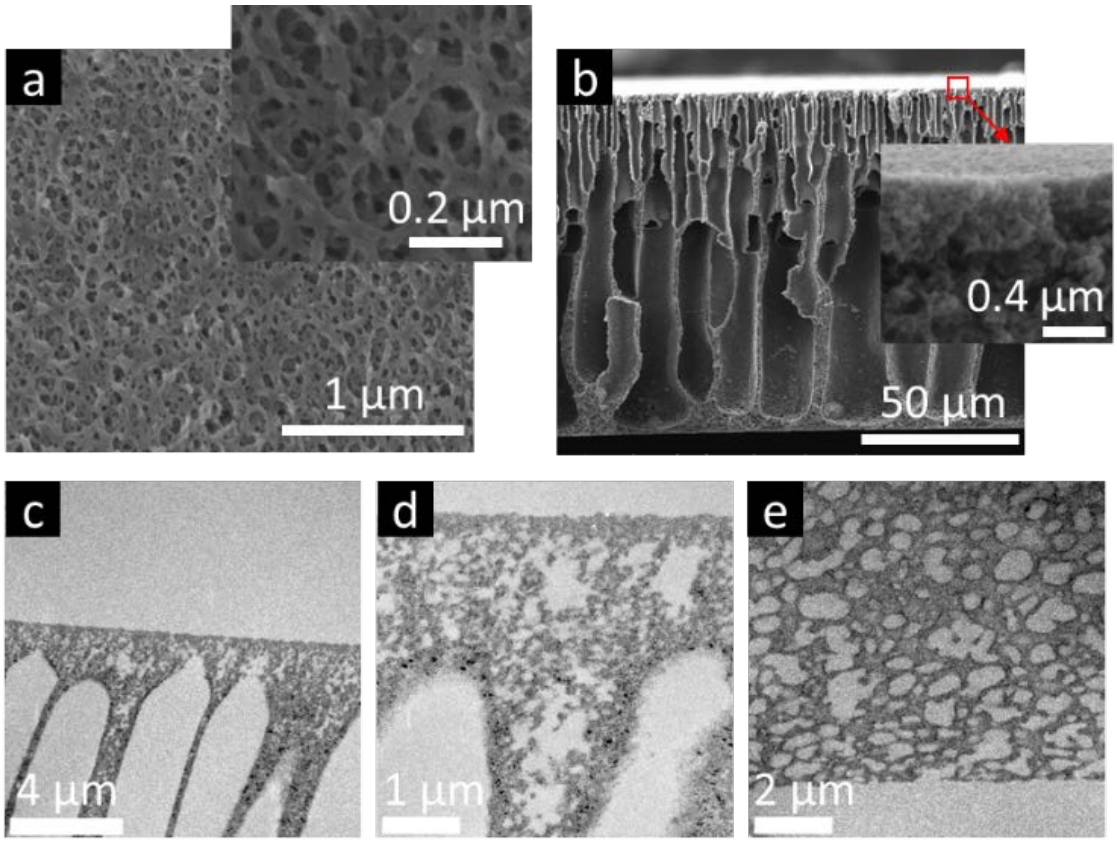

Figure 2.6. FESEM of P*t*BA-PSU-P*t*BA membrane (a) surface and (b) cross-section; TEM of P*t*BA-PSU-P*t*BA membrane cross-section near the (c and d) top surface and (e) bottom.

happens with homopolymer solutions in the formation of asymmetric membranes. The polymer-poor phase forms the pores and the polymer-rich phase forms the membrane structure fixed by gelation/solidification, when the polymer concentration in this phase is high enough. Since the top membrane layer is fast solidified before the macrophase separation even starts. On the other hand, far from the water-solution interface, phase separation proceeds to a further extent before solidification starts, leading to larger segregated phases (incipient pores). Based on this principle, an asymmetric membrane is expected. Indeed, the FESEM image for the membrane cross-section (Figure 2.6b) confirms a pronounced asymmetry: a high density of small pores is seen on the top (see

high magnification image in the inset) and disordered, larger pores predominate the part underneath the top layer. Moreover, long finger-like macrovoids extending to the bottom show up on the cross-section, which are not observed in PS-*b*-P4VP nanoporous membranes. They frequently appear in the commercial phase inversion membranes manufactured from homopolymers. This highly porous asymmetric structure spanning from top to bottom with the coexistence of sponge- and finger-like pores is also supported by TEM as shown in Figure 2.6c-e.

This membrane is promising for filtration application with pore size in the ultrafiltration (UF) range (2~50 nm) and high porosity resulting from the micelle network. Mechanical stability is also an important quality for membrane application. The typical stress-strain curves from dynamic mechanical analysis (DMA) tensile test for PSU homopolymer and P*t*BA-PSU-P*t*BA triblock copolymer membranes prepared under same conditions are plotted in Figure 2.7. The Young's modulus (E) and ultimate stress of PSU are higher than those of copolymer, while the maximum elongation of copolymer is larger. It shows that the presence of low T_g (46 °C) P*t*BA domain renders a more ductile membrane, allows the membrane to be deformed to a larger extent, whereas the stress resistance is slightly compromised compared to the PSU membrane which is more rigid. The area under the stress-strain curve of copolymer membrane, representing its toughness, defined as the maximum energy a material can absorb before rupturing, is 607 kJ m^{-3}, doubles that of 306 kJ m^{-3} toughness of PSU membrane Phillip et al.[19] reported for PS-*b*-P4VP and PS-*b*-PI-*b*-P4VP maximum stress values similar to those measured in this work, but with strain values lower than 0.5 %. For OH-PSU-OH and P*t*BA-PSU-P*t*BA membranes we reached strain values up to 28 %. This leads to toughness values, which are 34 to 67-

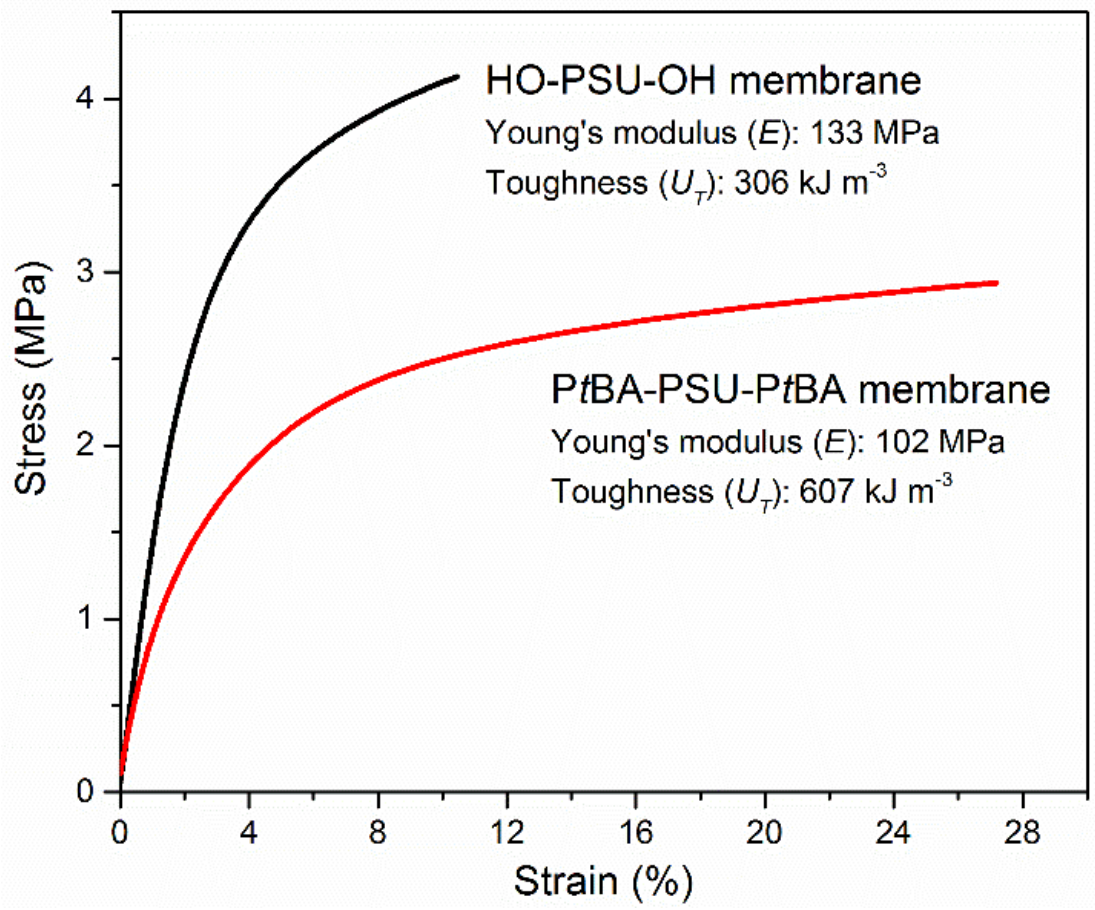

Figure 2.7. Stress-strain curves for HO-PSU-OH and P*t*BA-PSU-P*t*BA membranes.

fold higher for PSU-based copolymers than for the polystyrene-based ones. Toughness values reported for another previously reported membrane based now on polyisoprene-*b*-polystyrene-*b*-poly(N,N-dimethylacrylamide),[21] are two orders of magnitude lower than that of the PSU-block membrane.

2.3.3 Hydrolysis and Metal Complexation of Membranes

P*t*BA can be easily hydrolyzed into poly(acrylic acid) (PAA) by acid treatment, or by

using $ZnBr_2$ without acid.[65] This dramatically increases the hydrophilicity of the copolymer and the prepared membranes. However since the PSU block is relatively small, the pure hydrolysis leads then to films, which can highly swell in water, behaving like a gel and not being convenient for membrane applications. We found out that if the hydrolysis is immediately followed by complexation with transition metal ions, e.g. Cu^{2+} and Fe^{3+}, stable hydrophilic porous membranes are formed with a surface morphology different than that before the modification. Figure 2.8d describes the procedure for modification and the possible structures of PAA-metal complexes.[66] Partial hydrolysis of *tert*-butyl ester units on the surface of membrane, by treating with concentrated hydrochloric acid (HCl) aqueous solution (37 %, w/w), leads to the formation of carboxylic acid groups, analogous to reports for other copolymers containing P*t*BA.[67] The hydrolysis time has been optimized to achieve sufficient surface hydrolysis without damaging the bulk membrane strength. Then the membrane was taken out of the acid bath and plunged into a solution containing 0.1 M Cu^{2+} or Fe^{3+} metal solution. The product of hydrolysis, the poly(acrylic acid) (PAA) segment, is well known as anionic polyelectrolyte capable of complexing metals.[68] Functional membranes taking advantage of this property for separation purposes have been reported. For instance, Weidman et al. hydrolyzed polyisoprene-*b*-polystyrene-*b*-poly(*N*,*N*-dimethylacrylamide) nanostructured membranes to obtain pores with exposed PAA blocks for series of metal ions to PAA has been investigated at various degrees of dissociation, indicating also the formation of multidentate ligand complexes[69], which would explain the crosslinking of membrane, as illustrated in Figure 2.8d. The intermolecular polymer-metal binding has been utilized to form hydrogels[70] for dental

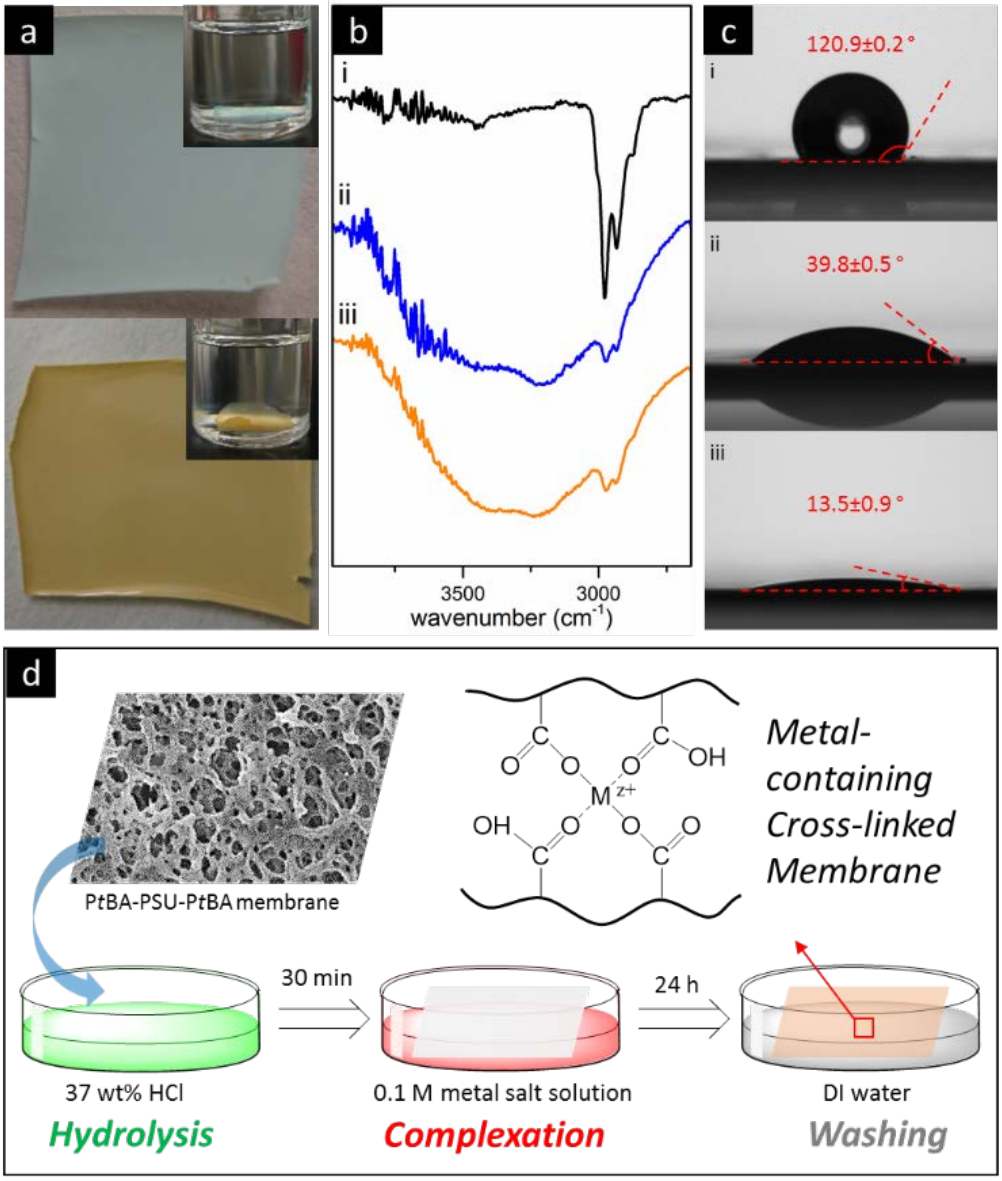

Figure 2.8. (a) Photographs of PSU-PAA-Cu^{2+} (top) and PSU-PAA-Fe^{3+} (bottom) membranes in dry state and immersed in DMF (insets); (b) FTIR spectra and (c) contact angle measurement for original (i) P*t*BA-PSU-P*t*BA, (ii) PSU-PAA-Cu^{2+} and (iii) PSU-PAA-Fe^{3+} membranes; (d) Surface modification of P*t*BA-PSU-P*t*BA membrane *via* hydrolysis and metal complexation.

application. Recently the complexation of thiourea- and triazole-based polymers with different metal ions has been used to induce phase inversion and fabricate high metal

loading membranes with thin selective layer.[71, 72] The complexation of metals in our case can be visualized by the strong color of the Cu(II)- (blue) and Fe(III)-complexed membranes (brown), denoted as PSU-PAA-Cu^{2+} and PSU-PAA-Fe^{3+}, respectively (see Figure 2.8a). The insets in Figure 2.8a show that when immersed in DMF, a good solvent for the parent triblock copolymer, these two membranes were not dissolved thanks to the crosslinking. They just swell and become more transparent. FTIR spectra of the metal complex membranes are shown in Figure 2.8b and display a broad band at 3000-3850 cm^{-1} due to the stretching vibration of O-H groups in PAA units from the hydrolysis of P*t*BA. As we expected, the presence of negatively charged PAA and metal ions on the surface made the membrane more hydrophilic. The contact angle of PSU-PAA-Cu^{2+} and PSU-PAA-Fe^{3+} membrane dramatically decreased to 39.8 ° and 13.5 ° respectively from 120.9 ° of the original membrane comprising of hydrophobic PSU and P*t*BA before hydrolysis, as shown in Figure 2.8c. The weight fractions of Cu^{2+} and Fe^{3+} were found to be 1.4 % in the metal-complexed membranes by analyzing their TGA curves and assuming that the metal ions were fully converted to their oxides, when heated in air (Figure A2.3 in Appendices). Beside copper and iron, various transition metals were able to form complex with the PAA block in the membrane. This can be seen by the different colors of membranes exposed to different metals under the same condition (Figure A2.4 in Appendices).

By comparing Figures 2.6a to 2.9a and 2.9e it is clear that the membrane surface morphology significantly changed. The membranes after hydrolysis and complexation are smoother. The membranes prepared by complexation with Cu^{2+} have more regular pores and the pore density is higher than by complexation with Fe^{3+}. We believe that

during the hydrolysis, as the P*t*BA blocks are transformed into PAA, the cores become

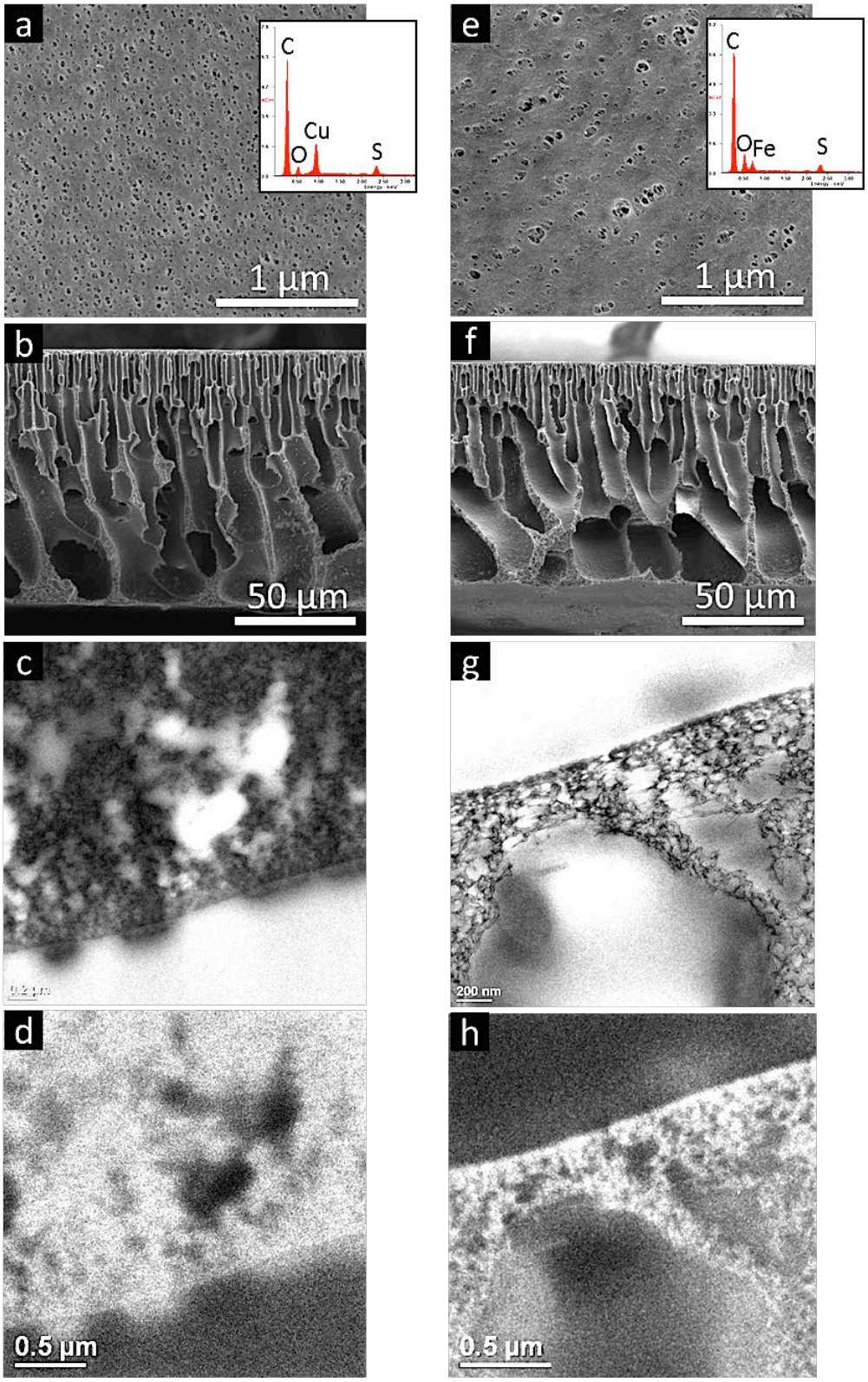

Figure 2.9. (a) Surface and (b) cross-sectional FESEM images of PSU-PAA-Cu^{2+}, and (e and f) PSU-PAA-Fe^{3+}; The insets are EDS spectra recorded from the corresponding membrane surface; TEM elastic electron images of (c) PSU-PAA-Cu^{2+} and (g) PSU-PAA-Fe^{3+}, and energy loss element specific image of (d) PSU-PAA-Cu^{2+} (Cu-L edge at 931 eV) and (h) PSU-PAA-Fe^{3+} (Fe-L edge at 721 eV), obtained with inelastic electron.

highly swollen. Since the PAA blocks constitute the higher fraction of the membrane, in contact with water the previous structure dominated by “flower-like micelles” tends to invert near the surface, re-arranging the surface morphology and switching the membrane hydrophilicity. If the complexation of the PAA carboxylate anions with metal ions like Cu^{2+} and Fe^{3+} is immediately promoted, a physical crosslinking takes place and the anions becomes less available to interact with water. Water uptake is then suppressed. This de-swelling effect has been reported in PAA-containing hydrogels.[73] Also, the more rigid cross-linked PAA structure becomes less expanded or swollen than in the case of the free polyelectrolyte without metal ions. Along with FESEM, the surface elemental analysis was carried out by energy-dispersive X-ray spectroscopy (EDS). The spectra strongly indicate the presence of metals at 0.94 keV for copper Lα and 0.705 keV for iron Lα in PSU-PAA-Cu^{2+} and PSU-PAA-Fe^{3+} membranes, respectively (insets in Figures 2.9a and 2.9e). Electron energy loss spectroscopy (EELS) and the corresponding element specific image coupled with TEM (Figures 2.9c-d and 2.9g-h) confirm the presence and homogeneous distribution of copper and iron in the membranes. The cross-sectional FESEM images (Figures 2.9b and 2.9f) show that the morphology far from the surface did not change. The same asymmetric macro-porous structure can be seen. In a control experiment, when we transferred the hydrolyzed membrane from the acid bath to a pure

water bath directly, without metal ion, the membrane immediately became a transparent film and too soft to handle because of the quick deprotonation and water swelling. Figure 2.9e suggests that the porosity of PSU-PAA- Fe^{3+} seems to be lower than that of copper-complexed membranes. The surface of the PSU-PAA-Fe^{3+} membrane is however more hydrophilic, indicated by lower contact angle. This difference can be explained by the stronger complexation ability of Fe^{3+} [73], which acts as a stronger driving force to expose the PAA segments from the micelle core to the surface in contact to water. Furthermore Fe^{3+} has higher valence than Cu^{2+} and smaller ionic radius[74] and this also helps its diffusion into membrane to complex and promote the crosslink.

2.3.4 Ultrafiltration Performance and Anti-bacterial Activity of Membranes

The results of ultrafiltration experiment for the original P*t*BA-PSU-P*t*BA membrane and two cross-linked membranes containing copper (II) and iron (III) respectively were summarized in Table 2.2. The pure water permeance (PWP) of P*t*BA-PSU-P*t*BA membrane is 555 L m^{-2} h^{-1} bar^{-1}. Its molecular weight cut-off (MWCO) determined by poly(ethylene glycol) (PEG) filtration test is 28 kg mol^{-1}. This means that the smallest PEG that the membrane can effectively reject has a hydrodynamic diameter of 8 nm, calculated using an empirical equation as reported by Lentsch et al.[75] Considering the MWCO, its water permeance is much higher than common UF membranes. For instance, Zhou et al. reported 30 and 10 L m^{-2} h^{-1} bar^{-1} for polysulfone and regenerated cellulose membranes (MWCO 30 kg mol^{-1}) respectively, purchased from Hydration Technology Innovations (HTI), LLC (Albany, OR);[76] Kanagaraj reported 52 to 94 L m^{-2} h^{-1} bar^{-1} for

Table 2.2. Summary of membrane ultrafiltration performance

Membrane	MFP size (nm)	PWP (L m^{-2} h^{-1} bar^{-1})[b]	$MWCO_{PEG}$ (kg mol^{-1})[c]
P*t*BA-PSU-P*t*BA	30.4 ± 1.4	555 ± 176	28
PSU-PAA-Cu^{2+}	--[a)]	653 ± 191	60
PSU-PAA-Fe^{3+}	--[a)]	131 ± 6	8

[a] Too brittle to measure mean flow pore (MFP) size in the dry state; [b] pure water permeance; [c] molecular weight cut-off (MWCO) for 90 % PEG rejection (Figure A2.5).

polyvinylpyrrolidone-blended polyetherimide membrane (MWCO 45 kg mol^{-1}).[77] The high water flux can be attributed to the porous structure with an exceptionally high porosity. When measuring the pore size on the membrane selective layer by capillary flow porometry we obtained values of 30.4 ± 1.4 nm (mean flow pore or MFP size) with a narrow distribution as shown in Figure A2.6, Appendix. This value is obviously larger than the PEG hydrodynamic diameter corresponding to its MWCO. The reason is the presumption of capillary flow porometry measurement that all surface pores are separated close to the perfect cylindrical pores fails when applied to the P*t*BA-PSU-P*t*BA membrane containing a highly interconnected porous morphology on the top selective layer. The analysis of the high magnification FESEM image reveals that the membrane has a wide range of pore size from sub-10 nm to above 50 nm in the 3D interconnected porous structure.

The smallest pores inside the porous network are responsible for the retention of low molecular weight PEG. Although small solutes can go through the surface pores larger than their hydrodynamic size, they are trapped by the underneath "spider web". The PSU-PAA-Cu^{2+} membrane exhibits a slightly higher water flux while its MWCO is two times of that of the parent membrane. The improved hydrophilicity could be a reason for this result. On the other hand, the water flux and MWCO of PSU-PAA-Fe^{3+} decreases dramatically to 131 L m^{-2} h^{-1} bar^{-1} and 8 kg mol^{-1} due to the lower porosity and higher cross-linking.

Figure 2.10 shows that the number of viable bacterial cells attached on PSU-PAA-

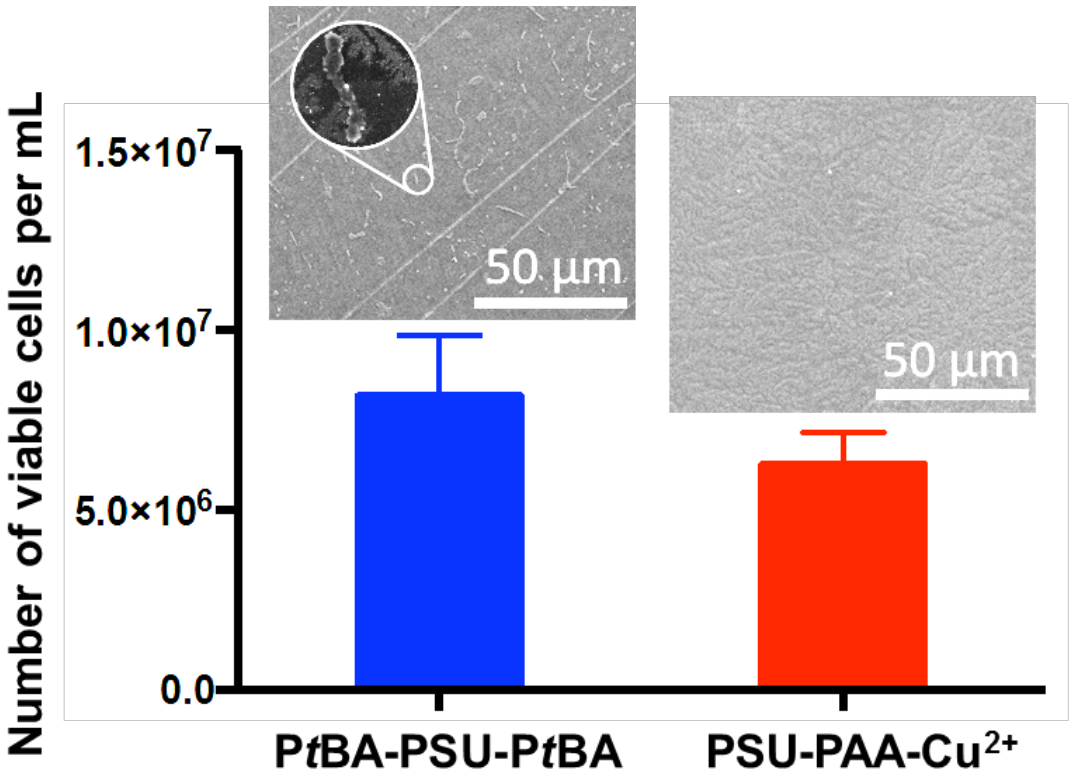

Figure 2.10. The number of viable bacterial cells attached on membrane surface and counted by flow cytometry; FESEM images of corresponding membranes after exposure to *Pseudomonas aeruginosa* PAO1 for 24 h.

Cu^{2+} membrane decreased by about 25.1% when compared to the ones on P*t*BA-PSU-P*t*BA membrane. This observation is in agreement with the previous works that demonstrated copper to exhibit antibacterial effects.[78-80] FESEM images reveal more bacteria attached on P*t*BA-PSU-P*t*BA membrane compared to PSU-PAA-Cu^{2+} membrane, which further verifies the antibacterial efficacy. The decrease in the number of viable cells on membranes chelated with copper as demonstrated by both flow cytometry and FESEM confirms that the presence of copper can inhibit the attachment of bacteria onto the membrane surface, which is one of the key initiation steps in biofouling.[81]

2.4 Conclusions

We successfully synthesized for the first time poly(*tert*-butyl acrylate)-*b*-polysulfone-*b*-poly(*tert*-butyl acrylate) (P*t*BA-*b*-PSU-*b*-P*t*BA) copolymers. End-group modification, with trithiocarbonate RAFT agent on telechelic hydroxyl-terminated polysulfone from step-growth condensation, produced CTA-capped polysulfone for subsequent reversible-deactivation radical polymerization. This macro-CTA was further used in RAFT polymerization to obtain $PtBA_{30k}$-*b*-PSU_{14k}-*b*-$PtBA_{30k}$. The chemical structure of the triblock copolymer and precursors were verified by characteristic adsorption peaks in NMR and FTIR spectra. Thermal studies confirm the presence of P*t*BA blocks in the copolymer with characteristic weight loss at 220 °C measured by TGA and shift of T_g revealed by DSC. The GPC peak moved to the shorter retention time without any shoulder after the chain extension towards the triblock copolymer. This result strongly suggests RAFT polymerization was carried out in a controlled manner, which led to a

narrowing of molar mass distribution from 2.1 to 1.4. The relatively low PDI allows the as-synthesized triblock copolymers to assemble into worm-like cylindrical micelles in DMAc. This self-assembly process was observed from solution cryo-FESEM micrograph. Based on Hansen solubility parameter, we propose a “flower-like” BAB arrangement with the PSU central block as the shell protecting the less solvated P*t*BA segments. The high polymer concentration, low composition of PSU, and highly swelled micelle cores are important factors in forming the specific micelle morphology as supported by our computational models. Once the same solution was cast and immersed into water, the worm-like cylindrical micelles on the surface were frozen, giving rise to the nanostructured membrane with a highly porous interconnected skin layer on top of graded finger-like macrovoids which are present in the lower portion. This asymmetric nanostructured membrane formed *via* SNIPS has high pure water permeance of 555 L m^{-2} h^{-1} bar^{-1} with molecular weight cut-off of 28 kg mol^{-1} compared to the normal phase inversion membranes. The combination of soft P*t*BA and rigid PSU blocks makes its mechanical strength comparable to commercial homopolymer membranes. A membrane surface modification method was proposed to obtain metal-containing cross-linked membranes by hydrolysis of P*t*BA and complexation with transition metals. The characterization of copper and iron-chelated membranes demonstrates that the surface morphology, water flux and MWCO could be successfully tuned by this modification. The copper-containing membrane shows improved antibacterial efficacy. With these properties, we propose their application as low fouling, solvent resistant and catalytic membranes.

2.5 References

1. K.-V. Peinemann, V. Abetz and P. F. W. Simon, *Nat. Mater.*, 2007, 6, 992-996.
2. H. Ahn, S. Park, S.-W. Kim, P. J. Yoo, D. Y. Ryu and T. P. Russell, *ACS Nano*, 2014, 8, 11745-11752.
3. E. A. Jackson and M. A. Hillmyer, *ACS Nano*, 2010, 4, 3548-3553.
4. Y. Zhang, J. L. Sargent, B. W. Boudouris and W. A. Phillip, *J. Appl. Polym. Sci.*, 2015, 132, 41683.
5. S. E. Querelle, E. A. Jackson, E. L. Cussler and M. A. Hillmyer, *ACS Appl. Mater. Interfaces*, 2013, 5, 5044-5050.
6. D. S. Marques, R. M. Dorin, U. Wiesner, D. M. Smilgies, A. R. Behzad, U. Vainio, K. V. Peinemann and S. P. Nunes, *Polymer (United Kingdom)*, 2014, 55, 1327-1332.
7. D. S. Marques, U. Vainio, N. M. Chaparro, V. M. Calo, A. R. Bezahd, J. W. Pitera, K. V. Peinemann and S. P. Nunes, *Soft Matter*, 2013, 9, 5557-5564.
8. R. M. Dorin, D. S. Marques, H. Sai, U. Vainio, W. A. Phillip, K. V. Peinemann, S. P. Nunes and U. Wiesner, *ACS Macro Letters*, 2012, 1, 614-617.
9. S. P. Nunes, M. Karunakaran, N. Pradeep, A. R. Behzad, B. Hooghan, R. Sougrat, H. He and K. V. Peinemann, *Langmuir*, 2011, 27, 10184-10190.
10. S. P. Nunes, A. R. Behzad, B. Hooghan, R. Sougrat, M. Karunakaran, N. Pradeep, U. Vainio and K. V. Peinemann, *ACS Nano*, 2011, 5, 3516-3522.
11. S. P. Nunes, R. Sougrat, B. Hooghan, D. H. Anjum, A. R. Behzad, L. Zhao, N. Pradeep, I. Pinnau, U. Vainio and K. V. Peinemann, *Macromolecules*, 2010, 43, 8079-8085.
12. R. Hilke, N. Pradeep, P. Madhavan, U. Vainio, A. R. Behzad, R. Sougrat, S. P. Nunes and K.-V. Peinemann, *ACS Appl. Mater. Interfaces*, 2013, 5, 7001-7006.
13. P. Madhavan, P.-Y. Hong, R. Sougrat and S. P. Nunes, *ACS Appl. Mater. Interfaces*, 2014, 6, 18497-18501.
14. X. Qiu, H. Yu, M. Karunakaran, N. Pradeep, S. P. Nunes and K.-V. Peinemann, *ACS Nano*, 2013, 7, 768-776.
15. H. Yu, X. Qiu, S. P. Nunes and K.-V. Peinemann, *Angew. Chem. Int. Ed.*, 2014, 53, 10072-10076.
16. S. P. Nunes and A. Car, *Industrial & Engineering Chemistry Research*, 2013, 52, 993-1003.

17. A. Jung, S. Rangou, C. Abetz, V. Filiz and V. Abetz, *Macromolecular Materials and Engineering*, 2012, 297, 790-798.

18. J. Hahn, V. Filiz, S. Rangou, B. Lademann, K. Buhr, J. I. Clodt, A. Jung, C. Abetz and V. Abetz, *Macromolecular Materials and Engineering*, 2013, 298, 1315-1321.

19. W. A. Phillip, R. Mika Dorin, J. Werner, E. M. V. Hoek, U. Wiesner and M. Elimelech, *Nano Letters*, 2011, 11, 2892-2900.

20. M. Karunakaran, S. P. Nunes, X. Qiu, H. Yu and K. V. Peinemann, *Journal of Membrane Science*, 2014, 453, 471-477.

21. R. A. Mulvenna, J. L. Weidman, B. Jing, J. A. Pople, Y. Zhu, B. W. Boudouris and W. A. Phillip, *Journal of Membrane Science*, 2014, 470, 246-256.

22. Y. Mai and A. Eisenberg, *Chemical Society Reviews*, 2012, 41, 5969-5985.

23. Y. Xie, N. Moreno, V. M. Calo, H. Cheng, P.-Y. Hong, R. Sougrat, A. R. Behzad, R. Tayouo and S. P. Nunes, *Polym. Chem.*, 2016, 7, 3076-3089.

24. Y. Xie, R. Tayouo and S. P. Nunes, *J. Appl. Polym. Sci.*, 2015, 132, 41549.

25. C. Dizman, M. A. Tasdelen and Y. Yagci, *Polymer International*, 2013, 62, 991-1007.

26. J. Chiefari, Y. K. Chong, F. Ercole, J. Krstina, J. Jeffery, T. P. T. Le, R. T. A. Mayadunne, G. F. Meijs, C. L. Moad, G. Moad, E. Rizzardo and S. H. Thang, *Macromolecules*, 1998, 31, 5559-5562.

27. R. Viswanathan, B. C. Johnson and J. E. McGrath, *Polymer*, 1984, 25, 1827-1836.

28. O. Celebi, C. H. Lee, Y. Lin, J. E. McGrath and J. S. Riffle, *Polymer*, 2011, 52, 4718-4726.

29. Z. Yi, L.-P. Zhu, Y.-F. Zhao, B.-K. Zhu and Y.-Y. Xu, *J. Membr. Sci.*, 2012, 390–391, 48-57.

30. Y. Zhang, I. S. Chung, J. Huang, K. Matyjaszewski and T. Pakula, *Macromol. Chem. Phys.*, 2005, 206, 33-42.

31. B. Neises and W. Steglich, *Angew. Chem. Int. Ed.*, 1978, 17, 522-524.

32. P. Español and P. Warren, *EPL*, 1995, 30, 191.

33. P. J. Hoogerbrugge and J. M. V. A. Koelman, *EPL*, 1992, 19, 155.

34. S. Plimpton, *J. Comput. Phys.*, 1995, 117, 1-19.

35. R. D. Groot and P. B. Warren, *J. Chem. Phys.*, 1997, 107, 4423-4435.

36. N. Moreno, S. P. Nunes, K.-V. Peinemann and V. M. Calo, *Macromolecules*, 2015,

48, 8036-8044.

37. S. Alexander, *Model. Simul. Mater. Sci. Eng.*, 2010, 18, 015012.

38. P. H. H. Duong, S. Chisca, P.-Y. Hong, H. Cheng, S. P. Nunes and T.-S. Chung, *ACS Appl. Mater. Interfaces*, 2015, 7, 3960-3973.

39. A. Sandeau, S. Mazières and M. Destarac, *Polymer*, 2012, 53, 5601-5618.

40. Y. Yagci and M. Atilla Tasdelen, *Prog. Polym. Sci.*, 2006, 31, 1133-1170.

41. S. G. Gaynor and K. Matyjaszewski, *Macromolecules*, 1997, 30, 4241-4243.

42. J. Wang, Y. Xu, L. Zhu, J. Li and B. Zhu, *Polymer*, 2008, 49, 3256-3264.

43. Z. Shao, A. Sannigrahi and P. Jannasch, *J. Polym. Sci., Part A: Polym. Chem.*, 2013, 51, 4657-4666.

44. N. A. Agudelo, A. M. Elsen, H. He, B. L. López and K. Matyjaszewski, *J. Polym. Sci., Part A: Polym. Chem.*, 2015, 53, 228-238.

45. S. Kumar, S. G. Roy and P. De, *Polym. Chem.*, 2012, 3, 1239-1248.

46. L. V. Brownell, J. Shin and C. Bae, *J. Polym. Sci., Part A: Polym. Chem.*, 2009, 47, 6655-6667.

47. C. Liu, G. Wang, Y. Zhang and J. Huang, *J. Appl. Polym. Sci.*, 2008, 108, 777-784.

48. C. Camacho-Zuniga, F. A. Ruiz-Trevino, S. Hernandez-Lopez, M. G. Zolotukhin, F. H. J. Maurer and A. Gonzalez-Montiel, *J. Membr. Sci.*, 2009, 340, 221-226.

49. G. Socrates, *Infrared Characteristic Group Frequencies: Tables and Charts. Second Edition*, 1994.

50. K. Ponnusamy, R. P. Babu and R. Dhamodharan, *J. Polym. Sci., Part A: Polym. Chem.*, 2013, 51, 1066-1078.

51. A. Ramakrishnan and R. Dhamodharan, *Macromolecules*, 2003, 36, 1039-1046.

52. M. Fernández-García, J. L. d. l. Fuente, M. a. L. Cerrada and E. L. Madruga, *Polymer*, 2002, 43, 3173-3179.

53. C. M. Hansen, *Hansen solubility parameters: a user's handbook*, CRC press, 2007.

54. T. Liu, Z. Zhou, C. Wu, B. Chu, D. K. Schneider and V. M. Nace, *J. Phys. Chem. B*, 1997, 101, 8808-8815.

55. Z. Zhou, B. Chu and D. G. Peiffer, *Langmuir*, 1995, 11, 1956-1965.

56. N. P. Balsara, M. Tirrell and T. P. Lodge, *Macromolecules*, 1991, 24, 1975-1986.

57. A. J. de Graaf, K. W. M. Boere, J. Kemmink, R. G. Fokkink, C. F. van Nostrum, D. T. S. Rijkers, J. van der Gucht, H. Wienk, M. Baldus, E. Mastrobattista, T. Vermonden and W. E. Hennink, *Langmuir*, 2011, 27, 9843-9848.

58. F. C. Giacomelli, I. C. Riegel, C. L. Petzhold, N. P. d. Silveira and P. Štěpánek, *Langmuir*, 2009, 25, 3487-3493.

59. X. Tang, L. Gao, X. Fan, X. Liang and Q. Zhou, *Macromol. Chem. Phys.*, 2009, 210, 1556-1562.

60. F. C. Giacomelli, I. C. Riegel, C. L. Petzhold, N. P. da Silveira and P. Štěpánek, *Langmuir*, 2009, 25, 731-738.

61. J. N. Israelachvili, *Intermolecular and surface forces: revised third edition*, Academic press, 2011.

62. L. Zhang and A. Eisenberg, *Macromolecules*, 1999, 32, 2239-2249.

63. Y. Yu, L. Zhang and A. Eisenberg, *Macromolecules*, 1998, 31, 1144-1154.

64. D. Quémener, G. Bonniol, T. N. T. Phan, D. Gigmes, D. Bertin and A. Deratani, *Macromolecules*, 2010, 43, 5060-5065.

65. R. Kaul, Y. Brouillette, Z. Sajjadi, K. A. Hansford and W. D. Lubell, *J. Org. Chem.*, 2004, 69, 6131-6133.

66. T. Tomida, K. Hamaguchi, S. Tunashima, M. Katoh and S. Masuda, *Ind. Eng. Chem. Res.*, 2001, 40, 3557-3562.

67. C. Pottier, G. Morandi, V. Dulong, Z. Souguir, L. Picton and D. Le Cerf, *J. Polym. Sci., Part A: Polym. Chem.*, 2015, 53, 2606-2616.

68. T. Radeva, *Physical chemistry of polyelectrolytes*, CRC Press, 2001.

69. T. Miyajima, M. Mori and S.-i. Ishiguro, *J. Colloid Interface Sci.*, 1997, 187, 259-266.

70. L.-å. Lindén and J. F. Rabek, *J. Appl. Polym. Sci.*, 1993, 50, 1331-1341.

71. L. F. Villalobos, M. Karunakaran and K.-V. Peinemann, *Nano Lett.*, 2015, 15, 3166-3171.

72. L. F. Villalobos, Y. Xie, S. P. Nunes and K.-V. Peinemann, *Macromol. Rapid Commun.*, 2016, 37, 700-704.

73. I. Katime and E. Rodríguez, *J. Macromol. Sci., Part A: Pure Appl. Chem.*, 2001, 38, 543-558.

74. R. Shannon, *Acta Crystallogr. Sect. A*, 1976, 32, 751-767.

75. S. Lentsch, P. Aimar and J. L. Orozco, *Biotechnol. Bioeng.*, 1993, 41, 1039-1047.

76. J. Zhou, D. Wandera and S. M. Husson, *J. Membr. Sci.*, 2015, 488, 103-110.

77. P. Kanagaraj, A. Nagendran, D. Rana, T. Matsuura, S. Neelakandan and K. Malarvizhi, *Ind. Eng. Chem. Res.*, 2015, 54, 4832-4838.

78. G. Mary, S. K. Bajpai and N. Chand, *J. Appl. Polym. Sci.*, 2009, 113, 757-766.

79. C. H. Hu, Z. R. Xu and M. S. Xia, *Veterinary Microbiology*, 2005, 109, 83-88.

80. Z. G. Dan, H. W. Ni, B. F. Xu, J. Xiong and P. Y. Xiong, *Thin Solid Films*, 2005, 492, 93-100.

81. P. Stoodley, K. Sauer, D. G. Davies and J. W. Costerton, *Annu. Rev. Microbiol.*, 2002, 56, 187-209.

CHAPTER 3

Biomemetic Membranes from Amphiphilic Polysulfone-Based Copolymers Containing Water-soluble Segments

3.1 Introduction

Membrane technology is widely recognized as one of the most cost-efficient and greenest separation processes for a broad range of applications.[1] While nanofiltration (NF) and reverse osmosis (RO) membranes based on polyamide thin film composite (TFC) have been fully commercialized in the industry of water treatment and desalination over the last few decades,[2, 3] the global water scarcity demands novel membrane materials with enhanced permeability, solute rejection, and fouling resistance. One of the most promising and burgeoning area is biomimetic or bioinspired membranes that are fabricated based on the principle, structure or materials that natural cell membranes utilize for exceptionally high transport rate and selectivity.[4-6] The water channel proteins across cell membranes, Aquaporins (AQPs), are largely responsible for the high efficiency of water transport in biological cells.[7] Since Kumar et al. experimentally proved the excellent water permeability and salt rejection of AQPs inserted into lipid-bilayer-like block copolymer vesicles,[8] many designs have been proposed to incorporate AQPs into impermeable membrane matrix.[9, 10] However, the robustness and scalability of aquaporin-based biomimetic membranes still remain big challenges towards the practical application.

An alternative approach is to use synthetic analogs of AQPs to construct artificial water channels in parallel to the biomolecular structure. Among them, aligned carbon nanotubes (CNTs) have been applied in membrane and gained significant attention since 2004.[11-14] The mechanism of their extraordinarily fast water transport, which is comparable to natural AQPs, has been extensively studied using molecular dynamics (MD) simulation.[15-18] It is found that the atomic smoothness, inherent hydrophobicity and narrow diameter induce the frictionless single-file transport of water molecules connected by strong hydrogen bonding chains, which resembles the process observed in AQPs.[19, 20] Their main limitations have been non-sufficient salt rejection and alignment of CNTs in a large-scale manner.[5]

Organic nanochannels that are assembled from organic subunits as building blocks *via* various noncovalent forces are another new trend to be explored.[21, 22] So far only several structures have been published: (1) helical channels from zwitterionic coordination zinc polymers[23], (2) self-assembled cylindrical pores from dendritic dipeptide *via* peripheral π-stacking[24], (3) imidazole I-quartet superstructures stabilized by inner dipolar water wires[25], (4) organic nanotubes through the coassembly of cyclic peptide and block copolymers[26], (5) single-molecular water channels formed from the hydrazide-[27] and peptide-appended pillar[5]arenes[28], and (6) well-defined nanotubes from shape-persistent macrocycles multiple hydrogen bonding and π-stacking[29]. Until now most of the organic artificial water channels suffer from poor permeability, a few orders of magnitude lower than AQPs, and lack reliable tests in practical membranes except in lipid vesicles.[5]

Apart from the CNTs and small organic molecules pathways, nanostructured block copolymer membranes are widely considered as biomimetic materials based on the similar interaction mechanism and self-assembly principle to natural biomacromolecules.[6] Isoporous membranes fabricated from amphiphilic block copolymers with show exceptionally high water flux at ultrafiltration (UF) range with mesopores larger than 10 nm.[30-32] To reduce the pore diameter to sub-10 nm for NF application, Yu et al. blended polystyrene-*b*-poly(4-vinyl pyridine) (PS-*b*-P4VP) and polystyrene-*b*-poly(acrylic acid) (PS-*b*-PAA) which can interact through hydrogen bonding, to form nanoscale pores between densely packed spherical micelles in the BCP membrane.[33] These highly hydrophilic PAA-lined nanopores afford a large number of water channels that facilitate the fast water transport.

Inspired by this work, we aimed to fabricate water channel-containing membranes from different amphiphilic polysulfone-based block copolymers. First we report the synthesis of poly(acrylic acid)-*b*-Polysulfone-*b*-Poly(acrylic acid) (PAA_{17k}-PSU_{14k}-PAA_{17k}) triblock copolymers. A thin film composite membrane was formed *via* bulk self-assembly induced by thermal annealing, in which 50 nm vertically aligned PAA microdomains are densely packed in PSU matrix. Stable membranes could be prepared through a novel "self-assembly and chelation-assisted non-solvent induced phase separation" (SCNIPS) process. The presence of copper ions in the coagulation bath preserves the morphology of spherical micelles with PAA corona, which spontaneously assembled in casting solution, by forming strong metal-PAA complexes. On the membrane surface, the ordered space between micelles is filled with PAA acting as preferential water channels. In the same manner, we successfully obtained membranes that carries silver ions, which can be

reduced to silver nanoparticles. In the second part, we describe the synthesis of another triblock copolymers, poly(ethylene glycol)-*b*-polysulfone-*b*-poly(ethylene glycol) (PEG_{2k}-PSU_{14k}-PEG_{2k}), and a pentablock terpolymer, poly(ethylene glycol)-*b*-poly(N-isopropylacrylamide)-*b*-polysulfone-*b*-poly(N-isopropylacrylamide)-*b*-poly(ethylene glycol) (PEG_{2k}-$PNIPAM_{2k}$-PSU_{14k}-$PNIPAM_{2k}$-PEG_{2k}), through SET-LRP and coupling copolymerization. In the further study, we will continue to explore the potential of these amphiphilic copolymers with water-soluble segments on self-assembly-driven water channel formation.

3.2 Experimental Section

3.2.1 Materials

Poly(*tert*-butyl acrylate)-*b*-polysulfone-*b*-poly(*tert*-butyl acrylate) (P*t*BA_{30k}-PSU_{14k}-P*t*BA_{30k}) copolymers (PDI = 1.4) and α,ω-dihydroxy-terminated polysulfone (HO-PSU_{14k}-OH) (PDI = 2.1) were synthesized according to the method reported in Chapter 2. Dichloromethane (DCM, ≥ 99.9%, Aldrich), *N*,*N*-dimethylformamide (DMF, anhydrous, 99.8%, Sigma-Aldrich), diethyl ether (for HPLC, VWR), trifluoroacetic acid (TFA, 99%), poly(ethylene glycol) methyl ether (PEG, M_n = 2000, Aldrich), tetrahydrofuran (THF, anhydrous, ≥99.9%, Sigma-Aldrich), triethylamine (TEA, ≥99%, Sigma-Aldrich), *p*-Toluenesulfonyl chloride (TsCl, 98%, Alfa Aesar), sodium hydride **(**NaH, 60 % dispersion in mineral oil, Aldrich), α-bromoisobutyryl bromide (BiBB, 98%, ACROS), *N*-isopropylacrylamide (NIPAM, 97%, Aldrich), potassium carbonate (K_2CO_3, ≥99.0%,

Sigma-Aldrich), acetone (for HPLC, VWR), methanol (≥ 99%, Fisher), copper(II) sulfate pentahydrate (98-102%, Fisher), 0.1 M silver nitrate solution (Fluka) and sodium borohydride ($NaBH_4$, ≥96%, Aldrich) were used as received without further purification. *N*,*N*,*N'*,*N '*,*N''*,*N*"-Hexamethyl-[tris(aminoethyl)amine] (Me_6TREN) was synthesized according to literature[34] and stored under a nitrogen atmosphere prior to use. Copper (I) bromide (CuBr, 98%, Aldrich) was purified overnight by reflux in glacial acetic acid, then filtering and washing solids three times with absolute ethanol, twice with diethyl ether and then dried under vacuum. Membrane dialysis tube (cellulose ester, 0.5-1 kD, Spectra/Por® Float-A-Lyzer®) was purchased from Spectrum Labs. Polyester nonwoven was purchased from Hirose Paper. Ceramic disc membrane with a molecular weight cut-off of 50 kD was purchased from TAMI Industries.

3.2.2 Synthesis of Poly(acrylic acid)-*b*-Polusulfone-*b*-Poly(acrylic acid)

3 g P*t*BA-PSU-P*t*BA ($M_{n,NMR}$ = 75 kg/mol, PDI = 1.4, 19 mmol of *tert*-butyl group) was dissolved in 50 mL dichloromethane and 14.6 mL trifluoroacetic acid (10 equiv to *tert*-butyl) was added. The reaction mixture was stirred at room temperature for 24 h under nitrogen. Then, the solution was concentrated by rotavapor and precipitated into diethyl ether. The solids were collected by filtration, dissolved in DMF and reprecipitated in ether (3 times). The final product PAA_{17k}-PSU_{14k}-PAA_{17k} as a white powder was obtained by drying in vacuum oven at 60 °C.

3.2.3 Synthesis of Poly(ethylene glycol)-*b*-Polysulfone-*b*-Poly(ethylene glycol)

3.2.3a Tosylated Poly(ethylene glycol) methyl ether (PEG-Ts)

To a 100 mL round-bottom flask, poly(ethylene glycol) methyl ether (M = 2000 g/mol, 10 g, 5 mmol) and dichlormethane (40 mL) were charged. After complete dissolution, three-fold molar excess triethylamine (2.1 mL, 15mmol) and *p*-toluenesulfonyl chloride (2.86 g, 15 mmol) was added to the solution. The reaction mixture was stirred for 24 h at room temperature under nitrogen and then filtered off the salt. Afterwards, the solution was poured into a large amount of diethyl ether. The precipitate was collected by filtration, dissolved in THF and reprecipitated in ether. After repeating the process for three times, the purified poly(ethylene glycol) capped with mono tosyl group (PEG_{2k}-Ts) was dried under vacuum at 40 °C.

3.2.3b Poly(ethylene glycol)-b-Polusulfone-b-Poly(ethylene glycol) (PEG-PSU-PEG)

5 g HO-PSU-OH (M_n = 14.4 kg/mol, PDI = 2.1) was kept in vacuum oven at 80 °C overnight to remove trace water before solubilizing with 100 mL anhydrous THF in a three-neck round bottom flask equipped with a condenser. Then 73 mg sodium hydride (1.8 mmol, 5 equiv) was added at 0 °C and the mixture was allowed to stir under N_2 for three hours until no bubbling. 3.9 g Ts-PEG_{2000} (1.8 mmol, 5 equiv) was dissolved in 20 mL anhydrous THF and added through syringe to the solution dropwise. The reaction mixture was stirred for 72 h at room temperature followed by passing through filter paper. The solution was then concentrated with rotavapor and precipitated in methanol. The crude product was washed with water, methanol and hexane. Finally it was

solubilized in THF, precipitated in methanol and dried in vacuum oven at 60 °C overnight to obtain PEG_{2k}-PSU_{14k}-PEG_{2k}.

3.2.4 Synthesis of Poly(ethylene glycol)-*b*-Poly(*N*-isopropylacrylamide)-*b*-Polysulfone-*b*-Poly(*N*-isopropylacrylamide)- *b*-Poly(ethylene glycol)

3.2.4a Poly(ethylene glycol) SET-LRP Macro-initiator (PEG-I)

To a 250 mL round-bottom flask, poly(ethylene glycol) methyl ether (M = 2000 g/mol, 10 g, 5 mmol) and anhydrous THF (100 mL) were charged. After complete dissolution, three-fold molar excess trimethylamine (2.1 mL, 15mmol) added to the solution. The mixture was cooled to 0 °C with an ice bath. Then α-bromoisobutyryl bromide (1.9 mL, 15mmol) was added dropwise through a syringe. The solution was allowed to warm to room temperature and kept stirring for 24 h. The reaction mixture was filtered and concentrated by rotavapor. Afterwards, it was poured into a large amount of diethyl ether. The precipitate was collected by filtration, dissolved in THF and reprecipitated in ether for three times. The poly(ethylene glycol) with a tertiary alkyl bromide end group (PEG_{2k}-I) was obtained upon drying under vacuum at 40 °C.

3.2.4b OH-Terminated Poly(ethylene glycol)-*b*-Poly(*N*-isopropylacrylamide) (PEG-PNIPAM-OH)

Poly(ethylene glycol)-*b*-Poly(N-isopropylacrylamide) (PEG-PNIPAM) was synthesized via SET-LRP in water. In a typical polymerization of NIPAM with DP = 20, to a 50 mL round bottom flask fitted with a magnetic stir bar and a rubber septum, Me_6TREN (107

μL, 0.4 mmol), CuBr (57 mg, 0.4 mmol) and H_2O (5 mL) were charged and the mixture was bubbled with nitrogen and stirred for 30 min at 0 °C. At the same time, to another 50 mL flask fitted with a magnetic stir bar and a rubber septum, H_2O (20 mL), macro-initiator PEG_{2k}-I (2.282 g, 1 mmol) and NIPAM (2.263 g, 20 mmol) were charged and the mixture was bubbled with nitrogen for 30 min. Then, the degassed monomer/initiator aqueous solution was transferred *via* syringe to the flask with Cu^0/ $CuBr_2$/Me_6TREN catalyst. The mixed solution was allowed to polymerize with the 0 °C ice bath for 30 min. The reaction was quenched by opening the flask and kept stirring under the air overnight. Afterwards, the aqueous solution was dialyzed against water for three days using a dialysis tube (MWCO = 0.5-1 kD). The purified PEG-PNIPAM diblock copolymer was recovered by free-drying.

3.2.4c Tosylated Poly(ethylene glycol)-*b*-Poly(*N*-isopropylacrylamide) (PEG-PNIPAM-Ts)

To a 25 mL round-bottom flask, PEG_{2k}-$PNIPAM_{2k}$ (DP = 20, $M_{n,NMR}$ = 4527 g/mol, 2 g, 0.44 mmol) and dichlormethane (10 mL) were charged. After complete dissolution, three-fold molar excess triethylamine (0.19 mL, 1.33 mmol) and *p*-toluenesulfonyl chloride (0.253 g, 1.33 mmol) was added to the solution. The reaction mixture was stirred for 24 h at room temperature under nitrogen. After the reaction, the solvent was evaporated and the mixture was dissolved in water. The solution was then transferred into a dialysis tube (MWCO = 0.5-1 kD) and dialyzed against water for three days. The tosylated PEG_{2k}-$PNIPAM_{2k}$ was obtained via freeze-drying.

3.2.4d Poly(ethylene glycol)-*b*-Poly(N-isopropylacrylamide)-*b*-Polysulfone-*b*-Poly(N-isopropylacrylamide)-*b*-Poly(ethylene glycol) (PEG-PNIPAM-PSU-PNIPAM-PEG)

A mixture of 0.5 g HO-PSU-OH (M_n = 13.8 kg/mol, PDI = 2.1) and 0.85 g tosylated PEG-PNIPAM (M_n = 4.7 kg/mol, 0.18 mmol, 5 equiv) was kept in vacuum oven at 80 °C overnight to remove trace water before solubilizing with 5 mL anhydrous DMF in a round bottom flask. Then 25 mg potassium carbonate (0.18 mmol, 5 equiv) was added and the mixture was flushed in N_2 for 30 min and kept stirring for 72 h at 60 °C. The solution was then concentrated and precipitated in water. The collected crude product was solubilized in THF, precipitated in methanol and dried in vacuum oven at 60 °C overnight.

3.2.5 Polymer Characterization

^{1}H and ^{13}C NMR spectra of polymers were recorded with a Bruker AVANCE-III spectrometer at a frequency of 600 MHz at room temperature and deuterated solvents containing tetramethylsilane $Si(CH_3)_4$ as an internal standard. Polymer molecular weight and distribution were determined by triple detection gel permeation chromatography (GPC) from Viscotek using a GPCmax module (model VE-2001) and a GPC-TDA 305 system equipped with two columns (LT4000L, Mixed, Low Org. 300 mm X 8.0 mm, exclusion limit 400 kDa for polystyrene) eluted at 1.0 mL min^{-1} in stabilized THF at 35 °C. Three detectors are light scattering (RALS and LALS), refractive index, and viscometer. Matrix assisted laser desorption ionization - time of flight mass spectroscopy (MALDI-TOF MS) experiments were performed on a Bruker UltraFLEX II TOF/TOF-

MS instrument in reflectron mode. Each sample was prepared by mixing 5 µL polymer (1 mg/mL) with 2 µL sodium trifluroacetate (10 mg/mL) and 20 µL *trans*-2-[3-(4-*tert*-butylphenyl)-2-methyl-2-propenylidene]malononitrile (DCTB) matrix (20 mg/mL) in THF. 0.5µL of the mixture was then spotted onto the target plate for analysis. Absolute molecular weights were determined using polystyrene standards for calibration. Fourier transform infrared - attenuated total reflectance (FTIR-ATR) spectra were recorded at room temperature on a Thermo Nicolet iS10. Solid membrane was placed over the ATR crystal and maximum pressure was applied using the slip-clutch mechanism. Thermogravimetric analysis (TGA) was conducted using a TGA Q50 (TA instruments) with a heating rate of 10 °C min^{-1} under nitrogen flow from 25 to 800 °C. Differential scanning calorimetry (DSC) was carried out on a Perkin-Elmer DSC 204 F1 NETZSCH under nitrogen flow. The heating rate was 10 °C min^{-1} and the cooling rate was 5 °C min^{-1} in the range of temperature from -50 to 180 °C. The glass transition temperature (T_g) was taken from the second heating scan.

3.2.6 Membrane Fabrication

3.2.6a PAA-PSU-PAA Thin Film Composite Membranes

The 3 wt% PAA-PSU-PAA casting solution was prepared by dissolving the as-synthesized triblock copolymer in anhydrous THF and filtered using 0.45 µm syringe filter prior to coating. For dip-coating membranes, porous polyacrylonitrile (PAN) membranes, previously manufactured by phase inversion in a continuous machine, was immersed in the casting solution for different time (30, 60 and 120 s). After taken out

from the solution, the coated membranes were dried in the ambient condition completely. The spin-coated thin films were prepared by dropping the solution onto the clean silicon wafer or ceramic membrane, which was fixed in a spin-coater, following by spinning at 2000 rpm for one minute. For thermal annealing, the as-coated membrane was placed in a 180 °C oven for five days under vacuum. The samples were then abruptly brought from the oven to room temperature.

3.2.6b PAA-PSU-PAA Membranes Prepared by SCNIPS Process

The membrane fabrication procedure with self-assembly and chelation assisted non-solvent induced phase separation (SCNIPS) is the following. The casting solution from 20 wt % PAA_{17k}-PSU_{14k}-PAA_{17k} in a solvent mixture (DMF/THF/Acetone = 10/45/45) was stirred for 12 h to obtain a homogeneous solution and kept still for another 12 h to release bubbles. This viscous solution was cast onto a polyester nonwoven support by a doctor blade with 250 μm gap. After an evaporation time of 5 min , the membrane was then immersed quickly and smoothly into the coagulation bath of 0.1 M $CuSO_4$ or $AgNO_3$ solution at room temperature and kept overnight for exhaustive extraction of solvent. Then it was transferred to a water bath and to remove excess metallic salt solution for 30 min. Fresh water in the bath was changed for several times. The silver-containing membrane was immersed in 0.2 mM $NaBH_4$ solution for 30 min and washed with water afterwards. The final membranes were freeze-dried for microscopic characterizations.

3.2.7 Membrane Characterization

The surface and cross-section morphologies of the membranes were observed by field emission scanning electron microscopy (FESEM) in a FEI Nova Nano SEM. For surface imaging, a small piece of membrane sample was mounted on a flat aluminum stub, fixed by aluminum conductive tapes. For cross-section, the membrane sample was freeze-fractured in liquid nitrogen, and mounted on a 90° aluminum stub vertically with tapes. The samples were sputter-coated with 2 nm iridium nanoparticles to prevent electron charging using Quorum Q150T before imaging.

Topography and phase images of the PAA-*b*-PSU-*b*-PAA thin films were obtained using Agilent 5500 AFM in tapping (ACAFM) mode. The measurements were performed using silicon cantilevers with 76-263 kHz resonance frequency and 1.2-29 Nm^{-1} force constant. PicoView 1.8 software was used to control the measurement and the acquired data were post-processed using Gwyddion software.

Transmission electron microscopy (TEM) images of the membranes and micelles in the diluted casting solution were acquired using FEI Tecnai 12 microscope with an accelerating voltage of 120 kV. The membranes were embedded in an epoxy resin (EMS Embed 812) and cured in an oven at 60 °C for 24 h. The cured blocks were trimmed using Leica EM TRIM2 to remove the resin excess before sectioning into ultrathin slices with 60 nm thickness using ultra microtome (Leica EM UC6) with a diamond knife. The thin slices were placed on a 300-mesh copper grid before imaging. The sample for micelle characterization was prepared by dissolving the copolymer in a solvent or mixture with a polymer concentration of 0.1 wt% followed by stirring overnight. A drop of the solution (1.5 μL) was placed onto a carbon-coated copper grid while the solvent

was removed by blotting with a filter paper placed under the grid. The grid was further dried at room temperature before imaging.

Dynamic Light Scattering (DLS) measurements were performed using Malvern Zetasizer Nano ZS to analyze the micellar size distribution of the copolymer in a diluted casting solution (0.1 wt%) followed by stirring overnight. The solution was filtered through a 0.45 μm PTFE syringe filter before loading into a glass cuvette with square aperture. Three measurements were done for each sample with 16 runs per measurement.

3.3 Results and Discussion

3.3.1 Synthesis and Characterization of PAA-PSU-PAA

In chapter 2, we reported the partial hydrolysis on P*t*BA-PSU-P*t*BA membrane surface in HCl aqueous solution. Here pure poly(acrylic acid)-*b*-Polusulfone-*b*-Poly(acrylic acid) (PAA-PSU-PAA) triblock copolymer was obtained by hydrolyzing the polymer precursor P*t*BA-PSU-P*t*BA with trifluoroacetic acid in organic medium, as illustrated in Scheme

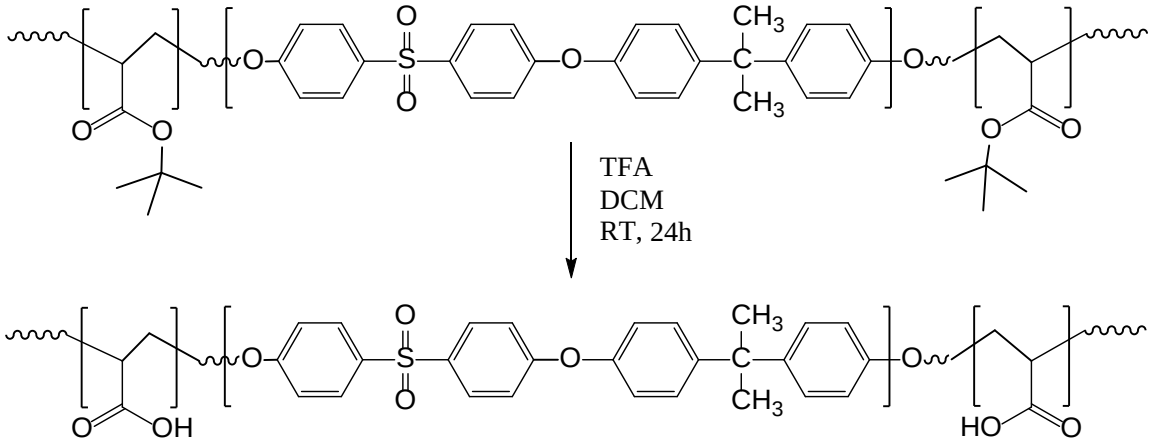

Scheme 3.1. Synthesis route of poly(acrylic acid)-*b*-polysulfone-*b*-poly(acrylic acid).

3.1. This facile approach has been widely used in the literature, as a deprotection method for PAA.[35-37]

From ^{1}H NMR, as shown in Figure 3.1, the disappearance of the strong peak at 1.46 ppm

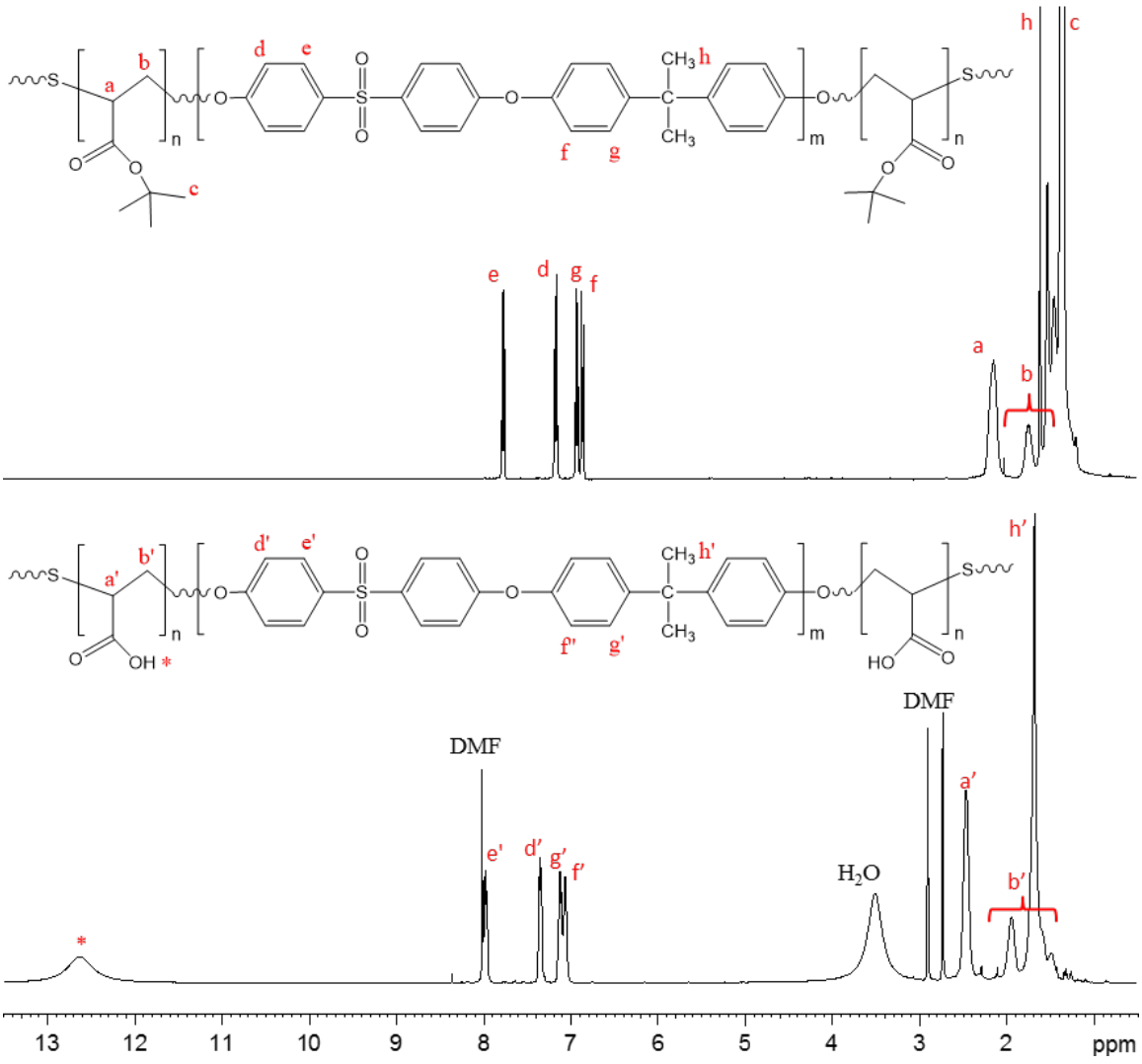

Figure 3.1. ^{1}H NMR spectra for P*t*BA-PSU-P*t*BA in $CDCl_3$ and PAA-PSU-PAA in DMF-d7.

(peak “c”) corresponding to the -C$\boldsymbol{H_3}$ protons of the *tert*-butyl group demonstrates the

quantitative hydrolysis reaction.[38, 39] In addition, a new peak can be found at 12.63 ppm

(peak “*”) after hydrolysis, which is attributed to the proton of -COO***H*** group.[40] The

complete cleavage of *tert*-butyl group in P*t*BA block is also confirmed by ^{13}C NMR (see

Figure 3.2), where the signals from -***C***(CH_3) and -C(***C***H_3) previously at 80.4 (peak “4”)

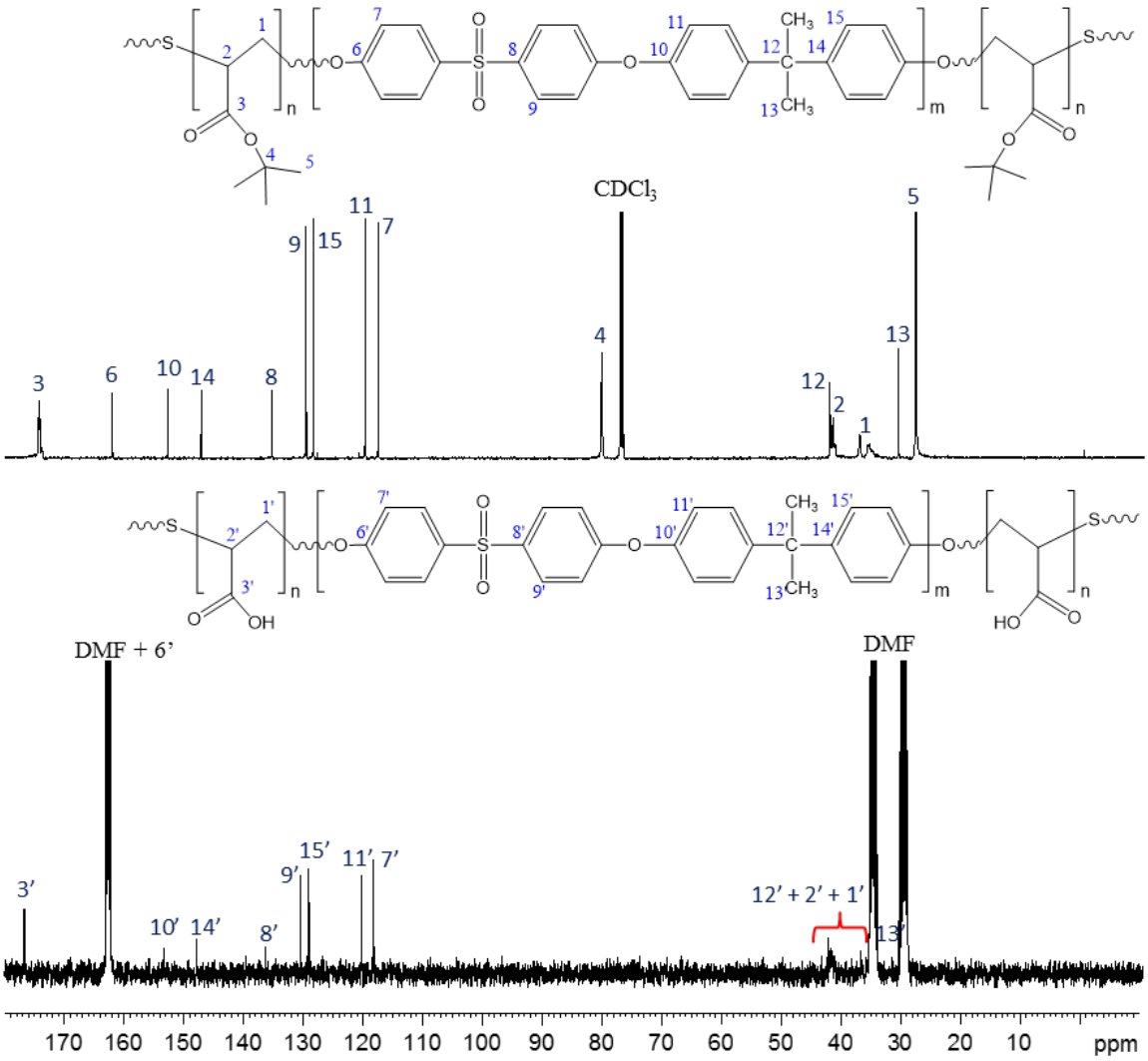

Figure 3.2. ^{13}C NMR spectra for P*t*BA-PSU-P*t*BA in $CDCl_3$ and PAA-PSU-PAA in DMF-d7.

and 28.1 ppm (peal “5”), respectively, are absent from the spectrum of PAA-PSU-

PAA.[40, 41] Furthermore, a new characteristic broad band of carboxylic acid O-H stretch

around 2700-3500 cm^{-1} observed from FTIR spectrum for the hydrolysis product, clearly

indicates the formation of PAA segment, as shown in Figure 3.3. Meanwhile, the peak of

C=O carbonyl stretch shifts from 1724 to 1701 cm^{-1} due to the transformation of ester to

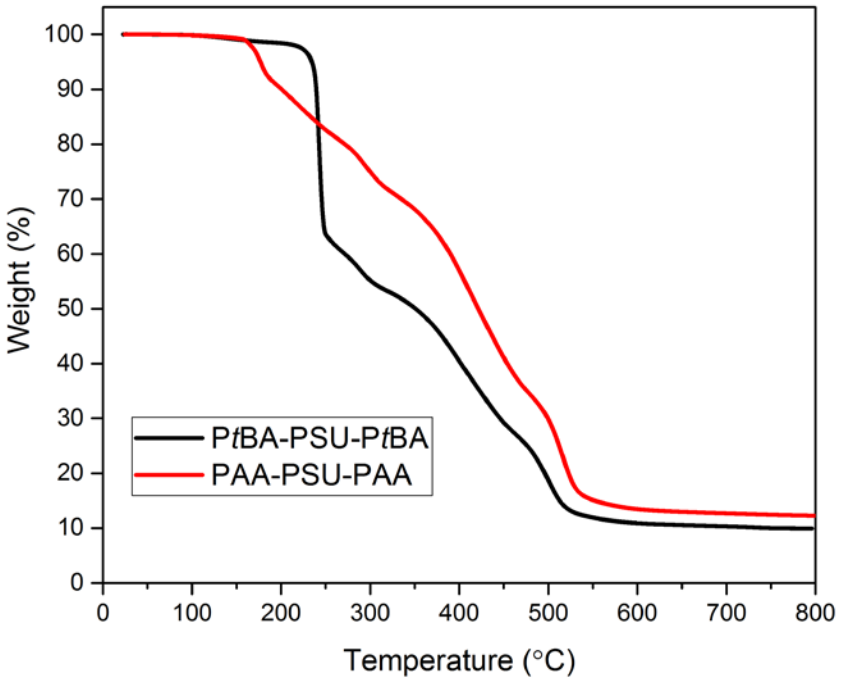

Figure 3.4. TGA curves for P*t*BA-PSU-P*t*BA and PAA-PSU-PAA under N_2.

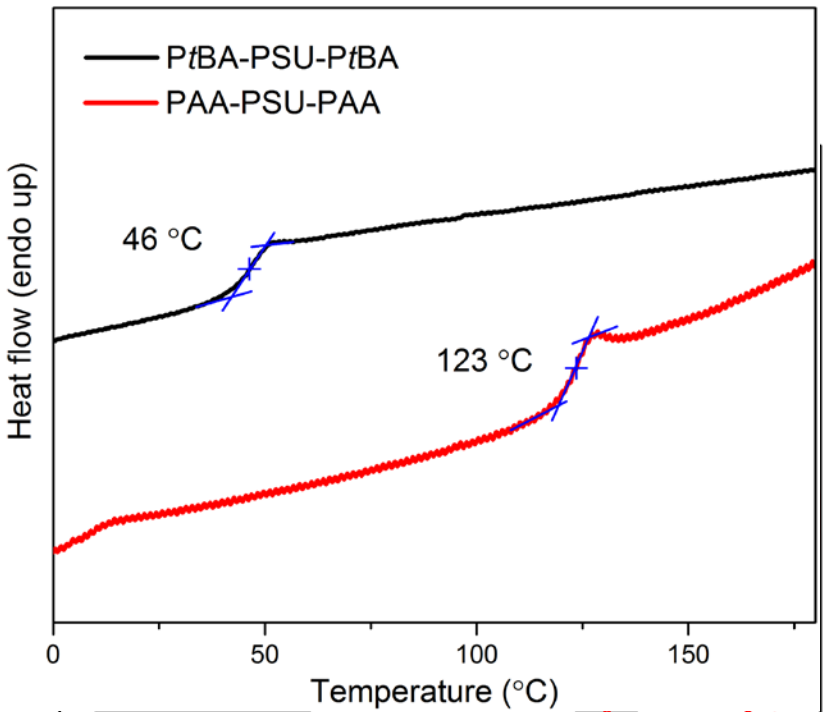

Figure 3.5. DSC curves for P*t*BA-PSU-P*t*BA and PAA-PSU-PAA under N_2.

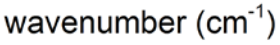

Figure 3.3. FTIR spectra for (a) P*t*BA-PSU-P*t*BA and (b) PAA-PSU-PAA.

its acid form.[39, 40]

The thermal properties of PAA-PSU-PAA was investigated by TGA and DSC. Figure 3.4 shows the TGA curve of PAA-PSU-PAA triblock under nitrogen. The first stage of decomposition accompanied by a small weight loss starts from 160 °C, which is associated with the dehydration of carboxylic acid groups to form six-member cyclic anhydride structure and release of water.[42] Although P*t*BA-PSU-P*t*BA thermogram shows an initial weight loss at higher temperature around 220 °C arising from the elimination of *tert*-butyl group, the similar subsequent weight loss profile to PAA-PSU-PAA suggests that anhydride formation is also involved in the next stage.[43-45] The decarboxylation of the anhydride occurs from 190 °C to 350 °C, which breaks the

anhydride ring and releases CO_2. When heated up to 350 °C, the P*t*BA or PAA backbone undergoes chain scission, followed by the decomposition of PSU mid-block above 400 °C.[46] As shown in Figure 3.5, DSC study reveals that the thermal transition peak centered at 46 °C in P*t*BA-PSU-P*t*BA curve corresponding to P*t*BA segment completely disappears after hydrolysis. The glass transition temperature (T_g) of the new copolymer increases to 123 °C, which is close to the T_g of poly(acrylic acid) homopolymer reported in the literature.[47]

3.3.2 PAA-PSU-PAA Thin Film Composite Membranes

When the as-synthesized PAA-PSU-PAA was dissolved in THF, they form spherical micelles by self-assembly in the organic medium. Figure 3.6a shows the transmission electron microscopy (TEM) image of PAA-PSU-PAA micelles in 0.1 wt% THF solution. The spherical micelles with ~30 nm diameter can be clearly observed, which tend to

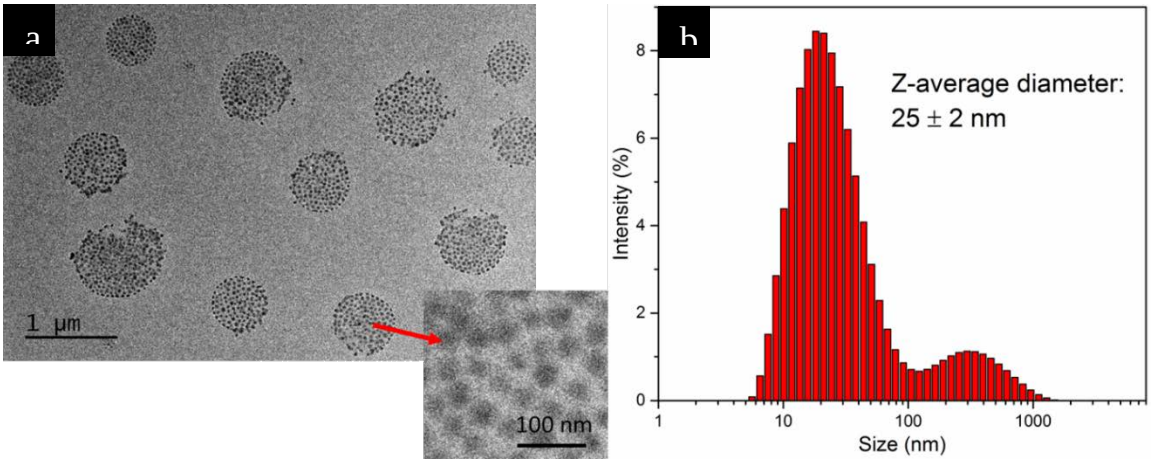

Figure 3.6. TEM images (a) of PAA-PSU-PAA micelles from 0.1 wt% THF solution and hydrodynamic size distribution (b) determined by DLS.

attract each other and form bigger aggregates. Dynamic light scattering (DLS) results confirm the presence of two groups of species in the size distribution as shown in Figure 3.6b. The main peak represents the isolated single micelles with the Z-average diameter of 25 ± 2 nm, consistent with the TEM micrograph. The adjacent broader peak corresponds to the large clusters composed of small micelles with diverse sizes ranging from 100 to 1000 nm.

Table 3.1. Values of Hansen solubility parameter for polymer segments and solvents

	δ^a [MPa]$^{1/2}$				
	δ_D	δ_P	δ_H	δ_T	dielectric constant (ε)
PAA	17.3	12.2	18.6	28.2	--
PSU	16.6	6.0	6.6	18.8	--
PS	18.5	4.5	2.9	19.2	--
THF	16.8	5.7	8.0	19.5	7.6
DMF	17.4	13.7	11.3	24.9	30.7
Acetone	15.5	10.4	7.0	19.9	20.7

[a] δ of PAA is calculated by HSPiP software 4th Edition, others are cited from reference 52, $\delta_T = (\delta_D^2 + \delta_H^2 + \delta_P^2)^{1/2}$

A wide range of self-organized morphologies have been prepared from amphiphilic diblock copolymer, polystyrene-*b*-poly(acrylic acid) (PS-*b*-PAA) in aqueous solution.[48] THF is frequently used as a common solvent to dissolve the copolymers prior to the addition of water.[49-51] In our system, both PSU and PAA are soluble in THF, but segregation in micelles clearly happens as shown in Fig. 3.6. Table 3.1 shows that all contributions to the three dimensional Hansen solubility parameter,[52] δ (i.e., dispersion force (δ_D), polarity (δ_P), and hydrogen bonding (δ_H)) of THF are closer to PSU than to PAA. This is much more evident than in the case of PS-*b*-PAA copolymers. The poorer interaction between THF and PAA block forces the block copolymers to adopt a "flower-like" morphology, as depicted in chapter 2 for P*t*BA-PSU-P*t*BA. To decrease the total

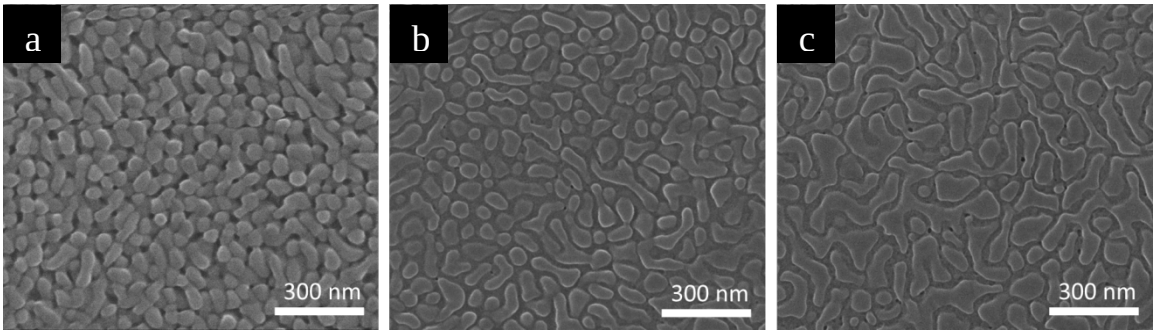

Figure 3.7. SEM images of PAA-PSU-PAA dip-coating membranes from 3 wt% THF solution with (a) 30 s, (b) 60 s and (c) 120 s coating time.

free energy, the middle PSU blocks constitute the corona in the form of loops, which shield the PAA core. Highly solvated PSU chains could then associate with corona chains of neighboring micelles to bridge them. [53-55] This process could explain the presence of large micelle aggregates in the solution.

We then prepared multilayer membranes by dip-coating 3 wt% THF solution of PAA-PSU-PAA copolymer onto polyacrylonitrile (PAN) porous supports. Figure 3.7 shows the surface SEM images of membranes prepared with different coating times. When the membrane is immersed in polymer solution for 30 s, worm-like cylindrical structure can be seen on the top of the support (Figure 3.7a). The morphological transition from spherical micelles in dilute solution (0.1 wt%) for solution characterizations to elongated cylinders at higher concentration (3 wt%) for membrane preparation is related to the balance of enthalpic and competing entropic contributions determines the total free energy.[48] The higher copolymer concentration tends to increase the micelle size. The larger micelles have lower total interfacial area and thus energetically favorable, while an entropic penalty arising from the higher extent of core stretching offsets the free energy gain. To alleviate it, non-spherical micelles, e.g., rods or cylinders form since they cost

less deformation energy to confine PAA segments into the core. The similar concentration effect on the micelle morphologies has been revealed by simulation using DPD model in chapter 2 for P*t*BA-PSU-P*t*BA/DMAc system. The results imply that the worm-like cylinder is likely to have a fused corona and an array of segregated cores. If the PAN support is immersed in copolymer solution for a longer period, it should take more time for the thin film to evaporate THF. It allows PAA-PSU-PAA flower-like micelles to merge into larger supramolecular structures before they lose mobility by drying. From Figure 3.7b and c, we can clearly observe the evolution of micelle morphologies due to prolonged dip-coating time (one and two minutes).

By assuming the flower-like arrangement and after the observations we have, we believe that the as-coated thin films would be incapable of mimicking water channel-like structures that facilitate fast water transport because the hydrophilic PAA blocks are embedded inside the core. In addition, SEM images indicate that the membranes might have free space between micelles, which could lead to low solute rejection. Therefore we

decided to add a thermal annealing step. Thermal annealing is widely used to induce the self-assembly of block copolymers in the bulk owing to the incompatibility of different polymer segments.[56] A thin film of PAA-PSU-PAA was first deposited on the silicon wafer *via* spin-coating from the same THF solution, followed by heating at 180 °C in a vacuum oven. The nanoscale surface smoothness is confirmed by SEM image, and

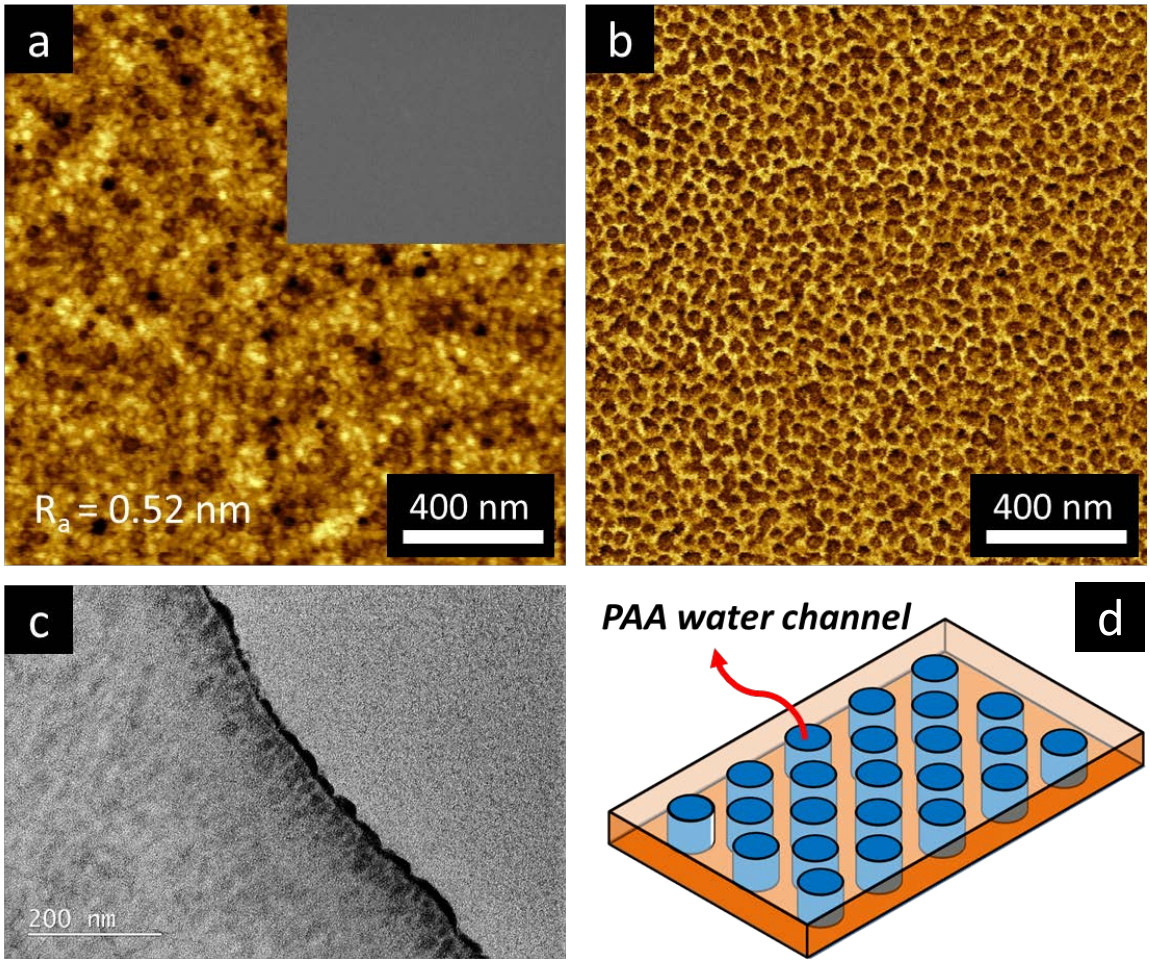

Figure 3.8. (a) Topographic AFM image and (inset) SEM image of PAA-PSU-PAA thin film on silicon wafer after thermal annealing, and corresponding (b) phase image; (c) TEM image of cross-section of annealed PAA-PSU-PAA bulk, stained by RuO_4; (d) illustration of cylindrical morphology of the thin film with PAA nanochannels (blue color) in PSU matrix (brown color).

topographic (height) image from atomic force microscopy (AFM) (Figure 3.8a) with a sub-nanometer roughness ($R_a = 0.52\ nm$). On the other hand, AFM phase imaging clearly indicates that microphase separation occurred on the annealed PAA-PSU-PAA film. Two domains can be distinguished by the strong contrast between them, which does not originate from surface topography as we have observed.[57] As shown in Figure

3.8b, the phase image is composed of dark round-shaped domains with a diameter about 50 nm, separated by a continuous brighter structure. The dark areas can be assigned to the "soft" PAA phase with lower viscoelasticity in comparison to the "stiff" PSU that constitutes the bright matrix. PSU has a high Young's modulus of 2.5-2.6 GPa.[58, 59] Moreover, the dark objects occupy a larger surface area than the bright zones, which is consistent with the fraction of PAA in the triblock copolymer (71 wt%). In order to study the inner nanostructure of the annealed thin film, transmission electron microscopy (TEM) was used to characterize the cross-section of a thicker free standing film, after slicing it with an ultramicrotome. Figure 3.8c exhibits the thin-section TEM image, in which stripe-like vertical PSU domains selectively stained by RuO_4 vapor can be observed near the surface.[60] The AFM and TEM evidence suggests that annealing at a high temperature (180 °C) provides sufficient mobility to PAA-PSU-PAA chains to transform from loosely packed flower-like micelles to a dense thin film with a channel-like morphology. PAA should form channels perpendicular to the surface, as illustrated in Figure 3.8d. However their lateral distribution is not perfectly hexagonal as previously observed for PS-*b*-P4VP or PS-*b*-PEO block copolymer membranes prepared by phase inversion. The main reason is probably the broader molecular weight polydispersity.

This nanostructured thin film is expected to have high water transport rate through the aligned PAA cylindrical channels. To verify our hypothesis, we prepared a thin film composite membrane with the same strategy, using an ultrafiltration (molecular weight cut-off of 50,000 kg mol^{-1}) porous ceramic membrane as support. Ceramic was chosen, because most polymeric membranes would not resist the thermal annealing step without deformation. The AFM phase image, as shown in Figure A3.1, Appendices, reveals that

the surface morphology is reproducible on the ceramic membrane and similar cylindrical domains are observed. However, almost no water passed through this membrane when its water flux was tested in the pressurized filtration cell, under the pressure of 4 bar. This might indicate that the PAA domains are not connected to the open pores on the support owing to roughness of ceramic membrane. We have the expectation that by changing the support this could be improved. A possibility is to use anodic aluminum oxide membranes (AAO) because of their smooth surface, uniform pore size and high porosity.[61]

3.3.3 Self-assembly and Chelation Assisted Non-solvent Induced Phase Separation (SCNIPS)

Block copolymers assemble into micelles in selective solvents. Our group demonstrated that casting solutions have already order before immersion in water during SNIPS process to form membranes.[62] The rational design of selective solvent mixture plays a decisive role on the successful fabrication of nanoporous membranes. In order to obtain a spherical micelle structure with hydrophilic PAA segments extruding as the corona, reminiscent of PS-*b*-P4VP, we propose a tertiary solvent system composed of DMF, THF and acetone in a ratio of 10/45/45. Although THF can solubilize both of the blocks, it favors PSU rendering flower-like micelles with PAA being shielded inside, as we have observed in the previous section. To reverse this arrangement, an equal amount of acetone is added to the mixture. From the δ values shown in Table 3.1, the selectivity of acetone towards PAA seems to be weak. However, solubility test indicates that it can

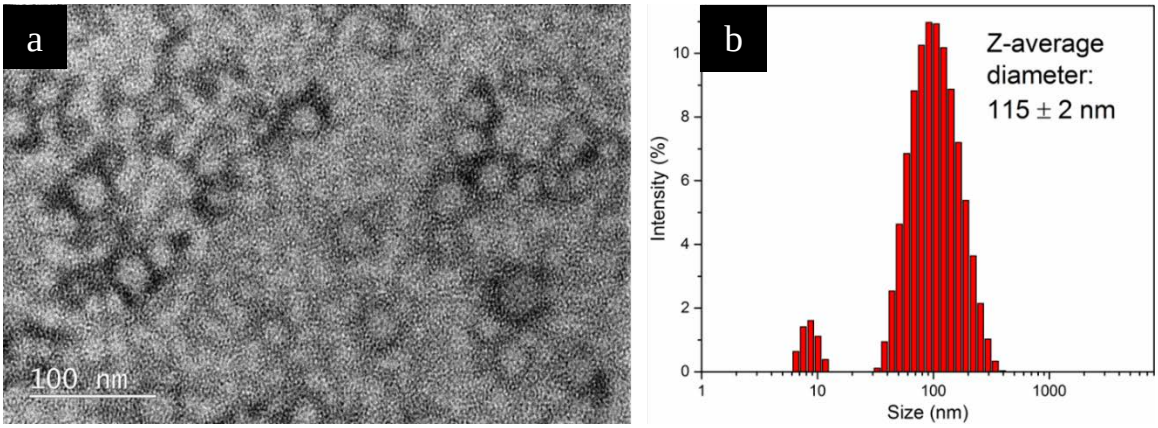

Figure 3.9. TEM images (a) of PAA-PSU-PAA micelles from 0.1 wt% DMF/THF/acetone solution (10/45/45) stained with uranyl acetate, and hydrodynamic size distribution (b) determined by DLS.

solubilize PAA but just swell PSU homopolymer. The introduction of non-solvent forces PSU segment to be incorporated into the micelle core. An important feature of acetone is its relatively lower polarity as its δ_H and dielectric constant ε lie between THF and DMF. It might hinder the complete ionization of PAA, reduce the repulsion between PAA segments and make them less stretched. This effect helps to form a compact and less deformable corona, which has a critical influence on the membrane regularity.[63] Finally, a small portion of common solvent DMF (10%) is required to obtain a homogeneous solution that cannot be achieved by THF/acetone alone. The δ valuess in Table 3.1 show that DMF also contributes to the micelle formation due to the stronger affinity to PAA than to PSU.

Figure 3.9a shows the transmission electron microscopy (TEM) image of PAA-PSU-PAA micelles from a dilute solution (0.1 wt% polymer concentration) in the ternary solvent system that we described above. The spherical micelles can be observed with an apparent core-shell structure. The corona is formed from PAA since the outer shell is

darker after treating the sample after slicing with uranyl acetate, which binds to carboxylic acid and is widely used as a selective staining material for PAA.[60] Because the micelles aggregated upon drying during the sample preparation, it is hard to identify the boundary of the micelle shell. Only the size of the brighter PSU core can be estimated to be ~30 nm in the TEM image. Dynamic light scattering (DLS) indicates a main peak with the Z-average diameter of 115 ± 2 nm, which reflects the hydrodynamic size of the whole spherical micelles (Figure 3.9b). The presence of small particles below 10 nm suggests that some free unassociated polymer chains probably coexist in the solution.

A concentrated triblock copolymer solution (20 wt%) with the same solvent condition was prepared to fabricate SNIPS membranes. After being cast on the polyester nonwoven support and allowed to evaporate for 5 min, the thin film was immersed into a water bath. The SEM image shows that a rough membrane surface full of large visible defects was formed with this process as shown in Figure A3.2, Appendices. This result implies that the water-soluble PAA block is detrimental to the good membrane formation property of PSU, especially when it covers PSU in the micellar structure. In chapter 2 we reported a two-step surface modification for P*t*BA-PSU-P*t*BA membrane in which the membrane is hydrolyzed with acid then directly complexes with metal ions. The rapid carboxylic acid-metal chelation on the surface competes with the swelling from water uptake and gives a physically stable cross-linked membrane. With this experience in mind, we extend the idea of metal complexation to membrane formation *via* SNIPS. By adding $CuSO_4$ or $AgNO_3$ to the coagulation bath, we are able to obtain defect-free nanostructured membranes with sufficient mechanical strength. Based on the combination of two processes, we give the name “self-assembly and chelation assisted non-solvent induced

phase separation (SCNIPS)” to this method. The as-formed membranes display characteristic colors from the chelated metal ions, blue for membrane formed in a 0.1 M

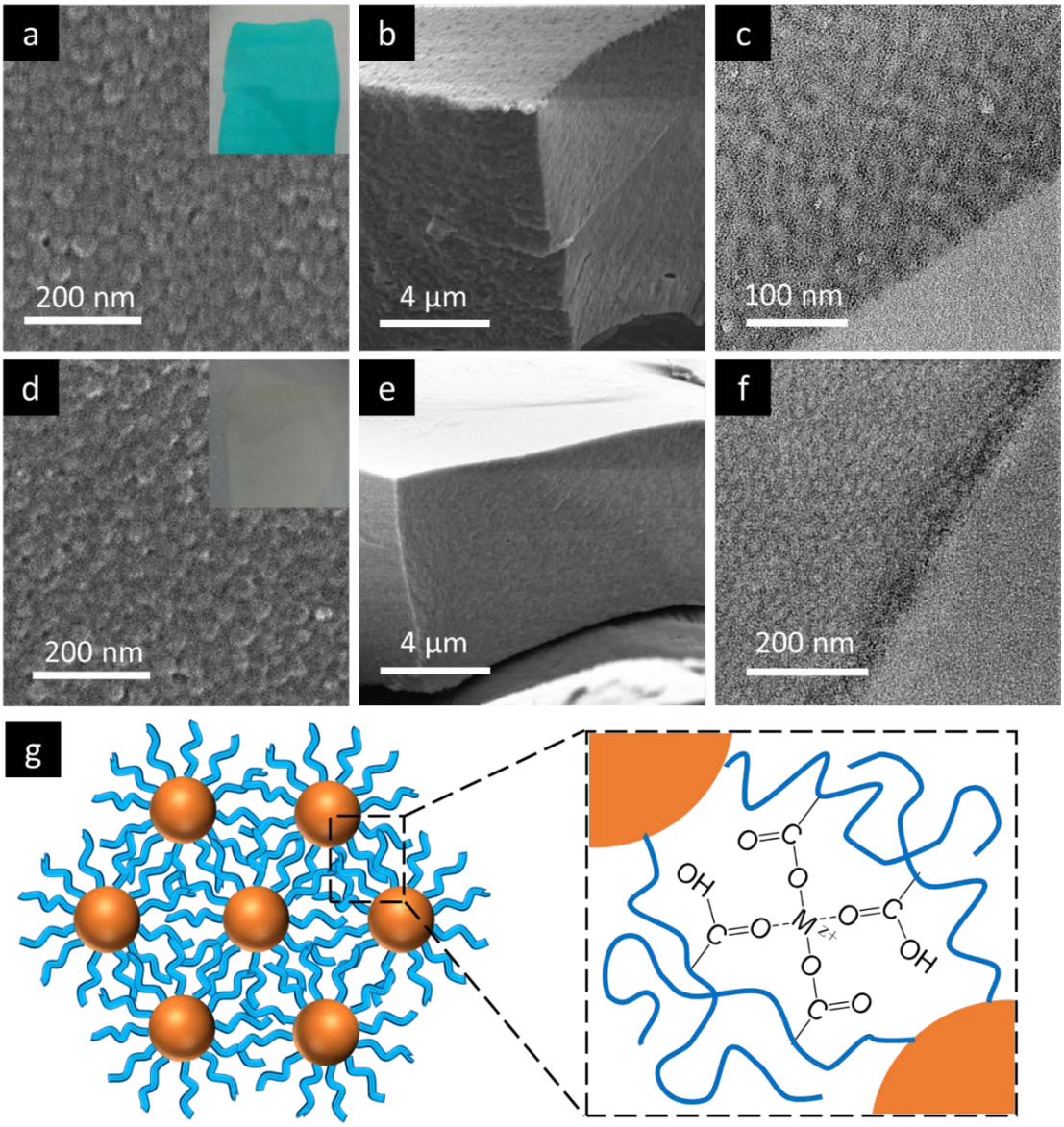

Figure 3.10. (a) Surface, (b) cross-sectional SEM images and (c) TEM images of PAA-PSU-PAA membranes from 20 wt% polymer solution in DMF/THF/acetone solution (10/45/45) with 0.1 M $CuSO_4$ and (d, e, and f) 0.1 M $AgNO_3$ bath; insets in a and d: photographs of the corresponding membranes; (g) illustration of supramolecular nanostructure in membranes.

$CuSO_4$ bath and yellowish for that formed in 0.1 M $AgNO_3$, as shown in the insets of Figure 3.10a and d, respectively. The SEM image in Figure 3.10a suggests that the

spherical micelles observed in dilute solution are densely packed on the membrane surface. The thickness of this dense film is about a few microns and no large voids appear in the lower part of membrane, revealed by the cross-sectional SEM (Figure 3.10b). TEM of the membrane thin section provides more solid evidence to prove the whole membrane is comprised of PAA-PSU-PAA micelles. The strong contrast between segregated PSU and PAA blocks demonstrates the core-shell structure from self-assembly. Electron microscopy studies (Figure 3.10d, e and f) for the membrane formed by immersing in $AgNO_3$ solution indicate that it has the same surface morphology. Ag^+ complexes with PAA chains as well as Cu^{2+} in SCNIPS process, leading to membranes with a pronounced nanostructure from the supramolecular assembly of micelles, as illustrated by the drawing in Figure 3.10g. This arrangement features a highly water-conductive PAA channels merged from the micelle corona surrounding the PSU core that could facilitate the fast water transport. Metal chelation does not only helped in the macroscopic scale to promote the solidification of membranes, but also increased the micelle-micelle interconnectivity, preserving their morphology in the final membrane. A similar effect has been reported by our group[64] using metal salt as additives in PS-*b*-P4VP casting solution. Sufficient evaporation time before immersion in aqueous medium is needed to rapidly increase the concentration of copolymer and assure a stable supramolecular order. Figure A3.3 in Appendices shows the surface of a membrane prepared with a reduced evaporation time, having a disturbed morphology with noticeable disordered open pores.

The SCNIPS technique is a one-step method to prepare membranes, by complexing with a high density of metal ions, which could be used as functional materials for a variety of applications. The silver-containing membrane is of particular interest because the

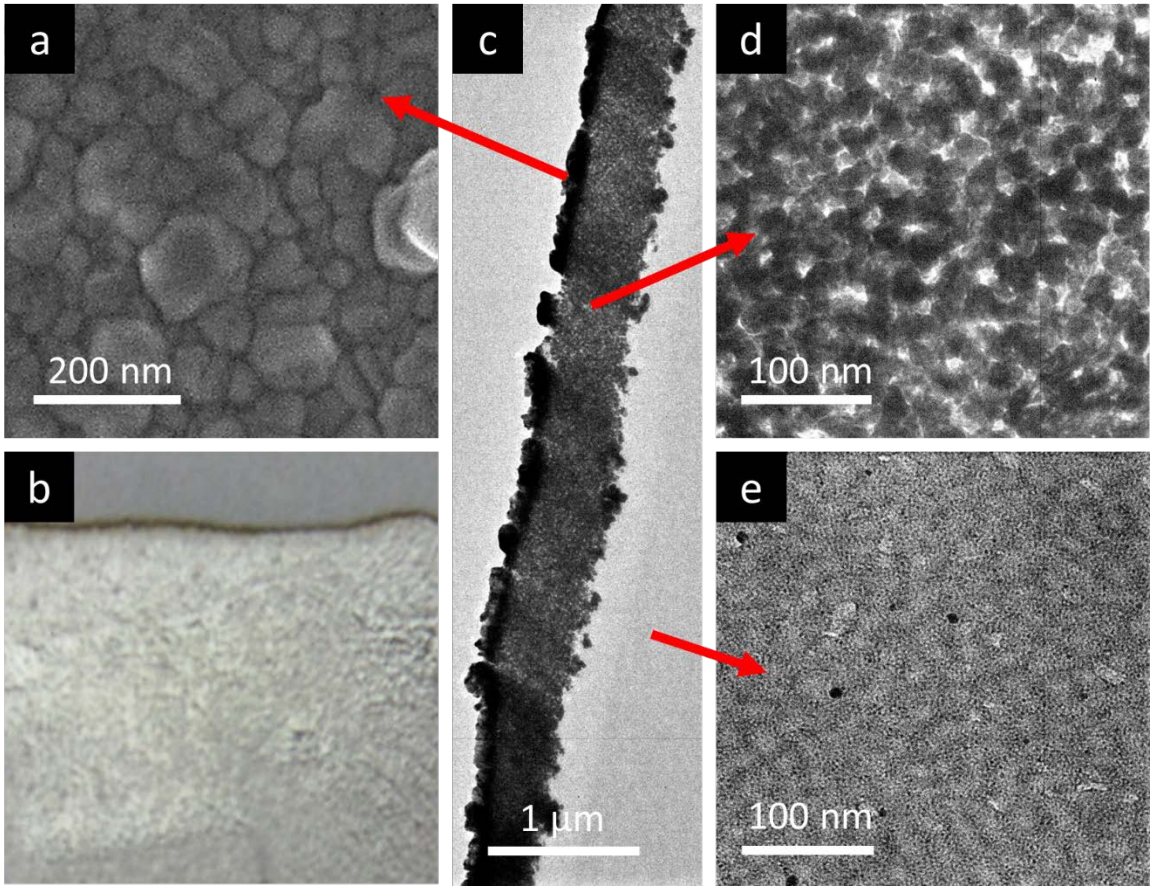

Figure 3.11. (a) SEM image and (b) photograph for the surface of reduced silver-decorated PAA-PSU-PAA membrane; TEM images for (c) the entire membrane at low magnification, (d) the sublayer from 150 to 600 nm under the surface, and (e) the bottom layer of membrane.

incorporated Ag^{2+} can be readily reduced to Ag^0 nanoparticles immobilized in the membrane matrix.[65, 66] Once the PAA-PSU-PAA membrane formed by immersion in $AgNO_3$ aqueous solution was transferred to a 0.2 mM $NaBH_4$ solution, its surface immediately turned to dark yellow and then shiny silver in few minutes (Figure 3.11b). The surface of the obtained membrane is fully covered with silver nanoparticle with a grain size of around 100 nm, as shown by the surface SEM in Figure 3.11a. By analyzing the TEM image of the membrane, we can easily identify a heterogeneous structure on the

membrane cross-section with three distinct layers (Figure 3.11c). Underneath the 150 nm thick top layer consisting of large Ag^0 nanoparticles, there is a sublayer of 500 nm thickness, in which smaller nanoparticles with a diameter of ~20 nm are densely packed, as shown in Figure 3.11d. The reduction of $NaBH_4$ cannot reach the bottom area deeper than this layer since no nanoparticle is observed below it. Figure 3.11e confirms that the micellar morphology from the pristine membrane prepared with Ag^+ bath remains intact in the region away from the surface.

3.3.4 Synthesis and Characterization of PEG-PSU-PEG

Poly(ethylene glycol) (PEG) is a water-soluble polymer, which is widely accepted as biomaterial with good biocompatibility and resistance to protein adsorption.[67, 68] The covalent linking of PEG blocks to segments of membrane forming polymer, such as PSU, has received considerable attention, to enhance flux and fouling resistance. In copolymers the hydrophobic segments avoid leaching out of PEG and improve the miscibility with

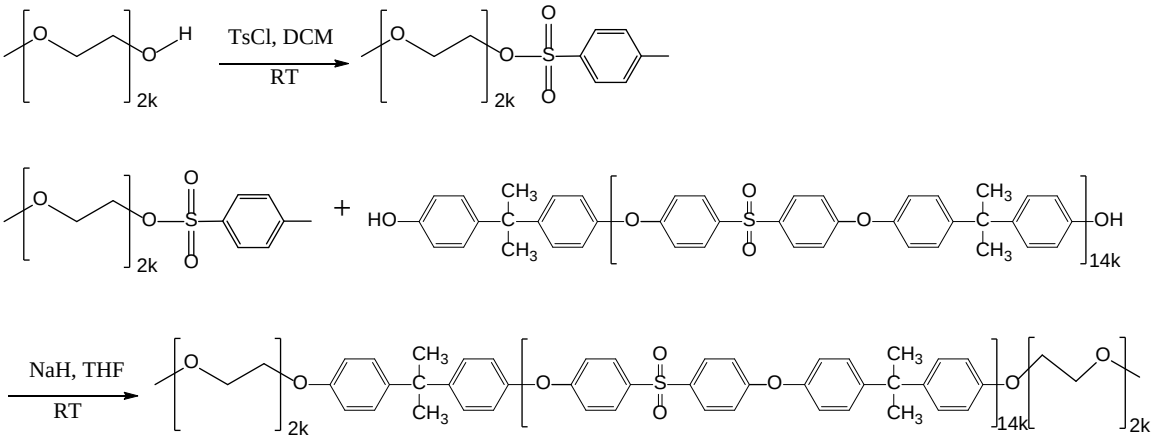

Scheme 3.2. Synthesis route of poly(ethylene glycol)-*b*-polysulfone-*b*-poly(ethylene glycol).

membrane materials, when used blending additives.[69-72] Moreover, a PEG-containing block copolymer, PS-*b*-PEG has proved to be suitable for isoporous asymmetric membrane formation *via* SNIPS.[73, 74] Thus we believe our target triblock copolymer PEG-PSU-PEG has a tremendous potential for the fabrication of nanostructured membranes, based on its self-assembly in selective solvents.

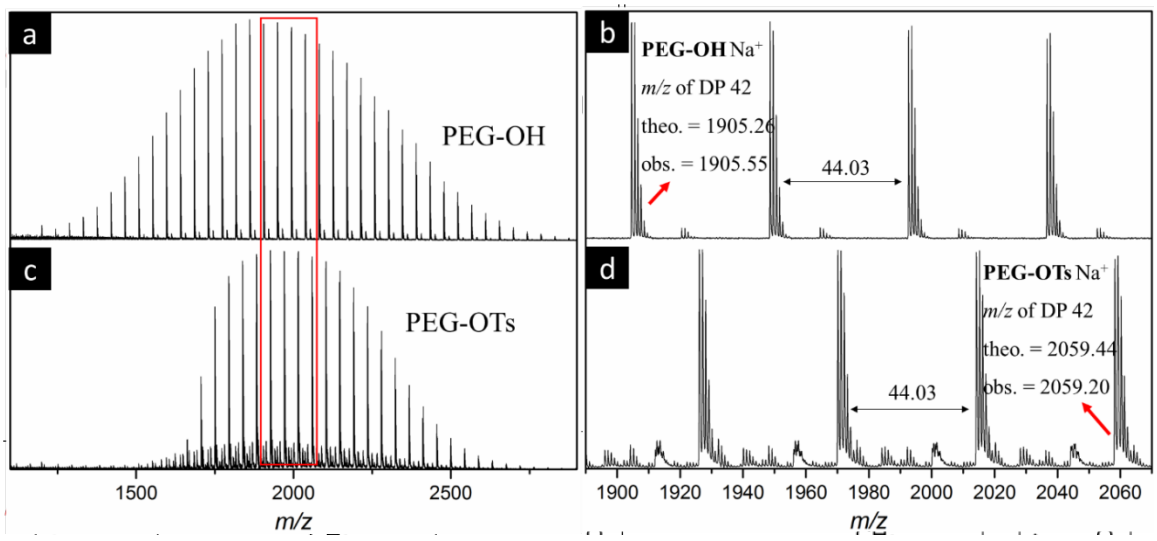

Figure 3.13. MALDI-TOF MS spectra of (a) PEG-OH and (b) expansion, (c) PEG-OTs and (d) expansion.

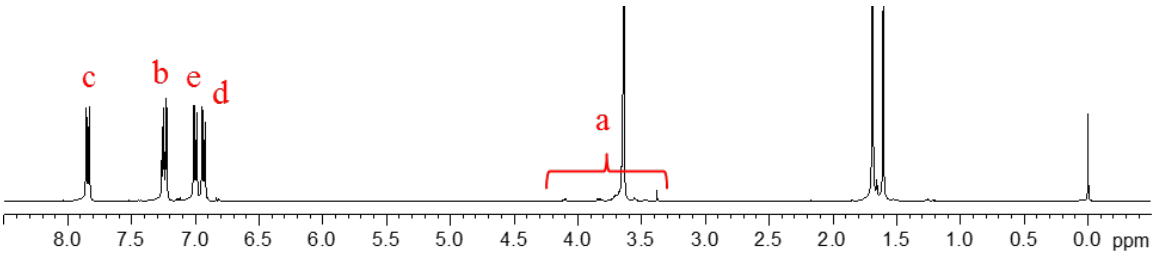

Figure 3.12. ^{1}H NMR spectra for PEG-Ts and PEG-PSU-PEG in $CDCl_3$.

Hancock et al. reported linear PSU-*b*-PEG multiblock copolymers *via* direct polycondensation.[70, 75] But the sequence and number of blocks are not well-defined. Similar strategy was utilized by Kim et al. to synthesize PSU-PEG random copolymer.[76] Park et al. prepared a graft copolymer PSU-*g*-PEG by using Williamson ether synthesis on the chloromethylated PSU backbone.[71] Wang et al. [72] synthesized an amphiphilic copolymers containing PEG brushes by extending the bifunctional PSU block with poly(ethylene glycol) methyl ether methacrylate (PEGMA) *via* atom transfer radical polymerization (ATRP). Here we prepared a PEG-PSU-PEG linear triblock copolymer through a coupling reaction based on Williamson ether synthesis between the telechelic

OH-terminated polysulfone that we reported before and the tosylated monofunctional PEG, as illustrated in Scheme 3.2. The first step is the tosylation of PEG 2000 monomethyl ether. Figure 3.12 shows ^{1}H NMR spectrum of PEG-Ts. The presence of two aromatic peaks at 7.80 and 7.35 ppm (peak "d" and "e") and a single peak at 2.45 ppm corresponding to the aryl-C$\boldsymbol{H_3}$ proton confirms the complete tosylation on the terminal OH group of PEG.[77] Chemical shifts from PEG backbone can also be detected, including 4.16 ppm (t, CH_2-C$\boldsymbol{H_2}$-OTs), 3.65 ppm (s, (($C\boldsymbol{H_2}$)$_2$-O)$_n$) and 3.38 ppm (s, O-C$\boldsymbol{H_3}$). Matrix assisted laser desorption ionization - time of flight mass spectroscopy (MALDI-TOF MS) technique is a powerful tool to determine the accurate molecular weight of short polymer chains and analyze their end group chemistry at a single-molecular level. Figure 3.13a and c suggest that some part of PEG with low molecular weight was lost during the purification step. Based on the expanded MALDI-TOF MS spectra as shown in Figure 3.13, the quantitative substitution of the terminal OH with tosyl group was again observed. The peak corresponding to PEG DP 42 in the starting material (Figure 3.13b) shifts to a higher *m/z* value having an excellent agreement with the theoretical molar mass of the new tosylated species (Figure 3.13d).

In the next step, the triblock copolymer PEG_{2k}-PSU_{14k}-PEG_{2k} was synthesized *via* a nucleophilic substitution. The hydroxyl-terminated bifunctional PSU was first reacted with NaH to deprotonate -OH. As a strong nucleophile, the activated phenoxide can readily substitute the tosyl group on the chain end of modified PEG and build an ether linkage between PEG and PSU segment. The chemical structure of the final triblock copolymer is studied by using NMR. The signals which belong to PEG repeat unit -$O(CH_2)_2$-, 3.64 ppm for ^{1}H NMR (Figure 3.12) and 70.55 ppm for ^{13}C NMR (Figure

A3.4, Appendices), appear in the spectra of purified copolymer after exhaustive washing with water to remove excess PEG. Based on the ratio of the integral of ^{1}H NMR peak for PEG backbone (δ = 3.64 ppm) to aromatic proton at the ortho position to sulfonyl group (δ = 7.84 ppm) on PSU, we can estimate the molar mass of PEG blocks in the triblock copolymer to be 3.6 kg/mol, which is close to two times of the molecular weight of PEG starting material. Taking the $M_{n,NMR}$ of PSU (14.4 kg/mol) into account, the NMR calculated number average molecular weight ($M_{n,NMR}$) of the triblock is 18 kg/mol. This value is consistent with the GPC M_n of 19.7 kg/mol, calibrated by PS standard. As shown in Figure A3.5 in Appendices, the GPC curve is a single peak without apparent shoulder or tail indicating efficient coupling reaction. It agrees with a lower polydispersity index (PDI) of 1.5 than that of the PSU homopolymer of 2.1, thanks to the incorporation of

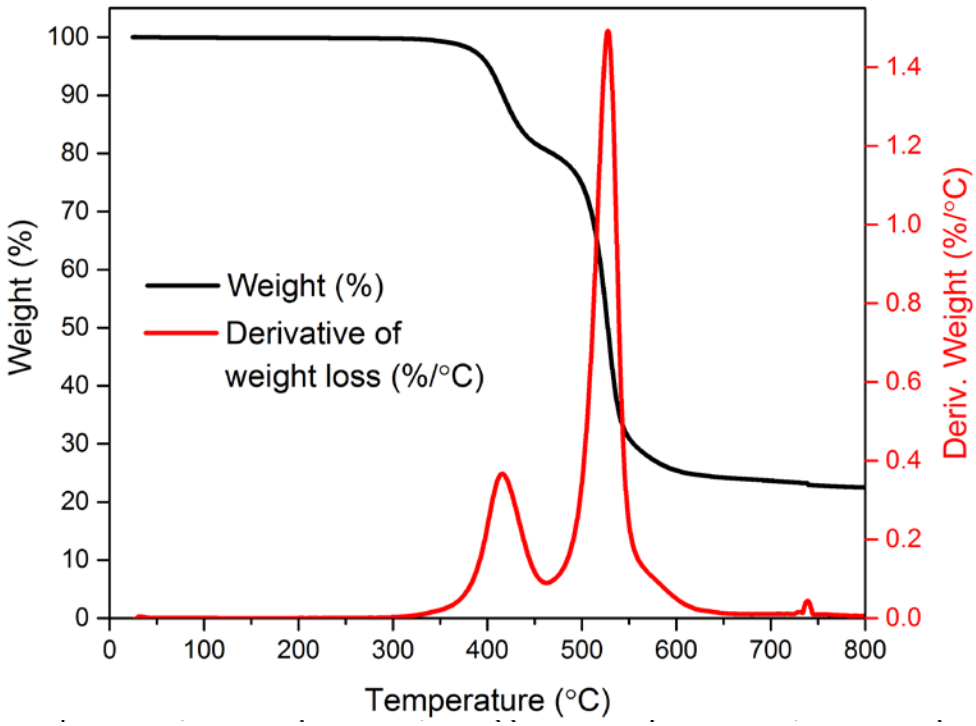

Figure 3.15. TGA (a) weight curve and (b) derivative curve for PEG-PSU-PEG under N_2.

well-defined PEG blocks. A comparison of FTIR spectrum of PSU and PEG-PSU-PEG is shown in Figure 3.14. In both cases, the fingerprint region with wavenumber lower than 1700 cm^{-1} containing various absorption bands from PSU backbone keeps unchanged. In the spectrum of triblock, the peak at 2870 cm^{-1} is attributed to the stretch of alkyl C-H bond next to the aromatic C-H peak (2966 cm^{-1}), whose intensity is increased because of the appearance of repeating methylene groups from PEG. Moreover a small broad band from 3020 to 3130 cm^{-1} correlated to the O-H stretching represents the water molecules adsorbed on the hydroscopic PEG segment from atmosphere.[72] The TGA study indicates two distinguishable weight loss steps that occur during the thermal decomposition under N_2 as shown in Figure 3.15. The weight loss begins with the degradation of PEG segments from 350 to 460 °C,[76] while the PSU middle block continues to decompose and

reaches the highest rate at 530 °C as a second sharp peak in the derivative weight curve (Figure 3.15b). A single glass transition temperature (T_g) was observed for PEG-PSU-PEG at 76 °C from the DSC curve (Figure A3.6, Appendices), indicating a homogeneous material. The measured T_g agrees with the theoretical value (70 °C) for a miscible PSU/PEG mixture predicted by using the following Flory-Fox equation,[75, 76]

$$\frac{1}{T_{g,PSU/PEG}} = \frac{w_{PSU}}{T_{g,PSU}} + \frac{w_{PEG}}{T_{g,PEG}}$$

Equation 3.1

where the weight fraction of component in the binary system, w_{PSU} (78 wt%) and w_{PEG} (22 wt%) is the same as our copolymer, the glass transition temperature $T_{g,PSU}$ and $T_{g,PSU}$ is 167 (see chapter 2) and -80 °C,[76] respectively.

3.3.5 Synthesis of PEG-PNIPAM-PSU-PNIPAM-PEG

The synthesis of a pentablock terpolymer, poly(ethylene glycol)-*b*-Poly(*N*-isopropylacrylamide)-*b*-Polysulfone-*b*-Poly(*N*-isopropylacrylamide)-*b*-Poly(ethylene glycol) (PEG-PNIPAM-PSU-PNIPAM-PEG) was attempted by using the same strategy that we employed for PEG-PSU-PEG triblock. Poly(*N*-isopropylacrylamide) (PNIPAM) is a well-known temperature-responsive polymer, changing hydrophilicity and hydrophobicity abruptly at its lower critical solution temperature (LCST). This property

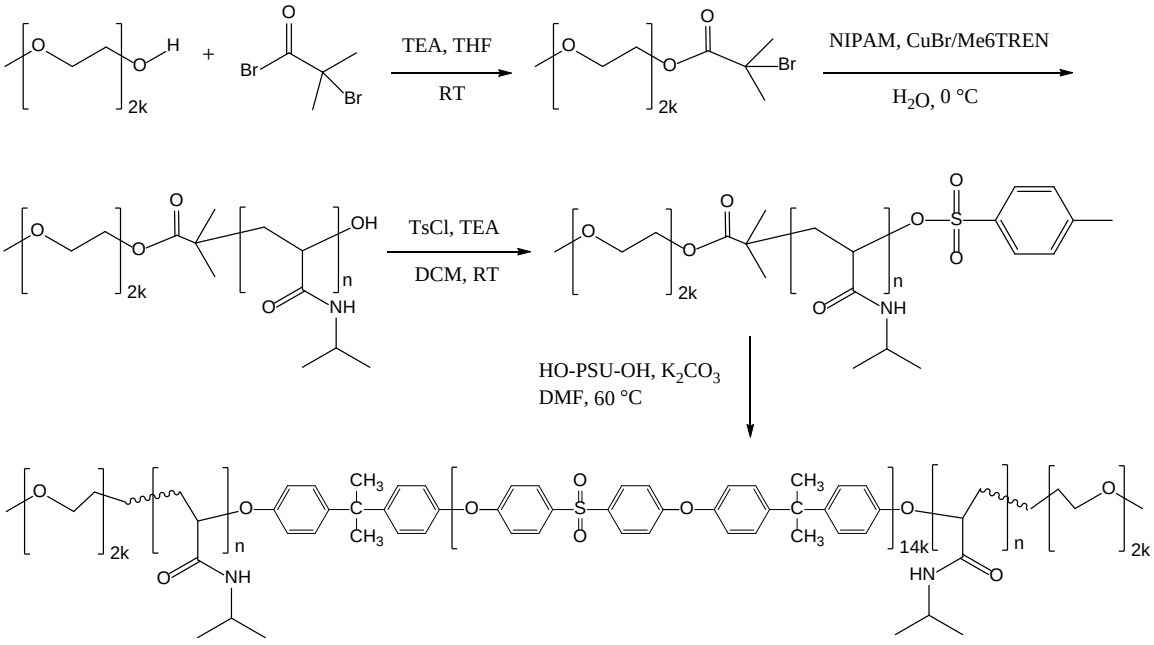

Scheme 3.3. Synthesis route of poly(ethylene glycol)-*b*-Poly(*N*-isopropylacrylamide)-*b*-Polysulfone-*b*-Poly(*N*-isopropylacrylamide)-*b*-Poly(ethylene glycol).

makes thermosensitive PNIPAM microgels and 3D assemblies desirable for biomedical applications from controlled drug delivery to tissue engineering.[78] Zhang et al. developed a facile approach to synthesize PNIPAM with well-controlled chain length in pure water *via* single-electron transfer living radical polymerization (SET-LRP), featuring the in-situ full disproportionation of CuBr/Me_6TREN to catalytic Cu^0 and $CuBr_2$ pair.[79] Here we follow their procedure with small modification to prepare the PEG-PNIPAM diblock

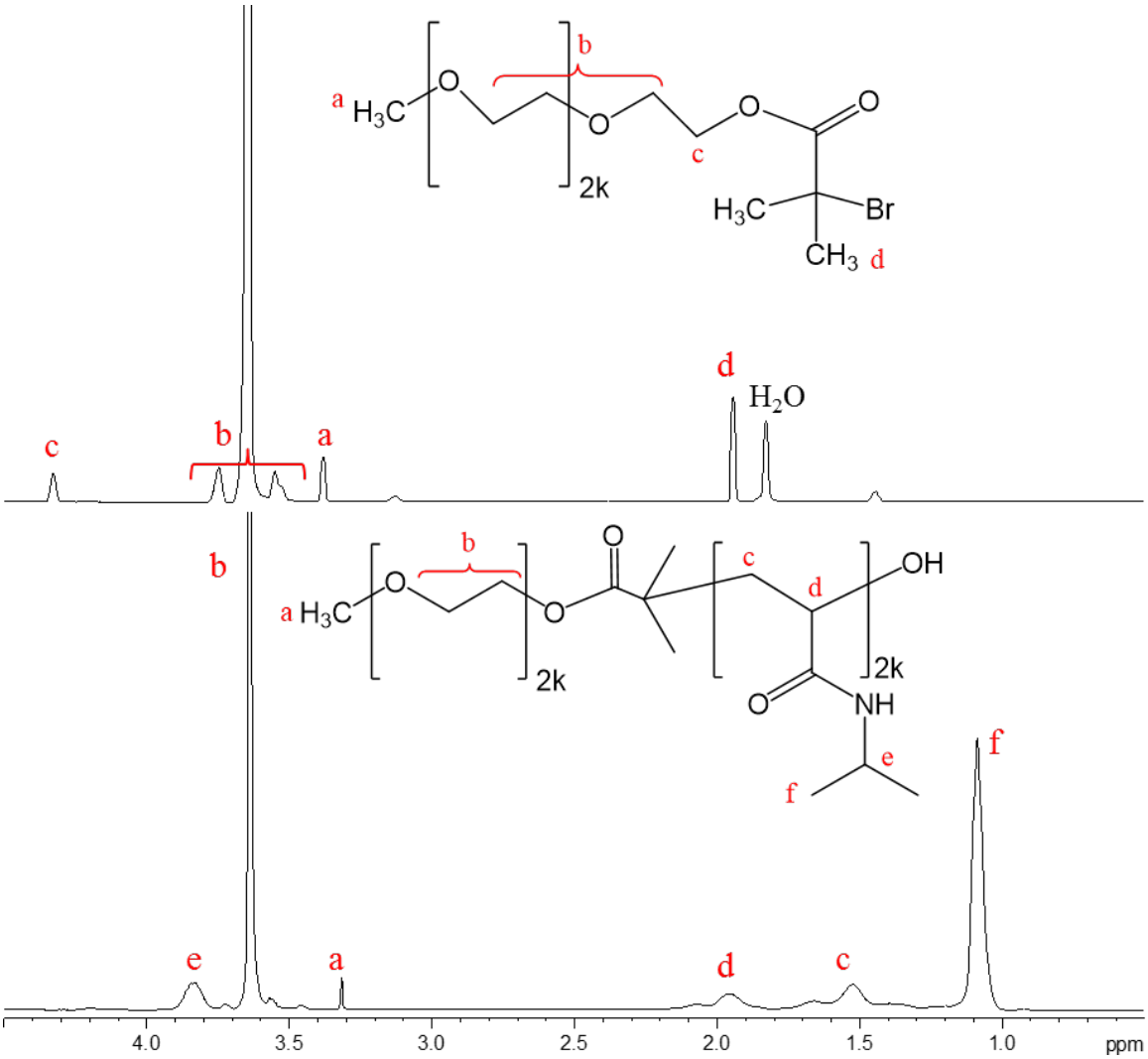

Figure 3.16. ^{1}H NMR spectra for PEG-I (in $CDCl_3$) and PEG-PNIPAM (in D_2O) obtained *via* SET-LRP in water at 0 °C for 30 min, [NIPAM]:[PEG-I]:[CuBr]:[Me_6TREN] = 20:1:0.4:0.4.

copolymers, which can be further coupled with PSU leading to pentablock copolymers in the same manner as triblock. Scheme 3.3 outlines the complete synthesis route.

First, a macroinitiator PEG-I was obtained by reacting PEG_{2000} monomethyl ether with α-bromoisobutyryl bromide (BiBB). The similar method has been reported for oligo(ethylene oxide)$_{350}$-derived initiators.[80, 81] The successful synthesis of PEG-I can be proved by NMR and MALDI-TOF MS. Figure 3.16 shows ^{1}H NMR spectrum of PEG-I, in which a new peak corresponding to -C(C$\boldsymbol{H_3}$)$_2$Br protons in 2-bromoisobutyryl end group was observed at 1.94 ppm. MALDI-TOF MS spectrum of PEG-I confirms the

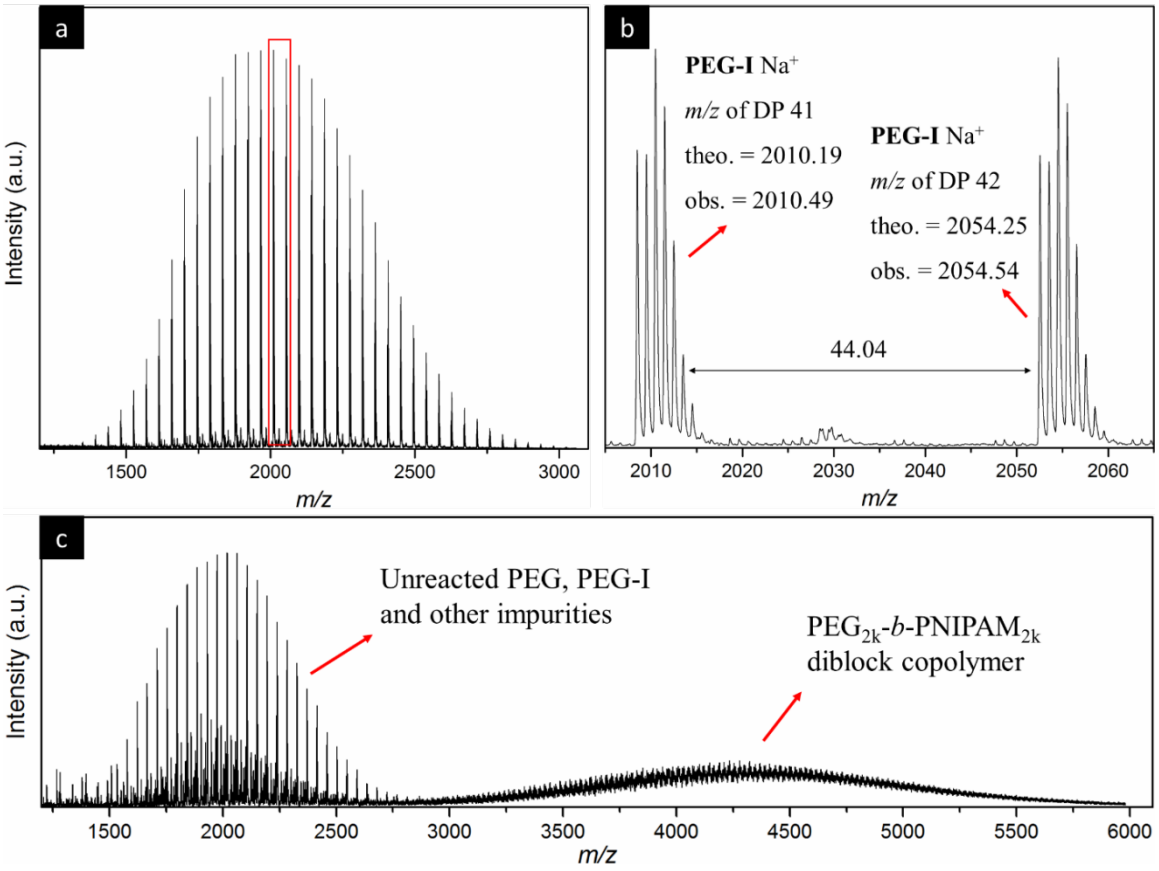

Figure 3.17. MALDI-TOF MS spectra of (a) PEG-I and (b) expansion, (c) sample after SET-LRP in water at 0 °C for 30 min, [NIPAM]:[PEG-I]:[CuBr]:[Me_6TREN] = 20:1:0.4:0.4.

quantitative esterification between OH group and acyl bromide to yield the PEG capped with a tertiary bromide which can initiate copper-mediated living polymerization. Figure 3.17b illustrates that the *m/z* values of two PEG macroinitiators with one repeat unit difference (DP =41 and 42) match the theoretical molar mass of them perfectly.

The SET-LRP of NIPAM was performed according to the literature.[79] Copper bromide powder and Me6TREN ligand were well mixed in water to get a light green solution with some sediments of red Cu^0 fine power, indicating complete disproportionation of Cu^I, followed by addition of monomers and initiator. For DP = 10, 20, and 40, polymerizations were conducted using a ratio of [PEG-I]:[CuBr]:[Me6TREN] = 1:0.4:0.4 at 0 °C to alleviate rapid heat build-up from the highly exothermic monomer addition. ^{1}H NMR analysis of the samples taken directly from the solution after the polymerizations demonstrates in all cases full conversion was attained in 30 min as no signal from alkene monomer existed (not shown here). The chemical structure of the dialysis purified diblock copolymer with DP = 20 is studied by ^{1}H NMR. As shown in Figure 3.16, two broad peaks ranging from 1.3 to 2.2 ppm belong to alkyl protons on the PNIPAM main chain. The protons in *N*-isopropyl group contribute to the peaks at 1.09 ppm (-CH(C***H3***)$_2$) and 3.84 ppm (-C***H***(CH3)$_2$). The average DP determined by comparing the ^{1}H NMR integral of PEG and PNIPAM peaks is 19.8, a good agreement with the target DP, considering the average molecular weight of PEG is 2000. GPC curves of all diblock copolymers revealed narrow molecular weight distributions (PDI <1.2) with symmetrical peak shapes without tailing (Figure 3.18). For each DP, its M_n determined by GPC using THF as eluent is lower than the $M_{n,NMR}$, contradicting the observation of 100% conversion. The solvent THF with a relatively lower polarity might underestimate

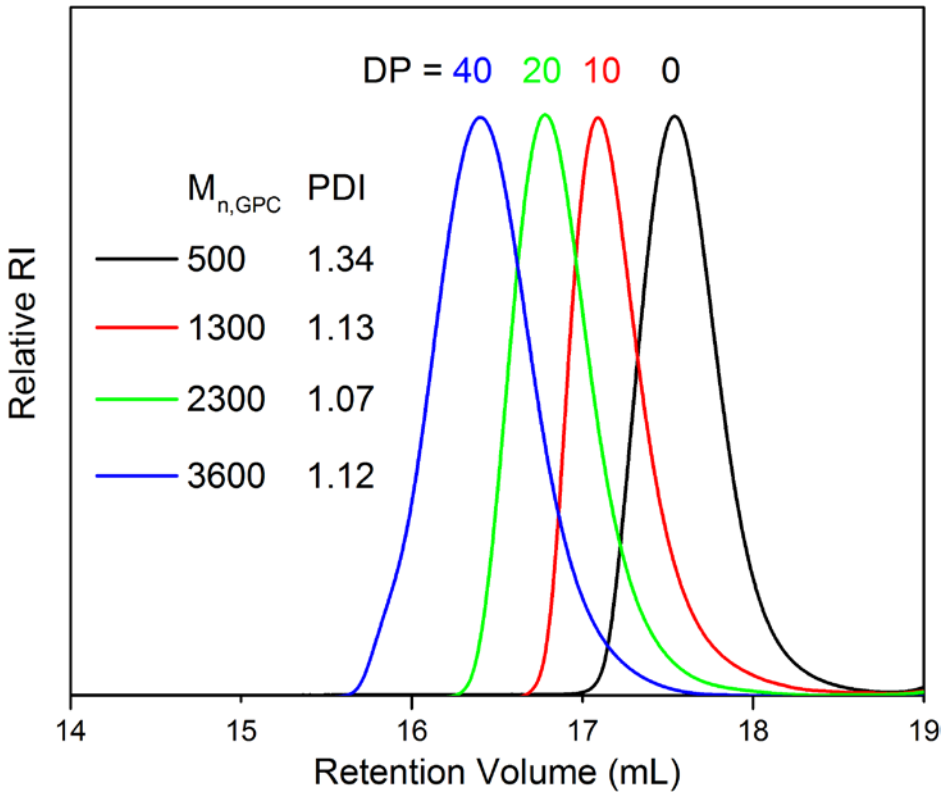

Figure 3.18. GPC curves of PEG (DP = 0) and PEG-PNIPAM obtained *via* SET-LRP in water at 0 °C for 30 min, [PEG-I]:[CuBr]:[Me_6TREN] = 20:1:0.4:0.4, with varying DP (10, 20, 40).

the highly polar solvents by reducing their hydrodynamic size. The GPC characterization for PEG shows it also has a measured $M_{n,GPC,}$ lower than the actual molar mass. The sample of DP 20 after the polymerization was analyzed with MALDI-TOF MS. But the measuring condition is not optimal for the diblock copolymer. As shown in Figure 3.17c, only a small bump with a highest intensity at ~4000 *m/z* can be observed. It is likely to be composed of dispersed PEG-PNIPAM species, but we are unable to further verify by molar mass analysis for discrete peaks due to the low resolution. At the low molar mass region, PEG-based impurity mixture can be found including unreacted PEG monomethyl ether and PEG macroinitiator that did not participate in the polymerization. It should be

pointed out that the intensity of MALDI-TOF peak does not always reflect the relative number of components. The amount of impurities could be negligible to PEG-PNIPAM, while the latter was not properly ionized and collected by the detector in the MALDI-TOF MS with the current conditions.

After the polymerization, the as-obtained PEG-PNIPAM diblock bearing primary bromide as the end group could react directly with HO-PSU-OH in the presence of base catalyst to get the final pentablock terpolymer. Unfortunately, it has been proved that the terminal halogen group undergoes hydrolysis easily *via* a cyclic onium intermediate during the aqueous polymerization especially at full conversion.[79] Although the chain end

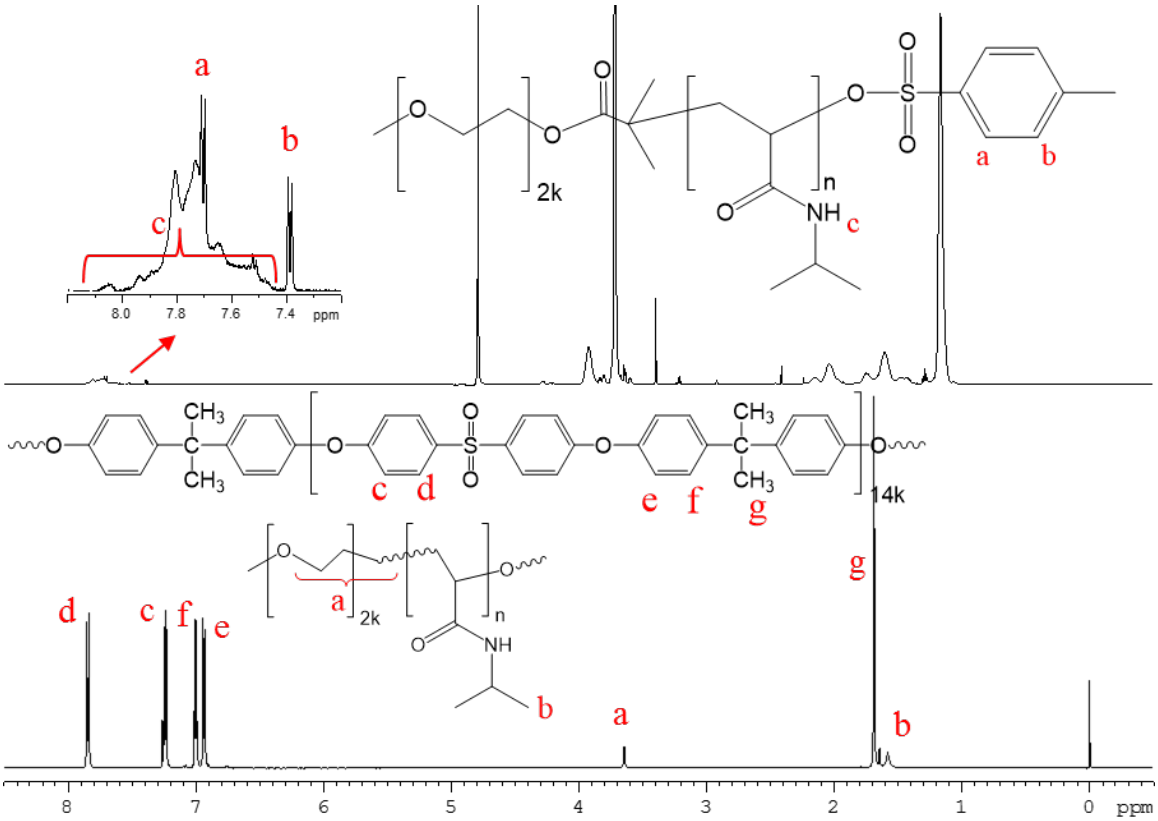

Figure 3.19. ^{1}H NMR spectra for PEG-PNIPAM-Ts, DP 20 (in D_2O), and sample obtained from copolmerization of PEG-PNIPAM and PSU (in $CDCl_3$).

fidelity can be partially improved by using lower reaction temperature, the transformation of bromide to OH end group in the polymer isolation step is almost inevitable. Thus we attempted to convert the terminal OH produced from hydrolysis to tosyl group, another good leaving group capable of being substituted in the subsequent Williamson ether synthesis. The presence of aromatic protons from tosyl group at 7.71 and 7.39 ppm overlapped with a broad peak of -N***H***-, is revealed by ^{1}H NMR spectrum of tosylated PEG-PNIPAM (Figure 3.19). A weak base K_2CO_3 was used instead of NaH to catalyze the coupling reaction between PEG-PNIPAM-Ts and HO-PSU-OH because NaH would potentially deprotonate the nitrogen in the amide group leading to undesired *N*-alkylation. However ^{1}H NMR spectrum of the sample after the reaction in Figure 3.19 suggests that few PEG-PNIPAM chain is incorporated into the PSU backbone. The integral of PEG protons is 18 times lower than that expected for PEG_{2k}-$PNIPAM_{2k}$-PSU_{14k}-$PNIPAM_{2k}$-PEG_{2k}. A careful investigation of the end group chemistry of PEG-PNIPAM is needed in order to explain the unsuccessful synthesis of pentablock copolymer. It requires us to improve the quality of MALDI-TOF MS spectrum of the diblock copolymer, being the only feasible tool to characterize the end group, while NMR provides very limited information because of severe peak overlapping. One possible reason is that elimination of HBr forming internal alkene is the predominant pathway for termination of PNIPAM growing chain in our system, which could deactivate the further end group modification.

3.4 Conclusions

The goal of this chapter is to fabricate biomimetic membranes with water channels from different amphiphilic polysulfone-based block copolymers that contain water-soluble segments. First poly(acrylic acid)-*b*-polysulfone-*b*-poly(acrylic acid) (PAA_{17k}-PSU_{14k}-PAA_{17k}) triblock copolymers was successfully synthesized by hydrolyzing poly(*tert*-butyl acrylate)-*b*-polysulfone-*b*-poly(*tert*-butyl acrylate) with trifluoroacetic acid in anhydrous medium. Its chemical structure was verified by characteristic adsorption peaks in NMR and FTIR spectra. Thermal studies confirm the presence of PAA blocks in the copolymer with characteristic weight loss at 160 °C measured by TGA, featuring a dehydration process and formation of anhydride structure. The T_g increases to 123 °C revealed by DSC due to the conversion to PAA. TEM and DLS studies indicate that PAA-PSU-PAA can assemble into 30 nm spherical micelles in THF with a flower-like arrangement. The thin film formed from PAA-PSU-PAA 3 wt% THF solution has a surface packed with worm-like micelles, which can transform to a dense film with 50 nm vertically aligned PAA microdomains inserted in PSU matrix *via* bulk self-assembly induced by thermal annealing at 180 °C. This thin film was well characterized by TEM, SEM and AFM topography and phase imaging. A composite membrane was fabricated by using a porous ceramic membrane as support. Although surface morphology study shows the presence of the same water channel-like structure, it exhibit no permeability to water, which could be attributed to the roughness of support material. A new strategy "self-assembly and chelation-assisted non-solvent induced phase separation" (SCNIPS) was devised to prepare stable PAA-PSU-PAA phase inversion membranes with the help of metal ions in the coagulation bath by forming strong metal-PAA complexes. Solution TEM and DLS confirms the formation of large micelles (> 100 nm) in a selective solvent

mixture DMF/THF/acetone (10/45/45) which drives PAA block to organize into the corona to protect PSU inner core from its non-solvent. SEM and thin section TEM demonstrate that both copper and silver ions can preserve the morphology of spherical micelles assembled in casting solution, leading to the ordered space between micelles filled with PAA which could act as preferential water channels. The silver nanoparticle decorated membrane was obtained by surface reduction with $NaBH_4$. Three distinct layers with different nanoparticle sizes were found by TEM. It is worth to challenge the PAA-PSU-PAA nanostructured membranes that we synthesized *via* SCINPS with nanofiltration experiment and explore more applications of the membrane nanoparticles. Besides PAA-PSU-PAA, we synthesized another triblock copolymer, poly(ethylene glycol)-*b*-polysulfone-*b*-poly(ethylene glycol) (PEG_{2k}-PSU_{14k}-PEG_{2k}). PEG monomethyl ether was modified to have a terminal tosyl group, which can couple with the telechelic PSU capped with OH through Williamson ether synthesis. The modification of PEG and copolymerization were characterized by NMR, MALDI-TOF and FTIR. GPC result shows PEG-PSU-PEG has a narrower molecular weight distribution than PSU. It has good thermal stability up to 400 °C, while T_g decreases to 76 °C due to the incorporation of PEG which is compatible with PSU. The self-assembly study for PEG-PSU-PEG towards nanoporous membranes and water channel formation is undergoing. Finally we attempted to prepare a pentablock terpolymer, poly(ethylene glycol)-*b*-poly(N-isopropylacrylamide)-*b*-polysulfone-*b*-poly(N-isopropylacrylamide)-*b*-poly(ethylene glycol) (PEG_{2k}-$PNIPAM_{2k}$-PSU_{14k}-$PNIPAM_{2k}$-PEG_{2k}). PEG2000 bromide-macroinitiator was prepared from PEG monomethyl ether. Its structure was verified by using NMR and MALDI-TOF MS. PEG-PNIPAM diblock copolymer was then obtained

via SET-LRP with CuBr/Me_6TREN. The polymerizations reach full conversion within 30 min. GPC characterization of copolymers with various DP shows the chain length of PNIPAM was well-controlled and all have reasonable molecular weight distribution (< 1.2). The obtained diblock copolymer was tosylated to have a good leaving group as the chain end. Although the chemical composition was studied by NMR, the chain end chemistry cannot be quantitatively confirmed by MALDI-TOF MS, which failed to measure the accurate molar mass of PEG-PNIPAM. Coupling reaction did not give the pentablock terpolymer with expected mass fraction of water-soluble segment.

3.5 References

1. S. P. Nunes and K.-V. Peinemann, *Membrane technology: in the chemical industry*, John Wiley & Sons, 2006.

2. K. P. Lee, T. C. Arnot and D. Mattia, *J. Membr. Sci.*, 2011, 370, 1-22.

3. M. M. Pendergast and E. M. V. Hoek, *Energy Environ. Sci.*, 2011, 4, 1946-1971.

4. R. Sengur-Tasdemir, S. Aydin, T. Turken, E. A. Genceli and I. Koyuncu, *Sep. Purif. Rev.*, 2016, 45, 122-140.

5. Y.-x. Shen, P. O. Saboe, I. T. Sines, M. Erbakan and M. Kumar, *J. Membr. Sci.*, 2014, 454, 359-381.

6. J. Zhao, X. Zhao, Z. Jiang, Z. Li, X. Fan, J. Zhu, H. Wu, Y. Su, D. Yang, F. Pan and J. Shi, *Prog. Polym. Sci.*, 2014, 39, 1668-1720.

7. P. Agre, *Angew. Chem. Int. Ed.*, 2004, 43, 4278-4290.

8. M. Kumar, M. Grzelakowski, J. Zilles, M. Clark and W. Meier, *Proc. Natl. Acad. Sci. USA*, 2007, 104, 20719-20724.

9. C. Tang, Z. Wang, I. Petrinić, A. G. Fane and C. Hélix-Nielsen, *Desalination*, 2015, 368, 89-105.

10. C. Y. Tang, Y. Zhao, R. Wang, C. Hélix-Nielsen and A. G. Fane, *Desalination*, 2013, 308, 34-40.

11. B. J. Hinds, N. Chopra, T. Rantell, R. Andrews, V. Gavalas and L. G. Bachas, *Science*, 2004, 303, 62-65.

12. M. Majumder, N. Chopra and B. J. Hinds, *J. Am. Chem. Soc.*, 2005, 127, 9062-9070.

13. J. K. Holt, H. G. Park, Y. Wang, M. Stadermann, A. B. Artyukhin, C. P. Grigoropoulos, A. Noy and O. Bakajin, *Science*, 2006, 312, 1034-1037.

14. F. Fornasiero, H. G. Park, J. K. Holt, M. Stadermann, C. P. Grigoropoulos, A. Noy and O. Bakajin, *Proc. Natl. Acad. Sci. USA*, 2008, 105, 17250-17255.

15. A. Berezhkovskii and G. Hummer, *Phys. Rev. Lett.*, 2002, 89, 064503.

16. A. Kalra, S. Garde and G. Hummer, *Proc. Natl. Acad. Sci. USA*, 2003, 100, 10175-10180.

17. S. Joseph and N. R. Aluru, *Nano Lett.*, 2008, 8, 452-458.

18. J. A. Thomas and A. J. H. McGaughey, *Nano Lett.*, 2008, 8, 2788-2793.

19. K. Murata, K. Mitsuoka, T. Hirai, T. Walz, P. Agre, J. B. Heymann, A. Engel and Y. Fujiyoshi, *Nature*, 2000, 407, 599-605.

20. G. Hummer, J. C. Rasaiah and J. P. Noworyta, *Nature*, 2001, 414, 188-190.

21. M. Barboiu, *Angew. Chem. Int. Ed.*, 2012, 51, 11674-11676.

22. M. Barboiu and A. Gilles, *Acc. Chem. Res.*, 2013, 46, 2814-2823.

23. Z. Fei, D. Zhao, T. J. Geldbach, R. Scopelliti, P. J. Dyson, S. Antonijevic and G. Bodenhausen, *Angew. Chem. Int. Ed.*, 2005, 44, 5720-5725.

24. M. S. Kaucher, M. Peterca, A. E. Dulcey, A. J. Kim, S. A. Vinogradov, D. A. Hammer, P. A. Heiney and V. Percec, *J. Am. Chem. Soc.*, 2007, 129, 11698-11699.

25. Y. Le Duc, M. Michau, A. Gilles, V. Gence, Y.-M. Legrand, A. van der Lee, S. Tingry and M. Barboiu, *Angew. Chem. Int. Ed.*, 2011, 50, 11366-11372.

26. T. Xu, N. Zhao, F. Ren, R. Hourani, M. T. Lee, J. Y. Shu, S. Mao and B. A. Helms, *ACS Nano*, 2011, 5, 1376-1384.

27. X.-B. Hu, Z. Chen, G. Tang, J.-L. Hou and Z.-T. Li, *J. Am. Chem. Soc.*, 2012, 134, 8384-8387.

28. Y.-x. Shen, W. Si, M. Erbakan, K. Decker, R. De Zorzi, P. O. Saboe, Y. J. Kang, S. Majd, P. J. Butler, T. Walz, A. Aksimentiev, J.-l. Hou and M. Kumar, *Proc. Natl. Acad. Sci. USA*, 2015, 112, 9810-9815.

29. X. Zhou, G. Liu, K. Yamato, Y. Shen, R. Cheng, X. Wei, W. Bai, Y. Gao, H. Li, Y. Liu, F. Liu, D. M. Czajkowsky, J. Wang, M. J. Dabney, Z. Cai, J. Hu, F. V. Bright, L. He, X. C. Zeng, Z. Shao and B. Gong, *Nat. Commun.*, 2012, 3, 949.

30. S. P. Nunes and A. Car, *Ind. Eng. Chem. Res.*, 2013, 52, 993-1003.

31. K.-V. Peinemann, V. Abetz and P. F. W. Simon, *Nat. Mater.*, 2007, 6, 992-996.

32. S. P. Nunes, R. Sougrat, B. Hooghan, D. H. Anjum, A. R. Behzad, L. Zhao, N. Pradeep, I. Pinnau, U. Vainio and K. V. Peinemann, *Macromolecules*, 2010, 43, 8079-8085.

33. H. Yu, X. Qiu, N. Moreno, Z. Ma, V. M. Calo, S. P. Nunes and K.-V. Peinemann, *Angew. Chem. Int. Ed.*, 2015, 54, 13937-13941.

34. J. Queffelec, S. G. Gaynor and K. Matyjaszewski, *Macromolecules*, 2000, 33, 8629-8639.

35. Q. Ma and K. L. Wooley, *J. Polym. Sci. A Polym. Chem.*, 2000, 38, 4805-4820.

36. C. Burguière, S. Pascual, C. Bui, J.-P. Vairon, B. Charleux, K. A. Davis, K. Matyjaszewski and I. Bétremieux, *Macromolecules*, 2001, 34, 4439-4450.

37. M. Zhang, T. Breiner, H. Mori and A. H. E. Müller, *Polymer*, 2003, 44, 1449-1458.

38. X. André, M. Zhang and A. H. E. Müller, *Macromol. Rapid Commun.*, 2005, 26, 558-563.

39. A. C. Greene, J. Zhu, D. J. Pochan, X. Jia and K. L. Kiick, *Macromolecules*, 2011, 44, 1942-1951.

40. Y. Zhang, Z. Shen, D. Yang, C. Feng, J. Hu, G. Lu and X. Huang, *Macromolecules*, 2010, 43, 117-125.

41. O. Colombani, M. Ruppel, F. Schubert, H. Zettl, D. V. Pergushov and A. H. E. Müller, *Macromolecules*, 2007, 40, 4338-4350.

42. S. Dubinsky, G. S. Grader, G. E. Shter and M. S. Silverstein, *Polym. Degrad. Stab.*, 2004, 86, 171-178.

43. M. Fernández-García, J. L. d. l. Fuente, M. a. L. Cerrada and E. L. Madruga, *Polymer*, 2002, 43, 3173-3179.

44. A. Ramakrishnan and R. Dhamodharan, *Macromolecules*, 2003, 36, 1039-1046.

45. M. A. Moharram and M. A. Allam, *J. Appl. Polym. Sci.*, 2007, 105, 3220-3227.

46. I. C. McNeill and S. M. T. Sadeghi, *Polym. Degrad. Stab.*, 1990, 29, 233-246.

47. J.-K. Park, D.-W. Kim, C.-H. Kim, K.-S. Maeng, T.-S. Hwang and Y.-C. Kim, *Polym. Eng. Sci.*, 1991, 31, 867-872.

48. Y. Mai and A. Eisenberg, *Chem. Soc. Rev.*, 2012, 41, 5969-5985.

49. Y. Yu, L. Zhang and A. Eisenberg, *Macromolecules*, 1998, 31, 1144-1154.

50. Y. Yu and A. Eisenberg, *J. Am. Chem. Soc.*, 1997, 119, 8383-8384.

51. T. Azzam and A. Eisenberg, *Angew. Chem. Int. Ed.*, 2006, 45, 7443-7447.

52. C. M. Hansen, *Hansen Solubility Parameters: A User's Handbook, Second Edition*, CRC Press, 2007.

53. X. Tang, L. Gao, X. Fan, X. Liang and Q. Zhou, *Macromol. Chem. Phys.*, 2009, 210, 1556-1562.

54. F. C. Giacomelli, I. C. Riegel, C. L. Petzhold, N. P. da Silveira and P. Štěpánek, *Langmuir*, 2009, 25, 731-738.

55. T. Liu, Z. Zhou, C. Wu, B. Chu, D. K. Schneider and V. M. Nace, *J. Phys. Chem. B*, 1997, 101, 8808-8815.

56. J. K. Kim, S. Y. Yang, Y. Lee and Y. Kim, *Prog. Polym. Sci.*, 2010, 35, 1325-1349.

57. P. Leclère, R. Lazzaroni, J. L. Brédas, J. M. Yu, P. Dubois and R. Jérôme, *Langmuir*, 1996, 12, 4317-4320.

58. J. E. Mark, *Physical properties of polymers handbook*, Springer, 1996.

59. Y. Wang, R. Song, Y. Li and J. Shen, *Surf. Sci.*, 2003, 530, 136-148.

60. Z. Lu, G. Liu and S. Duncan, *Macromolecules*, 2004, 37, 174-180.

61. Z. Zhang, X.-Y. Kong, K. Xiao, G. Xie, Q. Liu, Y. Tian, H. Zhang, J. Ma, L. Wen and L. Jiang, *Adv. Mater.*, 2016, 28, 144-150.

62. S. P. Nunes, *Macromolecules*, 2016, 49, 2905-2916.

63. S. P. Nunes, M. Karunakaran, N. Pradeep, A. R. Behzad, B. Hooghan, R. Sougrat, H. He and K. V. Peinemann, *Langmuir*, 2011, 27, 10184-10190.

64. S. P. Nunes, A. R. Behzad, B. Hooghan, R. Sougrat, M. Karunakaran, N. Pradeep, U. Vainio and K. V. Peinemann, *ACS Nano*, 2011, 5, 3516-3522.

65. H. Lu, L. Fan, Q. Liu, J. Wei, T. Ren and J. Du, *Polym. Chem.*, 2012, 3, 2217-2227.

66. P. Madhavan, P.-Y. Hong, R. Sougrat and S. P. Nunes, *ACS Appl. Mater. Interfaces*, 2014, 6, 18497-18501.

67. M. Amiji and K. Park, in *Polymers of Biological and Biomedical Significance*, American Chemical Society, 1993, vol. 540, ch. 11, pp. 135-146.

68. J. M. Harris, *Poly (ethylene glycol) chemistry: biotechnical and biomedical applications*, Springer Science & Business Media, 2013.

69. Y. H. Cho, H. W. Kim, S. Y. Nam and H. B. Park, *J. Membr. Sci.*, 2011, 379, 296-306.

70. L. F. Hancock, S. M. Fagan and M. S. Ziolo, *Biomaterials*, 2000, 21, 725-733.

71. J. Y. Park, M. H. Acar, A. Akthakul, W. Kuhlman and A. M. Mayes, *Biomaterials*, 2006, 27, 856-865.

72. J. Wang, Y. Xu, L. Zhu, J. Li and B. Zhu, *Polymer*, 2008, 49, 3256-3264.

73. M. Karunakaran, S. P. Nunes, X. Qiu, H. Yu and K. V. Peinemann, *J. Membr. Sci.*, 2014, 453, 471-477.

74. J. Hahn, V. Filiz, S. Rangou, J. Clodt, A. Jung, K. Buhr, C. Abetz and V. Abetz, *J. Polym. Sci. Part B Polym. Phys.*, 2013, 51, 281-290.

75. Y.-P. R. Ting and L. F. Hancock, *Macromolecules*, 1996, 29, 7619-7621.

76. H. W. Kim and H. B. Park, *J. Membr. Sci.*, 2011, 372, 116-124.

77. J. A. Opsteen and J. C. M. van Hest, *Chem. Commun.*, 2005, DOI: 10.1039/B412930J, 57-59.

78. Y. Guan and Y. Zhang, *Soft Matter*, 2011, 7, 6375-6384.

79. Q. Zhang, P. Wilson, Z. Li, R. McHale, J. Godfrey, A. Anastasaki, C. Waldron and D. M. Haddleton, *J. Am. Chem. Soc.*, 2013, 135, 7355-7363.

80. N. H. Nguyen, J. Kulis, H.-J. Sun, Z. Jia, B. van Beusekom, M. E. Levere, D. A. Wilson, M. J. Monteiro and V. Percec, *Polym. Chem.*, 2013, 4, 144-155.

81. X. S. Wang and S. P. Armes, *Macromolecules*, 2000, 33, 6640-6647.

CHAPTER 4

Polysulfone-*co*-Polytriazole Random and Triblock Copolymers for Hydrogen Bond-Mediated Self-assembly

4.1 Introduction

Membrane separation technology offers great promises to meet the more stringent regulatory requirements for water quality that cannot be easily reached by conventional treatment technologies. Needed separation membranes are strong, thermally stable, and resistant to oxidative or corrosive elements in the material to be separated such as acids or chloride ions.[1] Polysulfone (PSU) is one of the high performance polymer family widely used for fabrication of membranes. The developments of PSU membranes can be traced in the 1960s as an alternative to cellulosic membranes. A great advantage over cellulose acetate in terms of membrane applications is its resistance in extreme pH conditions and chlorinated disinfectants. Other excellent properties of PSU include good mechanical roughness, hydrolytic stability, as well as thermal stability with a T_g of 190 °C.[2, 3] PSU is soluble in many solvents, so can be easily applied in conventional phase separation processes with good pore forming behavior.[2] Due to these properties, polysulfones have been the basis of several applications, such as microfiltration membranes,[4] electrospun nanofibrous scaffold for thin film composite nanofiltration membranes,[5] mixed matrix membranes for gas separation,[6] proton exchange membranes for fuel cell,[7] and capillary fiber as a drug delivery device for intraocular applications.[8]

However, a drawback for the application of PSUs membranes for aqueous phase is their intrinsic hydrophobicity[9, 10] which causes fouling. To overcome this limitation, a good strategy for improving fouling resistance is the introduction of hydrophilic functionalities groups covalently bonded to the polysulfones backbone[11-13] or surface of polymer membranes.[10, 13, 14] Modified membranes are expected to have low adsorption of hydrophobic materials such as protein and other solutes.[11, 12, 15-18] It should affect the membrane processes such as reverse osmosis, nanofiltration, and ultrafiltration. It is also expected to control hydrophobic and hydrophilic nature within the membrane physical structure and enhances the transport properties.[10, 11, 18] Introduction of functionality to polysulfones can be accomplished by either using the functional monomer approach allowing modification at the polymerization stage (polycondensation) or by the post-functionalization of commercially available polymers.[2]

Introduced by Sharpless et al.,[19] the click chemistry concept enables the preparation of not only telechelic polymers but also side-group functionalized polymers using clickable initiators, monomers or polymers in nearly quantitative yields.[20-22] The click reaction is also well-known for the broad tolerance toward functional groups, low susceptibility to side reactions allowing mild reaction conditions and easy isolation of final products.[19] Owing to these merits click chemistry has been demonstrated as a powerful tool for the grafting modification of polymer materials.[23, 24] Our approach in the present work, is to modify polysulfone in different degree of functionalization by using a well-known click reaction, the copper(I)-catalyzed azide-alkyne cycloaddition (CuAAC) between an organic azide and a terminal alkyne.[19-22] Recently Dimitrov et al.[25, 26] grafted phosphonated poly(pentafluorostyrene) (PFS) onto polysulfone backbone via the click

chemistry approach to improve proton conductivity of dense membranes for fuel cell. In their work lithiation chemistry was employed to introduce 3-(chloromethyl)benzoyl pendent groups on polysulfone that was subsequently converted to the clickable 3-(azidomethyl)benzoyl groups. In this chapter we first synthesized a polysulfone-polytriazole random copolymer (PSU-TrN) by modifying the back bone of commercial polysuflone, which was chloromethylated on phenyl rings and finally yielded a stable 1,4-disubstituted 1,2,3-triazole ring having OH substituent through CuAAC. Using the modified polysulfone, we prepared ultrafiltration membranes and studied their morphologies and performance, and the effect of coagulation bath composition.[27]

Beyond its facile and modular synthesis *via* CuAAC to link two functional building blocks together, 1,2,3-triazole is an intriguing nitrogen-rich heterocycle with highly polarized structure offering various supramolecular interactions from hydrogen and halogen bonding to metal complexation.[28-31] Recently, this triazole-containing random copolymer was successfully used to fabricate asymmetric membranes with a large amount of palladium nanoparticles in only the top thin layer through complexation-induced phase separation (CIPS) for membrane catalysis.[32] Another study verified the antibacterial effect of the same palladium nanoparticle-decorated membranes which suppressed the growth of biofilm in the aerobic membrane bioreactor.[33] With the experience of random copolymer, we synthesized polytriazole-*b*-polysulfone-*b*-polytriazole (PTrN-PSU-PTrN) triblock copolymers. The precursor poly(4-vinylbenzyl chloride)-*b*-polysulfone-*b*-poly(4-vinylbenyl chloride) (PVBC-PSU-PVBC) was polymerized from the two ends of the PSU macro-CTA through RAFT technique. The subsequent azidation and click chemistry were performed in the same manner as the

synthesis of PSU-TrN. The final PTrN-PSU-PTrN triblock copolymer contains two outer block with a pendent triazole ring in each repeat unit. As a proof of concept, PTrN-PSU-PTrN and PAA-PSU-PAA were blended in a TrN/carboxylic acid ration of 1:1 in a selective solvent DMF to induce hydrogen bond-mediated self-assembly, leading to the formation of fused micelles with a core-shell structure. A highly porous membrane with highly porous surface morphology was obtained from the blend of PTrN- and PAA-containing copolymers with Cu^{2+} coagulation bath *via* SCNIPS that we proposed in Chapter 3.

4.2 Experimental Section

4.2.1 Materials

Polysulfone (PSU, Sigma Aldrich) was dried overnight at 110 °C in vacuum oven prior to use. Copper (I) bromide (CuBr, 98%, Sigma Aldrich) was purified overnight by reflux in acetic acid (glacial, Fisher Scientific), then filtering and washing solids five times with absolute ethanol (≥99.5%, Sigma Aldrich) and ten times with diethyl ether (≥99.5%, Carl Roth). It was then dried under vacuum to remove any residual solvents.[34] α,ω-dihydroxy-terminated polysulfone (HO-PSU_{14k}-OH) (PDI = 2.1) were synthesized according to the method reported in Chapter 2. Activated aluminum oxide (Al_2O_3, basic, Brockman I, Sigma Aldrich), N,N,N',N",N"-pentamethyldiethylenetriamine (PMDETA, 99%, Sigma Aldrich), tin(IV) chloride ($SnCl_4$, 99%, Sigma Aldrich), chlorotrimethylsilane (≥99%, Sigma Aldrich), paraformaldehyde ($(CH_2O)_n$, 95%, Sigma Aldrich), sodium azide

(NaN_3, ≥99.5%, Sigma Aldrich), propargyl alcohol (99%, Sigma Aldrich), ammonium in solution (volumetric, ~1% NH_3, ~2% Cl^- in H_2O, Sigma Aldrich), chloroform ($CHCl_3$, 99+%, Fisher Scientific), N,N-dimethylformamide (DMF, ≥99.5%, Carl Roth), tetrahydrofuran (THF, ≥99.5%, Carl Roth), methanol (≥ 99%, Fisher Scientific) and N-methylpyrrolidinone (NMP, ≥99.5%, Sigma Aldrich), potassium carbonate (K_2CO_3, ≥99.0%, Sigma-Aldrich), ethylene carbonate (98%, Aldrich), 4-Cyano-4-[(dodecylsulfanylthiocarbonyl)sulfanyl]pentanoic acid (97%, Aldrich), 4-(dimethylamino)pyridine (DMAP, ≥ 99%, Fluka), N,N'-dicyclohexylcarbodiimide (DCC, ≥ 99%, Fluka) and dichloromethane (DCM, ≥ 99.9%, Aldrich) were used as received. 2,2'-Azobis(2-methylpropionitrile) (AIBN, 98%, Aldrich) was recrystallized twice from hot methanol. 4-Vinylbenzyl chloride (VBC, 90%, Aldrich) was purified by passing through a short column of activated basic Al_2O_3 prior to the polymerization.

4.2.2 Synthesis of Triazole-Modified Polysulfone (PSU-TrN)

4.2.2a Chloromethylated Polysulfone (PSU-CH_2Cl)

Chloromethylation was performed following similar procedures reported by Avram and coworkers.[35] PSU (22g, corresponding to 49.71 mmol of repeating unit) was dissolved in 750 mL of $CHCl_3$ (2 wt% PSU) in a 1 L three-necked round bottom flask with a stir bar equipped with a reflux condenser under nitrogen atmosphere for 1h. Paraformaldehyde (15 g, 499.5 mmol) was added to the flask and the solution was mixed while raising the temperature to 52 °C; At 52 °C, chlorotrimethylsilane (63 mL, 497.14 mmol) and $SnCl_4$

(0.22 mL, 1.91 mmol) as catalyst were added. The headspace of the condenser was blanketed with nitrogen and sealed. The reaction was carried out at different times (24, 48, 72 and 84hrs) respectively to give rise to different degree of functionalization. At the end of the experiment, the reaction mixture was filtered. The filtrate was concentrated and precipitated in methanol. The polymer was subsequently dissolved in chloroform and reprecipitated in methanol, then filtered and dried under vacuum overnight at 60 °C yielding white amorphous solid, soluble in common organic solvents. Yield: 20g (91%). They are named with the degree of functionalization as PSU-$CH_2Cl_{0.23}$, PSU-$CH_2Cl_{0.49}$, PSU-$CH_2Cl_{0.56}$ and PSU-$CH_2Cl_{0.94}$. PSU-$CH_2Cl_{0.23}$: ^{1}H NMR (500 MHz, 298K, $CDCl_3$, ppm)δ: 7.89-7.82 (m, 4H, e protons), 7.36 (d, 1H, g proton), 7.24 (d, 2H, b protons), 7.16 (dd, 1H, b' protons), 7.05-6.97 (m, 4H, d protons), 6.94 (m, 2H, a protons) and 6.84 (m, 2H, a' protons), 4.53 (m, 2H, f protons), and 1.7 (m, 6H, c protons). PSU-$CH_2Cl_{0.23}$: ^{13}C NMR (500 MHz, 298K, $CDCl_3$, ppm)δ: 162.21-161.98 (C_{21}), 161.70 (C_{14}), 153.0-152.81 (C_1 and C_{13}), 151.08 (C_{13}), 147.86 (C_7), 146.86 (C_4), 147.28 ($C_{7'}$), 135.96 (C_{17}), 135.53-135.37 (C_{17} and C_{18}), 135.28 ($C_{17'}$), 129.97-129.68 (C_{16} and C_{20}), 129.56 (C_{10}), 129.11(C_{11}), 128.57 (C_3 and C_8), 120.28-119.84 (C_2 and C_9), 118.01-117.63 (C_{15} and C_{19}), 42.63-42.44 (C_5), 41.11 (C_{12}), and 31.13-30.93 (C_6). All the numbering of ^{1}H and ^{13}C for NMR chemical shifts can be found in Figure A4.1, appendices.

4.2.2b Azidomethyl Polysulfone (PSU-CH_2N_3)

Azidation was conducted with sodium azide in DMF.[36, 37] PSU-CH_2Cl (10g, 8.14 mmol chloromethyl group per repeat unit; 72hrs) was dissolved in 200 mL of DMF in a 2-necked round bottom flask. Sodium azide (1.66g, 24.45 mmol) was added to the solution.

The mixture was stirred at 60 °C under nitrogen for 24h. At the end of the experiment, the resulting product was precipitated into a mixture of methanol and water (4:1, v: v) and washed three time with water to remove the excess of sodium azide. After filtration, the obtained polymer (PSU-CH_2N_3) was dissolved in chloroform and reprecipitated in methanol, then filtered and dried under vacuum for 24h at 60 °C. Yield: 9g; (90%). PSU-$CH_2N_{3;0.23}$: ^{1}H NMR (500 MHz, 298K, $CDCl_3$, ppm)δ: 7.90-7.82 (m, 4H, e protons), 7.24 (m, 2H, b protons), 7.20 (m, 1H, b' protons), 7.05-6.97 (m, 4H, d protons), 6.94 (m, 2H, a protons) and 6.88 (m, 2H, a' protons), 4.28 (m, 2H, f' protons), and 1.7 (m, 6H, c protons). PSU-$CH_2N_{3;0.23}$: ^{13}C NMR (500 MHz, 298K, $CDCl_3$, ppm)δ: 162.21-161.98 (C_{21}), 161.70 (C_{14}), 153.0-152.81 (C_1 and C_{13}), 151.08 (C_{13}), 147.86 (C_7), 146.86 (C_4), 147.28 ($C_{7'}$), 135.96 (C_{17}), 135.53-135.37 (C_{17} and C_{18}), 135.28 ($C_{17'}$), 129.97-129.68 (C_{16} and C_{20}), 129.56 (C_{10}), 129.11(C_{11}), 128.57 (C_3 and C_8), 120.28-119.84 (C_2 and C_9), 118.01-117.63 (C_{15} and C_{19}), 49.86 ($C_{12'}$), 42.61-42.45 (C_5) and 31.23-30.55 (C_6).

4.2.2c Triazole-Modified Polysulfone (PSU-TrN)

In order to prepare polysulfone bearing 1,2,3-triazole functions; PSU-CH_2N_3 (7.0 g, 3.52 mmol of azidomethyl group, 1 equivalent; DF = 0.23) was dissolved in DMF (140 mL) in a round bottom schlenk flask sealed with a rubber septum. Next, degassed PMDETA (2.20 mL, 10.56 mmol, 3 equivalents) and propargyl alcohol (0.22 mL, 3.87 mmol, 1.1 equivalents) was added to the flask via syringe under nitrogen. The mixture was degassed by one freeze-pump-thaw cycle. Then CuBr (1.5148g, 10.56 mmol, 3 equivalents) was added quickly in the frozen state. Immediately after that, the flask was subjected to five additional freeze-pump-thaw cycles to remove oxygen. Finally, the flask was placed in a

constant-temperature oil bath at 60 °C and stirred for 24 h. After the reaction was terminated by exposure to air and cooled down to room temperature, the solution was then poured into 3 L of 0.5 % aqueous ammonia solution to remove majority of copper complex. The polymer was solubilized into a large amount of THF and filtered through a column of activated basic Al_2O_3. The filtrate was concentrated under reduced pressure and then, precipitated in an excess of methanol. The purified polymer was dried in vacuum oven at 60 °C for 24 hrs. The same procedure was carried out to synthesize PSU-$TrN_{0.49}$, PSU-$TrN_{0.56}$ and PSU-$TrN_{0.94}$, except that for PSU-$TrN_{0.94}$ the polymer was solubilized in DMF instead of THF in the purification stage. PSU-$TrN_{0.23}$: ^{1}H NMR (500 MHz, 298K, DMSO-d_6, ppm)δ: 7.94-7.79 (m, 4H, e proton), 7.78 (m, 1H, g proton), 7.32 (m, 1H, i proton), 7.29-7.10 (m, 3H, b, b' proton), 7.10-6.81 (m, 8H, d, a, a' proton), 5.45 (m, 2H, h proton), 5.11 (m, 1H, k proton), 4.31 (m, 2H, j proton) and 1.58 (m, 6H, c protons). PSU-$TrN_{0.23}$: ^{13}C NMR (500 MHz, 298K, DMSO-d_6, ppm)δ: 162.21-161.98 (C_{21}), 161.70 (C_{14}), 153.0-152.81 (C_1 and C_{13}), 151.08 (C_{13}), 147.86 (C_7), 146.86 (C_4), 147.28 ($C_{7'}$), 135.96 (C_{17}), 135.53-135.37 (C_{17} and C_{18}), 135.28 ($C_{17'}$), 129.97-129.68 (C_{16} and C_{20}), 129.56 (C_{10}), 129.11(C_{11}), 128.57 (C_3 and C_8), 120.28-119.84 (C_2 and C_9), 118.01-117.63 (C_{15} and C_{19}), 54.91 (C_{25}), 48.24 (C_{22}), 41.93 (C_5) and 30.49 (C_6).

4.2.3 Synthesis of Polytriazole-*b*-Polysulfone-*b*-Polytriazole Triblock Copolymer (PTrN-PSU-PTrN)

4.2.3a Hydroethyl-Terminated Polysulfone (HE-PSU-HE)

α,ω-dihydroxy-terminated polysulfone (HO-PSU_{14k}-OH) were ethoxylated with ethylene carbonate to obtain hydroxyethyl end groups. HO-PSU-OH (5 g, 0.35 mmol), ethylene carbonate (306 mg, 3.5 mmol, 10 equiv), K_2CO_3 (144 mg, 3.5 mmol, 10 equiv) and DMF (20 mL) were added to a round bottom flask. The mixture was purged with nitrogen for 30 min, then heated to 120 °C and kept stirred for 24 h. After the solution was cooled to room temperature, the polymer was precipitated in acidified water with 1 M HCl (aq). The collected crude product was washed with water and methanol, then dissolved in THF and precipitated in methanol again. The solid was filtered and dried at 60 °C overnight under vacuum to obtain hydroethyl-terminated polysulfone (HE-PSU-HE).

4.2.3b RAFT CTA-Terminated Polysulfone (CTA-PSU-CTA)

HE-PSU_{14k}-HE (4.5 g, 0.31 mmol) was dissolved with 40 mL dry dichloromethane in 100 mL three-neck round bottom flask equipped with a magnetic stirrer, a condenser and a gas inlet/outlet. 4-Cyano-4-[(dodecylsulfanylthiocarbonyl)sulfanyl]pentanoic acid (1.25 g, 3.1 mmol) and 4-(dimethylamino)pyridine (38 mg, 0.31 mmol) were added to the flask. The solution was stirred at 0 °C under nitrogen flow for 3 h. Then a solution of N,N'-dicyclohexylcarbodiimide (0.64 g, 3.1 mmol) dispersed in small amount of dichloromethane was added dropwise to the mixture. Subsequently the temperature was allowed to rise to room temperature and the reaction was continued under stirring for three days. The solution was filtered to remove catalyst and concentrated by rotavapor, followed by precipitation into methanol. The crude product was dissolved in dichloromethane again and reprecipitated into methanol (3 times), finally filtrated and dried in vacuum at 60 °C to obtain CTA-terminated polysulfone.

4.2.3c Poly(vinylbenzyl chloride)-*b*-Polysulfone-*b*-Poly(vinylbenzyl chloride) (PVBC-PSU-PVBC)

The RAFT polymerization of PVBC-PSU-PVBC was carried out using CTA-PSU_{14k}-CTA as macro chain transfer agent and 4-vinylbenzyl chloride (VBC) as monomer in bulk at 70 °C, as follows: CTA-PSU-CTA (0.5 g, 0.03 mmol) was first dissolved in VBC (3.7 mL, 26.2 mmol) in 25 ml dry schlenk tube equipped with a magnetic stirrer. Next, AIBN (2.7 mg, 0.016 mmol) were added quickly before the flask was sealed with a rubber septum, and then the reaction mixture was degassed by three freeze-pump-thaw cycles to switch the atmosphere to nitrogen. Finally, the schlenk tube with the reaction mixture was placed in a thermostatic bath at 70 °C for desired polymerization time. After the reaction mixture was stopped by exposure of the solution to air and cooled down to room temperature, it was precipitated into methanol. The precipitate was recovered by filtration, washed with methanol and dried in vacuum. Then the polymer was solubilized with THF and reprecipitated into methnaol. The purification step was repeated three times. After drying under reduced pressure, the triblock copolymer PVBC-PSU-PVBC was obtained as yellow solids.

4.2.3d Poly(vinylbenzyl azide)-*b*-Polysulfone-*b*-Poly(vinylbenzyl azide) (PN_3-PSU-PN_3)

$PVBC_{32k}$-PSU_{14k}-$PVBC_{32k}$ (1.9 g, 10.2 mmmol chloromethyl group) was dissolved in 14 mL of DMF in a round bottom flask. Sodium azide (2g, 30.6 mmol) was added to the solution. The mixture was stirred at room temperature under nitrogen for 24h. At the end of the experiment, the resulting product was precipitated into water and washed three time with fresh water to remove the excess of sodium azide. After filtration, the obtained

polymer ($PN_{3,34k}$-PSU_{14k}-$PN_{3,34k}$) was dissolved in THF and reprecipitated in methanol, then filtered and dried under vacuum for 24 h at 60 °C.

4.2.3e Polytriazole-*b*-Polysulfone-*b*-Polytriazole (PTrN-PSU-PTrN)

$PN_{3,34k}$-PSU_{14k}-$PN_{3,34k}$ (1.5 g, 7.8 mmol of azidomethyl group) was dissolved in DMF (12 mL) in a round bottom schlenk flask sealed with a rubber septum. Next, degassed PMDETA (0.16 mL, 0.78 mmol, 0.1 equiv) and propargyl alcohol (0.55 mL, 9.3 mmol, 1.2 equiv) was added to the flask via syringe under nitrogen. The mixture was degassed by one freeze-pump-thaw cycle. Then CuBr (0.11 g, 0.78 mmol, 0.1 equiv) was added quickly in the frozen state. Immediately after that, the flask was subjected to five additional freeze-pump-thaw cycles to remove oxygen. Finally, the flask was placed in a constant-temperature oil bath at 60 °C and stirred for 24 h. After the reaction was terminated by exposure to air and cooled down to room temperature, the solution was then poured into a mixture of water and methanol (2:1, v/v) containing 0.5 % ammonia to remove copper complex. The polymer was collected, then dissolved in DMF and precipitated in the water/methanol mixture with ammonia again. This step was repeated for several times until no green colour was observed in the polymer. After it was washed with water, the purified $PTrN_{46k}$-PSU_{14k}-$PTrN_{46k}$ was dried in vacuum oven at 60 °C for 24 h as brown solids.

4.2.4 Polymer Characterization

^{1}H and ^{13}C NMR spectra were recorded with a Bruker AVANCE-III spectrometer at a frequency of 500 MHz using a cryo probe at room temperature and deuterated solvents with tetramethylsilane $Si(CH_3)_4$ as an internal standard. The polymer's molar mass and its distribution were determined by tetra detection gel permeation chromatography (GPC) from Viscotek employing a GPCmax module (model VE-2001) and a GPC-TDA 305 system equipped with two columns (LT4000L, Mixed, Low Org. 300×8.0 mm, exclusion limit 400 kDa for polystyrene) eluted at 1.0 mL/min in stabilized THF eluent at 35°C and with four detectors: UV, light scattering (RALS and LALS), refractive index (RI) and viscometer. Absolute molecular weights were determined using polystyrene standards for calibration. Samples were stirred for 12h in stabilized THF and then, passed through a 25 mm × 0.45 μm teflon filter before measurement. Fourier transform infrared-attenuated total reflectance (FTIR-ATR) spectra were recorded at room temperature on a Perkin-Elmer 100 equipped with a universal ATR. Solid membrane was placed over the ATR crystal and maximum pressure was applied using the slip-clutch mechanism. Data were collected over 16 scans with a resolution of 4 cm^{-1}. Elemental analysis was made on a Perkin Elmer 2400 Series II, CHNS/O Analyzer equipped with AD6 Autobalance Controller. Thermogravimetric analysis (TGA) was conducted using a TGA Q50 (TA instruments) with a heating rate of 10 °C.min^{-1} under nitrogen flow from 30 to 800 °C. Differential scanning calorimetry (DSC) was carried out on a Perkin-Elmer DSC 204 F1 NETZSCH under nitrogen flow. The heating rate was 10 °C.min^{-1} and the cooling rate was 5 °C.min^{-1} in the range of temperature from -50 to 220 °C. The samples were placed in aluminium pans and heated from -50 to 220 °C under a nitrogen flow rate. The glass transition temperature (T_g) of each sample was taken from the second heating scan.

4.2.5 Membrane Fabrication

4.2.5a Preparation of PSU-TrN Membranes

All the PSU-TrN membranes in this work were prepared via a typical non-solvent induced phase separation (NIPS) method.[38, 39] The casting solution from 18 wt% Polymer-NMP was stirred for 12 h to obtain a homogeneous solution. The solution was sonicated for 15 minutes and kept still for 12 h to release bubbles. The viscous solution was cast onto a clean glass plate with a 200 μm high casting knife. The plate was then immersed quickly and smoothly into the coagulation bath with varying water/solvent ratio by weight at room temperature. After a period of time (3-5 min.) in the primary coagulation bath, the plate was removed and the membrane was placed in a deionised water bath for exhaustive extraction of solvent during 12 h before the experiment. The resulting opaque porous films had an average thickness of 100 μm.

4.2.5b Preparation of PTrN-PSU-TrN/PAA-PSU-PAA Membranes through SCINPS

The casting solution from 18 wt % $PTrN_{46k}$-PSU_{14k}-$PTrN_{46k}$/PAA_{17k}-PSU_{14k}-PAA_{17k} blend with a mass ration of 2.43:1 (equal number of PTrN and PAA repeat unit) in DMF was stirred for 12 h to obtain a homogeneous solution and kept still for another 12 h to release bubbles. This viscous solution was cast onto a polyester nonwoven support by a doctor blade with 250 μm gate height. The membrane was then immersed quickly and smoothly into the coagulation bath of 0.1 M $CuSO_4$ solution at room temperature and kept overnight for exhaustive extraction of solvent. Then it was transferred to a water

bath and to remove excess metallic salt solution for 30 min. Fresh water in the bath was changed for several times.

4.2.6 Membrane Characterization

Contact angle measurement was performed on a Krüss Easydrop equipment in static mode at ambient temperature. Membranes formed in pure water coagulation bath were used to investigate the hydrophilicity of corresponding polymers. Each contact angle was reported as the average from three measurements.

The surface and cross section morphology of the membranes were observed by field emission scanning electron microscopy (FE-SEM) in a FEI Quanta 200 FEG SEM. For surface imaging, a small piece of membrane sample was mounted on a flat aluminium stub, fixed by aluminium conductive tapes. For cross section, the membrane sample was freeze-fractured in liquid nitrogen, and mounted on a 90° aluminium stub vertically with double-coated carbon tapes. The samples were sputter-coated with Au/Pd for 20s at 20mA to prevent electron charging using a K575X Emitech equipment. All the images were taken using a secondary electrons detector, at 5 kV, 16 pA and working distance of 5 mm. Images were obtained at different magnifications. Each sample was imaged at more than five locations to ensure the reproducibility of the features observed.

Capillary flow porometry was measured in POROLUX™ 1000 porometer to obtain the pore size distribution of membranes. Porefill (16 mN/m) was used as the wetting liquid, which was displaced by nitrogen gas flow with the pressure up to 34.5 bar.

Transmission electron microscopy (TEM) images of the micelles in the diluted casting solution were acquired using FEI Tecnai 12 microscope with an accelerating voltage of 120 kV. The sample was prepared by dissolving the copolymer in a solvent or mixture with a polymer concentration of 0.1 wt% followed by stirring overnight. A drop of the solution (1.5 μL) was placed onto a carbon-coated copper grid while the solvent was removed by blotting with a filter paper placed under the grid. The grid was further dried at room temperature before imaging.

Dynamic Light Scattering (DLS) measurements were performed using Malvern Zetasizer Nano ZS to analyze the micellar size distribution of the copolymer in a diluted casting solution (0.1 wt%) followed by stirring overnight. The solution was filtered through a 0.45 μm PTFE syringe filter before loading into a glass cuvette with square aperture. Three measurements were done for each sample with 16 runs per measurement.

4.2.7 Ultrafiltration Experiments

Ultrafiltration experiments were conducted using a dead-end magnetically stirred Amicon cell with an effective membrane area of 4.1 cm^2 to evaluate the membranes performance. The membrane was pre-compacted by deionized water for one hour at operation pressure of 2 bars and the stable pure water permeance was recorded denoted as J_{w1}. The permeance was calculated by using the following equation,

$$J = \frac{V}{tS\Delta P}$$

Equation 4.1

where V and t are the volume of the permeate and the time to collect it, respectively; S is the effective membrane area; ΔP is the transmembrane pressure. Afterwards, the feed solution was replaced by 1 mg/mL of bovine serum albumin solution to conduct protein filtration test for one hour. The permeance of protein filtration was measured as J_p. The γ-Globulin rejection ratio R was calculated according to the equation below,

$$R = \left(1 - \frac{C_p}{C_b}\right) \times 100\%$$

Equation 4.2

where C_p and C_b are the bovine serum albumin concentrations of the permeate solution and bulk solution in the feed side, respectively. The concentration was determined by a UV-Vis spectrophotometer (Shimadzu, UV 2550) at 278 nm. Then the membrane was vigorously flushed by deionized water for 10 min. Subsequently, pure water permeance of the cleaned membrane was measured again as J_{w2} in the same manner.

4.3 Results and Discussion

4.3.1 Functionalization of Polysulfone with Triazole

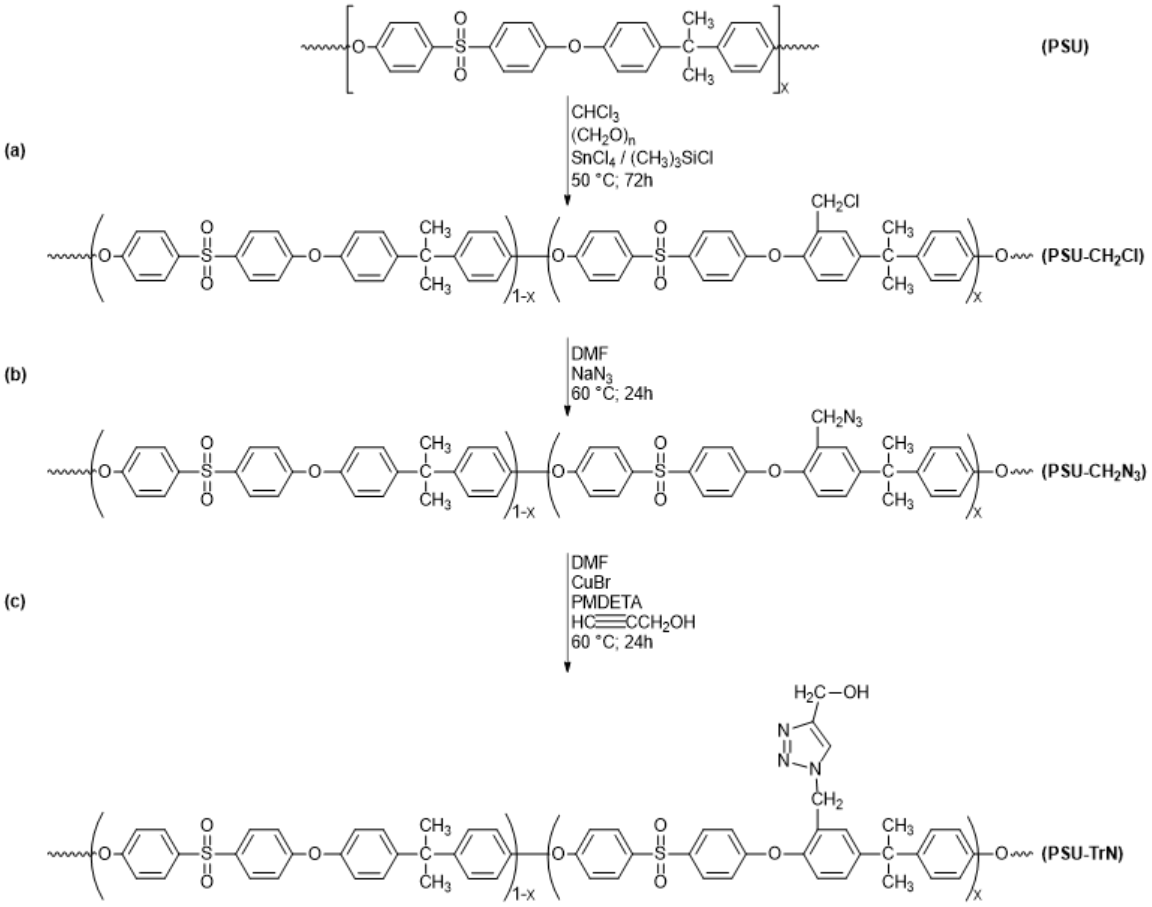

Scheme 4.1. Synthetic route of (a) chloromethylated polysulfone (PSU-CH_2Cl), (b) azidomethylated polysulfone (PSU-CH_2N_3) and (c) polysulfone random copolymer bearing 1,2,3-triazole groups by click reaction (PSU-PTrN).

As depicted in Scheme 4.1, the first step of the modification was the chloromethylation of polysulfone polymer (Scheme 4.1a), following a procedure analogous to that described by Avram et al.[35] The precursor chloromethylating reagent was formed in chloroform from paraformaldehyde, chlorotrimethylsilane, and $SnCl_4$ as a catalyst. The overall molar ratio of polymer to reagents was 1:10:10 and with polysulfone concentration in $CHC1_3$ of 2%. The reaction proceeded at 50 °C until the desired degree of functionalization (DF) was achieved. Four polymers (PSU-CH_2Cl_i, with i = DF) were synthesized at different experiment times such as 24, 48, 72 and 84 hours leading to DF of 23, 49, 56 and 94 mol

% respectively. The yields of the corresponding random copolymers were up to 92 wt.%. It is important to note that the soluble chloromethylated polysulfones can be obtained only when the chloromethylation is performed at the high dilution and low catalyst amounts. The increase of the reaction time or reagent concentration degrades the polymer. The chloromethyl side groups of PSU-CH_2Cl were reacted with sodium azide in DMF at 60 °C. Thus, PSU was quantitatively converted into a backbone carrying "clickable" azide side groups, PSU-CH_2N_3[36, 37] (Scheme 4.1b).

Finally, the click chemistry reaction was performed by using PSU-CH_2N_3 and propargyl

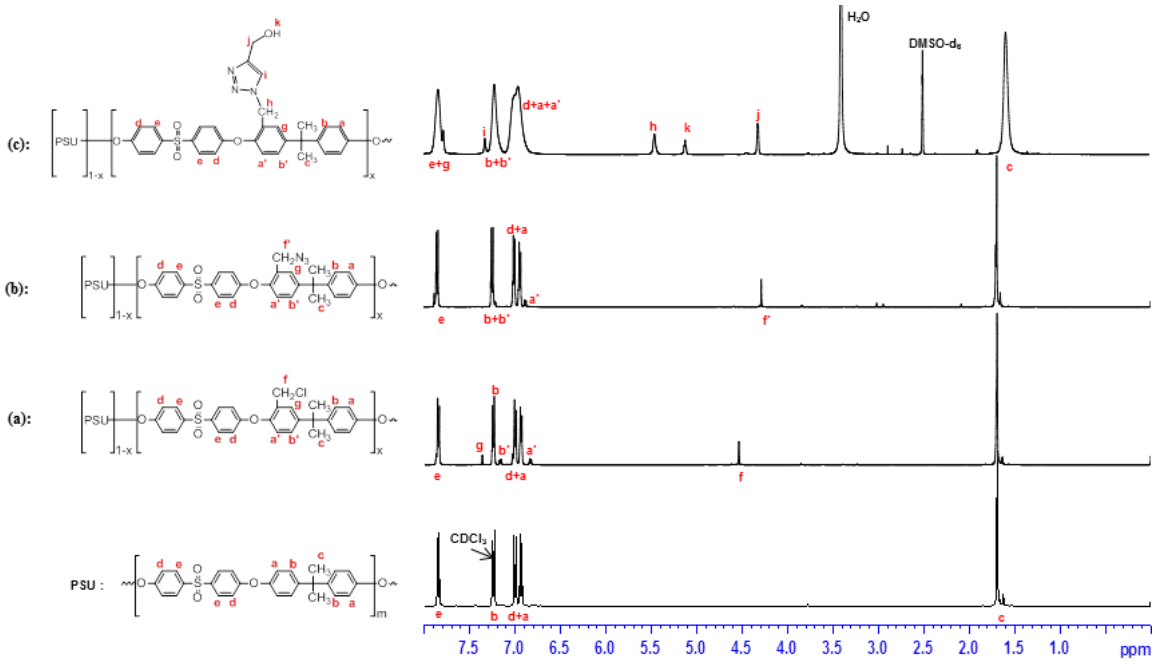

Figure 4.1. ^{1}H NMR for PSU, PSU-$CH_2Cl_{0.23}$, PSU-$CH_2N_{3;0.23}$ recorded in $CDCl_3$ and PSU-$TrN_{0.23}$ recorded in DMSO.

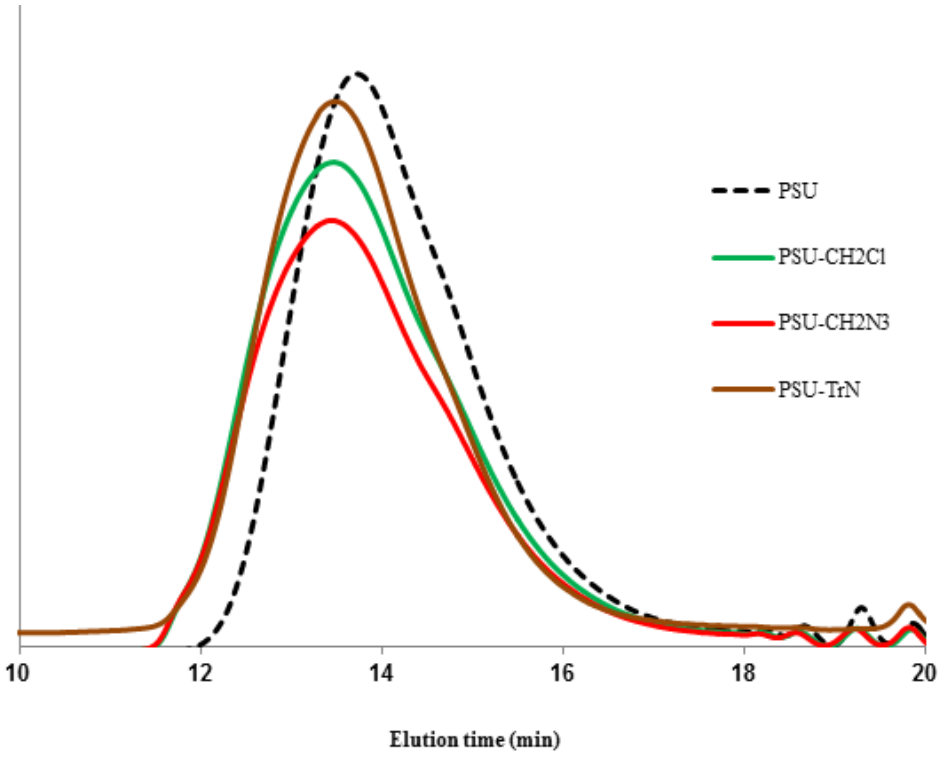

Figure 4.2. GPC curves for PSU, PSU-$CH_2Cl_{0.56}$, PSU-$CH_2N_{3;0.56}$ and PSU-$TrN_{0.56}$ in THF.

alcohol to obtain good yield of modified polysulfone bearing 1,2,3-triazole groups (PSU-TrN) (Scheme 4.1c).[3, 36, 37] In each step of synthesis the resulting polymer was recovered with more than 90 % yield. All these steps were characterized by NMR (^1H and ^{13}C) spectroscopy to confirm the polymer structure. Typical ^1H NMR spectra are given in Figure 4.1 for unmodified PSU, PSU-$CH_2Cl_{0.23}$, PSU-$CH_2N_{3;0.23}$ and PSU-$TrN_{0.23}$ obtained after a reaction time of 24hrs during chloromethylation step. As seen in the spectra, the chemical shifts at δ = 6.80-7.95 ppm are assigned to the protons of phenyl rings of the PSU backbone. For the resonance at δ = 4.53 ppm (Figure 4.1a), it can be assigned to the methylene protons of the repeating unit of PSU-CH_2Cl (i.e., -CH_2-Cl). Subsequently, after the substitution reaction, the resonance for the CH_2Cl protons at 4.53

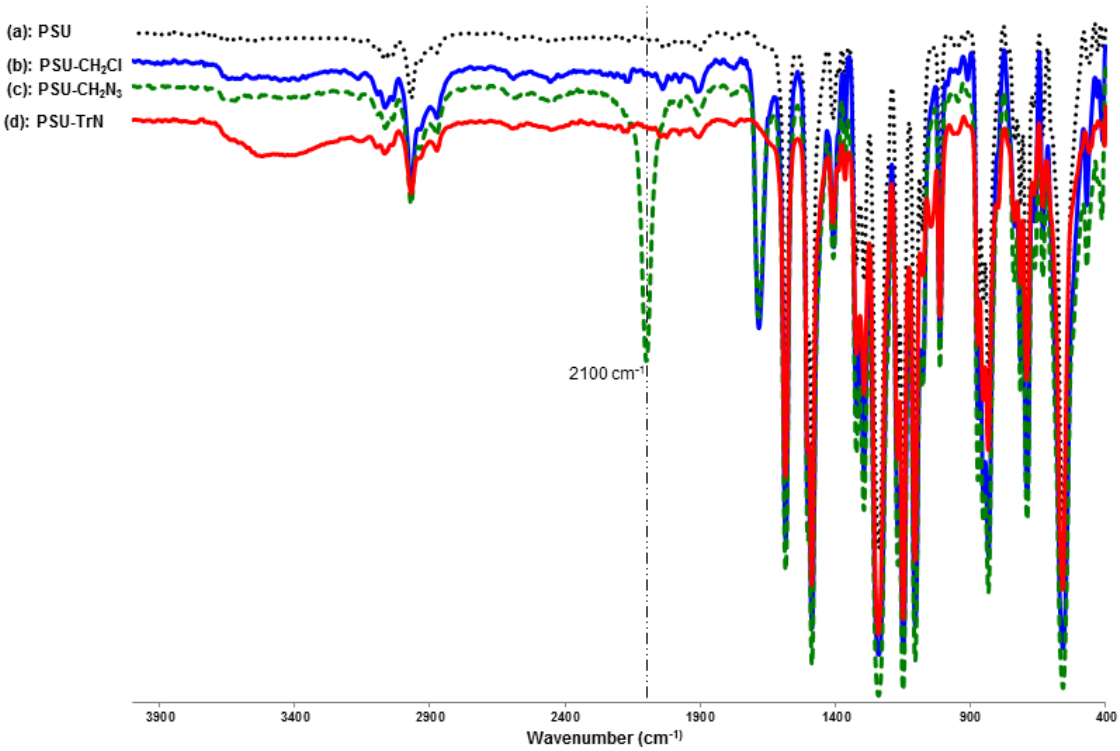

Figure 4.3. FTIR spectra for (a) unmodified PSU, (b) PSU-$CH_2Cl_{0.94}$, (c) PSU-$CH_2N_{3;\ 0.94}$ and (d) PSU-$TrN_{0.94}$.

ppm completely disappeared in the NMR spectrum of the product whereas a new resonance at 4.28 ppm (Figure 4.1b) with the same intensity corresponding to the methylene protons of the repeating unit of PSU-CH_2N_3 (i.e., -CH_2N_3) appeared. Furthermore, not only there was no apparent change in the polydispersity of the PSU-CH_2N_3 compared to the precursor PSU-CH_2Cl according to SEC analysis (Figure 4.2; i.e., DF = 0.56), but PSU-CH_2N_3 displayed the characteristic stretching band of $–N_3$ which appeared at 2100 cm^{-1} in the FTIR spectrum (Figure 4.3c). The “click” chemistry approach was performed in the presence of CuBr/PMDETA in DMF at 60 °C and was also shown to proceed in quantitative yields as the absorption band of azide at 2100 cm^{-1} disappeared in the FTIR spectrum (Figure 4.3d), suggesting complete functionalization. A

Table 4.1. Characteristics of the modified polymers

	DF[a]	DF[b]	M_n (g/mol)[c]	PDI
PSU-$CH_2Cl_{0.23}$	0.23	--	39300	1.9
PSU-$CH_2Cl_{0.49}$	0.49	--	44900	2.0
PSU-$CH_2Cl_{0.56}$	0.56	--	44300	2.2
PSU-$CH_2Cl_{0.94}$	0.94	--	58700	3.8
PSU-$N_{3,0.23}$	0.26	0.25	39500	1.9
PSU-$N_{3,0.49}$	0.49	0.44	42800	2.2
PSU-$N_{3,0.56}$	0.56	0.55	43100	2.3
PSU-$N_{3,0.94}$	0.06	0.92	60800	3.7

[a] Degree of Functionalization per repeating unit determined by 1H NMR; [b] Degree of Functionalization determined from elemental composition of Nitrogen; [c] Determined by GPC with PS standards.

new and broad band at 3150-3770 cm^{-1} also appeared due to the stretching vibration of O–H groups[40] linked to the triazole ring. Moreover, a resonance at 5.45 ppm corresponding to the methylene protons linking the phenyl ring and the triazole ring in the side chains was clearly visible in the NMR spectrum of the product (Figure 4.1c). In addition, we can also observe the emergence of three new peaks: A resonance at 5.11 ppm assigned to the proton of the hydroxyl group, a resonance at 4.31 ppm assigned to the methylene protons located in the alpha position of the hydroxyl group and the resonance at 7.32 ppm assigned to the proton of the triazole ring.

^{1}H NMR and elemental analysis (Table 4.1) easily quantitates the DF of the product

materials for PSU-CH_2Cl and PSU-CH_2N_3. From elemental analysis, the DF was determined from the nitrogen content of PSU-CH_2N_3, and varies with different chloromethylation time from 24 to 84hrs. On the other hand from ^1H NMR, DF can be estimated from the integration ratio of the -CH_2 protons from the chloromethyl protons of the side groups at $\delta = 4.53$ to the integrals of the signals at 7.95-7.80 ppm of the four meta protons (e protons, Figure 4.1) of the phenyl ring adjacent to the sulfonyl group. The molecular weights of the obtained polymers are listed in Table 4.1. In principle, there

should be no large deviation of the M_n of these polymers since only small units (-Cl, -N_3 and triazole) were attached to the same backbone. For polymers with the highest degree of functionalization, exceptionally high values for M_n and PDI were detected. We believe that the anomalous value for PSU-$CH_2Cl_{0.94}$ and PSU-$N_{3;0.94}$ could be attributed to the formation of intermolecular methylene bridges during the chloromethylation,[3] under the high degree of functionalization (94 %). From Figure 4.3, the absorption bands at 1293, 1150 and 1082 cm^{-1} are assigned to the symmetric and asymmetric stretching

Table 4.2. Thermal properties of polymers

Sample	T_g (°C)	$T_{d,5\%}$ (°C)	$T_{d,10\%}$ (°C)
PSU	190	460	467
PSU-CH2Cl0.23	192	399	442
PSU-CH2Cl0.49	184	333	397
PSU-CH2Cl0.56	193	325	392
PSU-CH2Cl0.94	179	320	392
PSU-CH2N3; 0.23	199	401	426
PSU-CH2N3; 0.49	208	366	403
PSU-CH2N3; 0.56	210	363	405
PSU-CH2N3; 0.94	203	305	380
PSU-TrN0.23	183	376	418
PSU-TrN0.49	179	330	380
PSU-TrN0.56	178	342	376
PSU-TrN0.94	170	387	420

vibrations of –S=O present in backbone of polymer chains.[40, 41] The absorption bands at 2966 and 2924 cm^{-1} are attributed to the aromatic and aliphatic stretching vibrations of $–CH_2$ groups. The peaks at 1579 and 1483 cm^{-1} are assigned to the stretching vibration of aromatic hydrocarbons. The absorption band at 1232 cm^{-1} is ascribed to asymmetric vibration of the ether linkage.

The thermal properties of the functionalized copolymers as well as those of the precursor PSU were evaluated by their thermal decomposition and glass transition data as listed in Table 4.2. Figure 4.4 shows the TGA curves of the precursor and modified PSU wherein a three-step weight loss was observed in all the modified polymers. The first and lower loss appeared in the range of 250 to 366 °C, 175 to 275 °C and 241 to 416 °C respectively for PSU-CH_2Cl, PSU-CH_2N_3 and PSU-TrN, was presumably due to the elimination of the functional unit. The main decomposition occurs in the second or third steps[42] and was related to the degradation of the polymer backbone. At $T_{d5\%}$, the chemical modification reaction and subsequent substitution reaction of chlorine with azide and 1,2,3-triazole derivatives led to a significant decrease of the thermal stability of

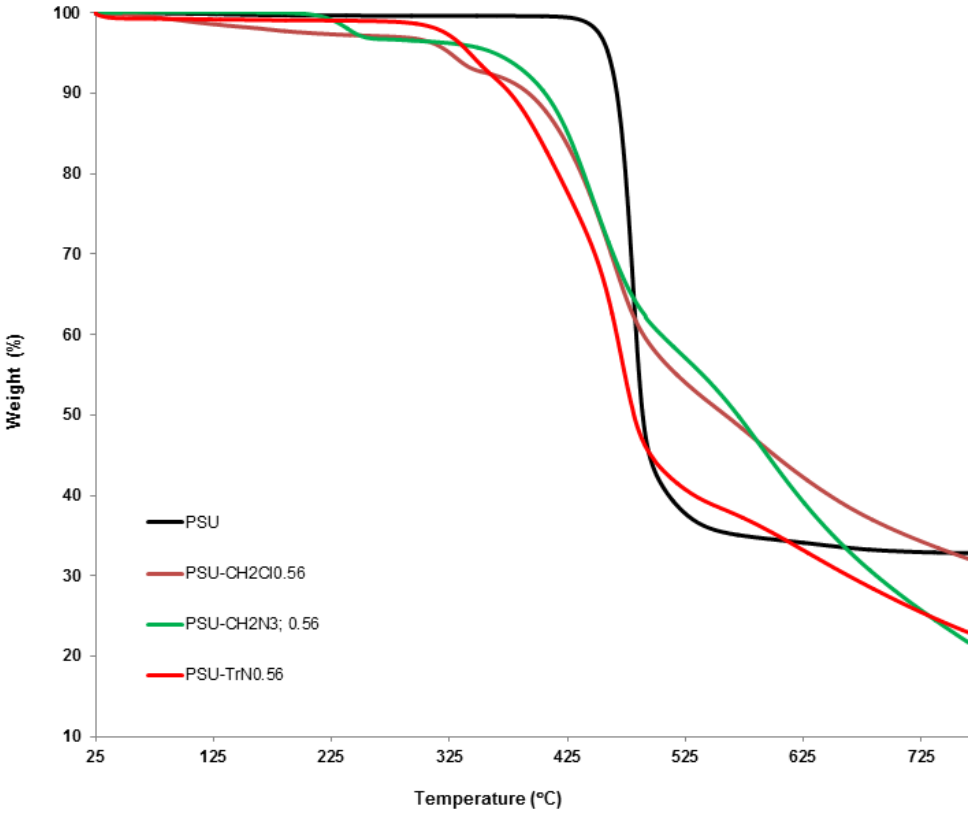

Figure 4.4. TGA curves for PSU, PSU-$CH_2Cl_{0.56}$, PSU$CH_2N_{3;\ 0.56}$ and PSU- $TrN_{0.56}$.

PSU.[42] It is also observed that the thermal stability of chloromethylated and azido polymers decreases with the increase of the DF.

As expected from the DSC measurements, we observed for the triazole functionalized polymers that the increase of the degree of functionalization led to a decrease of T_g. The T_g of the PSU (190 °C) decreased gradually to 183 °C for PSU-$TrN_{0.23}$ and 170 °C for PSU-$TrN_{0.94}$ (Table 4.2, Figure 4.5). The triazole-OH side groups might act as spacers, creating more space between the polysulfone chains. This disfavors the strong interaction between polar SO_2 groups from different chains, as observed before by Gaina et al.[37] for chloromethylated polysulfones. Furthermore the functionalization is random, affecting

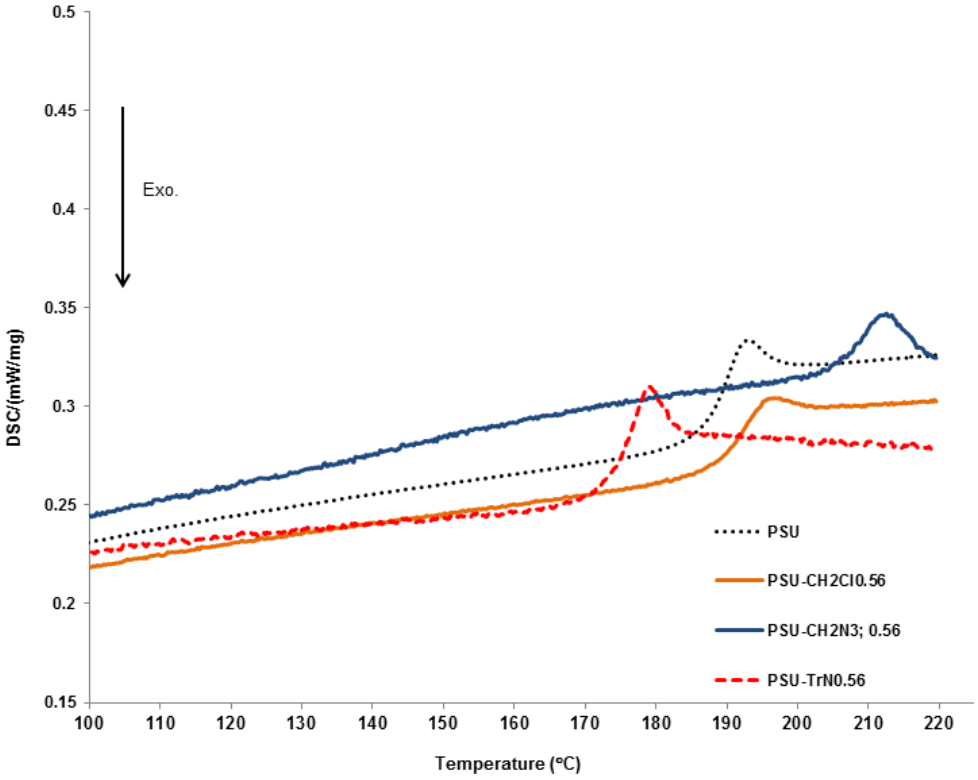

Figure 4.5. DSC curves for for PSU, PSU-$CH_2Cl_{0.56}$, PSU$CH_2N_{3;\ 0.56}$ and PSU-$TrN_{0.56}$.

the regularity of the repeating units and again disturbing, intermolecular packing. As a result the functionalization decreases T_g.

4.3.2 Hydrophilicity and Morphology of PSU-TrN Membranes

All the polymers were readily soluble in polar aprotic solvents such as DMSO, DMF, DMAc, and NMP. The membranes in this work were all fabricated by solution casting and phase inversion method.[38, 39] All membranes were very robust, easy to handle and had good film forming properties. The compositions of the casting solution and coagulation bath were shown in Table 4.3.

Table 4.3. Permeability and contact angle of membranes prepared from 18 wt % polymer casting solutions in NMP, with different coagulation baths

Polymer	Coagulation bath (v/v%)	Contact angle (°)	Permeability (L m^{-2} h^{-1} bar^{-1})
PSU	100 H_2O	80.7 ± 2.5	7.6 ± 3.9
	40 H_2O, 60 NMP	--	0
PSU-$TrN_{0.23}$	100 H_2O	77.0 ± 0.2	18.6 ± 3.0
	40 H_2O, 60 NMP	--	5.4 ± 3.4
PSU- $TrN_{0.49}$	100 H_2O	74.5 ± 1.3	55.4 ± 18.6
	40 H_2O, 60 NMP	--	52.3 ± 1.2
PSU-$TrN_{0.56}$	100 H_2O	71.2 ± 1.5	121.6 ± 66.4
	40 H_2O, 60 NMP	--	46.8 ± 3.9
PSU-$TrN_{0.94}$	100 H_2O	70.0 ± 2.0	187.0 ± 56.5
	40 H_2O, 60 NMP	--	72.0 ± 28.8

Membranes' hydrophilicity was evaluated with contact angle measurements using deionized water on all membranes. The observed contact angles are presented in Table 4.3. As expected, the contact angle of the plain PSU membrane was high (81°), confirming the hydrophobic nature. The contact angle monotonously decreased with increase of the degree of functionalization of the membrane, indicating that the functionalization effectively increased the hydrophilicity of PSU membranes. The lowest contact angle (70°) was obtained for membrane cast from PSU-$TrN_{0.94}$. This is due to the attachment of hydrophilic group (1,2,3-triazol-4-CH_2OH) on the PSU backbone and

responsible for the formation of tight hydration layer on the membrane surface through hydrogen bonding with water molecules.

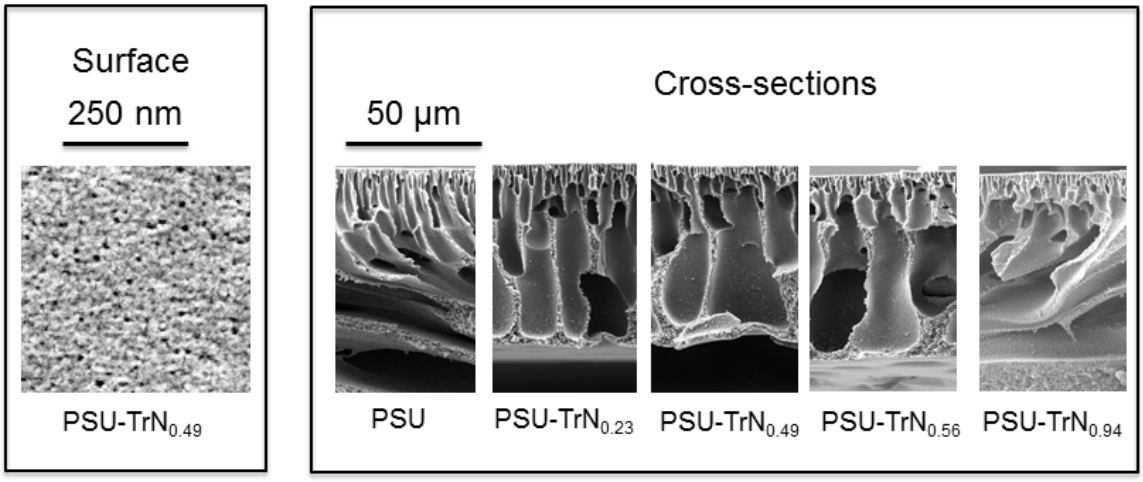

Figure 4.6. Morphology of surfaces and cross sections of membranes prepared by phase inversion in water.

The membrane surface and the cross-section FESEM images are shown in Figure 4.6 and 4.7. A surface image for a membrane prepared from PSU-$TrN_{0.49}$ membrane is shown in Figure 4.6. Similar morphology was observed for the surface of other membranes prepared with different degrees of functionalization are similar, indicating similar pore size and pore density. As confirmed by the cross-section images, all membranes obtained by coagulation in water bath exhibited a typical asymmetric structure with finger-like macrovoids.[43] The formation of the large macrovoids is due to fast exchange rate between solvent and non-solvent during the membrane preparation.[43, 44] Figure 4.7 shows that when solvent (NMP) is added to the coagulation bath the surface porous structure changes. The surface porosity decreases and pores are more heterogeneous as macropores are formed among the smaller pores. Although finger-like cavities are still present in membranes coagulated in a mixture of water and NMP, a sponge-like structure co-occurs and predominates for polymers with higher degree of functionalization. The use of

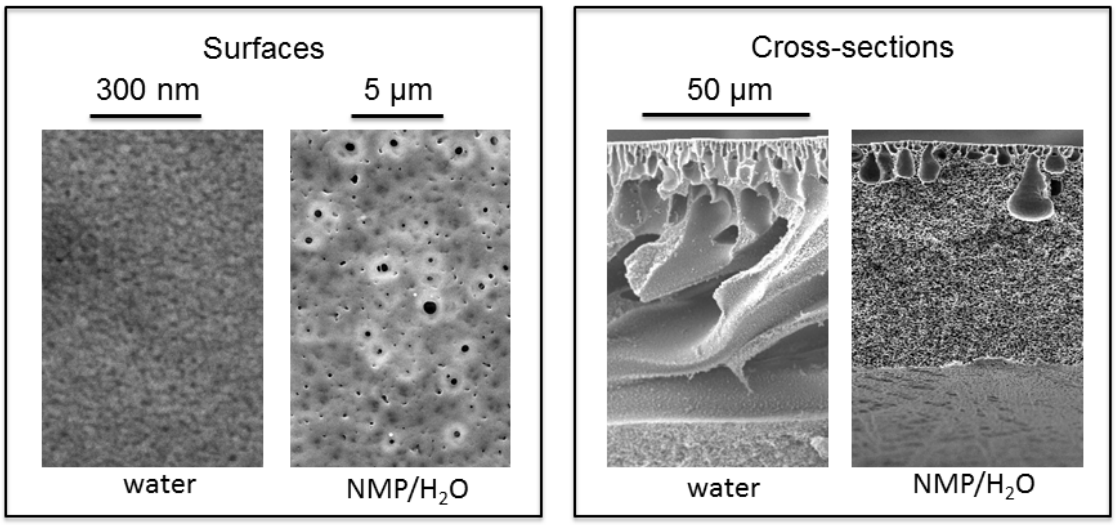

Figure 4.7. Morphology of surfaces and cross sections of membranes prepared from PSU-$TrN_{0.94}$ in water and NMP/H_2O (60/40).

NMP/H_2O (60/40) in coagulation bath slows the phase inversion kinetics. The driving force for solvent–non solvent exchange between polymer solution and NMP/H_2O non-solvent bath is smaller (smaller osmotic pressure), the top skin is slowly formed as well as the sub layer leading to the more homogeneous sponge structure. When the coagulation bath has only water, the membrane skin is formed fast, while still a large amount of solvent is still present in the sub-layer. The driving force for solvent-nonsolvent exchange is large. Water penetrates the polymer solution layer preferentially in weaker points (interfacial tension inhomogeneities) of the incipient skin and finger like cavities are formed. When very hydrophobic polymers are used for the “phase inversion” membrane manufacture, the penetration of small amount of water is enough to induce immediate polymer coagulation. A thin and dense skin is formed along the path of water penetration resulting in the finger-like cavities of most hydrophobic membranes in Figure 4.6. For hydrophilic polymers the homogeneous part of the water-NMP-polymer phase

diagram is expected to be larger. Even with larger amount of water, the solution might not phase-separate, since the hydrophilic OH groups improves the thermodynamic interaction between polymer and water-solvent mixture. Phase separation will start only, when water-solvent exchange proceeds to a larger extent than in the case of unmodified PSU. Water-solvent exchange also leads to gelation. The morphology induced by phase separation will evolve until gelation reduces the mobility of the polymer-rich phase enough to "freeze" the system. The sizes of pores and the porous structure depend on how far the starting condition for phase separation is from gelation. This explains the differences in morphology observed for different degrees of functionalization.

4.3.3 Ultrafiltration Performance and Anti-Fouling Property of PSU-TrN Membranes

Water fluxes were measured and the results are depicted in Figure 4.8 and Table 4.3. The water flux values increased proportionally to the increase of the degree of functionalization: 8, 55, 122 and 187 L m^{-2} h^{-1} bar^{-1} respectively for degrees of functionalization 23, 49, 56 and 94 mol%. These results can also be associated with the increase of the hydrophilicity (contact angle) observed in Table 4.3. The improved hydrophilicity enhances the water permeability by facilitating wetting and transport through the membrane. Moreover, the pores size and their interconnectivity at least as relevant for the membrane permeability as the hydrophilicity, as well as the thickness of the most selective layer or top region with smallest pores, contributing most to the flux resistance.

The pores imaged on the membranes surfaces do not change much, although the most

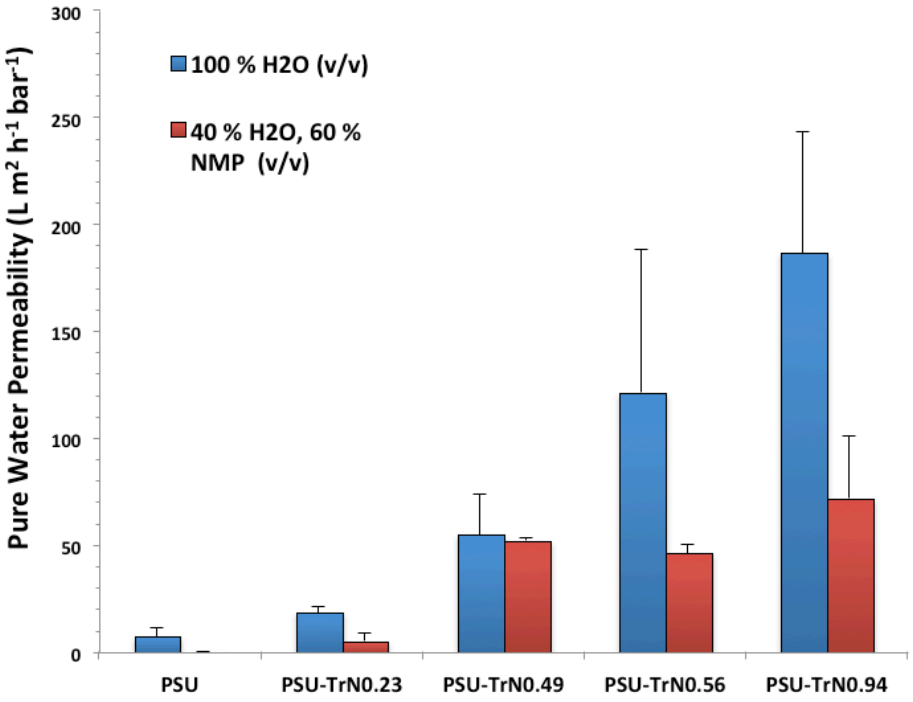

Figure 4.8. Pure water permeability of the fabricated membranes from different polymers and coagulation baths.

hydrophilic membranes coagulated in NMP/H_2O seem to be larger. For the same polymer, the pure water permeability of membranes prepared in NMP/H_2O coagulation bath is lower than that of membranes prepared in water. It is proposed that the sponge like structures obtained in NMP/H_2O probably contains closed cells, which are not accessible for water transport in the final membrane. The lack of interconnectivity is indicated by the pore size distribution obtained from a gas-liquid displacement capillary flow porometer. As shown in Figure A4.2 (appendices), the diameter of most of the pores inside the membranes is measured to be around 100 nm. This value is far smaller than the pore size observed from SEM images of membrane surfaces. The absence of large surface pores in the porometry suggests that these pores are either “dead”, completely closed by the cells that are not interconnected, or limited by the smaller openings

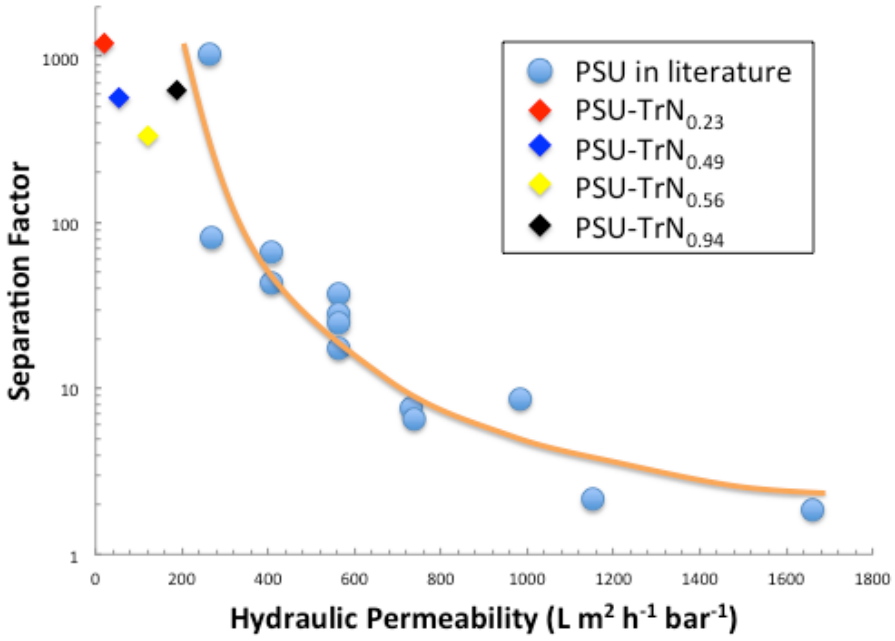

Figure 4.9. Separation factor-permeability trade-off curve for ultrafiltration polysulfone membranes using BSA. Light blue points reproduced from Mehta and Zydney in reference 45.

between the cells in the sponge-like sub-layer. Thus they are unable to contribute to the water permeation.

The membranes' selectivity for bovine albumin, which has a molecular weight of 69 kg /mol was evaluated. The retention is higher than 99% for all membranes. If permeability and separation factors are plotted for the different membranes together with values for other polysulfone membranes reported in the literature, similar to the plot published by Mehta and Zydney,[45] as shown in Figure 4.9. Our membranes are characterized by very high separation factors, compared to other available membranes. The most hydrophilic membranes are on the front limit of the trend curve, while the hydrophobic membranes are far from the curve. The literature values depicted in Figure 4.9 include polysulfone and the more hydrophilic polyethersulfone membranes, without distinguishing them, also

without specifying molecular weight, membrane preparation conditions and presence of additives. The plot however gives us a rough indication on how the characteristics of the new developed membranes are, when compared to previously reported values. Hydrophilic additives like poly(vinyl pyrrolidone) are frequently added to casting solutions to make membranes more hydrophilic. However hydrophilic additives are frequently soluble and washed out during long time operation. Incorporation of hydrophilic groups by click chemistry is much better controlled and stable alternative.

In long filtration experiments with albumin solutions, fouling becomes evident. This is a common effect in ultrafiltration membranes. Apart from numerous attempts and strategies to minimize fouling, it can hardly be completely avoided. Important is how much the water flux can be recovered after simple washing procedure or how reversible fouling is. To evaluate the anti-fouling properties of our developed membranes, a three-step filtration protocol adopted by many studies[18, 46, 47] was employed. It included pure water permeation of pristine membranes, BSA solution filtration, and pure water permeation of cleaned membranes. Resistance-in-series model[48] was used to describe the fouling mechanism and compare the membrane performance. According to this model, the fouling layer formed by protein adsorption during the filtration introduces additional hydraulic resistances on the feed side to the transport across the membrane, leading to flux decline. The hydraulic resistances caused by BSA fouling are determined by the following equations:

$$J_{w1} = \frac{\Delta P}{\eta_w R_m}$$

Equation 4.3

$$J_p = \frac{\Delta P}{\eta_w (R_m + R_r + R_{ir})}$$

Equation 4.4

$$J_{w2} = \frac{\Delta P}{\eta_w (R_m + R_{ir})}$$

Equation 4.5

where η_w is the viscosity of the permeate , which is 1.002×10^{-3} Pa S for water at 20 °C; R_m, R_r and R_{ir} denote the clean membrane hydraulic resistance, reversible fouling layer resistance and irreversible fouling layer resistance, respectively. R_r and R_{ir} contribute to

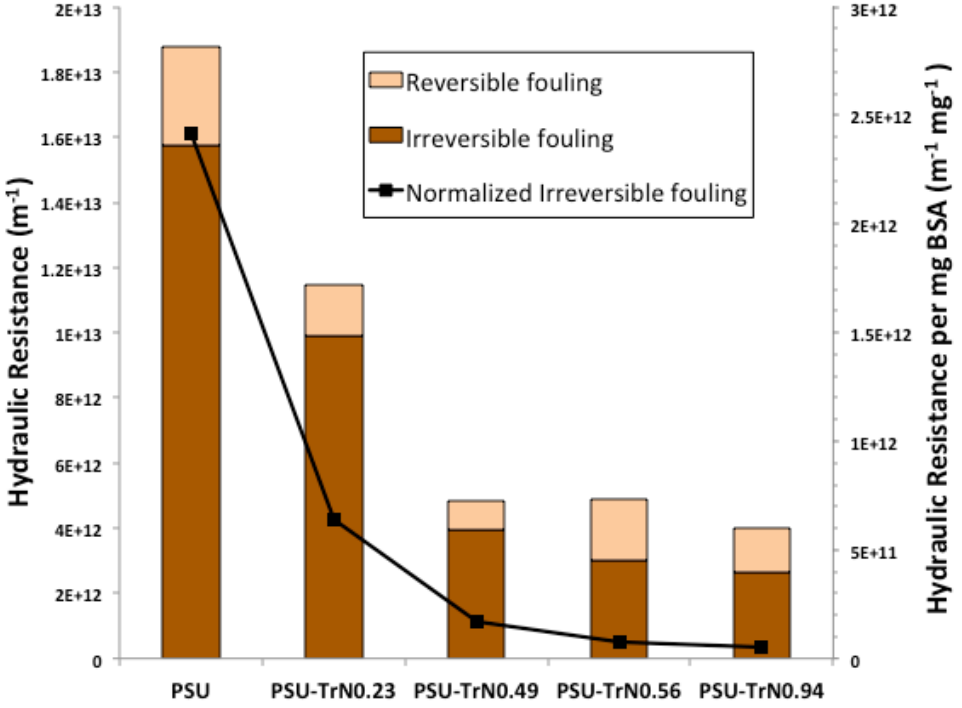

Figure 4.10. Reversible and irreversible fouling of the fabricated membranes from BSA filtration.

the total fouling resistance during the protein filtration. The value of R_r reflects the fouling caused by protein deposit on the membrane surface with a weak interaction, while R_{ir} shows the degree of fouling from permanent attachment of protein to the membrane, which cannot be removed by hydraulic cleaning process. Figure 4.10 shows that the total fouling and especially irreversible fouling of membranes were clearly reduced with increased degree of functionalization. It means membranes with higher degree of functionalization are less prone to fouling and the fouling is more reversible, which enables higher extent of flux recovery. Furthermore if we take the amount of separated albumin protein into account, the normalized irreversible fouling resistance of unit BSA exhibits a stronger descending trend since the filtrate flux is increased with degree of functionalization. The improved anti-fouling property of polysulfone membranes is attributed to the grafting of hydrophilic side-group to the polymer backbone, which forms a hydration layer to minimize the affinity of protein molecules to the surface.

4.3.4 Synthesis of Polytriazole-*b*-Polysulfone-*b*-Polytriazole (PTrN-PSU-PTrN)

Scheme 4.2 depicts synthesis route of polytriazole-*b*-polysulfone-*b*-polytriazole (PTrN-PSU-PTrN) triblock copolymer with multiple steps. It requires the preparation of a precursor poly(4-vinylbenzyl chloride)-*b*-polysulfone-*b*-poly(4-vinylbenzyl chloride) (PVBC-PSU-PVBC), followed by azidation and click reaction in almost identical conditions for the random polytriazole copolymer. 4-Vinyl benzyl chloride (VBC) is a monomer that can readily undergo various post-polymerization functionalization through the pendant chloride group.[49] Successful RAFT polymerization of VBC, using

trithiocarbonate chain transfer agent (CTA), has been previously reported.[49-52] Herein, we

attempted to polymerize VBC with the PSU macro-CTA that we used for P*t*BA-PSU-

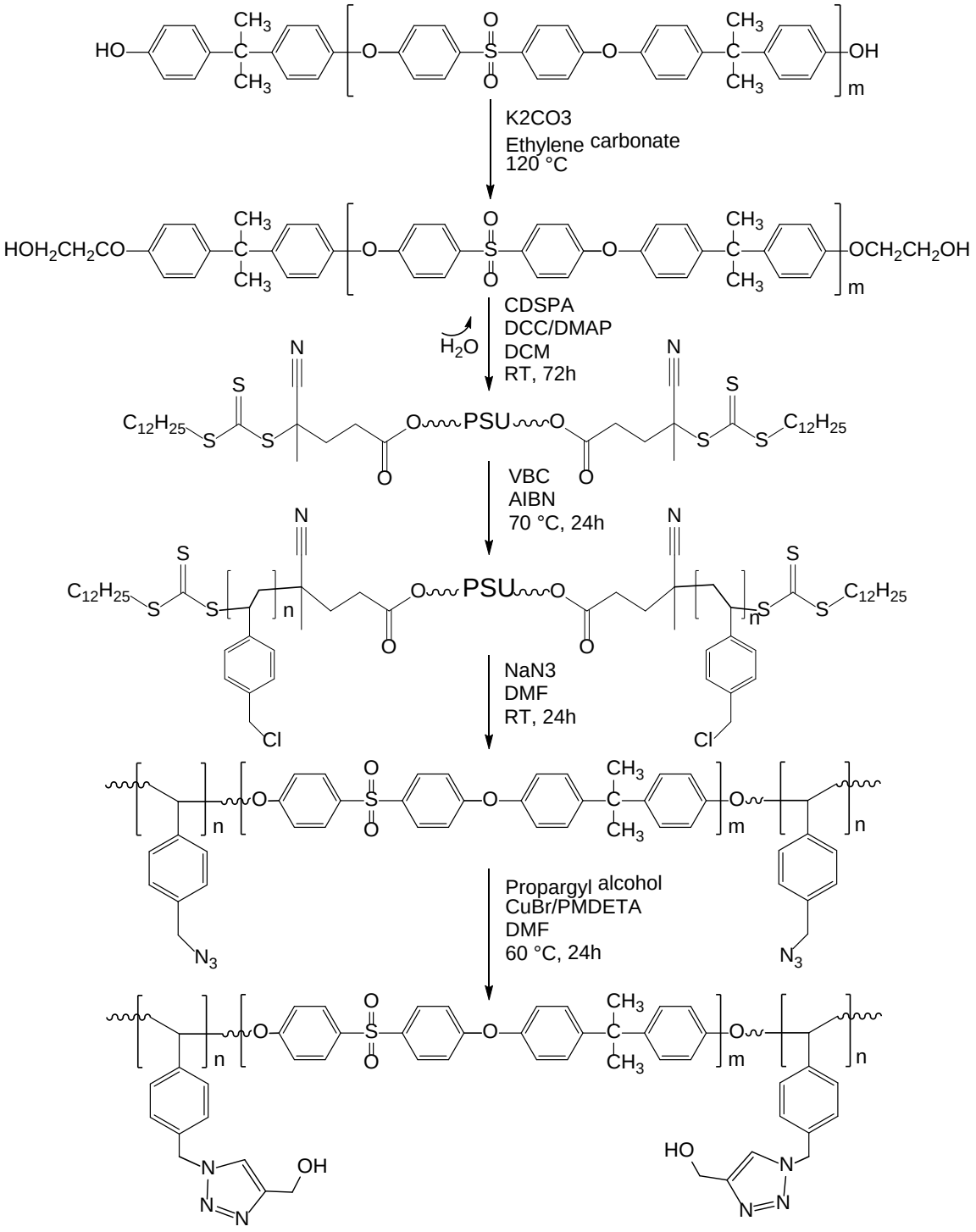

Scheme 4.2. Synthesis route of polytriazole-*b*-polysulfone-*b*-polytriazole.

P*t*BA in Chapter 2. However, the ^{1}H NMR spectrum (Figure A4.3, appendices) after the

click reaction shows that the relative integral of -C$\boldsymbol{H_2}$TrN to PSU protons is significantly lower than that of -C$\boldsymbol{H_2}$Cl expected if PVBC-PSU-PVBC would have been successfully synthesized. It should be identical in principle. In combination with the presence of phenol proton in the spectrum, we believe that during the azidation step, sodium azide as a strong base attacked the labile phenyl ester linkage between PSU and PVBC block in parallel to the nucleophilic substitution toward chloride. Phenoxide anion is a good leaving group due to the acidity of phenol. The consequence of this hydrolysis side-reaction is a mixture of PSU homopolymers converted back to OH-capped state, and polar PTrN free chains, which could be washed out easily with purification. This problem was solved by transforming the phenyl alcohol to an aliphatic primary alcohol through

the condensation of ethylene carbonate with phenol in the presence of K_2CO_3.[53-55] The mechanism involves first nucleophilic attack of the phenoxide ion at one of the alkyl carbons in the cyclic ethylene carbonate, leading to the ring-opening and loss of CO_2 to yield the 2-hydroxyethyl ether end group.[53] The conversion of this hydroxyethyl group to RAFT CTA, containing trithiocarbonate, was attained by applying the same Steglich esterification for HO-PSU-OH as described in Chapter 2. The quantitative yield of the end group modification was confirmed by ^{1}H NMR spectra of HE-PSU-HE and CTA-PSU-CTA in Appendices (Figure A4.4).

The RAFT polymerization was carried out towards triblock copolymer PVBC-PSU-

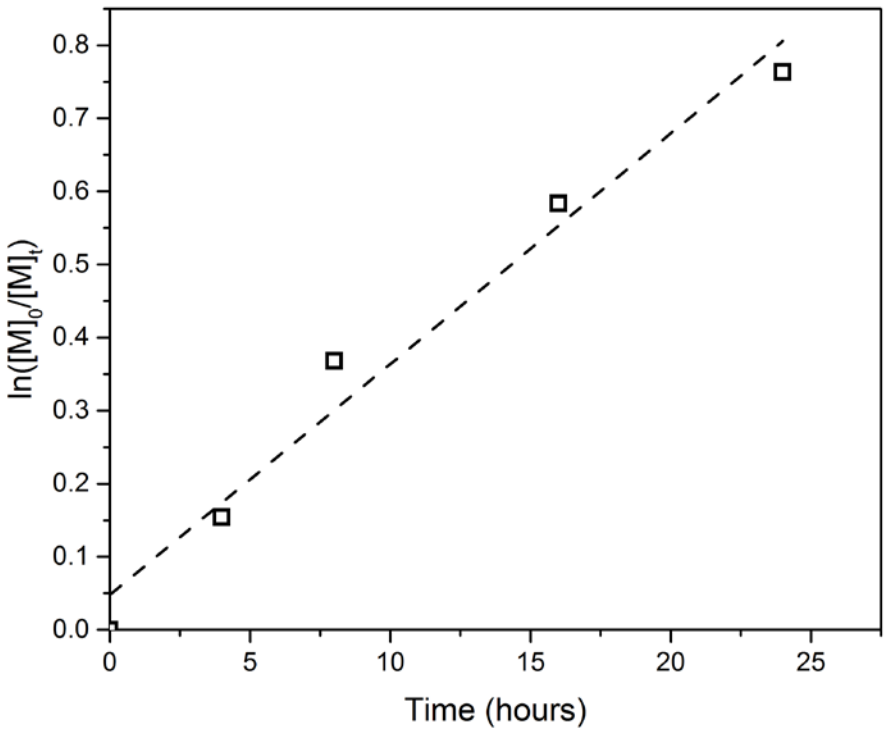

Figure 4.11. Semilog kinetic plot of $\ln([M]_0/[M]_t)$ versus time for RAFT polymerization with [AIBN]: [CTA-PSU-CTA]: [VBC] = 0.25: 1: 400 in bulk at 70 °C, with dashed line indicating linear fits of the data.

PVBC with [AIBN]: [CTA-PSU-CTA]: [VBC] = 0.25: 1: 400 in bulk at 70 °C. The

viscosity of the solution increased constantly with the increase of time. The

Table 4.4. Characteristics of the polymers produced by RAFT with [AIBN]: [CTA-PSU-CTA]: [VBC] = 0.25: 1: 400 in bulk at 70 °C

Polymers	Time (h)	Conversion	$M_{n,GPC}$ (kg/mol)	$M_{n,NMR}$ (kg/mol)	P
PSU_{14k}	0	--	13.8	14.4	2
$PVBC_{12k}$-PSU_{14k}-$PVBC_{12k}$	4	14 %	24.3	37.9	1
$PVBC_{19k}$-PSU_{14k}-$PVBC_{19k}$	8	31 %	27.2	51.9	1
$PVBC_{29k}$-PSU_{14k}-$PVBC_{29k}$	16	44 %	28.7	71.7	1
$PVBC_{32k}$-PSU_{14k}-$PVBC_{32k}$	24	53 %	34.0	79.5	1

polymerization kinetics was studied by monitoring the conversion rate of monomer at

different reaction times. The conversion was calculated by the decrease of ^{1}H NMR peak integral, corresponding to vinylic monomer protons in the sample, directly taken and diluted from the reaction mixture. The evolution of ^{1}H NMR spectra of the

polymerization product can be found in Figure A4.5, Appendices. Based on that, a linear relationship between $\ln([M]_0/[M]_t)$ and time was plotted in Figure 4.11, indicating an approximately first order radical polymerization with a steady state propagation within

the studied range. GPC characterization suggests all the copolymers prepared with different reaction times and monomer conversions have a lower polydispersity than PSU (< 2.0). As shown in Figure 4.12, their GPC curves shift to shorter elution time as the

reaction time increase and keep a similar shape of the monomodal peak, while it shows a small shoulder representing low molecular species which could be ascribed by the dead PVBC chains initiated by AIBN, which is more severe at high conversion. Table 4.4

summarizes the characteristics of all the PVBC-PSU-PVBC synthesized by RAFT in this study.

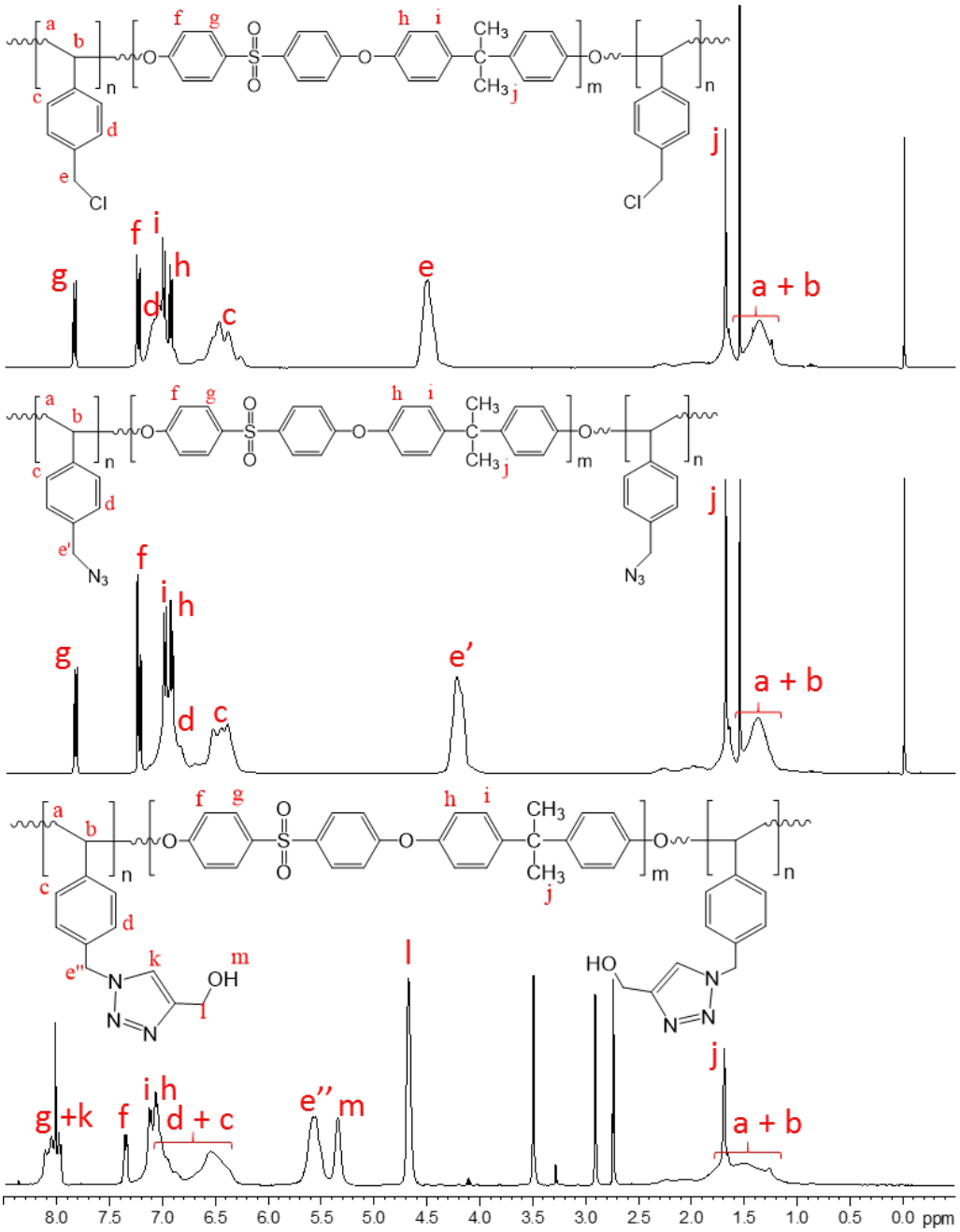

Figure 4.13. ^{1}H NMR spectra of $PVBC_{32k}$-PSU_{14k}-$PVBC_{32k}$, $PN_{3,34k}$-PSU_{14k}-$PN_{3,34k}$ in $CDCl_3$, and $PTrN_{46k}$-PSU_{14k}-$PTrN_{46k}$ in DMF-d7.

The $PVBC_{46k}$-PSU_{14k}-$PVBC_{46k}$ copolymer obtained after 24 h RAFT polymerization with highest conversion of 53 % was subject to the further post-polymerization modification and ended up with the targeted PTrN-PSU-PTrN triblock. The chemical structures of the copolymer at each step was confirmed by ^{1}H NMR spectra (Figure 4.13). All the characteristic signals that belong to the specific pendent groups can be found at the similar shifts as PSU-CH_2Cl, PSU-N_3 and PSU-TrN. FTIR spectra verify the presence of azide group with a strong adsorption band at 2100 cm^{-1} and the clicked hydroxyl group with a broad band at 3150-3770 cm^{-1} (Figure A4.6, Appendices). The thermal properties of the series of triblock copolymers with different chemical composition were studied as well using TGA and DSC. These results can be found in Figure A4.7 and A4.8, Appendices. The final PTrN-PSU-PTrN has good thermal stability with a 5 % weight loss at 350 °C under N_2 atmosphere and has a single glass transition point at 90 °C.

One interesting observation is that the GPC curve of PN_3-PSU-PN_3 deviates from the monomodality of PVBC-PSU-PVBC, showing a high molar mass peak along with the broadened main peak (Figure 4.14). This phenomenon can be explained by the coupling reaction between the triblock copolymers. The thiocarbonythio group is well known to react with primary or secondary amine as a nucleophile to convert it to a thiol.[56, 57] This aminolysis reaction can be used to remove RAFT end groups from polymers or facilitate a number of modifications.[58] But the free thiols are prone to simultaneous oxidation to disulfide that connects two polymer chains together in the presence of oxygen.[56] Recent studies indicate that NaN_3 is also capable of cleaving the trithiocarbonate, which is still attached to the PVBC chain end after polymerization to thiol.[59, 60] Thus we believe the

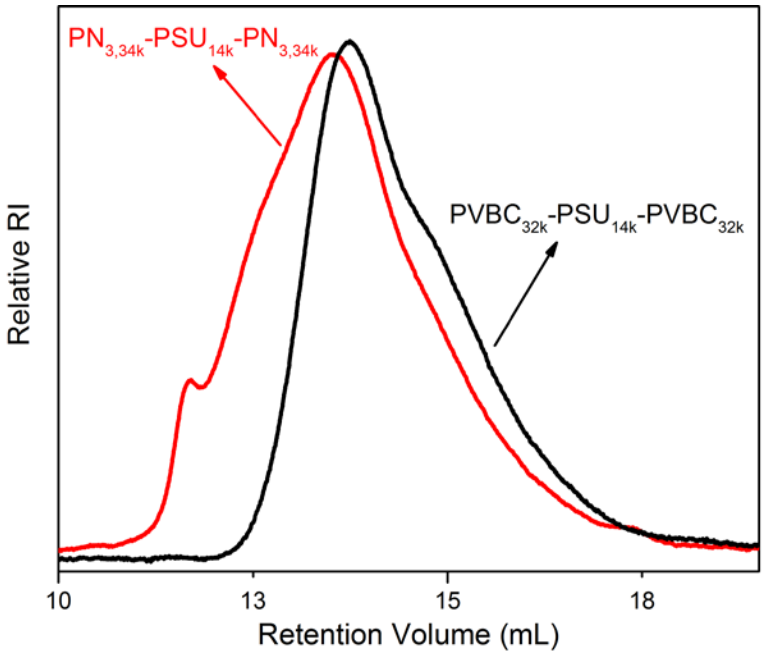

Figure 4.14. GPC curves of $PVBC_{32k}$-PSU_{14k}-$PVBC_{32k}$ (black) and $PN_{3,34k}$-PSU_{14k}-$PN_{3,34k}$ (red) obtained *via* azidation with sodium azide.

thiol-thiol coupling reaction occurred during the azidation with insufficient deoxygenation or more likely isolation of the products. As a result, the final PTrN-PSU-PTrN triblock should be contaminated with certain amount of high molecular weight multiblock copolymers. To eliminate this effect and obtain well-defined triblock, we can add acrylates and reducing agents in the azidation step to trap the generated thiols in-situ through a thio-ene Micheal addition.[60, 61] An alternative solution is to react the disulfide-linked PTrN-PSU-PTrN final product with various acrylates in the presence of phosphine acting as both reducing agent and catalyst for Michael addition.[62, 63]

4.3.5 Hydrogen Bond-Mediated Self-assembly of PTrN-PSU-PTrN/PAA-PSU-PAA Blend

The triazole moiety structurally resembles the trans-amide functionality due to its planarity and strong dipole moment, which impart similar hydrogen bonding characteristics to the triazole.[28-31]. The trizole ring contains both hydrogen-bond donor (H-donor) and hydrogen-acceptor (H-acceptor) as shown in Figure 4.15a. While 1-position nitrogen (N1) has partial positive charge, the 2- (N2) and 3-nitrogen atoms (N3) are negatively charged. These two pyridine-like sp2 hybridized nitrogen atoms (N2 and N3) can function as H-acceptors with their lone pairs, mimicking the carbonyl oxygen in amide. Between the two nitrogen atoms, N3 lone pair has a higher basicity than the N2 one, suggesting the former is a better H-acceptor and metal ligating center.[31] Interestingly, the three nitrogen atoms of the 1,2,3-triazole nested on one side of the ring cause a strong polarization of the aromatic *p* system and the *s* framework, resulting in a large ~5-debye dipole moment almost aligned with the C–H bond in the 5-position

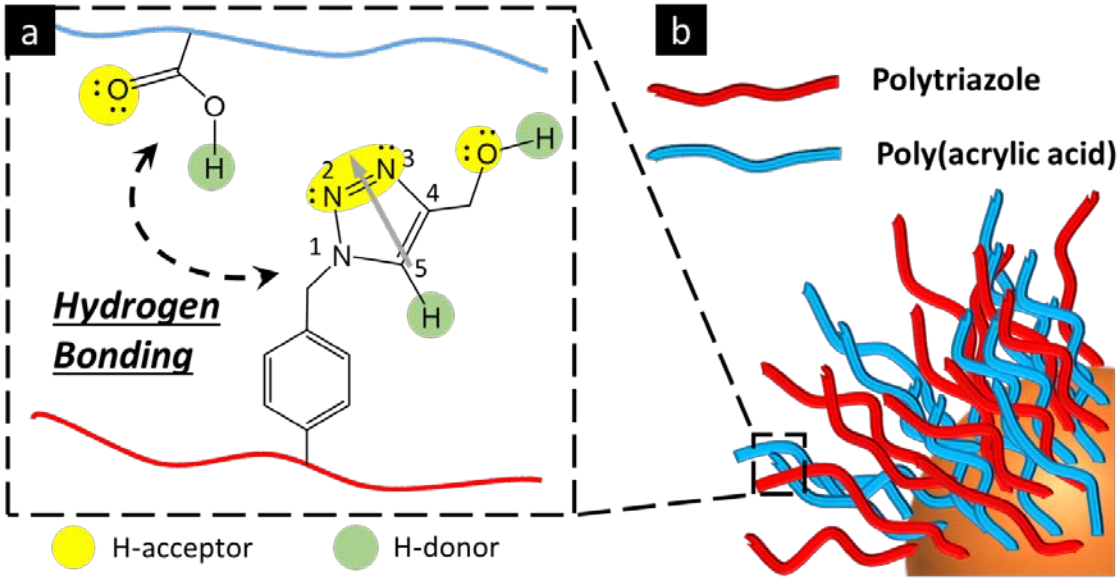

Figure 4.15. Schematic representation of (a) hygrogen bonding interaction between 1,2,3-triazole and carboxylic acid unit and (b) micellar structure of PTrN-PSU-PTrN and PAA-PSU-PAA blend in DMF.

(C5).[29, 31] So the highly polarized C-H bond sitting in the positive end of this dipole creates a potent H-donor, comparable to the classical, intrinsically polarized donors (e.g., N–H, O–H). The strong acidity of C-H in 1,2,3-triazole has also been utilized to bind halide anions.[64, 65] In our system, a primary OH group in the 4-position substituent provides additional H-bonding sites. On the other hand, carboxylic acid is another well-known hydrogen bond forming group with a positive hydrogen atom and a lone pair on the negative oxygen, which produce dimers by intermolecular hydrogen bonding. The complementary H-bonding interaction between 1,2,3-[66] or 1,2,4-triazole[67] and carboxylic acid has been corroborated by spectroscopy, X-ray crystallography and simulation studies. The formation of H-bonding pairs such as triazole nitrogen atom with terminal OH group in acid, and aromatic hydrogen atom (C5-H) in triazole with carbonyl oxygen was confirmed.[66, 67]

It was envisaged that blending PTrN-PSU-PTrN with the carboxylic acid-containing triblock PAA-PSU-PAA, which we reported in the previous chapter, would induce a strong multiple intra- and inter-molecular interactions between PTrN and PAA segments, leading to interesting micellar morphologies. A PTrN/PAA copolymer blend at a stoichiometric ratio of acid/base was solubilized in DMF, which is a selective solvent favoring the polar PTrN and PAA blocks indicated by their HSP values (Table 4.5).[68] A core-shell structure is expected to emerge with PSU being the core surrounded by PTrN/PAA chains as depicted in Figure 4.15b. TEM image shows string-like aggregates in DMF (Figure 4.16a). Their hydrodynamic diameter determined by DLS is around 81 nm, much smaller then what we observed in TEM image. It suggests these large aggregates were fused by small micelles when they were concentrated by air-drying

Table 4.5. Values of Hansen solubility parameter for polymer segments and solvents

	δ^a [MPa]$^{1/2}$				
	δ_D	δ_P	δ_H	δ_T	dielectric constant (ε)
PTrN[a]	19.3	12.9	14.9	27.6	--
PAA[b]	17.3	12.2	18.6	28.2	--
PSU	16.6	6.0	6.6	18.8	--
DMF	17.4	13.7	11.3	24.9	30.7

[a] δ of PTrN is obtained by fitting the HSP sphere to experimental solubility data with 44 solvents (Table A4.1, Appendices); [b] δ of PAA is calculated by HSPiP software 4th Edition, others are cited from reference 68; $\delta_T = (\delta_D^2 + \delta_H^2 + \delta_P^2)^{1/2}$

before imaging. PTrN-PSU-PTrN alone forms discrete spherical micelles with soft coronas (Figure 4.16c). Aggregates of PSU-PTrN-PSU with hydrodynamic diameter of 68 nm are smaller than the self-assembled PTrN-PSU-PTrN/PAA-PSU-PAA copolymer micelles and has no tendency to fuse into larger objects. This can be explained by taking into account that the area per chain in the corona or at the interface between corona and core (A_c) decreases, since the PAA and PTrN chains are attracted to each other and tightly packed in the corona. As A_c reduces, the micelles are allowed to grow to larger aggregates with a smaller total interfacial area. When this enthalpy-favorable process is counterbalanced by the entropic penalty of increased core stretching, the micelles can change from spheres to cylinders and other complex morphologies.[69]

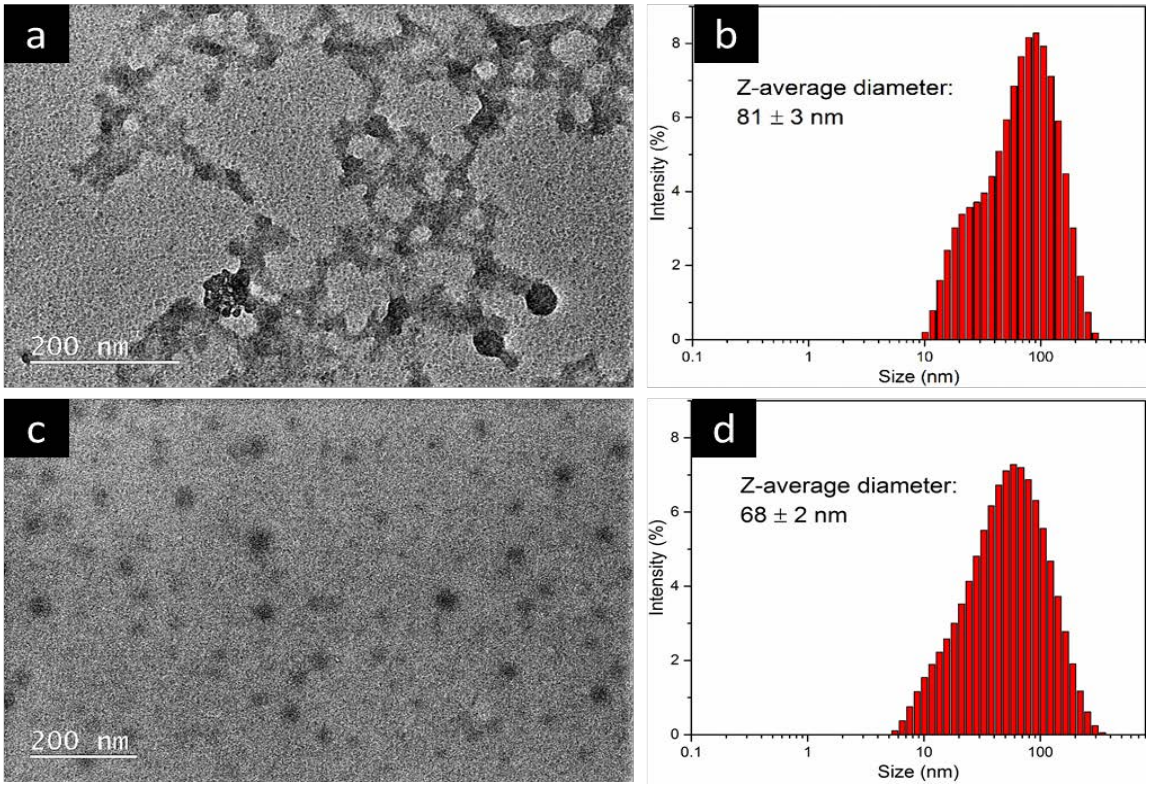

Figure 4.16. TEM images (a) of PTrN-PSU-PTrN/PAA-PSU-PAA stoichiometric blend and (c) PTrN-PSU-PTrN micelles from 0.1 wt% DMF solution, stained with iodine, and their hydrodynamic size distribution (b and d) determined by DLS.

It is worth noting that micellization can be driven by the introduction of noncovalent

interactions such as hydrogen bonding, electrostatic interactions, and metal–ligand coordinative bonds, as proposed in the literature.[70] This self-assembly process relies on complexes formed by the strong attraction force between blocks, such as the mixture of PS-*b*-P4VP and PS-*b*-PAA or PAA homoplymer.[71-73] If the solvent is common for all the blocks, those blocks with strong tendency to complex will gather to form the core and the non-interacting soluble block would be exposed to the solvent, forming the corona. However our system is essentially different because the base strength of the σ lone pairs

of the nitrogen in 1,2,3-triazole is lower than that in pyridine (1,2,3-triazole < pyrazole < pyridine < imidazole).[31] As a weaker H-acceptor, 1,2,3-triazole is unable to form strong hydrogen-bonding complexes with PAA. This is confirmed by the solubility of PTrN and PAA homopolymer mixtures in DMF. They do not assemble into insoluble aggregates. Therefore, we believe PTrN/PAA segments should be located in the outer shell of the micelles, due to higher similarities between solubility parameters of these blocks and

those of DMF, compared to PSU blocks.

Phase inversion membranes have been prepared from the 18 wt% PTrN-PSU-PTrN and PAA-PSU-PAA stoichiometric blend (TrN: AA = 1: 1) solution with DMF. The surface membrane morphology, imaged by SEM, is shown in Figure 4.17. A highly porous surface containing can be observed for the membrane prepared from the blend. This was formed by immersion in 0.1 M $CuSO_4$ coagulation bath via SCNIPS (Figure 4.17a). This

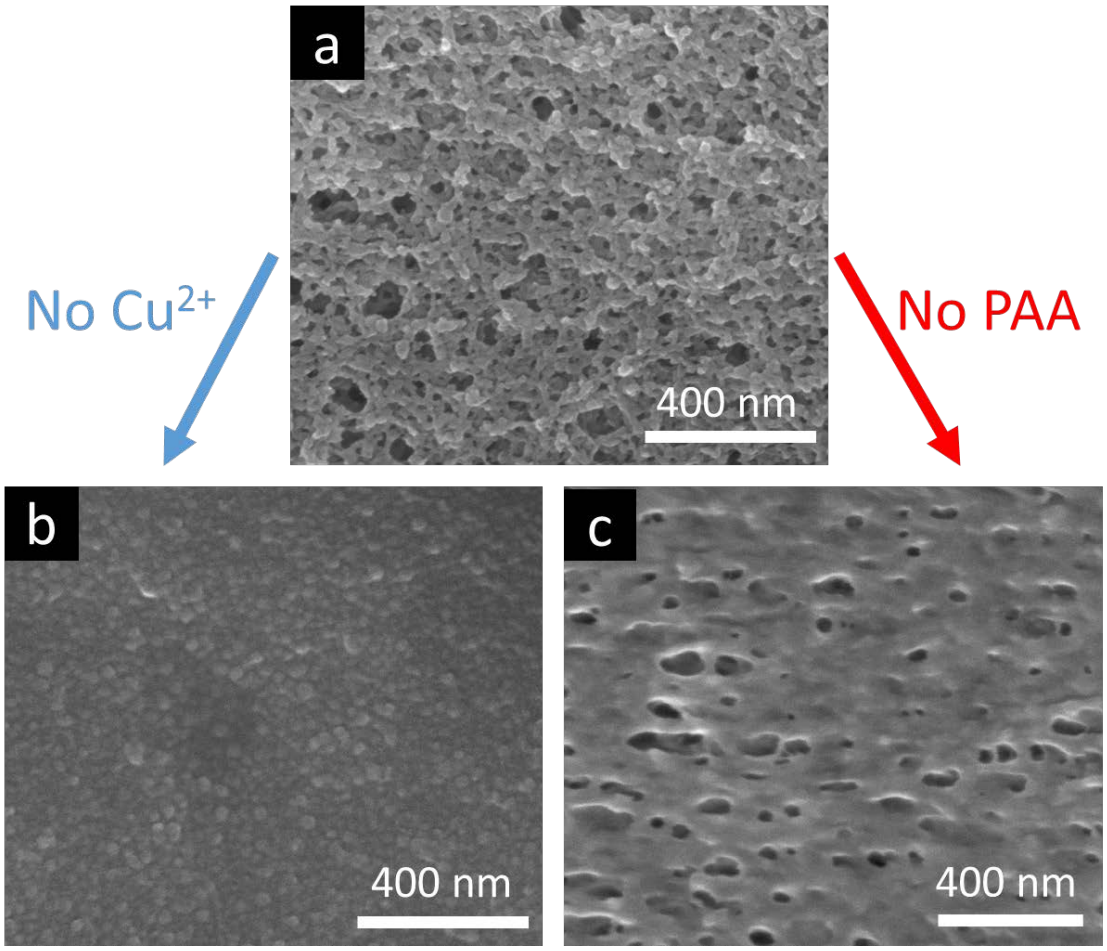

Figure 4.17. SEM images of PTrN-PSU-PTrN/PAA-PSU-PAA membranes formed by immersion in (a) $CuSO_4$ coagulation bath and (b) pure water; (c) PTrN-PSU-PTrN membrane formed by immersion in $CuSO_4$ coagulation bath.

nanostructure is probably directly derived from the fused micelles that are already formed in solution. Figure 4.17b shows the morphology of the membrane formed by normal phase inversion, precipitated in pure water. The surface is composed of densely packed small aggregates with lack of porous structure. The striking difference on membrane morphology is ascribed to the metal complexation ability of PAA and PTrN. This is analogous to what is reported in chapter 2 and 3. Triazole has been used to develop versatile metal ligands for coordination chemistry,[74] and metal-containing membranes by our group.[32, 33] The chelation of metal ions with carboxylic acid and triazole groups leads to the cross-linking of the corona constituted of PAA and PTrN, and rapidly immobilizes the morphology of the interconnected micelles. When the membrane was immersed in pure water, the water molecules with a high dipole moment competitively interrupted the hydrogen-bonding between PTrN and PAA, and swelled the two hydrophilic polymers to an extent that the original micellar structure cannot be preserved. In a control experiment, PTrN-PSU-PTrN membrane was prepared without blending. This membrane has no ordered structure on the surface but typical large pores formed by non-solvent induced phase separation as shown by Figure 4.17c.

For PS-*b*-P4VP system, our group has previously demonstrated hydrogen bonding interaction by addition of small molecules with multi-hydroxyl/acids functional groups or by blending with PAA copolymers can induce the formation of isoporous membranes or alter the pore size of the ordered morphology.[75, 76] We believe PTrN/PAA binary copolymer system is an expansion of this concept. It is worth to investigate the supramolecular interaction and its influence on self-assembly in more details in the future, for example, by tuning the copolymer ratio and solvent quality.

4.4 Conclusions

In this chapter we report the synthesis of random and block copolymers of polysulfone and polytriazole and their application for membrane manufacture. The first part focuses on the random copolymers or controlled functionalization of polysulfone. We demonstrate how click chemistry can be used to address one of the most critical issues in membranes for water filtration: the flux reduction by fouling under operation. Well-controlled functionalization of polysulfone, by anchoring 1,2,3-triazole ring substituents containing OH groups to the backbone, successfully increased the hydrophilicity. Different degrees of functionalization (23%, 49%, 56% and 94%) were achieved. The modified ultrafiltration membranes exhibited water permeability up to 187 L m^{-2} h^{-1} bar^{-1}. The modification reduced the extent of irreversible fouling during filtration of bovine serum albumin proteins while keeping high protein rejection ratio (> 99%). The second part of this chapter reports the successful synthesis of polytriazole-*b*-polysulfone-*b*-polytriazole (PTrN-PSU-PTrN) triblock copolymers by a combination of RAFT polymerization and click chemistry. A new PSU macro-CTA with an ethyl ester linkage was prepared to avoid hydrolysis in the subsequent modification. The RAFT polymerization of 4-vinylbenzyl chloride towards a polymer precursor PVBC-PSU-PVBC follows an approximately first order kinetics in a controlled manner. The chemical structures of the final triblock copolymer and intermediates were well characterized by NMR and FTIR spectroscopy. Their thermal properties were investigated by TGA and DSC. Finally, we proposed a hydrogen bond-mediated self-assembly approach for

nanostructured membranes, by blending PTrN-PSU-PTrN and PAA-PSU-PAA at stoichiometric ratio in DMF. Fused micelles in a network were observed in both the diluted solution, and membrane surface after its formation in coagulation bath containing Cu^{2+} ions.

4.5 References

1. J. Mulder, *Basic Principles of Membrane Technology*, Springer Netherlands, 1996.

2. J. B. Rose, *Polymer*, 1974, 15, 456-465.

3. C. Dizman, M. A. Tasdelen and Y. Yagci, *Polym. Int.*, 2013, 62, 991-1007.

4. H. Susanto, N. Stahra and M. Ulbricht, *J. Membr. Sci.*, 2009, 342, 153-164.

5. Z. Tang, C. Qiu, J. R. McCutcheon, K. Yoon, H. Ma, D. Fang, E. Lee, C. Kopp, B. S. Hsiao and B. Chu, *J. Polym. Sci. Part B Polym. Phys.*, 2009, 47, 2288-2300.

6. B. Zornoza, S. Irusta, C. Téllez and J. Coronas, *Langmuir*, 2009, 25, 5903-5909.

7. Y. Yang, Z. Shi and S. Holdcroft, *Macromolecules*, 2004, 37, 1678-1681.

8. M. H. Rahimy, G. A. Peyman, S. Y. Chin, R. Golshani, C. Aras, H. Borhani and H. Thompson, *J. Drug Target.*, 1994, 2, 289-298.

9. B. C. Johnson, İ. Yilgör, C. Tran, M. Iqbal, J. P. Wightman, D. R. Lloyd and J. E. McGrath, *J. Polym. Sci. Polym. Chem. Ed.*, 1984, 22, 721-737.

10. D. Rana and T. Matsuura, *Chem. Rev.*, 2010, 110, 2448-2471.

11. Y. H. Cho, H. W. Kim, S. Y. Nam and H. B. Park, *J. Membr. Sci.*, 2011, 379, 296-306.

12. G. Yilmaz, H. Toiserkani, D. O. Demirkol, S. Sakarya, S. Timur, L. Torun and Y. Yagci, *Mater. Sci. Eng., C*, 2011, 31, 1091-1097.

13. C. Zhao, J. Xue, F. Ran and S. Sun, *Prog. Mater Sci.*, 2013, 58, 76-150.

14. M. Ulbricht and G. Belfort, *J. Membr. Sci.*, 1996, 111, 193-215.

15. J. Y. Park, M. H. Acar, A. Akthakul, W. Kuhlman and A. M. Mayes, *Biomaterials*, 2006, 27, 856-865.

16. Z. Yi, L.-P. Zhu, Y.-F. Zhao, B.-K. Zhu and Y.-Y. Xu, *J. Membr. Sci.*, 2012, 390–391, 48-57.

17. W.-W. Yue, H.-J. Li, T. Xiang, H. Qin, S.-D. Sun and C.-S. Zhao, *J. Membr. Sci.*, 2013, 446, 79-91.

18. Y.-F. Zhao, L.-P. Zhu, Z. Yi, B.-K. Zhu and Y.-Y. Xu, *J. Membr. Sci.*, 2013, 440, 40-47.

19. H. C. Kolb, M. G. Finn and K. B. Sharpless, *Angew. Chem. Int. Ed.*, 2001, 40, 2004-2021.

20. D. Fournier, R. Hoogenboom and U. S. Schubert, *Chem. Soc. Rev.*, 2007, 36, 1369-1380.

21. U. Mansfeld, C. Pietsch, R. Hoogenboom, C. R. Becer and U. S. Schubert, *Polym. Chem.*, 2010, 1, 1560-1598.

22. W. H. Binder and R. Sachsenhofer, *Macromol. Rapid Commun.*, 2007, 28, 15-54.

23. C. Hou, J. Hu, G. Liu, J. Wang, F. Liu, H. Hu, G. Zhang, H. Zou, Y. Tu and B. Liao, *Macromolecules*, 2013, 46, 4053-4063.

24. F. Liu, J. Hu, G. Liu, C. Hou, S. Lin, H. Zou, G. Zhang, J. Sun, H. Luo and Y. Tu, *Macromolecules*, 2013, 46, 2646-2657.

25. I. Dimitrov, S. Takamuku, K. Jankova, P. Jannasch and S. Hvilsted, *Macromol. Rapid Commun.*, 2012, 33, 1368-1374.

26. I. Dimitrov, S. Takamuku, K. Jankova, P. Jannasch and S. Hvilsted, *J. Membr. Sci.*, 2014, 450, 362-368.

27. Y. Xie, R. Tayouo and S. P. Nunes, *J. Appl. Polym. Sci.*, 2015, 132, 41549.

28. H.-F. Chow, K.-N. Lau, Z. Ke, Y. Liang and C.-M. Lo, *Chem. Commun.*, 2010, 46, 3437-3453.

29. Y. Hua and A. H. Flood, *Chem. Soc. Rev.*, 2010, 39, 1262-1271.

30. H.-F. Chow, T.-K. Chui and Q. Qi, *Synlett*, 2014, 25, 2246-2255.

31. B. Schulze and U. S. Schubert, *Chem. Soc. Rev.*, 2014, 43, 2522-2571.

32. L. F. Villalobos, Y. Xie, S. P. Nunes and K.-V. Peinemann, *Macromol. Rapid Commun.*, 2016, 37, 700-704.

33. H. Cheng, Y. Xie, L. F. Villalobos, L. Song, K.-V. Peinemann, S. Nunes and P.-Y. Hong, *Sci. Rep.*, 2016, 6, 24289.

34. K. A. Davis, B. Charleux and K. Matyjaszewski, *J. Polym. Sci. A Polym. Chem.*, 2000, 38, 2274-2283.

35. E. Avram, E. Butuc, C. Luca and I. Druta, *J. Macromol. Sci., A*, 1997, 34, 1701-1714.

36. H. Toiserkani, G. Yilmaz, Y. Yagci and L. Torun, *Macromol. Chem. Phys.*, 2010, 211, 2389-2395.

37. C. Gaina, V. Gaina and D. Ionita, *Polym. Int.*, 2011, 60, 296-303.

38. L. F. Hancock, *J. Appl. Polym. Sci.*, 1997, 66, 1353-1358.

39. K.-V. Peinemann, V. Abetz and P. F. W. Simon, *Nat. Mater.*, 2007, 6, 992-996.

40. G. Socrates, *Infrared and Raman characteristic group frequencies: tables and charts*, John Wiley & Sons, 2004.

41. C. Camacho-Zuñiga, F. A. Ruiz-Treviño, S. Hernández-López, M. G. Zolotukhin, F. H. J. Maurer and A. González-Montiel, *J. Membr. Sci.*, 2009, 340, 221-226.

42. E. Avram, M. A. Brebu, A. Warshawsky and C. Vasile, *Polym. Degrad. Stab.*, 2000, 69, 175-181.

43. S. A. McKelvey and W. J. Koros, *J. Membr. Sci.*, 1996, 112, 29-39.

44. Y. Yang and P. Wang, *Polymer*, 2006, 47, 2683-2688.

45. A. Mehta and A. L. Zydney, *J. Membr. Sci.*, 2005, 249, 245-249.

46. Y.-q. Wang, T. Wang, Y.-l. Su, F.-b. Peng, H. Wu and Z.-y. Jiang, *Langmuir*, 2005, 21, 11856-11862.

47. L.-P. Zhu, H.-B. Dong, X.-Z. Wei, Z. Yi, B.-K. Zhu and Y.-Y. Xu, *J. Membr. Sci.*, 2008, 320, 407-415.

48. R.-S. Juang, H.-L. Chen and Y.-S. Chen, *Sep. Purif. Technol.*, 2008, 63, 531-538.

49. J. Moraes, K. Ohno, G. Gody, T. Maschmeyer and S. Perrier, *Beilstein J. Org. Chem.*, 2013, 9, 1226-1234.

50. G. Couture and B. Améduri, *Eur. Polym. J.*, 2012, 48, 1348-1356.

51. T. Sato, Y. Ishida and A. Kameyama, *Polym. J.*, 2014, 46, 239-242.

52. O. I. Strube and G. Schmidt-Naake, *Macromol. Symp.*, 2009, 275–276, 13-23.

53. S. Jéol, F. Fenouillot, A. Rousseau, C. Monnet, K. Masenelli-Varlot and J.-F. Briois, *J. Polym. Sci. A Polym. Chem.*, 2008, 46, 3985-3991.

54. O. Celebi, C. H. Lee, Y. Lin, J. E. McGrath and J. S. Riffle, *Polymer*, 2011, 52, 4718-4726.

55. J. M. Dennis, G. B. Fahs, R. B. Moore, S. R. Turner and T. E. Long, *Macromolecules*, 2014, 47, 8171-8177.

56. H. Willcock and R. K. O'Reilly, *Polym. Chem.*, 2010, 1, 149-157.

57. G. Moad, E. Rizzardo and S. H. Thang, *Polym. Int.*, 2011, 60, 9-25.

58. P. J. Roth, C. Boyer, A. B. Lowe and T. P. Davis, *Macromol. Rapid Commun.*, 2011, 32, 1123-1143.

59. Y. Wu, Y. Zhou, J. Zhu, W. Zhang, X. Pan, Z. Zhang and X. Zhu, *Polym. Chem.*, 2014, 5, 5546-5550.

60. M. Guerre, B. Ameduri and V. Ladmiral, *Polym. Chem.*, 2016, 7, 441-450.

61. P. A. Woodfield, Y. Zhu, Y. Pei and P. J. Roth, *Macromolecules*, 2014, 47, 750-762.

62. J. A. Syrett, M. W. Jones and D. M. Haddleton, *Chem. Commun.*, 2010, 46, 7181-7183.

63. G.-Z. Li, R. K. Randev, A. H. Soeriyadi, G. Rees, C. Boyer, Z. Tong, T. P. Davis, C. R. Becer and D. M. Haddleton, *Polym. Chem.*, 2010, 1, 1196-1204.

64. F. Garcia, M. R. Torres, E. Matesanz and L. Sanchez, *Chem. Commun.*, 2011, 47, 5016-5018.

65. V. Haridas, S. Sahu and P. Venugopalan, *Tetrahedron*, 2011, 67, 727-733.

66. M.-H. Ryu, J.-W. Choi, H.-J. Kim, N. Park and B.-K. Cho, *Angew. Chem. Int. Ed.*, 2011, 50, 5737-5740.

67. A. D. Naik, M. M. Dîrtu, A. Léonard, B. Tinant, J. Marchand-Brynaert, B.-L. Su and Y. Garcia, *Cryst. Growth Des.*, 2010, 10, 1798-1807.

68. C. M. Hansen, *Hansen Solubility Parameters: A User's Handbook, Second Edition*, CRC Press, 2007.

69. Y. Mai and A. Eisenberg, *Chem. Soc. Rev.*, 2012, 41, 5969-5985.

70. S.-W. Kuo, *Polym. Int.*, 2009, 58, 455-464.

71. J. Gao, Y. Wei, B. Li and Y. Han, *Polymer*, 2008, 49, 2354-2361.

72. C. Guerlain, S. Piogé, C. Detrembleur, C.-A. Fustin and J.-F. Gohy, *J. Polym. Sci. A Polym. Chem.*, 2015, 53, 459-467.

73. N. Lefèvre, C.-A. Fustin, S. K. Varshney and J.-F. Gohy, *Polymer*, 2007, 48, 2306-2311.

74. J. P. Byrne, J. A. Kitchen and T. Gunnlaugsson, *Chem. Soc. Rev.*, 2014, 43, 5302-5325.

75. H. Yu, X. Qiu, N. Moreno, Z. Ma, V. M. Calo, S. P. Nunes and K.-V. Peinemann, *Angew. Chem. Int. Ed.*, 2015, 54, 13937-13941.

76. P. Madhavan, K. V. Peinemann and S. P. Nunes, *ACS Appl. Mater. Interfaces*, 2013, 5, 7152-7159.

CHAPTER 5

Conclusions and Outlook

The goal of this dissertation is to fabricate nanostructured membranes derived from polysulfone-based block copolymers through self-assembly and non-solvent induced phase separation (SNIPS). These membranes exhibit great advantages including the exceptionally high permeability and selectivity, over conventional phase inversion membranes, which dominate the water treatment industry. Self-assembly of block copolymers directs the formation of ordered isoporous nanostructure or sub-nanometer water channels. Block copolymers containing polysulfone are novel materials for this purpose in parallel to polystyrene-based polymers, which so far has been almost exclusively used. Polysulfone offers more merits, such as mechanical and thermal stability. Overall, this aim has been achieved. A range of nanostructured membranes were developed as reported in the previous chapters.

In Chapter 2, we synthesized a triblock copolymer membrane from poly(*tert*-butyl acrylate)-*b*-polsulfone-*b*-poly(*tert*-butyl acrylate) (P*t*BA-PSU-P*t*BA), which has a highly porous interconnected skin layer on the top of graded finger-like macrovoids in the lower portion. A lot of efforts has been made to elucidate the formation mechanism by using advanced electron microscopies, thermodynamic analysis and computational simulation. We found that worm-like elongated micelles were already assembled in solutions of triblock copolymers in selective solvent DMAc with a special “flower-like” arrangement having the PSU central block as the shell. These micelles on the membrane surface were

immobilized by solvent-water exchange, giving rise to the porous structure. This membrane has high pure water permeance, considering its molecular weight cut-off, when compared with normal phase inversion membranes, while its mechanical strength is not compromised. Membrane surface hydrolysis was carried out in a combination with metal complexation to obtain metal-chelated membranes. The copper-containing membrane shows improved antibacterial capability.

Chapter 3 targets biomimetic membranes with water channels of amphiphilic copolymers with segments, which are strongly solved by water. Poly(acrylic acid)-*b*-polysulfone-*b*-poly(acrylic acid) (PAA-PSU-PAA) triblock copolymers obtained by hydrolyzing P*t*BA-PSU-P*t*BA formed a thin film with a surface packed with worm-like assemblies having PSU as shell through dip-coating of its dilute solution in THF. Thermal annealing rearranged the surface morphology, resulting in a dense film with 50 nm cylindrical PAA microdomains inserted in PSU matrix. This copolymer was coated on a porous ceramic membrane in the same way. But it was impermeable to water, probably due to the lack of interconnectivity of PAA cylinders inside the film. We then prepared a phase inversion membrane with a new strategy: “self-assembly and chelation-assisted non-solvent induced phase separation” (SCNIPS). The metal ions in the coagulation bath formed strong metal-PAA complexes, which stabilized the large micelles with a PAA corona pre-formed in a DMF/THF/acetone mixture. These micelles packed into an ordered lattice in the membrane. The space between micelles was filled with PAA being potential water channels. The silver nanoparticle decorated membrane was obtained by surface reduction with $NaBH_4$. It has three distinct layers with different nanoparticle sizes.

We reported copolymer membranes manufactured from random and block copolymers of polysulfone and polytriazole in chapter 4. The first part focuses on the phase inversion membranes prepared by triazole-functionalized polysulfone, which can be considered as random copolymers. Well-controlled functionalization by "clicking" 1,2,3-triazole ring substituents containing OH groups to the backbone of polysulfone increased the hydrophilicity of membranes. The modified ultrafiltration membranes exhibited higher water permeability and reduced irreversible fouling during filtration of proteins while keeping complete protein rejection. Finally, we prepared a nanostructured blend membrane from polytriazole-*b*-polysulfone-*b*-polytriazole (PTrN-PSU-PTrN) and PAA-PSU-PAA. Its formation followed a hydrogen bond-mediated self-assembly process. String-like fused micelles formed in the dilute DMF with a stoichiometric ratio of triazole and acid, and were observed on membrane surface after its formation in coagulation bath containing Cu^{2+} ions.

The most important achievement of my Ph.D. study is that we have built a platform to synthesize block copolymers using polysulfone as the backbone. We have demonstrated a range of polysulfone-based block copolymers with various methodologies. The phenol-terminated telechelic polysulfone prepared by condensation using slightly excess bisphenol A is a powerful starting material that enables the modification of end group to extend the chain via a "grow from" mechanism. This approach was exemplified by P*t*BA-PSU-P*t*BA, PAA-PSU-PAA and PTrN-PSU-PTrN obtained through RAFT polymerization with the CTA-capped bifunctional polysulfone (PSU macro-CTA). The compatibility of RAFT technique with a large number of functional monomers allows us to incorporate more types of segments with diverse chemical functionalities.

The terminal OH groups can participate more reactions leading to block copolymers through an alternative “grow onto” approach. In this way we synthesized PEG-PSU-PEG by a simple coupling reaction between PSU and tosylated monofunctional PEG. This method allows us to pre-form each block independently in a separate system that would not be limited by the other block. One example is the synthesis of PEG-PNIPAM-PSU-PNIPAM-PEG pentablock terpolymer. A PEG-PNIPAM diblock copolymer was readily obtained *via* Cu^0-mediated SET-LRP in pure aqueous medium, while water is a non-solvent for polysulfone. Although eventually we did not succeed in coupling them with polysulfone for the targeted pentablock, it is a promising pathway to link even more chemically or architecturally diverse (co)polymers to polysulfone. Starting from OH group, we can further transform it to other reactive groups to facilitate further functionalization. For instance, primary OH was installed at the end of the polysulfone segment, which has been used to form a more stable linkage with CTA group and assure the integrity of polysulfone backbone during the post-polymerization modification. In the future, this aliphatic OH could be tosylated for nucleophilic substation with another polymer chain bearing nucleophiles such as -NH or -OH, or with NaN_3 to yield a “clickable” azide end group. On the other hand, its counterpart in CuAAC click reaction, alkyne group has been successfully attached to polysulfone, yet not shown in the dissertation. Besides CuAAC, thiol-yne click reaction is welcomed by the introduction of alkyne as well, leading to H-shaped copolymers.

There is no doubt that the complexity and diversity of polysulfone-based copolymers are only limited by our imagination. However some inherent problems of polysulfone have to be addressed for the nanostructured membranes. The first issue is its broad molecular

weight distribution due to the nature of polycondensation. This reason is largely responsible for the fact that we failed to obtain isoporous membranes, reminiscent of PS-*b*-P4VP, through all our studies with different materials, which require nearly monodispersed block copolymers to associate into uniformly sized spherical micelles that can further pack in a regular lattice having incipient pores. Chain-growth polycondensation is a promising synthesis technique for well-defined polysulfone or other condensation polymers. However so far the variety and molecular weight of accessible polymers are still very limited. The second problem is the molecular weight of polysulfone is sacrificed by the stoichiometric unbalance of the starting monomers in order to have phenol group exposed. As a consequence the polysulfone, which we made in this study, has a smaller molecular weight than the commercial polysulfone used as industrial commodity. It lowers the mechanical strength in particular when polysulfone is copolymerized with long hydrophilic segments. Except for P*t*BA-PSU-P*t*BA and PSU-TrN, all polymers prepared in this study have to be cast on the nonwoven support. Otherwise, they are too brittle to be handled as free standing membranes. Its low molecular weight and hydrophilic components deprive the block copolymer membranes of the merits of polysulfone. Finally, solubility parameters indicate that the compatibility of polysulfone with hydrophilic blocks is higher than normal highly hydrophobic blocks, such as polystyrene and poly(methyl methacrylate), which can easily undergo microphase separation with poly(4-vinyl pyridine) or poly(ethylene oxide). As we know, the extent of microphase separation or self-assembly depends on the product of the Flory-Huggins parameter χ and polymer chain length N. A better compatibility or lower χ and shorter polymer chains result in a smaller χN value, favouring a homogeneous morphology

instead of segregation in the bulk. Micellizaiton in solution is also less favoured with more restrict options of selective solvents.

Our research suggests that non-covalent interactions can greatly enhance the self-assembly of block copolymers apart from weak polymer-polymer or polymer-solvent interactions. These additional forces such as hydrogen bonding, metal-ligand coordination and electrostatic interaction contribute to the stability of micelles and the order of supramolecular assemblies. Two relevant concepts, self-assembly and chelation assisted non-solvent induced phase separation (SCNIPS) and hydrogen bond-mediated self-assembly by blending H-interacting block copolymers have been proposed in this dissertation. We believe that not only polysulfone-based systems, but other block polymers can also benefit from this powerful tool to design and construct various supramolecular structures with these strong, reversible and directional forces. The ultimate goal will be mimicking and approaching the precisely controlled natural structures from biomolecules, e.g., DNA and proteins.

APPENDICES

Page

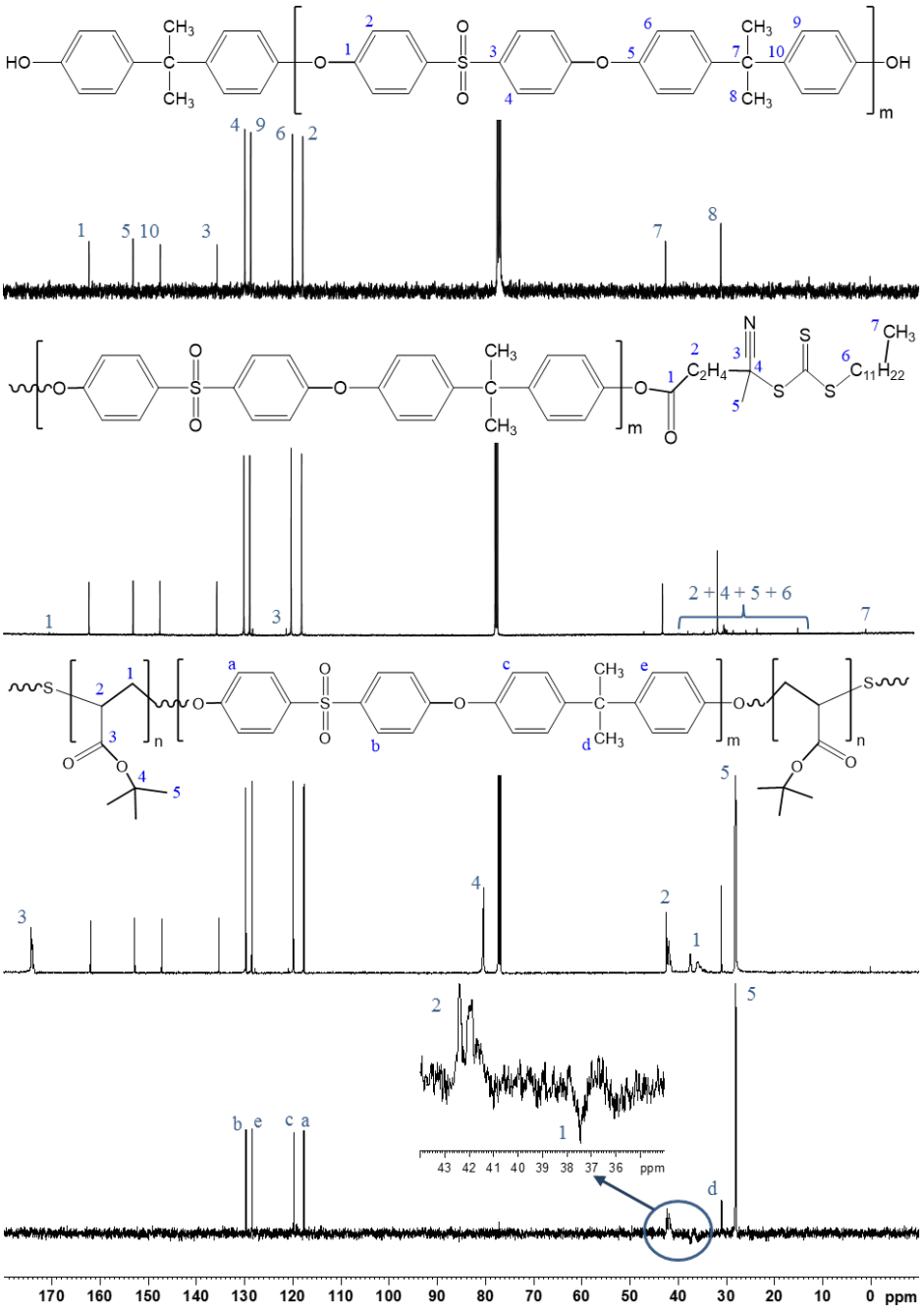

Figure A2.1. ^{13}C NMR spectra for HO-PSU-OH, CTA-PSU-CTA, P*t*BA-PSU-P*t*BA recorded in $CDCl_3$. DEPT ^{13}C NMR of P*t*BA-PSU-P*t*BA with 135° pulse angle is shown on the bottom. Note the negative peak corresponds to -CH_2- while primary and tertiary carbons are positive.

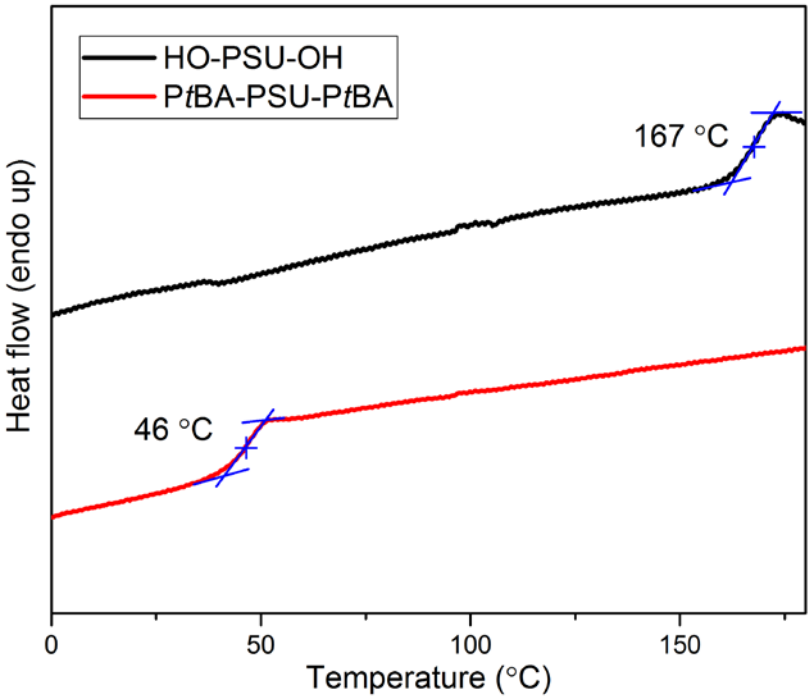

Figure A2.2. DSC curves for HO-PSU-OH and P*t*BA-PSU-P*t*BA. The glass transition temperature (T_g) of HO-PSU-OH is 167 °C, and that of P*t*BA-PSU-P*t*BA is 46 °C.

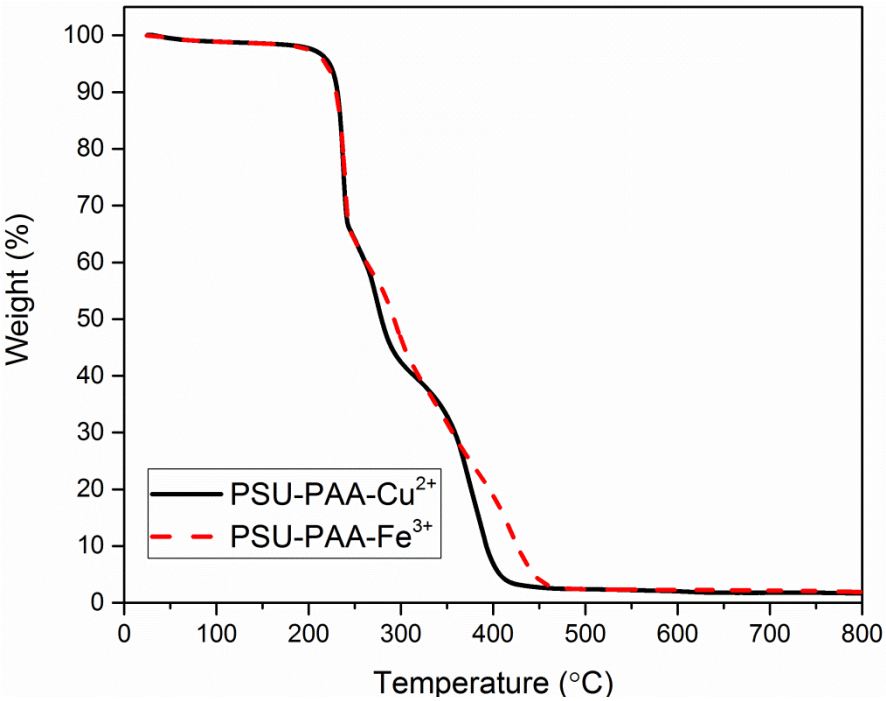

Figure A2.3. TGA curves for PSU-PAA-Cu^{2+}, PSU-PAA-Fe^{3+} under air.

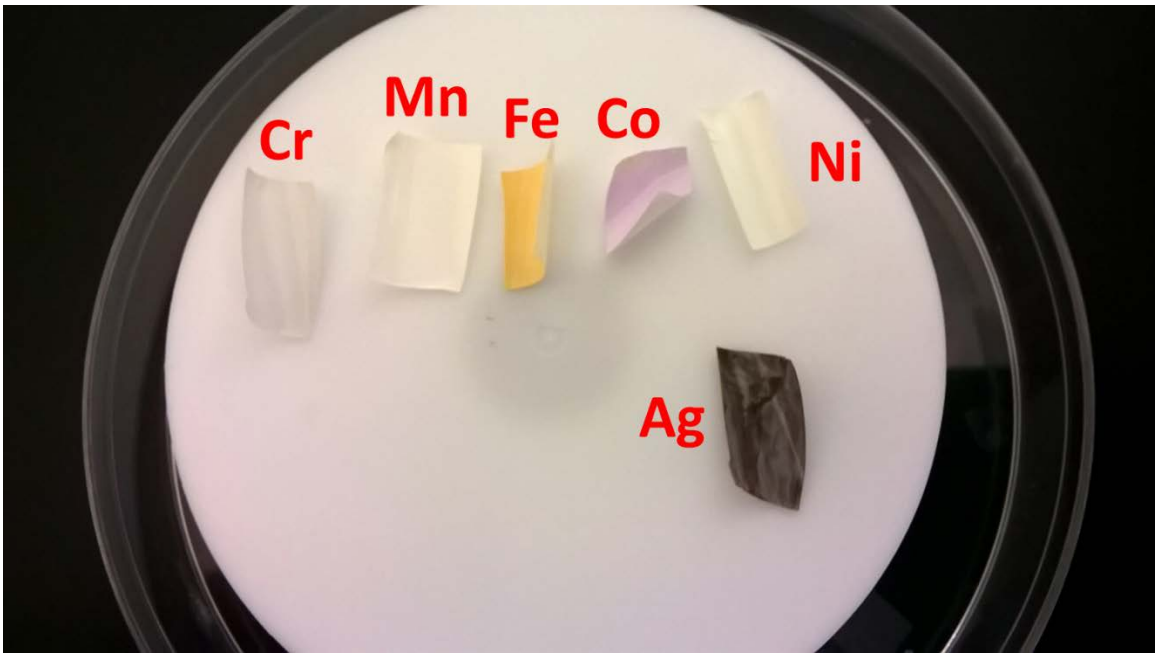

Figure A2.4. Membranes complexed with various transition metals after acid hydrolysis.

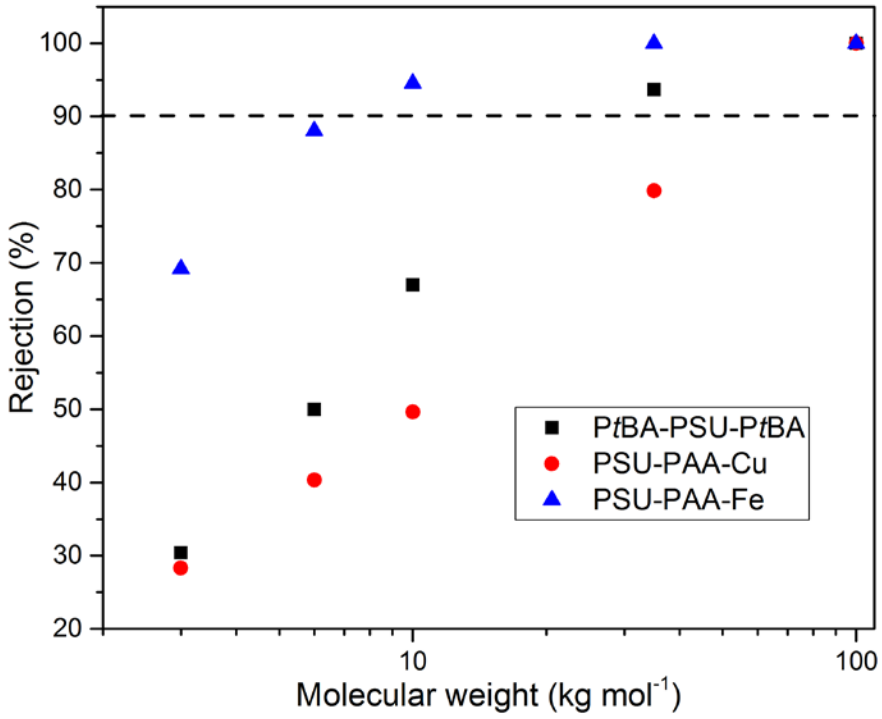

Figure A2.5. Rejection of poly(ethylene glycol) for the original and modified membranes as a function of molecular weight.

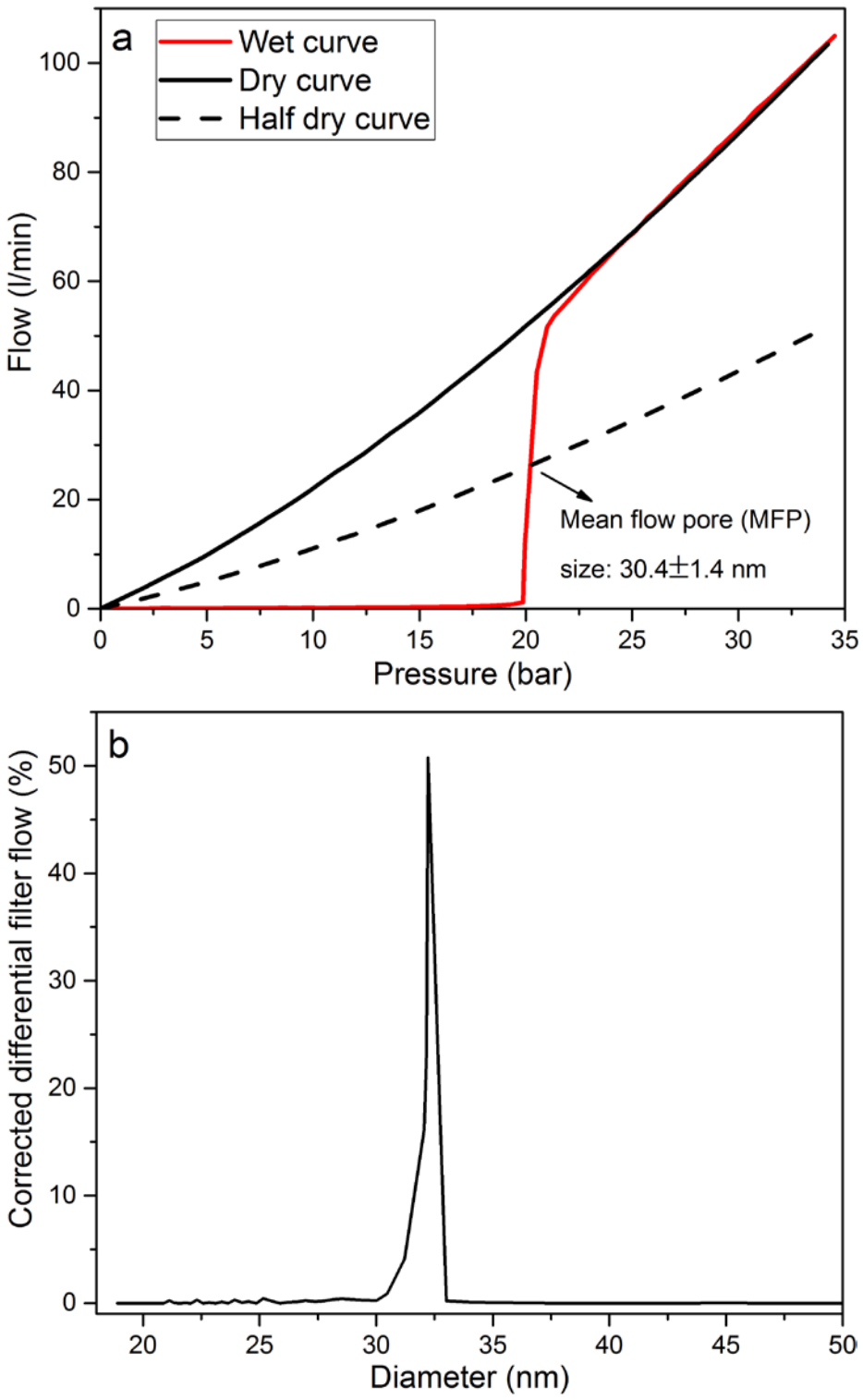

Figure A2.6. Flow-pressure curve (a) and pore size distribution (b) of P*t*BA-PSU-P*t*BA membrane obtained from capillary flow porometry.

Computational Model for P*t*BA-PSU-P*t*BA

Dissipative Particle Dynamics (DPD) Method

In DPD the dynamics and the balance of linear momentum are given by

$$\frac{d\mathbf{r}_i}{dt} = \mathbf{v}_i,$$
$$m_i \frac{d\mathbf{v}_i}{dt} = \mathbf{f}_i = \sum_{j \neq i} (\mathbf{F}_{ij}^C + \mathbf{F}_{ij}^D + \mathbf{F}_{ij}^R),$$

where r_i, v_i are the position and velocity of a particle *i*, respectively, m_i is its mass, and f_i is the net force on the particle. F_{ij}^C is a conservative contribution that models the affinity between particles, and can be related with the Flory-Huggins interactions parameters.[1] The term F_{ij}^D is a dissipative contribution that models viscous effects, and $F_{ij}^R$is a stochastic force. For polymeric systems the conservative force is decomposed in bead-bead (F_{ij}^B) and bead-spring (F_{ij}^S) (when particles are connected) interactions, where $F_{ij}^C = F_{ij}^B + F_{ij}^S$. In this work, the bead-bead and bead-spring potentials are given by

$$u_{ij}^B = \frac{a_{ij}}{2r_c}(r_{ij} - r_c)^2,$$
$$u_{ij}^S = \frac{K_s}{2}(r_{ij} - r_o)^2,$$

where a_{ij} accounts for the affinity between species i and j, K_s is the spring constant, and r_o is the equilibrium distance between connected particles.

The dissipative and random forces are defined as

$$\mathbf{F}_{ij}^{D} = -\gamma\omega^{D}(r_{ij})\left(\frac{\mathbf{r}_{ij}}{|r_{ij}|}\cdot\mathbf{v}_{ij}\right)\frac{\mathbf{r}_{ij}}{|r_{ij}|},$$
$$\mathbf{F}_{ij}^{R} = \sigma\omega^{R}(r_{ij})\zeta\Delta t^{-1/2}\frac{\mathbf{r}_{ij}}{|r_{ij}|},$$

where ω^D and ω^R are weighting function, such that $\omega^D(r_{ij}) = [\omega^R(r_{ij})]^2$, γ and σ are the friction coefficient and the noise amplitude, respectively. The term ζ is a random number with zero mean and unit variance. The parameters γ and σ are related by $\sigma^2 = 2\gamma k_B T$, where k_B is the Boltzmann constant and T is the equilibrium temperature. The most common form of the potential $\omega^D(r_{ij})$ is given by

$$\omega^{D}(r_{ij}) = [\omega^{R}(r_{ij})]^2 = \begin{cases} (1 - r_{ij}/r_c)^2; & (r_{ij} < r_c), \\ 0; & (r_{ij} \geq r_c), \end{cases}$$

Simulation Details

Triblock copolymers BAB were constructed using spring potentials, with spring constant $K_s = 50k_bT$ and equilibrium distance $r_o = 0.8$. The $PtBA_{30k}$-PSU_{14k}-$PtBA_{30k}$ molecules are discretized using 148 particles, while the solvent is modeled as a set of single solvent particles with a polymer-solvent interaction. The size of block is defined from the experimental composition of the block copolymer. The study of the polymer concentration influence over the morphology of the micelles, the amount of BAB in the simulations was varied from 2 to 18%.

According to the Flory-Huggins (F-H) interaction parameters the interaction parameters a_{ij} of the DPD model can be defined (R. D. Groot, P. B. Warren, The Journal of Chemical Physics 1997, 107, 4423). We choose a_{ij} according to the solvent quality for each block (N. Moreno, S. P. Nunes, K.-V. Peinemann, V. M. Calo, Macromolecules

2015, 48, 8036). The F-H parameters (χ_{is}) can be derived from the solubility parameters of the polymer and solvent (*i.e.*, δ_i and δ_s) by the equation

$$\chi_{is} = \frac{V_s}{RT}(\delta_i - \delta_s)^2,$$

where *R, T* are the gas constant and temperature, respectively. V_s = 92.5 cm^3/gmol is the molar volume of the solvent, DMAc. The solubility parameters can be computed from the Hansen's solubility parameters (*i.e.*, dispersive δ_d, polar δ_p, and hydrogen bond δ_h interactions), presented in Table A2.1 (C. M. Hansen, Hansen solubility parameters: a user's handbook, CRC press, 2007). The solvent quality and the phase diagram of the block copolymer solutions are governed by enthalpic (χ) and entropic (N) contributions, where N is the degree of polymerization. This contributions are typically expressed as the product, χN. In Table A2.2 the computed values of χ and χN are presented. Based on the magnitude of the F-H interactions the solvent is slightly poorer with PtBA block (χ > 0.5), while is practically a theta solvent ($\chi \approx 0.5$) for the PSU block. In the case of PtBA we must note that despite the larger value of the F-H parameter, it is known that the

Table A2.1. DPD interaction parameters used in the modeling of BAB block copolymer self-assembly

$\Delta a_{ij} = a_{ij} - a_{ss}$	P*t*BA	PSU	DMAc
P*t*BA	0.0	6.0	5.0
PSU		0.0	3.0
DMAc			0.0

Table A2.2. Flory-Huggins interaction parameters computed for the blocks P*t*BA$_{30k}$ and PSU$_{14k}$ in DMAc

	$\chi_{polymer\text{-}solvent}$	χN
P*t*BA	1.35	40.
PSU	0.49	7

homopolymer is soluble in DMAc. Therefore we use the magnitude of these parameters as a reference of the relative affinity between the species with the solvent.

Herein the affinity between the constituent is given by $\Delta a_{ij} = a_{ij} - a_{ss,}$ where $a_{ss} = 25.0$ is the solvent-solvent interactions. Interactions between components of the same type were chosen equal for any specie *i* (*i. e.*, $a_{ii} = 0$). Supplementary Table A2.1 compiles the values of Δa used in all the simulations.

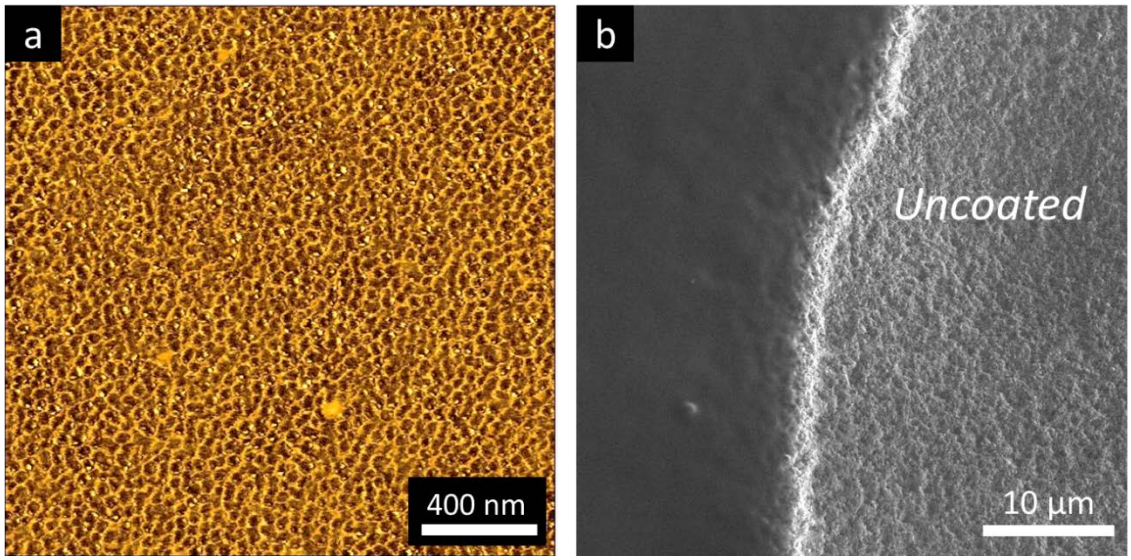

Figure A3.1. (a) AFM phase image of PAA-PSU-PAA thin film on ceramic membrane after thermal annealing and (b) SEM image of partially coated ceramic membrane on which right region is uncoated.

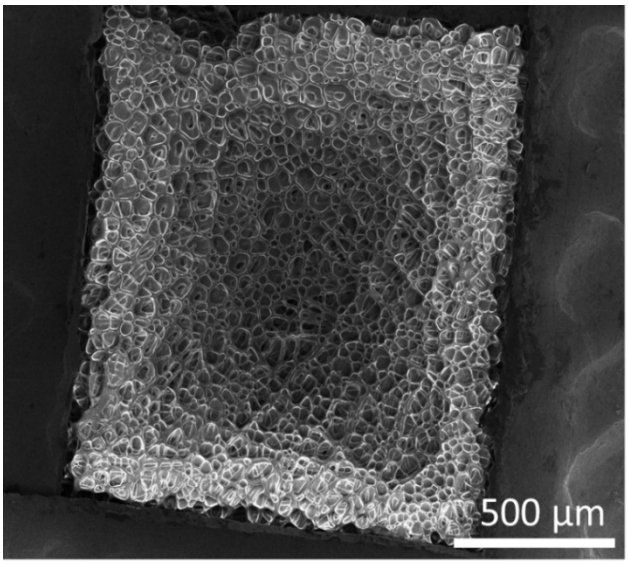

Figure A3.2. Surface SEM image of PAA-PSU-PAA membranes from 20 wt% polymer solution in DMF/THF/acetone solution (10/45/45) formed in a pure water coagulation bath.

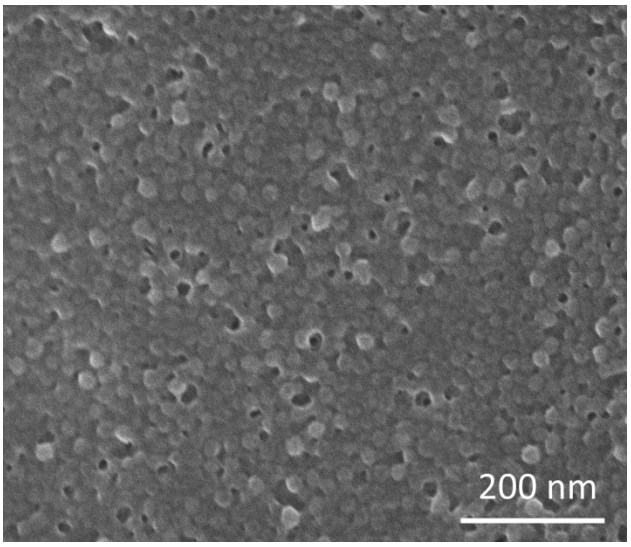

Figure A3.3. Surface SEM image of PAA-PSU-PAA membranes from 20 wt% polymer solution in DMF/THF/acetone solution (10/45/45) with 0.1 M $CuSO_4$ and a reduced evaporation time (1 min).

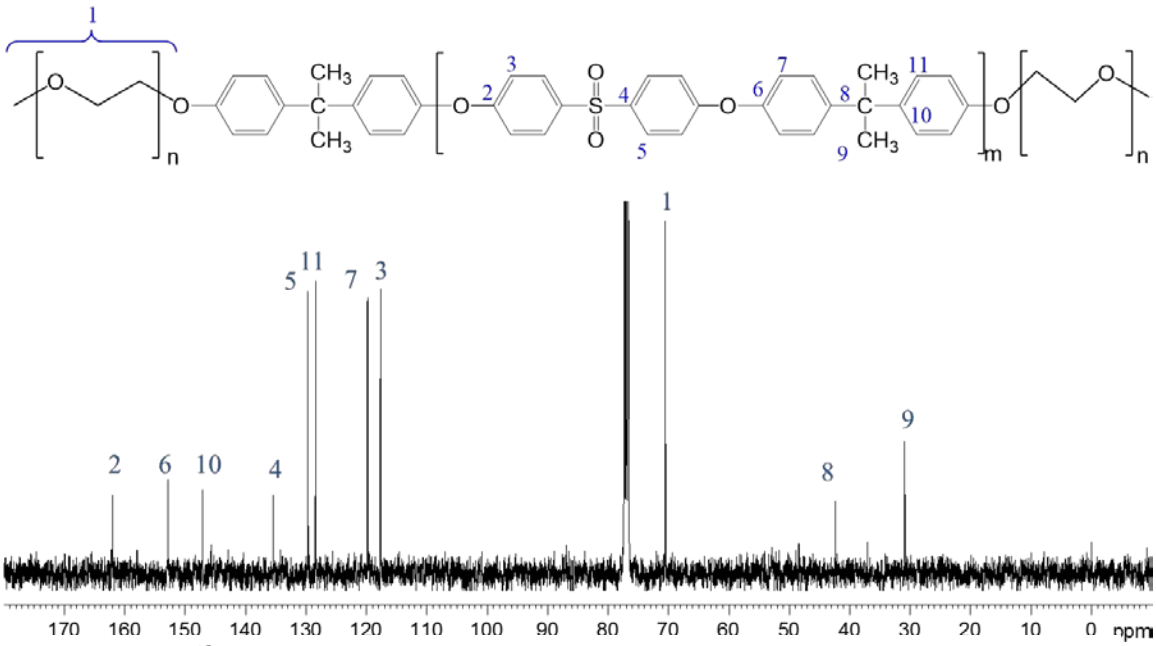

Figure A3.4. ^{13}C NMR spectrum for PEG-PSU-PEG in $CDCl_3$.

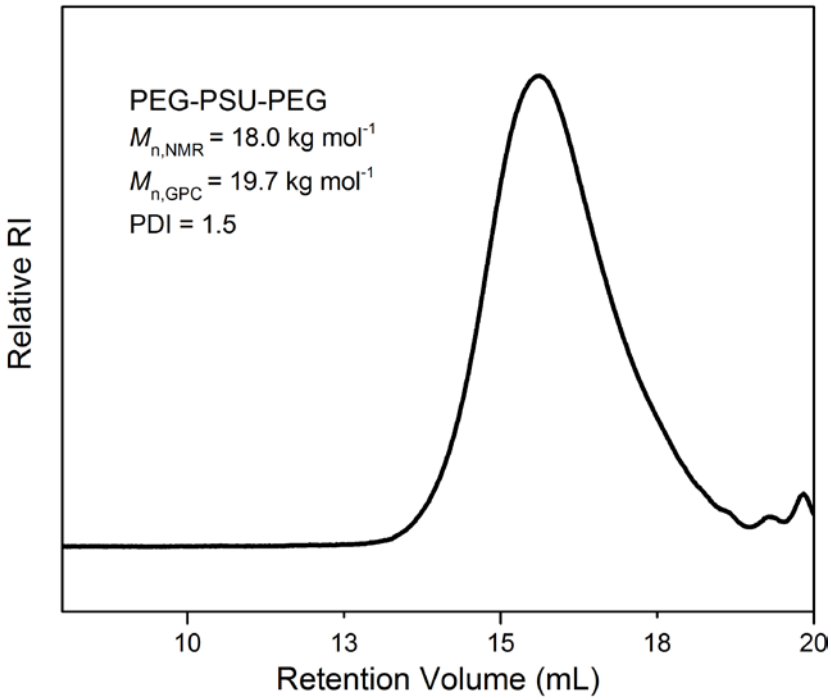

Figure A3.5. GPC curves of PEG-PSU-PEG in THF using PS standard.

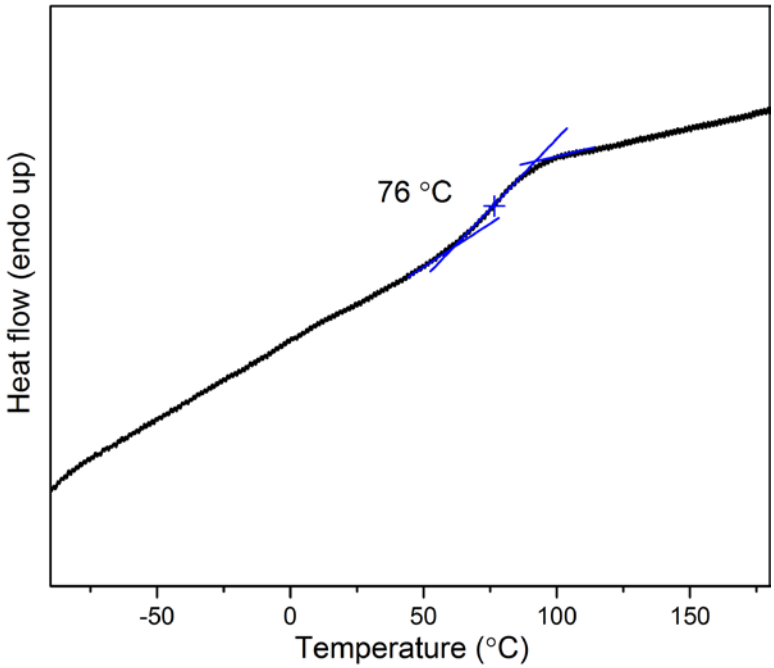

Figure A3.6. DSC curve for PEG-PSU-PEG having a glass transition temperature (T_g) of 76 °C.

PSU-$CH_2Cl_{0.23}$

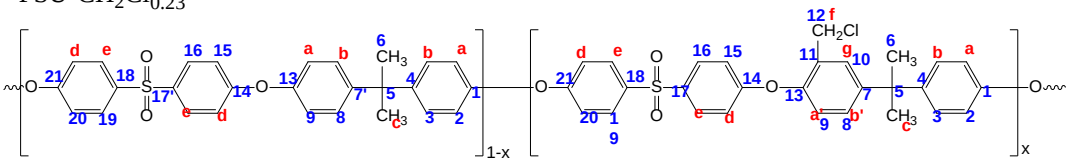

PSU-$CH_2N_{3;0.23}$

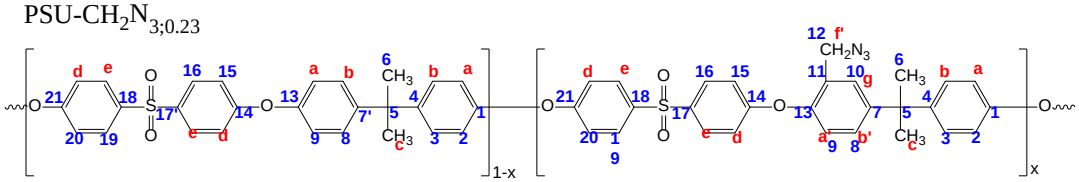

PSU-$TrN_{0.23}$

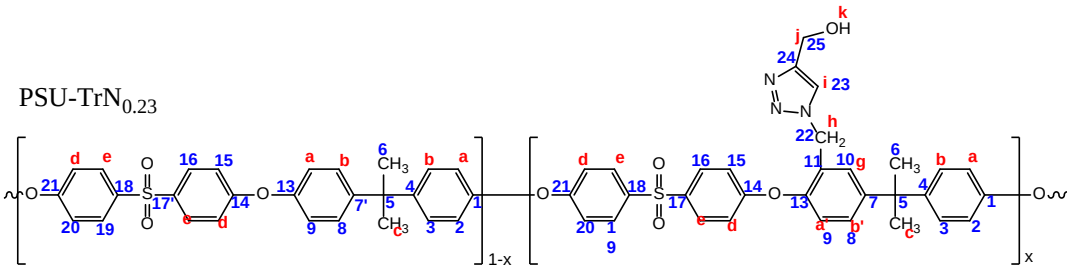

Figure A4.1. The numbering of ^{1}H and ^{13}C for NMR chemical shifts of PSU-$CH_2Cl_{0.23}$, PSU-$CH_2N_{3;0.23}$ and PSU-$TrN_{0.23}$.

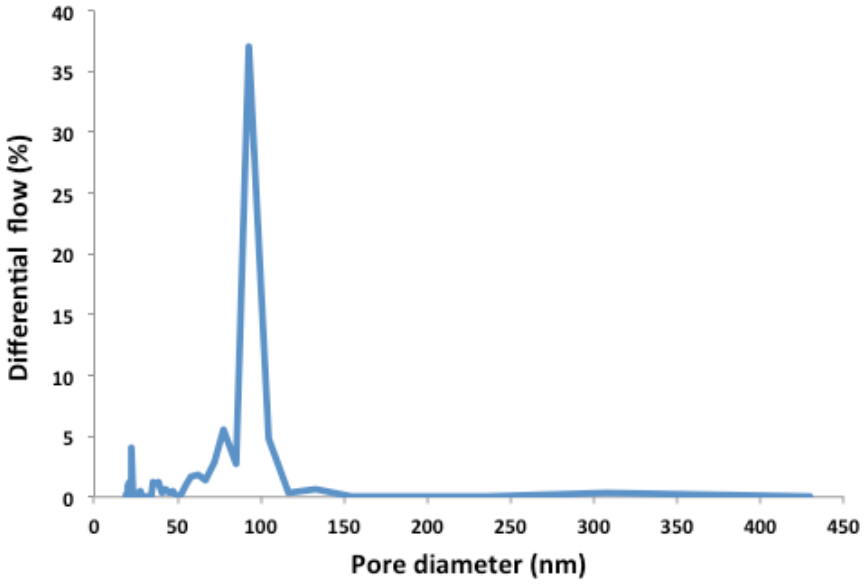

Figure A4.2. Pore size distribution of membrane prepared from PSU-$TrN_{0.94}$ in NMP/H_2O.

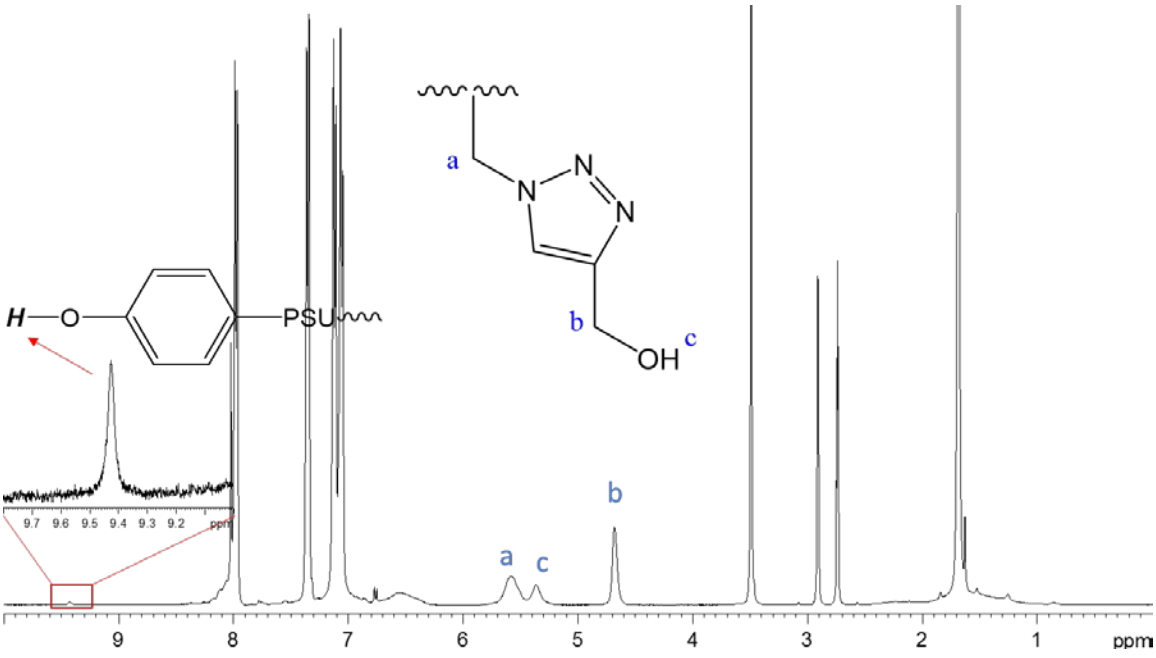

Figure A4.3. ^{1}H NMR spectrum of PTrN-PSU-PTrN in DMF-d7 prepared by using the same PSU maco-CTA for P*t*BA-PSU-P*t*BA.

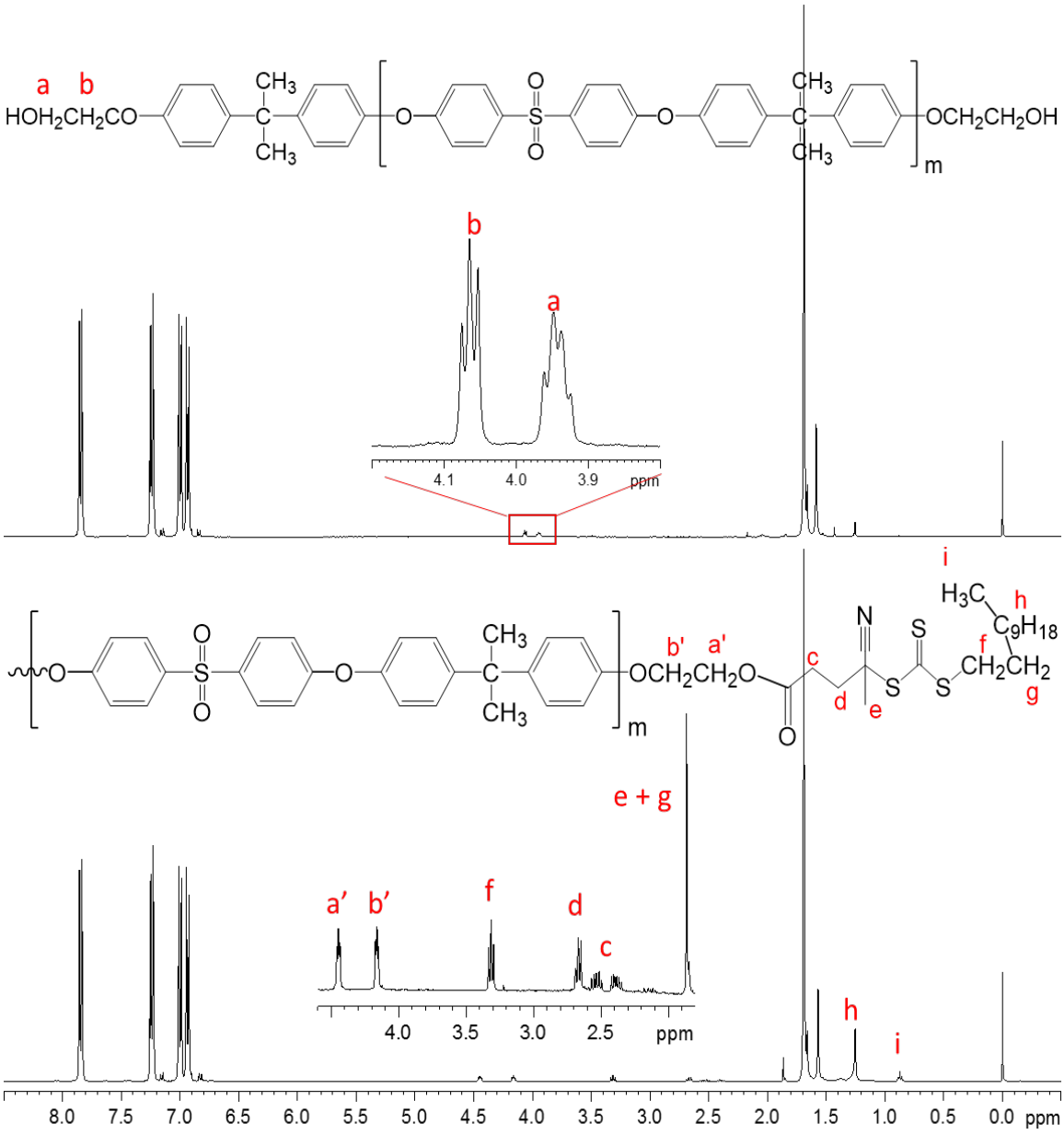

Figure A4.4. ^{1}H NMR spectra of HE-PSU-HE and its derivative, CTA-PSU-CTA in $CDCl_3$.

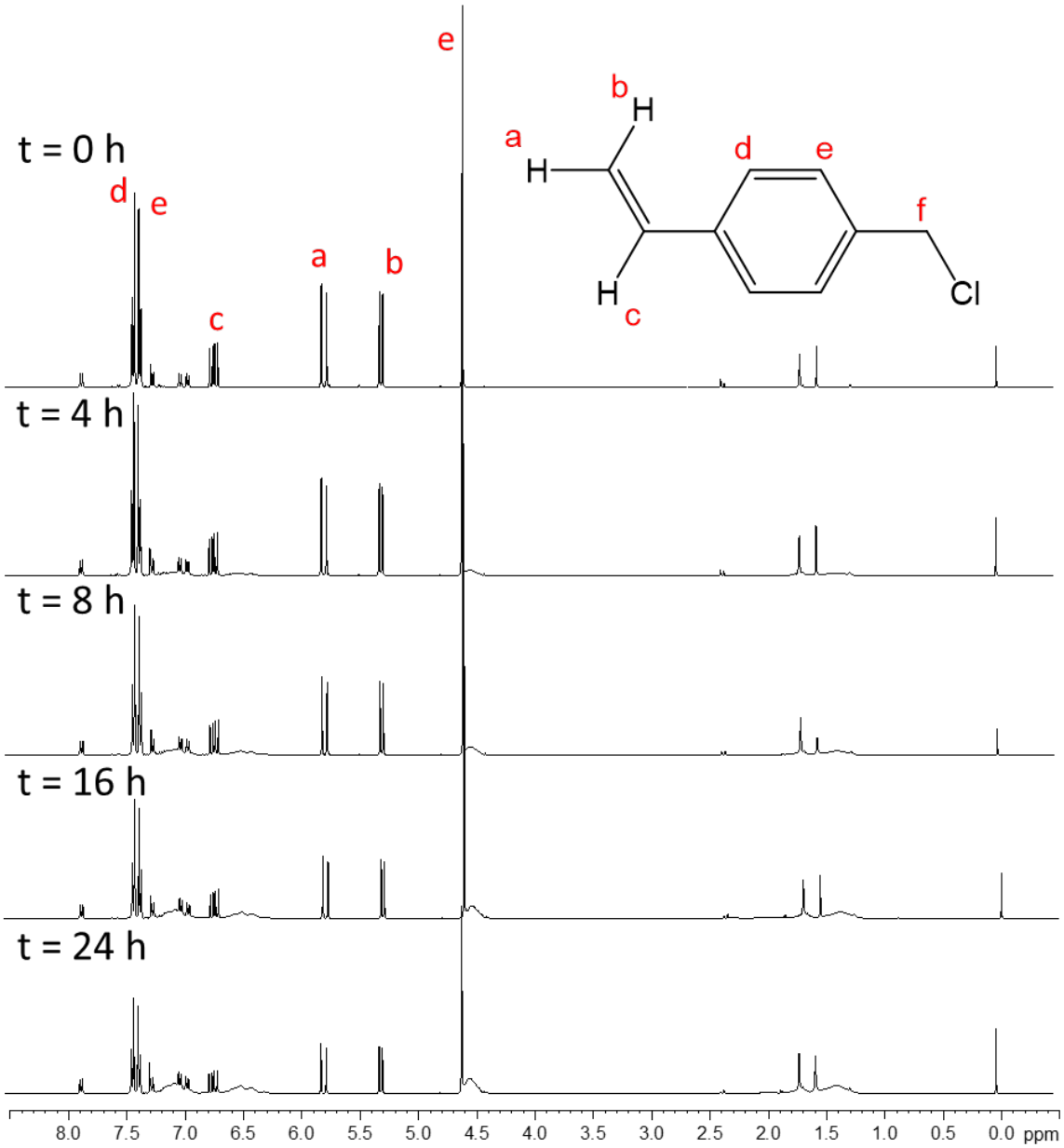

Figure A4.5. ^{1}H NMR spectra of samples in $CDCl_3$ taken from bulk solution of RAFT polymerization after different times, with [AIBN]: [CTA-PSU-CTA]: [VBC] = 0.25: 1: 400 in bulk at 70 °C.

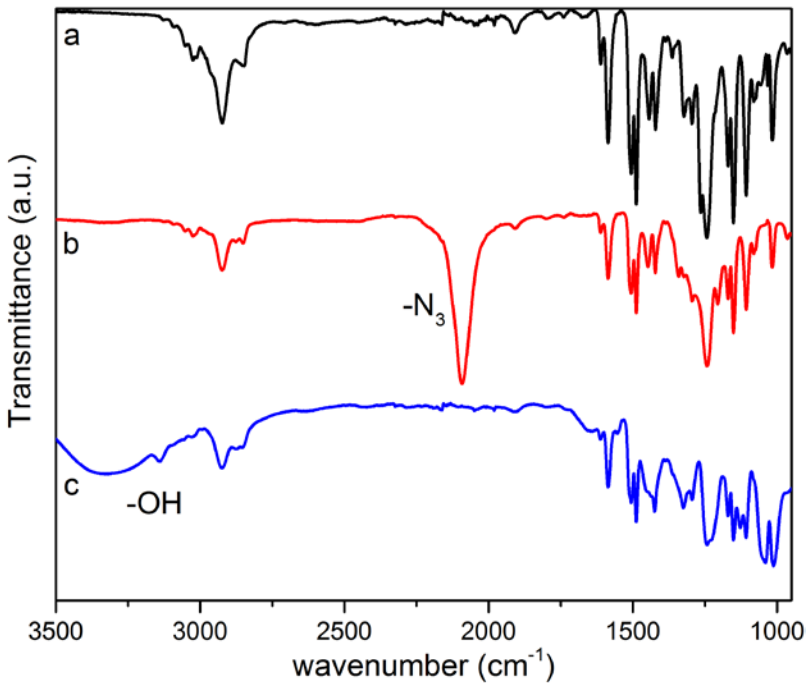

Figure A4.6. FTIR spectra of (a) PVBC-PSU-PVBC, (b) PN_3-PSU-PN_3 and (c) PTrN-PSU-PTrN.

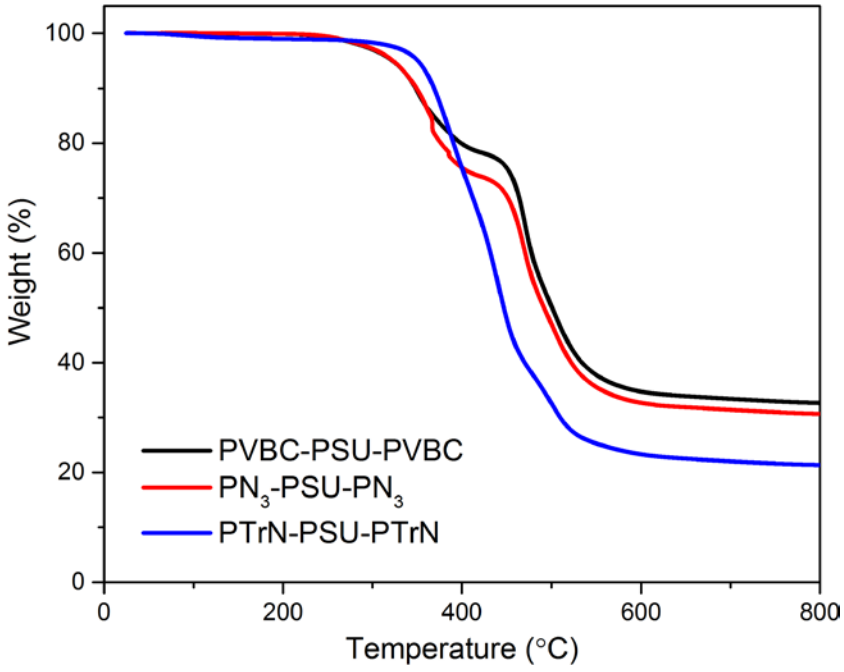

Figure A4.7. TGA curves of (a) PVBC-PSU-PVBC, (b) PN_3-PSU-PN_3 and (c) PTrN-PSU-PTrN under N_2.

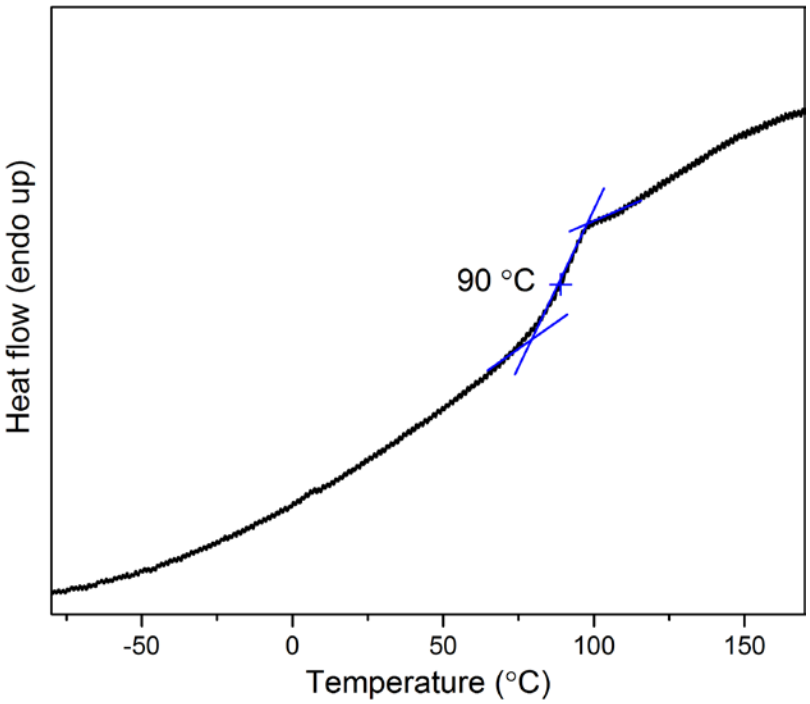

Figure A4.8. DSC curve of PTrN-PSU-PTrN having a glass transition temperature at 90 °C.

Table A4.1. Solubility of polytriazole homopolymer in different solvents (0 = insoluble; 1 = soluble)

Water	0	N,N-Dimethyl Acetamide	1
Methanol	0	Diethyl Ether	0
Ethanol	0	Tetrahydrofuran (THF)	0
1-Propanol	0	1,4-Dioxane	0
2-Propanol	0	Diphenyl Ether	0
1-Butanol	0	Dibenzyl Ether	0
Ethylene Glycol	1	Ethyl Acetate	0
1,3-Propanediol	0	Acetic Acid	0

(Trimethyleneglycol)			
Triethylene Glycol	1	Hexane	0
Glycerol	0	Cyclohexane	0
1,4-Butanediol	0	Decane	0
Triethylene Glycol Monomethyl Ether	1	Benzene	0
Diethylene Glycol Monomethyl Ether	0	Aniline	0
Acetone	0	Anisole	0
Methyl Ethyl Ketone (MEK)	0	Toluene	0
Methyl Isobutyl Ketone (MIBK)	0	Pyridine	1
γ-Butyrolactone (GBL)	0	p-Xylene	0
Acetonitrile	0	Methylene Dichloride (Dichloromethane)	0
Sulfolane (Tetramethylene Sulfone)	0	Chloroform	0
Dimethyl Formamide (DMF)	1	1,1,2-Trichloroethane	0
Dimethyl Sulfoxide (DMSO)	1	Dimethyl Carbonate	0
N-Methyl-2-Pyrrolidone (NMP)	1	Propylene Carbonate	0